CZECH TECHNICAL UNIVERSITY IN PRAGUE
Faculty of Nuclear Sciences and Physical Engineering
Department of Physics

Doctoral thesis

Measurement of open-charm mesons in heavy-ion collisions by the STAR experiment

Ing. Jan Vaněk

Prague, 2022

ČESKÉ VYSOKÉ UČENÍ TECHNICKÉ V PRAZE
Fakulta Jaderná a Fyzikálně Inženýrská
Katedra Fyziky

Disertační práce

Měření mesonů s otevřeným půvabem v jádro-jaderných srážkách na experimentu STAR

Praha, 2022 **Ing. Jan Vaněk**

Prohlášení:

Prohlašuji, že jsem svou disertační práci vypracoval samostatně a použil jsem pouze podklady (literaturu, software, atd.) uvedené v přiloženém seznamu.

Nemám závažný důvod proti užití tohoto školního díla ve smyslu §60 Zákona č. 121/2000 Sb., o právu autorském, o právech souvisejících s právem autorským a o změně některých zákonů (autorský zákon).

V Praze dne 09. 05. 2022 Ing. Jan Vaněk

Bibliographic entry

Author	Ing. Jan Vaněk
Title	Measurement of open-charm mesons in heavy-ion collisions by the STAR experiment
Degree programme	Application of natural sciences
Field of study	Nuclear engineering
Supervisor	doc. Mgr. Jaroslav Bielčík, Ph.D., Physics Department Faculty of Nuclear Sciences and Physical Engineering Czech Technical University in Prague
Supervisor specialist	doc. RNDr. Jana Bielčíková, Ph.D., Nuclear Physics Institute Czech Academy of Sciences
Academic year	2021/2022
Number of pages	233
Key words	Heavy-ion collisions, open heavy-flavor mesons, quark-gluon plasma STAR experiment

Bibliografický záznam

Autor	Ing. Jan Vaněk
Název práce	Měření mezonů s otevřeným půvabem v jádro-jaderných srážkách na experimentu STAR
Studijní program	Aplikace přírodních věd
Studijní obor	Jaderné inženýrství
Školitel	doc. Mgr. Jaroslav Bielčík, Ph.D., Katedra fyziky Fakulta jaderná a fyzikálně inženýrská České vysoké učení technické v Praze
Školitel specialista	doc. RNDr. Jana Bielčíková, Ph.D., Ústav jaderné fyziky Akademie věd České republiky
Akademický rok	2021/2022
Počet stran	233
Klíčová slova	Jádro-jádrové srážky, mezony s otevřeným půvabem, kvark-gluonové plazma experiment STAR

Acknowledgement

I would like to thank Jaroslav Bielčík and Jana Bielčíková for their patient guidance and support throughout my Ph.D. studies. I am also very grateful to Xin Dong, Guannan Xie, and Xinyue Ju for their help with the analysis. Many thanks belong also to my colleagues from the Nuclear Physics Institute (NPI) of the Czech Academy of Sciences, Faculty of Nuclear Sciences and Physical Engineering of the Czech Technical University in Prague, and from STAR Heavy Flavor Physics Working Group. And last, but not least, I would like to thank my family and friends for their support.

Abstract

One of the main goals of the STAR experiment is to study properties of the Quark-Gluon Plasma (QGP). An excellent probe of the QGP are charm quarks, as they are created in very early stages of the heavy-in collisions in the hard partonic scatterings. As a result, they experience the whole evolution of the hot and dense medium. The STAR experiment is able to access information about charm quark production via direct topological reconstruction of hadronic decays of the open-charm hadrons, utilizing the excellent pointing resolution of the Heavy Flavor Tracker detector. This thesis discusses the analysis of $D^{\pm}$ meson production in Au+Au collisions at $\sqrt{s_{\mathrm{NN}}} = 200\,\mathrm{GeV}$ collected by the STAR experiment in year 2016. The $D^{\pm}$ mesons are reconstructed via their hadronic decay $D^{\pm} \to K^{\mp}\pi^{\pm}\pi^{\pm}$. The topological selection criteria are optimised using supervised machine learning techniques, utilizing the ROOT package TMVA. The measured 2016 invariant yield of $D^{\pm}$ mesons is combined with that measured in year 2014 and subsequently used to calculate the nuclear modification factor, $D^{\pm}/D^{0}$ yield ratio, and total charm production cross section in Au+Au collisions at $\sqrt{s_{\mathrm{NN}}} = 200\,\mathrm{GeV}$. The nuclear modification factor reveals significant suppression of high transverse momentum $D^{\pm}$ mesons in 0-10% central Au+Au collisions, which indicates significant energy loss of charm quarks in the QGP. The measured $D^{\pm}/D^{0}$ yield ratio appears to be consistent with PYTHIA calculation within the uncertainties. The total charm cross section per nucleon-nucleon collision in 10–40% Au+Au collisions at $\sqrt{s_{\mathrm{NN}}} = 200\,\mathrm{GeV}$ is found to be $113.3 \pm 6.2(\mathrm{stat}) \pm 27.2(\mathrm{sys})\ \mu\mathrm{b}$, consistent with the total cross section measured in p+p collisions at the same collision energy.

Abstrakt

Jedním z hlavních cílů experimentu STAR je studium vlastností kvark-gluonového plazmatu (QGP). Ideální sondou QGP jsou půvabné kvarky, protože se tvoří ve velmi rané fázi srážek těžkých jader, v tvrdých partonových srážkách. To znamená, že jsou přítomny po celou dobu evoluce QGP. V experimentu STAR je možné měřit produkci půvabných kvarků prostřednictvím přímé topologické rekonstrukce hadronových rozpadů hadronů s otevřeným půvabem, pomocí velmi přesného prostorového rozlišení detektoru Heavy Flavor Tracker. Tato práce obsahuje detailní popis analýzy produkce mezonů $D^{\pm}$ ve srážkách Au+Au při energii $\sqrt{s_{\mathrm{NN}}} = 200\,\mathrm{GeV}$, naměřených experimentem STAR v roce 2016. Mezony $D^{\pm}$ jsou rekonstruovány prostřednictvím jejich hadronového rozpadového kanálu $D^{\pm} \to K^{\mp}\pi^{\pm}\pi^{\pm}$. Topologická výběrová kritéria jsou optimalizována pomocí strojového učení s pomocí ROOT balíčku TMVA. Invariantní výtěžek $D^{\pm}$ mezonů naměřený v datech z roku 2016 je skombinován s měřením z roku 2014 a následně použit při výpočtu jaderného modifikačního faktoru, poměru výtěžků $D^{\pm}/D^{0}$ a celkového účinného průřezu produkce půvabných kvarků ve srážkách Au+Au při energii $\sqrt{s_{\mathrm{NN}}} = 200\,\mathrm{GeV}$. Z měření jaderného modifikačního faktoru je patrné signifikantní potlačení produkce $D^{\pm}$ mezonů s velkou příčnou hybností ve srážkách Au+Au s centralitou 0-10%, které je pravděpodobně způsobeno energetickými ztrátami půvabných kvarků v QGP. Poměr výtěžků $D^{\pm}/D^{0}$ se v rámci chyb měření neliší od teoretického výpočtu tohoto poměru pomocí PYTHIA. Celkový účinný průřez produkce půvabných kvarků ve srážkách Au+Au při energii $\sqrt{s_{\mathrm{NN}}} = 200\,\mathrm{GeV}$ s centralitou 10-40% byl změřen s hodnotou $113.3 \pm 6.2(\mathrm{stat}) \pm 27.2(\mathrm{sys})$ μb, která souhlasí s hodnotou změřenou ve srážkách p+p při stejné energii.

Contents

List of Figures **xx**

List of Tables **xxi**

Introduction **1**

1 Heavy-ion collisions **7**
1.1 Physics motivation 7
1.2 Heavy-ion collisions 9
1.2.1 General properties of heavy-ion collisions 9
1.2.2 Time evolution of heavy-ion collisions 11
1.3 Experimental signatures of the QGP 12

2 Open-charm hadrons **33**
2.1 Properties of open-charm hadrons 33
2.2 Open-charm hadrons in heavy-ion collisions 37
2.3 Recent measurements of open-charm in heavy-ion collisions 40
2.3.1 Open heavy-flavor hadrons measured by STAR 41
2.3.2 Open-heavy flavor hadrons measured by ALICE 48

3 The STAR experiment **53**
3.1 Relativistic Heavy-Ion Collider 53
3.2 STAR detector 55
3.2.1 Heavy Flavor Tracker 57
3.2.2 Time Projection Chamber 59
3.2.3 Time-Of-Flight detector 62
3.2.4 Trigger detectors 64
3.2.5 Other STAR detector systems 64

4 Reconstruction of $D^{\pm}$ mesons in Au+Au collisions at $\sqrt{s_{NN}} = 200\,GeV$ **67**
4.1 Data-set and event selection 68
4.1.1 Selection criteria 69

4.1.2 Raw yield extraction . . . 79
4.2 $D^{\pm}$ reconstruction efficiency . . . 80
4.2.1 Data-driven fast-simulator . . . 80
4.2.2 PID efficiency . . . 89
4.2.3 Total reconstruction efficiency . . . 96
4.3 Systematic uncertainties . . . 96
4.3.1 Invariant spectra . . . 96
4.3.2 Nuclear modification factor . . . 101
4.3.3 $D^{\pm}/D^{0}$ yield ratio . . . 102
4.4 Results . . . 107
4.4.1 Invariant spectrum of $D^{\pm}$ mesons . . . 107
4.4.2 Nuclear modification factor . . . 108
4.4.3 $D^{\pm}/D^{0}$ yield ratio . . . 109
4.4.4 Total charm cross section . . . 112

Summary and discussion **115**

Appendices **121**

A Data-set quality assurance **123**

B Invariant mass spectra **127**

C TMVA selection criteria optimization **135**

D TPC tracking efficiency **143**

E Other research activities **149**

F Internships **151**

G Public presentations **153**

H Publications **161**

List of Figures

1.1 Phase diagram of nuclear matter. 8
1.2 Coordinate system in heavy-ion collisions. 10
1.3 Impact parameter definition. 11
1.4 Phases of a heavy-ion collision. 12
1.5 Time evolution of a heavy-ion collision. 13
1.6 R_{AA} of charged and neutral particles measured by various experiments. . 14
1.7 Cartoon of melting temperature of different quarkonia and Υ(1S) and Υ(2S) measurements by CMS in Pb+Pb at $\sqrt{s_{\mathrm{NN}}} = 2.76\,\mathrm{TeV}$. 15
1.8 Proton/pion yield ratio measured in Au+Au and d+Au collisions by STAR. 17
1.9 Schematic view of a semi-central heavy-ion collision. 18
1.10 Glauber model simulation of a heavy-ion collision. 19
1.11 Glauber model simulation of Au+Au collision at $\sqrt{s_{\mathrm{NN}}} = 200\,\mathrm{GeV}$. . . . 20
1.12 Elliptic flow of light flavor hadrons in Au+Au collisions at $\sqrt{s_{\mathrm{NN}}} = 200\,\mathrm{GeV}$ by STAR. 21
1.13 Harmonic flow measured in Pb+Pb collisions at $\sqrt{s_{\mathrm{NN}}} = 2.76\,\mathrm{GeV}$ by ATLAS. 22
1.14 Schematic view of a heavy-ion collision in reaction plane (a) and in transverse plain (b). 23
1.15 Directed flow measured by STAR in 10-40% central Au+Au collisions at multiple energies. 23
1.16 Elliptic and triangular flow measured in p+p, p+Pb, and Pb+Pb collisions by CMS. 24
1.17 Schematic view of central heavy-ion collision with jets propagating through QGP. 26
1.18 Two-particle azimuthal distributions of charged hadrons in p+p, d+Au, and Au+Au collisions. 27
1.19 $I_{\mathrm{AA}}^{\mathrm{jet}}$ as a function of p_{T} measured in Pb+Pb collisions at $\sqrt{s_{\mathrm{NN}}} = 5.02\,\mathrm{TeV}$. 28
1.20 R_{AA} of charged jets in Au+Au and Pb+Pb collisions. 29
1.21 R_{AA} of jets in Au+Au from Hybrid model. 30

2.1 Discovery of D^0 meson. . . . 35
2.2 Discovery of $\Lambda_c^{\pm}$ baryon. . . . 36
2.3 Production cross section of D^0 and $D^{\pm}$ mesons measured by ALICE in p+p collisions at $\sqrt{s} = 7\,\mathrm{TeV}$. . . . 38
2.4 Theoretical prediction for dv_1/dy of D^0 and $\bar{D}^0$ mesons. . . . 39
2.5 R_{AA} of D^0, π mesons, and charged hadrons measured by STAR and ALICE. 42
2.6 Centrality of D^0 meson R_{AA} measured by STAR. . . . 43
2.7 The elliptic flow of D^0 mesons and light-flavor hadrons. . . . 44
2.8 The $\Lambda_c^{\pm}/D^0$ yield ratio as a function of p_T and collision centrality. . . . 45
2.9 $D_s^{\pm}/D^0$ yield ratio as a function of p_T for four Au+Au collision centralities. 46
2.10 Directed flow of D^0 and $\overline{D^0}$ mesons as a function rapidity y. . . . 46
2.11 Ratio of R_{CP} of electrons originating from decay of open-bottom and open-charm hadrons. . . . 47
2.12 R_{AA} of D mesons measured by ALICE in central Pb+Pb collisions. . . . 48
2.13 R_{AA} and v_2 of D mesons measured by ALICE in Pb+Pb collisions. . . . 49
2.14 Λ_c^+/D^0 yield ratio measured by ALICE in Pb+Pb collisions. . . . 50
2.15 R_{AA} of Λ_c baryons measured by ALICE in Pb+Pb collisions. . . . 51
2.16 Comparison of R_{AA} of non-promt and promt D^0 mesons measured by ALICE. . . . 52

3.1 Map of BNL accelerator complex. . . . 54
3.2 Summary of collision systems used at RHIC. . . . 55
3.3 The STAR detector. . . . 56
3.4 Schematic view of the STAR Heavy Flavor Tracker detector. . . . 57
3.5 Spatial resolution of the STAR HFT. . . . 58
3.6 Energy loss of charged tracks inside STAR TPC. . . . 59
3.7 Cutaway schematic view of the STAR TPC. . . . 60
3.8 STAR TPC MWPC module. . . . 61
3.9 STAR TOF MRPC module. . . . 62
3.10 PID resolution of STAR TOF system. . . . 63

4.1 Feynman diagram of two hadronic decay channels of $D^{\pm}$ mesons. . . . 67
4.2 Number of events statistics. . . . 70
4.3 The dE/dx (left) and $1/\beta$ (right) distributions from the TPC and TOF. . 71
4.4 Topology of a three body decay 72
4.5 Topological distributions for the TMVA. . . . 73
4.6 Output distributions from the TMVA. . . . 74
4.7 Performance of the TMVA when applied to the real data. . . . 75
4.8 Improvement of $D^{\pm}$ raw yield extraction with the TMVA. . . . 76
4.9 $K\pi\pi$ invariant mass spectra. . . . 79

4.10 Momentum resolution of π^+ mesons. 83
4.11 Momentum resolution of π^- mesons. 84
4.12 Momentum resolution of K^+ mesons. 84
4.13 Momentum resolution of K^- mesons. 85
4.14 TPC tracking efficiency of π^+ in *st_physics* stream. 85
4.15 TPC tracking efficiency of K^+ in *st_physics* stream. 86
4.16 The $\pi^+\pi^-$ pair invariant mass distribution before and after combinatorial background subtraction. 90
4.17 Fitted $n\sigma_\pi$ distributions. 91
4.18 Fitted $|1/\beta - 1/\beta_\pi|$ distributions. 92
4.19 PID efficiency of the TPC (left) and TOF (right) for $\pi^\pm$ mesons. 93
4.20 Fitted $n\sigma_K$ distributions. 93
4.21 Fitted $|1/\beta - 1/\beta_K|$ distributions. 94
4.22 PID efficiency of the TPC (left) and TOF (right) for $K^\pm$ mesons. 94
4.23 TOF matching efficiency of $\pi^\pm$ and $K^\pm$ mesons. 95
4.24 Total single particle PID efficiency of $\pi^\pm$ and $K^\pm$ mesons. 95
4.25 $D^\pm$ reconstruction efficiency in Run16. 96
4.26 Systematic uncertainties of Run16 invariant spectra. 97
4.27 Systematic uncertainties from cuts variation for loose and tight topological cuts. 99
4.28 Double ratio used for the TPC tracking efficiency systematic uncertainty of π^+. 100
4.29 Systematic uncertainties of the R_{AA}. 102
4.30 Systematic uncertainties of the Run14 $D^\pm/D^0$ yield ratio as a function of p_T. 103
4.31 Systematic uncertainties of the Run16 $D^\pm/D^0$ yield ratio as a function of p_T. 104
4.32 Systematic uncertainties of the Run14 $D^\pm/D^0$ yield ratio as a function of N_{part}. 106
4.33 Systematic uncertainties of the Run 16 $D^\pm/D^0$ yield ratio as a function of N_{part}. 106
4.34 Invariant spectra of D± mesons. 108
4.35 $(D^+ + D^-)/(D^0 + \overline{D^0})$ yield ratio from PYTHIA. 109
4.36 R_{AA} of D^0 and $D^\pm$ mesons measured in Au+Au collisions. 110
4.37 $(D^+ + D^-)/(D^0 + \overline{D^0})$ yield ratio as a function of p_T. 111
4.38 $(D^+ + D^-)/(D^0 + \overline{D^0})$ yield ratio as a function of centrality. 112

A.1 Mean RefMult per run in Run16 Au+Au at $\sqrt{s_{NN}} = 200\,GeV$ data-set. . 123

A.2 Mean TOF matching ratio per run in Run16 Au+Au at $\sqrt{s_{\mathrm{NN}}} = 200\,\mathrm{GeV}$ data-set. 124
A.3 Mean HFT matching ratio per run in Run16 Au+Au at $\sqrt{s_{\mathrm{NN}}} = 200\,\mathrm{GeV}$ data-set. 125

B.1 K$\pi\pi$ invariant mass spectra, 0-10% centrality. 128
B.2 K$\pi\pi$ invariant mass spectra, 0-10% centrality (continued). 129
B.3 K$\pi\pi$ invariant mass spectra, 10-40% centrality. 130
B.4 K$\pi\pi$ invariant mass spectra, 10-40% centrality (continued). 131
B.5 K$\pi\pi$ invariant mass spectra, 40-80% centrality. 132
B.6 K$\pi\pi$ invariant mass spectra, 40-80% centrality (continued). 133

C.1 (left) TMVA efficiencies with corresponding significance. (right) TMVA input distributions. Centrality 0-10%. 136
C.2 (left) TMVA efficiencies with corresponding significance. (right) TMVA input distributions. Centrality 0-10%. (continued) 137
C.3 (left) TMVA efficiencies with corresponding significance. (right) TMVA input distributions. Centrality 10-40%. 138
C.4 (left) TMVA efficiencies with corresponding significance. (right) TMVA input distributions. Centrality 10-40%. (continued) 139
C.5 (left) TMVA efficiencies with corresponding significance. (right) TMVA input distributions. Centrality 10-40%. (continued 2) 140
C.6 (left) TMVA efficiencies with corresponding significance. (right) TMVA input distributions. Centrality 40-80%. 141
C.7 (left) TMVA efficiencies with corresponding significance. (right) TMVA input distributions. Centrality 40-80%. (continued) 142

D.1 TPC tracking efficiency of π^- in *st_physics* stream. 143
D.2 TPC tracking efficiency of K^- in *st_physics* stream. 144
D.3 TPC tracking efficiency of π^+ in *st_sst* + *st_nosst* stream. 145
D.4 TPC tracking efficiency of π^- in *st_sst* + *st_nosst* stream. 146
D.5 TPC tracking efficiency of K^+ in *st_sst* + *st_nosst* stream. 147
D.6 TPC tracking efficiency of K^- in *st_sst* + *st_nosst* stream. 148

List of Tables

2.1 Basic properties of four ground states of open-charm hadrons. 34
2.2 List of open-charm hadrons measured at STAR using the HFT. 41

4.1 Basic properties of $D^{\pm}$ mesons. 67
4.2 List of centrality classes used in this analysis. 68
4.3 List of p_T bin edges used in this analysis. 68
4.4 Trigger IDs. 69
4.5 Event selection criteria. 69
4.6 Track selection criteria. 71
4.7 PID selection criteria. 71
4.8 Topological selection criteria. 72
4.9 $D^{\pm}$ meson raw yield for 0-10% central Au+Au collisions with TMVA. . . 77
4.10 $D^{\pm}$ meson raw yield for 10-40% central Au+Au collisions with TMVA. . . 77
4.11 $D^{\pm}$ meson raw yield for 40-80% central Au+Au collisions with TMVA. . . 78
4.12 Selection criteria used for momentum resolution and TPC tracking efficiency calculation. 82
4.13 Binning of space used for filling of DCA distributions. 87
4.14 Binning of space used for filling of HFT matching ratios. 87
4.15 Kinematic range used to generate $D^{\pm}$ mesons with EvtGen. 88
4.16 Topological selection criteria for K^0_s reconstruction. 89
4.17 Global systematic uncertainties of R_{AA}. 103
4.18 Total charm hadron production cross section in 10-40% central Au+Au collisions at $\sqrt{s_{NN}} = 200$ GeV. 113

Introduction

The STAR experiment is located at Brookhaven National Laboratory (BNL) on Long Island, New York, USA. It is the only experiment at the Relativistic Heavy-Ion Collider (RHIC) which is currently actively taking experimental data. Thanks to its full azimuthal and pseudorapidity $|\eta| < 1$ acceptance, combined with its exceptional capabilities in charged track reconstruction and particle identification, STAR is a very versatile detector which is able to study various physics topics. This versatility is further extended by the ability of RHIC to deliver beams of protons and many different nuclei species in a wide range of energies.

As a result, the physics program at STAR is rich and ranges from measurement of spin structure of proton, over mapping of the phase diagram of nuclear matter, to probing properties of the Quark-Gluon Plasma (QGP), to name a few. In this thesis, the main focus is on the last of the three aforementioned examples. The QGP is studied at large particle colliders via collisions of ultra-relativistic heavy ions. At RHIC, Au+Au collisions at energy of $\sqrt{s_{\mathrm{NN}}} = 200\,\mathrm{GeV}$ are used for this purpose. In such collisions, a large number of particles is produced. In central Au+Au collisions at STAR, the total number of charged particles observed in the final state at mid-rapidity ($|\eta| < 1$) can be around 700. In general, these particles come from various sources, which makes physics conclusions from any experimental measurements in ultra-relativistic heavy ion collisions a challenging task.

For that reason, various experimental methods have been developed which have provided solid experimental evidence for presence of the QGP in heavy-ion collisions and are now further used to investigate the QGP properties. One of the major evidences of the QGP is suppression of particle production and modification of jets in heavy-ion collisions compared to p+p collisions due to interactions of particles with QGP, or transverse momentum correlations of particles in plane transverse to the beam axis caused by a geometrical asymmetry of the QGP bulk in semi-central heavy-ion collisions. All of the aforementioned phenomena have been measured in detail at both RHIC and the Large Hadron Collider (LHC) and provided strong evidence of presence of the QGP in heavy-ion collisions and are used extensively to probe QGP properties. All of these signatures of the QGP are introduced in Sec. 1.2.

One possible way to do such measurements is to perform them for all charged (unidentified) particles, but it is also useful to focus on identified particles. It is particularly interesting to measure the charm quark production in heavy-ion collisions because at top RHIC energy, the charm quarks are produced exclusively in hard partonic scatterings, in very early stage of the Au+Au collisions. The QGP bulk is produced a bit later in the evolution of the Au+Au collision, which means that many of the produced charm quarks have to pass through the QGP, where they loose energy and momentum. This leads to modification of the spectrum of charm quarks in heavy-ion collisions with respect to the p+p collisions, in which no QGP is produced[1], i.e. where the charm quarks propagate through vacuum.

A convenient method used to access information about the charm quark production is reconstruction of open-charm hadrons. At STAR, it is possible to perform a direct topological reconstruction of hadronic decays of the open charm hadrons thanks to an exceptional pointing resolution of the Heavy Flavor Tracker (HFT) detector, which was installed in STAR from year 2014, to 2016. STAR has used this opportunity to measure the four major ground states of open charm hadrons (D^0, $D^{\pm}$, D_s, and Λ_c) in Au+Au collisions at $\sqrt{s_{NN}} = 200\,\text{GeV}$ and compare them to combined measurement of D^0 and $D^{\star}$ in p+p collisions at the same energy measured in the year 2009.

As it turned out, and as will be discussed in this thesis, the production of open charm hadrons in Au+Au collisions is not quite as simple as described above. There are multiple phenomena that have a significant influence on the observed spectra of open-charm hadrons in Au+Au collisions and on the difference to those measured in p+p collisions. One of them is the interaction of the charm quarks with the QGP, due to which they loose momentum and energy. In addition, the medium has a profound effect on the charm quark hadronization. Most commonly, two hadronization mechanisms are considered. The first one is the fragmentation hadronization in which the quark hadronizes with a (anti-)quark that originates from splitting of a previously radiated gluon. This mechanism is present in both the vacuum and in the medium. The second one is the coalescence hadronization in which the quark hadronizes with (anti-)quarks from the medium itself, meaning that this mechanism is present in the QGP only. One of the goals of the open-charm hadron measurements is to determine the importance of both contributions to the hadronization process in heavy-ion collisions.

At STAR, an important contribution to this study is the measurement of $D^{\pm}$ mesons in Au+Au collisions at $\sqrt{s_{NN}} = 200\,\text{GeV}$. The main goal of this thesis and work during my Ph.D. was extraction of invariant yields of $D^{\pm}$ mesons from 2016 Au+Au dataset, calculation of the nuclear modification factor of the $D^{\pm}$ mesons, and obtaining the

[1]There might be a very small droplet of QGP produced even in p+p collisions, as suggested by measurements of collectivity in p+p collisions at the LHC. The volume of the QGP in p+p would be so small that it would not affect the charm quark production.

$(D^+ + D^-)/(D^0 + \bar{D^0})$ yield ratio, all as a function of transverse momentum and collision centrality.

This thesis provides a detailed description of this measurement. The first chapter provides a general introduction to the properties of heavy-ion collisions. The second chapter focuses on properties of the open-charm hadrons and their role in the measurements of heavy-ion collisions. In the third chapter, the STAR detector and its most important sub-systems for this analysis are introduced and in the fourth chapter, a detailed description of the analysis itself is provided. Finally all achieved results are discussed in the closing section of this thesis.

Statement of author's contribution

I have started my Ph.D. in July of 2017, when I have joined the Department of nuclear spectroscopy at the Nuclear Physics Institute of the Czech Academy of Sciences. My main responsibility was the analysis presented in this thesis in Chapter 4, i.e. reconstruction of $D^{\pm}$ mesons in Au+Au collisions at $\sqrt{s_{NN}} = 200\,\text{GeV}$ measured by STAR in year 2016. I have been responsible for the whole chain of the analysis, starting with quality assurance (QA) of the 2016 data-set and creating a list of bad runs, over optimization of the topological selection criteria using ROOT package TMVA [1], extraction of $D^{\pm}$ raw yields from the data, calculating the total reconstruction efficiency and all systematic uncertainties. Finally I have used all of the aforementioned steps to calculate the invariant yield of $D^{\pm}$ mesons in the 2016 data-set which I have subsequently combined with the 2014 measurement. I have then used the combined spectra to calculate the nuclear modification factor of $D^{\pm}$ mesons and of the $(D^+ + D^-)/(D^0 + \bar{D^0})$ yield ratio as a function of both transverse momentum and collision centrality. The combined invariant spectrum of $D^{\pm}$ mesons in 10-40%, together with published spectra of D^0 [2] and D_s [3] mesons, and Λ_c baryons [4], was also used to calculate the total charm production cross section in 10-40% central Au+Au collisions at $\sqrt{s_{NN}} = 200\,\text{GeV}$.

In addition to the main analysis, I have also participated on multiple service tasks. Two of those involved calibrations and maintenance of STAR sub-detectors. The first one was calibration of STAR Barel Electromagnetic Calorimeter (BEMC) before data-production of Au+Au collisions at $\sqrt{s_{NN}} = 54\,\text{GeV}$ measured by STAR in 2017. During this task, I have created a database of states of individual BEMC towers throughout the data taking period. The main goal was to provide analyzers with a list of BEMC towers which were working properly and can be therefore used in the analysis. My second detector service task was maintenance of the STAR Zero Degree Calorimeters (ZDC). My duties involved calibrations and hardware checks of the ZDC before each data-taking period since 2018 and also help resolving any issues during the data-taking

periods[2]. In addition to the routine maintenance, I have also participated on exchange of ZDC photomultipliers (PMT) in early 2018, which involved testing about 100 old PMTs which were originally used by the BRAHMS experiment.

I have also been involved in was quality assurance of the 2016 Au+Au at $\sqrt{s_{\mathrm{NN}}} = 200\,\mathrm{GeV}$ data set. In addition to the main QA which was used to create the bad run list, as mentioned above, I have also performed QA of re-productions of this data-set. The re-productions were made in order to add detector information, e.g. BEMC, and to update the data format. My QA was done to ensure that information which was available in the older verified versions of the data files has not changed. At the same time, I was also involved in QA studies of simulations of performance of STAR Heavy Flavor Tracker (HFT) [5] and Time Projection Chamber (TPC)[3]. The main task was to verify that the ratio of number of tracks reconstructed by the HFT over number of tracks reconstructed by the TPC from the simulation matches that observed in the real data.

In order to work on my analysis and service tasks, I have been on regular visits to Brookhaven National Laboratory, Long Island, USA and Lawrence Berkeley National Laboratory, Berkeley, USA. Other visited institutions include Rice University in Houston, USA, or Warsaw University of Technologies, Warsaw, Poland. During my work on this thesis I have also been selected to present my results on behalf of the STAR collaboration at multiple international conferences as contributed talks (8 cases) and posters (6 cases). This includes cotributions at the most prestigious conferences, such as posters at three latest Quark Matter conferences (2018 in Venice, 2019 in Wuhan, and 2022 in Krakow) and at the 40th International Conference on High Energy Physics in Prague, and a talk at 2019 Strangeness in Quark Matter conference held in Bari, Italy.

As an active member of STAR collaboration, I am a coauthor of 44 published papers in scientific journals. Among them are two, to which I have significantly contributed. The first one is: J. Vaněk, for the STAR Collaboration, *Open-Charm Hadron Measurements in Au+Au Collisions at* $\sqrt{s_{\mathrm{NN}}} = 200\,\mathrm{GeV}$ *by the STAR Experiment*, Universe 2019, 5(9), 196, in which I have presented preliminary results (at the time of publication) of my analysis, including previously unpublished details about topological selection criteria, and results from other open-charm analyses at STAR. The second one is: J. Adam, *et al.* [STAR Collaboration], *Observation of* $D_s^{\pm}/D^0$ *Enhancement in* $\mathrm{Au} + \mathrm{Au}$ *Collisions at* $\sqrt{s_{\mathrm{NN}}} = 200\,\mathrm{GeV}$, Phys. Rev. Lett., 127:092301, for which I was a member of a review committee on position of Code QA. My contribution was a check of the analysis software and verification of the presented physics results. I was also involved in revision and approval of the text of the paper draft. In addition to the published publications,

[2] I have not been the main an on-call expert, but I have always been available to help with any issue if the current on-call expert needed help or discussion.

[3] At STAR, such detector performance simulations are called embedding.

I am also primary author of two collaboration papers which are currently under review within the STAR collaboration. The first one is: STAR Collaboration, *Measurement of $D^{\pm}$ meson production and total charm production yield at midrapidity in Au+Au collisions at $\sqrt{s_{\rm NN}}$ = 200 GeV*, which isto be submitted to Physics Letters B, that contains results from analysis presented in this thesis and for which I was responsible for preparation of the results, writing the paper draft and the analysis note. The second one is: STAR Collaboration, *Measurement of D^0 and $D^\star$ production in p+p collisions at* $\sqrt{s} = 500\,\mathrm{GeV}$, that is to be submitted to Physical Review D, for which I am responsible for determination of trigger efficiency of high-$p_{\rm T}$ D^0 mesons. I am also an author of number of proceedings, in which I have presented my results and results from other open-charm hadron production analyses from the STAR experiment.

Full list of my research activities, conference presentations and publications is provided in the Appendices G and H.

Chapter 1

Heavy-ion collisions

This chapter contains an introduction to properties of heavy-ion collisions. The goal of this chapter is to introduce the general physics motivation and the basic properties of the heavy-ion collisions, and experimental signatures of the QGP. The concepts described here serve as a general context to the main topic of this thesis.

1.1 Physics motivation

Two of the major goals of measurements of heavy-ion collisions are probing the properties of the QGP and mapping the phase diagram of the nuclear matter. They both arised from theoretical predictions of the theory of the strong force, the quantum chromodynamics (QCD). One of the first steps towards these theoretical QCD calculations was the prediction of existence of quarks and how they form hadrons (baryons and mesons) by Gell-Mann and Zweig [6,7] in early 1960's. At the time it was not clear, if quarks are real particles or just a theoretical concept which can be used to predict describe hadrons. One of main reasons for that was the fact that only hadrons were observed, but free quarks have not. It took a bit of time until late 1960's and early 1970's when Deep Inelastic Scattering (DIS) experiments at SLAC (Stanford Linear Accelerator Center) confirmed that protons consist of three point like particles [8], which was in agreement with Gell-Mann's and Zweig's prediction.

Soon after that scientists started to ask why we do not observe free quarks or gluons. This lead to development of theoretical calculations which tried to predict conditions, under which the quarks and gluons could be freed from being confined inside hadrons. Many of such works appeared later in 1970's, for example Ref. [9, 10]. It was also the time, when the contemporary terminology started to be used. The property of the hadronic matter at low temperatures, in which quarks and gluons are trapped inside hadrons, started to be referred as confinement and the property at high temperatures,

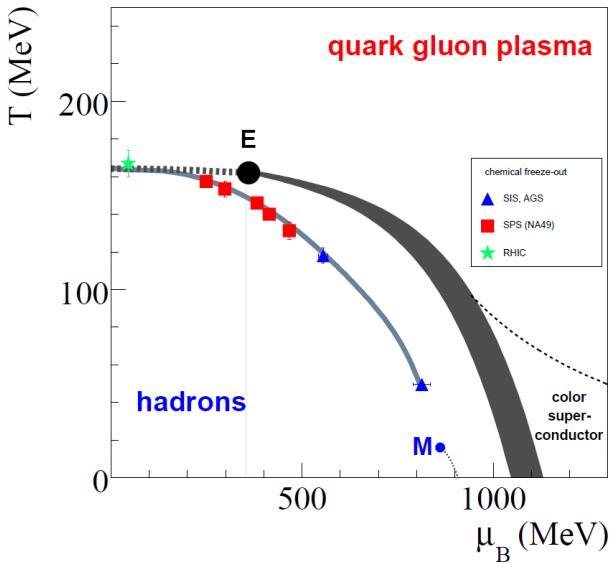

Fig. 1.1: Phase diagram of the QCD matter as predicted from lattice QCD theoretical calculation. The dashed line indicates position of cross-over phase transition, E is the critical point and the shaded band represents first order phase transition. The data points are from the grand canonical statistical model [16]. Point M indicates matter present inside atomic nuclei. At very large values of μ_B, a color superconductor phase is predicted [17, 18]. Figure taken from Ref. [19].

when they are asymptotically free (i.e. in the QGP), deconfinement[1].

Next obvious question was, what is the nature and place of the phase transition between the hadronic phase and the QGP. As can be found for example in Ref. [11], even at the end of the 1970's, there were attempts to determine the best way to identify the nature of the phase transition using different QCD calculations. From that time on, what can be seen in the scientific papers about this topic more and more often are non-perturbative QCD calculations on a lattice. These calculations relatively quickly lead to prediction of the value of the critical temperature $T_c \approx 175\,\mathrm{MeV}$ at which the phase transition should occur [12, 13] and that the the phase transition is most likely not first order, or second order phase transition [14]. In the last cited paper, the conclusion is that the QCD does not have a "finite-temperature phase transition", which is now interpreted as a rapid cross-over phase transition [15].

In general, the theoretical calculations mentioned above are for a specific case, where the baryon chemical potential $\mu_b = 0$. In simplified terms, μ_B quantifies the difference between the number of baryons and anti-baryons in the system. For $\mu_b = 0$, there is the same number of baryons and anti-baryons, which is a situation observed in heavy ion collisions at the LHC or at top energy at RHIC. Calculations for non-zero values of

[1] Confinement and deconfinement are properties of the strong interaction under given conditions. Hadronic phase and QGP are two different phases of the nuclear matter.

μ_B were developed relatively recently and are crucial for current picture of the phase diagram of nuclear matter, which is shown in Fig. 1.1. For low values of μ_B, a cross-over phase transition (dashed line at low μ_B and high temperature T) is expected which is consistent with observations from the LHC and RHIC. The theoretical calculations for larger values of μ_B are consistent with a first order phase transition (grey band), which implies an existence of a critical point (E) [15, 20]. At very high values of μ_B, a color super-conductor phase is predicted which shares some properties with "classical" super conductor, namely creation of Cooper pairs, in this case of quarks (electrons in the "classical" case) [17, 18]. The green star, red squares, and blue triangles show the position of chemical freeze-out[2] for different hadron multiplicities observed in heavy-ion collisions at various accelerators, as calculated in the statistical model [16]. Using various collision energies provides access to different values of μ_B. The last important point shown in this simple version of the phase diagram, is the point M, which denotes the state of nuclear matter present inside atomic nuclei.

1.2 Heavy-ion collisions

In this section provides a summary of basic properties of heavy-ion collisions. The main focus is to introduce the terminology and variables used for description of the system of two colliding nuclei. In the second part of the section, the time evolution of the heavy-ion collisions is described. The time evolution picture is also discussed in context of the phase diagram of nuclear matter.

1.2.1 General properties of heavy-ion collisions

One of the first things necessary for description of any physics phenomenon is an appropriate coordinate system. In the present, collider experiments typically use a laboratory system of coordinates with the following convention: the $(0, 0, 0)$ point is in the center of the detector with the z axis parallel to the particle beam and the x and y axes being perpendicular to the beam. The x axis is most often horizontal and the y axis vertical, as shown in Fig. 1.2.

The azimuthal angle ϕ is measured from the x axis in the xy plane. The second important angle is θ (not shown in Fig. 1.2) which is measured from the z axis. In practice, θ is not used very often, but pseudorapidity η which is defined as

$$\eta = -\ln\left[\tan\left(\frac{\theta}{2}\right)\right] \tag{1.1}$$

is used instead. One of the reasons is that value of η for high energy particles approaches that of rapidity y which is defined as

[2] Chemical freeze-out will be discussed in more detail in Sec. 1.2.

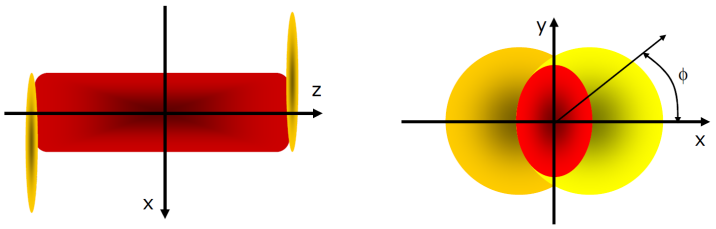

Fig. 1.2: Cartoon of a heavy-ion collision in the most commonly used coordinate system. The x and y axes define plane perpendicular to the beam axis. The z axis is then parallel to the beam axis. Azimuthal angle ϕ is measured in the xy plane from the x axis. The center of the coordinate system is typically placed in the center of the detector. Taken from Ref. [21].

$$y = \frac{1}{2} \ln \left(\frac{E + p_{\mathrm{z}}}{E - p_{\mathrm{z}}} \right), \tag{1.2}$$

where E is the energy of the particle and p_{z} is the component of the momentum of the particle that is parallel to the beam axis[3] Components of particle momentum p can then be written in terms of η and ϕ as follows:

$$\begin{aligned} p_{\mathrm{x}} &= p_{\mathrm{T}} \cos(\phi), \\ p_{\mathrm{x}} &= p_{\mathrm{T}} \sin(\phi), \\ p_{\mathrm{x}} &= p_{\mathrm{T}} \sinh(\eta), \end{aligned} \tag{1.3}$$

where $p_{\mathrm{T}} = \sqrt{p_{\mathrm{x}}^2 + p_{\mathrm{y}}^2}$ is the transverse momentum. One key advantage of such coordinate system is that ϕ and p_{T} are boost invariant (in z direction) and η (or y) can be easily transformed under such boost.

Since heavy nuclei used at large colliders as RHIC or LHC are relatively large objects, each heavy-ion collision is unique in terms of the overlap of the two projectiles. This overlap, called centrality of the collision, is quantified using a variable called impact parameter b which is simply a distance between the centres of the two colliding heavy-ions in the transverse plane, as shown in Fig. 1.3. Experimentally, it is essentially impossible to measure b directly. For that reason, at STAR collision centrality is determined by measured particle multiplicity inside the Time Projection Chamber, matched to a Glauber model simulation [22, 23].

[3] In the whole thesis, natural units are used, i.e. $c = 1$. A more general definition of y is used in special theory of relativity, but in scope of this thesis, when y is referred, it is defined using Eq. 1.2.

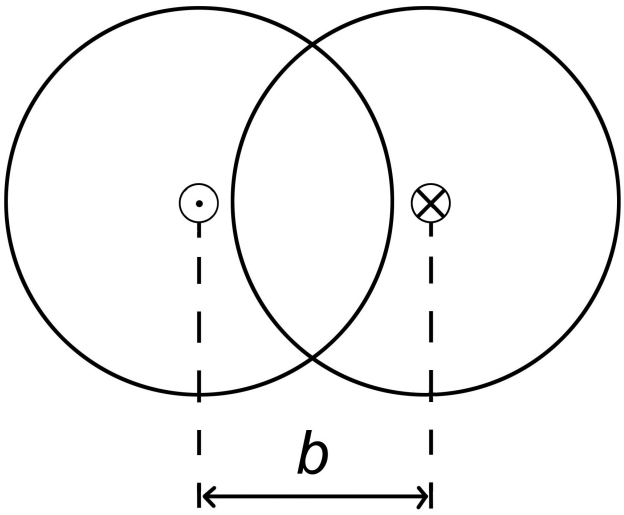

Fig. 1.3: A simple cartoon of a heavy-ion collision showing a definition of an impact parameter b. The impact parameter is simply defined as distance between the centers of the colliding nuclei.

1.2.2 Time evolution of heavy-ion collisions

Ultra-relativistic heavy ion collisions occur in a fraction of a second. Despite their very short duration, they have quite complex time evolution. In this section, a brief description of today's understanding of the time evolution of heavy-ion collisions is provided.

Figure 1.4 shows a simple overview of individual phases of a heavy-ion collision. The initial state, before the collision itself, can be described by various models, such as the Glauber model [22, 23] or the Color Glass Condensate [24]. This phase in not fully understood at the moment and both aforementioned models provide a simplified description, under specific conditions. The Glauber model, very simply speaking, calculates the position of the nucleons (protons and neutrons) in the two colliding nuclei and then the probability that the partons will interact with each other during the collision. In contrast, the CGC treats the colliding ions as two relativistically contracted plates of gluons.

The first interaction phase is the hard partonic scattering, which is a perturbative QCD process, in which most of the high p_{T} and all of the heavy flavor quarks are created. At this stage, no QGP is present yet. QGP is estimated to be formed approximately $1\,\mathrm{fm}/c$ after the hard partonic scattering [25]. The QGP bulk then expands following relativistic hydrodynamics up to the point when its temperature falls down to critical temperature T_{c}. Here, the cross-over phase transition from the QGP into a interacting hadron gas occurs.

In this phase, the confinement is restored, which means that quarks and gluons are bound inside hadrons, but the hadrons interact with each other, leading to changes of

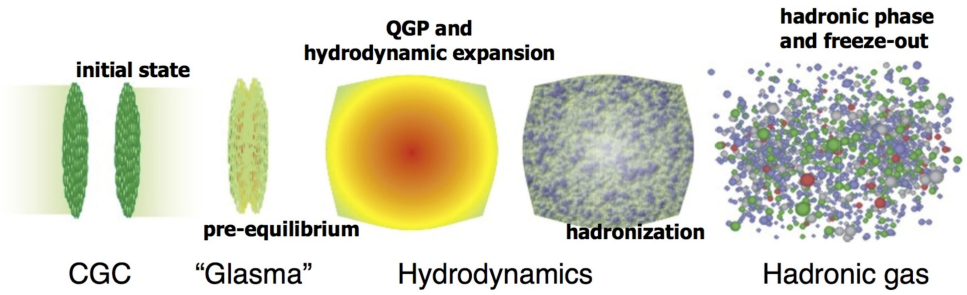

Fig. 1.4: Simplified overview of individual phases of a heavy-ion collision. CGC stands for Color Glass Condensate. Taken from Ref. [25].

hadron composition of the gas. When the temperature drops more to chemical freeze-out temperature T_{ch}, the composition of the gas is fixed, but the components can still interact with each other. The interactions stop when the kinetic freeze-out temperature T_{fo} is reached. The whole evolution of a heavy-ion collisions is schematically shown in Fig. 1.5, with all freeze-out temperatures.

One of the main challenges of heavy-ion collision measurements is that the detectors are able to detect only the final state particles, which survive the kinetic freeze-out. In addition, many of them are too short-lived, to enter the volume of the detector and need to be reconstructed via their decays. This is the case for the open-heavy flavor hadrons which are the main focus of this thesis. The following section provides a summary of observables used to probe the properties of the QGP from the final state particles.

1.3 Experimental signatures of the QGP

This section provides an overview of the main signatures of the QPG in ultra-relativistic heavy-ion collisions. The first experimental observations of QGP heavy-ion collisions was announced in the year 2000 by experiments at Super Proton Synchrotron (SPS) at CERN [27]. Observation from the SPS gave first hints of the QGP in heavy ion collisions, but a conclusive evidence of presence of the QGP in such collisions has been observed later at RHIC, and subsequently confirmed at the LHC.

Particle production modification

As already discussed above, in order to measure the properties of the QGP, experimental physicist had to develop methods to access information about the hot and dense medium. One of the most straightforward ones is the measurement of the nuclear modification factor R_{AA} which can be defined as

$$R_{\mathrm{AA}} = \frac{(\mathrm{d}N/\mathrm{d}p_{\mathrm{T}})_{\mathrm{AA}}}{\langle N_{\mathrm{coll}}\rangle (\mathrm{d}N/\mathrm{d}p_{\mathrm{T}})_{\mathrm{pp}}}, \tag{1.4}$$

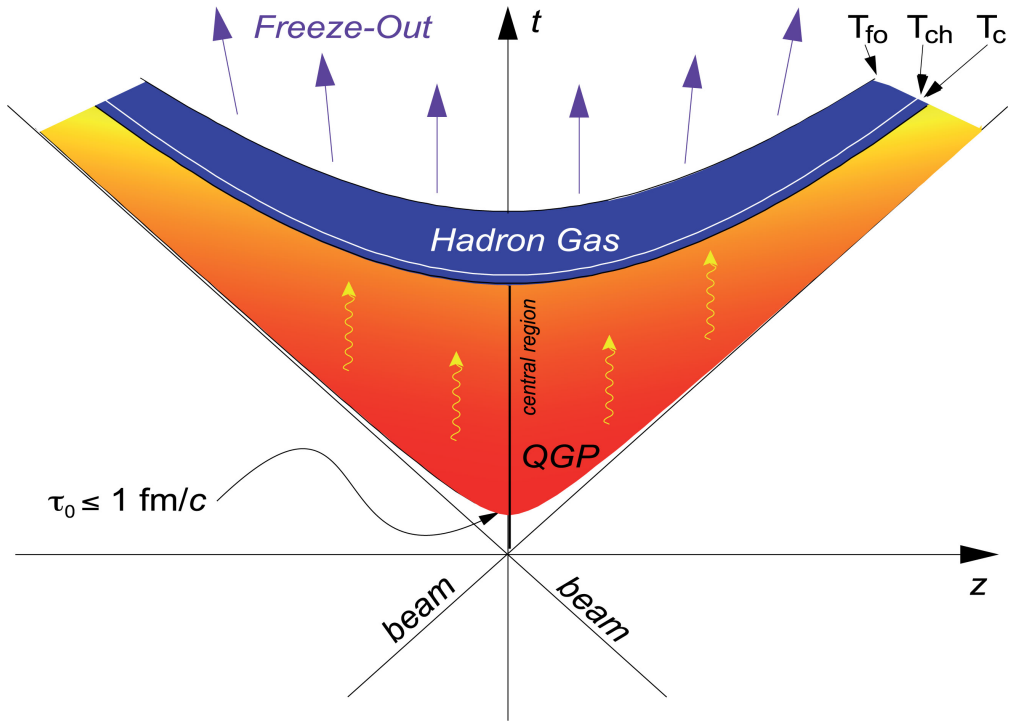

Fig. 1.5: Time evolution of a heavy-ion collision in tz plane. Individual freeze-out temperatures are also indicated. For details see the text. Taken from Ref. [26].

where $(\mathrm{d}N/\mathrm{d}p_\mathrm{T})_\mathrm{AA}$ is an invariant yield p_T spectrum of particles of interest, e.g. open-charm mesons, measured in heavy-ion collisions, $(\mathrm{d}N/\mathrm{d}p_\mathrm{T})_\mathrm{pp}$ is the same spectrum measured in p+p collisions and $\langle N_\mathrm{coll}\rangle$ is the mean number of binary collision, typically calculated using the Glauber model.

The nuclear modification is defined so that if heavy-ion collisions were just a simple superposition of $\langle N_\mathrm{coll}\rangle$ p+p collisions, then $R_\mathrm{AA} = 1$. As can be seen in Fig. 1.6, the observed R_AA depends on the collision energy. For collisions at low energy (compared to RHIC and the LHC) from the SPS [28, 29], no suppression of π^0 mesons with $p_\mathrm{T} > 2\,\mathrm{GeV}/c$ is observed. For lower p_T, the data fall under unity, which is caused by the fact that the $\langle N_\mathrm{coll}$ no longer holds for soft processes which are dominant in this p_T region [29]. Data from RHIC and the LHC for charged and neutral hadrons, one the other hand, show a substantial suppression over a wide range of p_T. Correct understanding of the R_AA of light particles is challenging, as they can originate from several different sources. On the other hand, high transverse momentum hadrons, with $p_\mathrm{T} > 4\,\mathrm{GeV}/c$ for RHIC and $p_\mathrm{T} > 10\,\mathrm{GeV}/c$ for the LHC, are most likely coming from hadronization of partons scattered in the hard partonic scattering. The suppression for high-p_T hadrons is probably caused by the energy loss inside the QGP. Mainly the LHC data, and with limited precision the RHIC data, show a rising trend with momentum in the high-p_T region which suggests that the medium is more transparent for particles with higher momenta. The data in this p_T region are compared to various theoretical model

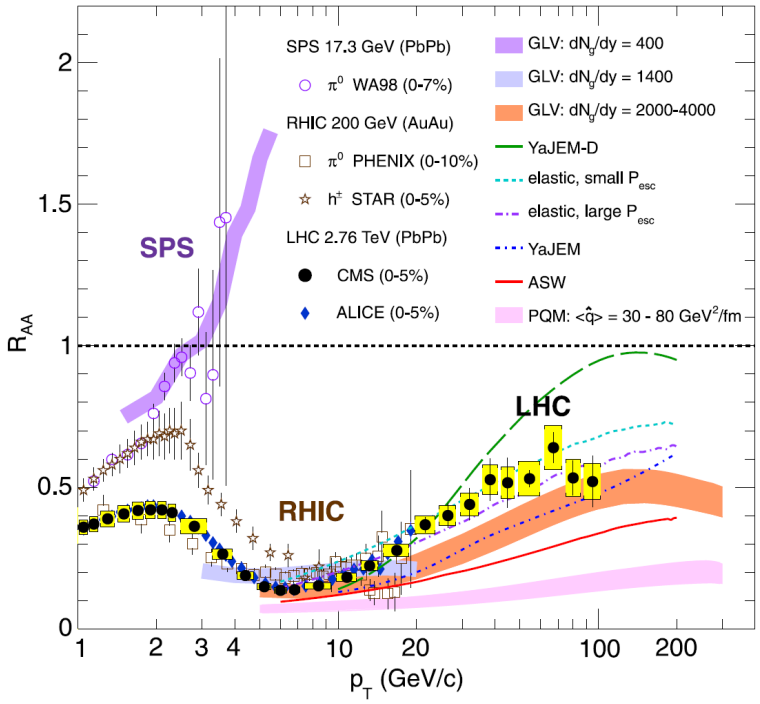

Fig. 1.6: Nuclear modification factor R_{AA} of multiple particle species measured by various experiments in heavy-ion collisions at different collision energies. Specifically, shown are results for π^0 measured by WA98 at SPS [28, 29] and by PHENIX at RHIC [30], charged hadrons by STAR at RHIC [31], and charged particles by ALICE [32] and CMS at the LHC [33]. For collision system, centrality and energy, see legend. The experimental data are compared to multiple theoretical models [34–39]. Taken from Ref. [33].

calculations. All these models attempt to describe the LHC data for large transverse momenta (ca. $p_{\mathrm{T}} > 5\,\mathrm{GeV}/c$), focusing exclusively on parton energy loss mechanism in the medium. The Parton Quenching Model (PQM) [34] and Gyulassy-Levai-Vitev (GLV) model [35, 36] calculations were done for Pb+Pb collisions at $\sqrt{s_{\mathrm{NN}}} = 5.5\,\mathrm{TeV}$ (LHC design energy), the Amesto–Salgado–Wiedemann (ASW) [37, 38] and Yet another Jet Energy-loss Model (YaJEM) [39] with elastic energy loss parametrization are done for the same Pb+Pb collision energy as the measured data, i.e. $\sqrt{s_{\mathrm{NN}}} = 2.76\,\mathrm{TeV}$. In general, all the models predict rising trend of the R_{AA} with p_{T}, but the quantitative agreement with the measured data varies which shows importance of such experimental measurements, which can provide constraints on theoretical calculations of energy loss of partons in the QGP.

Description of the R_{AA} of light flavor particles for lower momenta is quite a bit more challenging, as in this region they are originating from two main sources. One contribution is from particles from the hard partonic scattering, which have lost significant part of their momentum inside the medium, the second one is from hadronization of the QGP bulk. Distinguish which source are the particles coming from is not possible just

by simple measurement of the R_{AA}. In order to get a full picture, one needs to focus on spectra of identified heavy hadrons, or to measure additional experimental observables.

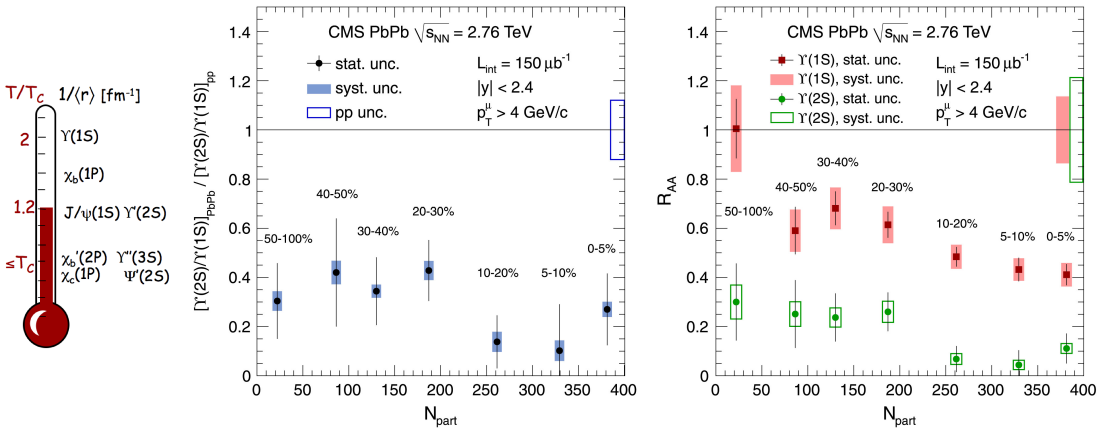

Fig. 1.7: **(left)** A cartoon showing different melting temperatures of multiple quarkonia. The temperature is given with respect to critical temperature T_{T}. The melting temperature is larger for quarkonia with smaller size $\langle r \rangle$. Taken from Ref. [40]. **(center, right)** The measurement of $[\Upsilon(1\mathrm{S})/\Upsilon(2\mathrm{S})]_{\mathrm{PbPb}}/[\Upsilon(1\mathrm{S})/\Upsilon(2\mathrm{S})]_{\mathrm{pp}}$ double ratio (left) and the R_{AA} (right) of $\Upsilon(1\mathrm{S})$ and $\Upsilon(2\mathrm{S})$ mesons in Pb+Pb collisions at $\sqrt{s_{\mathrm{NN}}} = 2.76\,\mathrm{TeV}$ for various collision centralities measured by CMS. Taken for Ref. [41].

One possible option for the identified particles are quarkonia, i.e. heavy flavor mesons consisting of $c\bar{c}$ (charmonia), or $b\bar{b}$ (bottomonia) quark-antiquark pairs. When a quarkonium is placed inside the QGP, might dissolve because of Debye-like screening, as first proposed by Matsui and Satz for J/ψ [42], which depends on the temperature of the medium. The melting mechanism works similarly to the Debye screening in classical plasma. The QGP is a bulk of asymptotically free color charges. At given temperature of the QGP, the density of the in-medium charges will be sufficient to shield the bound $q\bar{q}$ pairs and so melting the quarkonia inside the medium. If a given quarkonium will dissolve or not inside of the medium depends on its binding energy which can be relatively easily calculated for both their ground (charmed J/ψ(1S), beautiful $\Upsilon(1\mathrm{S})$) and excited states (e.g. ψ(2S), $\Upsilon(2\mathrm{S})$). The suppression of the various quarkonia species in haevy-ion collisions should be ordered based on their binding energy, where the ground states are more tightly bound than excited states and bottomonia are more tightly bound than charmonia (for a given state[4]). An illustration of such ordering in melting temperatures of quarkonia is shown in Fig. 1.7 (left). One of key measurements is therefore comparison of abundances of the individual quarkonia species measured in heavy-ion collisions and p+p collisions, for example using the R_{AA} or particle yield ratios.

An example of such measurement can be seen in Fig. 1.7 (center, right) which shows the $[\Upsilon(1\mathrm{S})/\Upsilon(2\mathrm{S})]_{\mathrm{PbPb}}/[\Upsilon(1\mathrm{S})/\Upsilon(2\mathrm{S})]_{\mathrm{pp}}$ double ratio (left) and the R_{AA} (right) of

[4]E.g. $\Upsilon(1\mathrm{S})$ is more tightly bound and has higher malting temperature than J/ψ(1S).

Υ(1S) and Υ(2S) mesons in Pb+Pb collisions at $\sqrt{s_{\mathrm{NN}}} = 2.76\,\mathrm{TeV}$ for various collision centralities measured by CMS. The measurement clearly indicates that both Υ states are suppressed in central Pb+Pb collisions. The suppression is the largest in central Pb+Pb collisions and gets smaller towards more peripheral collisions which suggests that it is a medium induced effect. Both states are suppressed for all centralities except for the 50-100% centrality class in which the Υ(1S) is not suppressed at all while Υ(2S) is. This suggests that there is QGP created in 50-100% central Pb+Pb collisions at $\sqrt{s_{\mathrm{NN}}} = 2.76\,\mathrm{TeV}$, but the temperature is not sufficient any more to melt tightly bound Υ(1S), but is still hight enough to dissolve Υ(2S). Furthermore, the Υ(2S) is clearly more suppressed than Υ(1S) in all studied centrality classes, which hints that the temperature is not high enough to dissolve both Υ states to the same level.

Similar measurements can be done for J/ψ(1S) and its excited states as well. In case of charmonia, the measurements can a bit more challenging than in case of previously presented bottomoia. The reasons is that at the LHC energies of Pb+Pb collisions, the charm quark production cross section is relatively large (compared to e.g. RHIC). As a result, the density of "melted" charm (anti-)quarks inside the QGP is large enough in Pb+Pb collisions at the LHC so that they can re-combine back into final state charmonium states [43]. This recombination effect therefore slightly enhances charmonium production in Pb+Pb collisions at the LHC compared to expectation with melting only. It is also important to distinguish between cahrmonia originating from charm quarks directly form the hard partonic scattering or those which are result of decay of hadrons containing b quark. Again, due to larger energies, this so-called b feed-down is much more significant at the LHC than at RHIC. At RHIC, the bottom quark production cross section is low enough so that b feed down for charmed mesons is mostly deemed negligible, but at the LHC it needs to be taken into account and actually opens e.g. possibilities to measure b-hadrons via decay to J/ψ. Overall, charmonium production is relatively complex challenge which requires a lot of sophisticated experimental methods to distinguish between charmonia from different sources, but at the same time gives access to different aspects and properties of ultra-relativistic heavy ion collisions and of the QGP.

Another interesting way to study properties of the QGP is by measurement of baryon/meson yield ratios. It is possible to measure such ratios in heavy-ion collisions and in small systems (e.g. p+p, p+Au, d+Au) which can then provide insight into hadronization process in heavy-ion collisions. Example of such measurement is shown in Fig. 1.8, specifically the p/π^+ (a) and $\bar{\mathrm{p}}/\pi^-$ (b) yield ratio measured in Au+Au [49] and d+Au collisions [44, 45] at $\sqrt{s_{\mathrm{NN}}} = 200\,\mathrm{GeV}$ by the STAR experiment. The ratio is clearly enhanced in central Au+Au collisions compared to peripheral Au+Au collisions and d+Au collisions in p_{T} interval $1 < p_{\mathrm{T}} < 4\,\mathrm{GeV}/c$. This observation is often referred as the baryon anomaly.

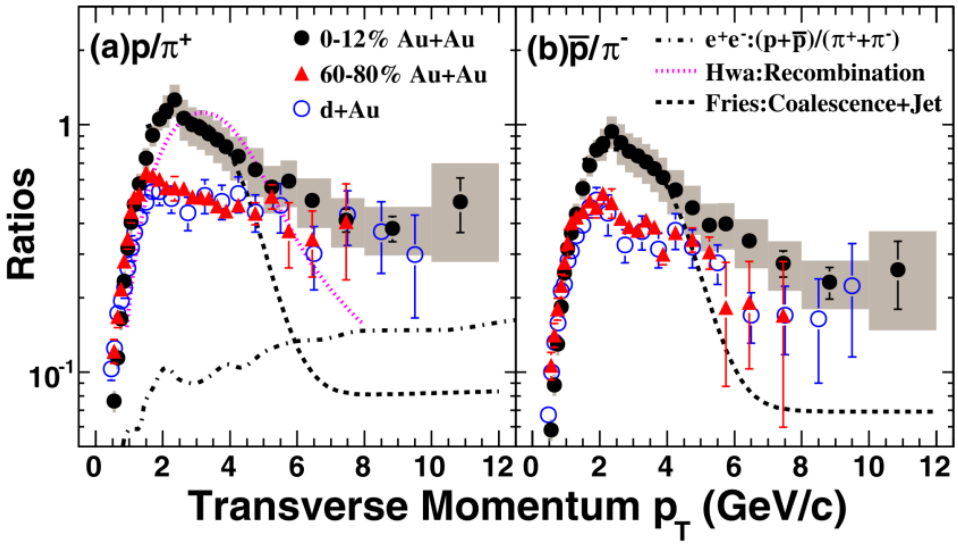

Fig. 1.8: The p/π^+ (a) and $\bar{\mathrm{p}}/\pi^-$ (b) yield ratio measured in Au+Au and d+Au collisions [44, 45] at $\sqrt{s_{\mathrm{NN}}} = 200\,\mathrm{GeV}$ by the STAR experiment. The STAR data are compared to measurement of $(\mathrm{p} + \bar{\mathrm{p}})/(\pi^+ + \pi^-)$ yield ratio obtained light flavor jets measured in $\mathrm{e}^+ + \mathrm{e}^-$ collisions at $\sqrt{s} = 91.2\,\mathrm{GeV}$ [46] and two model calculations for Au+Au collisions [47, 48]. Taken from Ref. [49].

In small systems and peripheral heavy-ion collisions, the dominant hadronization mechanism is fragmentation. In this case, the final state hadron (proton or pion in the example) is created inside a parton shower induced by a high-p_{T} parton originating in hard partonic scattering. This hadronization mechanism is present in central heavy-ion collisions as well, but an additional hadronization mechanism is possible thanks to presence of the QGP. The partons from the aforementioned shower and those present in the medium itself can hadronize with each other, if they are close to each other in space and have similar momenta. This mechanism is often referred to as coalescence hadronization [50]. In general, the spectra of partons inside the QGP is steeply falling towards higher p_{T}, meaning that there is larger abundance of partons with low transverse momenta compared to those with higher transverse momenta. Coalescence hadronization is therefore more likely to form a baryon with given p_{T} than to produce a meson with the same p_{T}. This leads to enhancement of the baryon/meson yield ratio for low-p_{T} hadrons in central Au+Au collisions compared to small systems.

Coalescence hadronization of light flavors can be somewhat complicated to describe, as the final state hadrons can be result of fragmentation hadronization inside the patron shower induced by a high-p_{T} parton from hard partonic scattering, or by coalescence hadronization of a parton inside the shower with quark from the medium, or coalescence hadronization of quarks inside the medium itself. This is where open-charm hadrons can help, as charm quarks are produced predominantly in hard partonic scattering. The

production mechanism of open-charm hadrons is therefore a bit more straightforward. The charm quarks can hadronize via fragmentation, which is present in both p+p and heavy-ion collisions, or via coalescence of the hard c-quark with the QGP, which can occur only in heavy-ionc collisions. At the same time, the charm quarks propagating through the QGP loose energy and momentum, which leads to modification of charm quark spectra in heavy-ion collisions. The measurement of open-charm hadrons therefore give direct access to energy losses and coalescence hadronization of charm quarks inside the QPG and are therefore very powerful tool in probing the QGP properties.

Collectivity

Up to this point, only measurements of particle yields integrated over full azimuthal angle were discussed. It is also important to perform ϕ-differential measurements. Interesting, in particular, are asymmetries in p_{T} azimuthal spectra of different particle species. Such asymmetries can be quantified using coefficients v_{n} of the Fourier decomposition of particle azimuthal distribution:

$$\frac{\mathrm{d}N}{\mathrm{d}\phi} \propto 1 + 2\sum_{n=1}^{\infty} v_{\mathrm{n}} \cos[n(\phi - \Psi_{\mathrm{n}})] \tag{1.5}$$

where ϕ is the azimuthal angle, under which a particle is observed and Ψ_{n} is the angle of the n-th order event plane, all measured from the x axis.

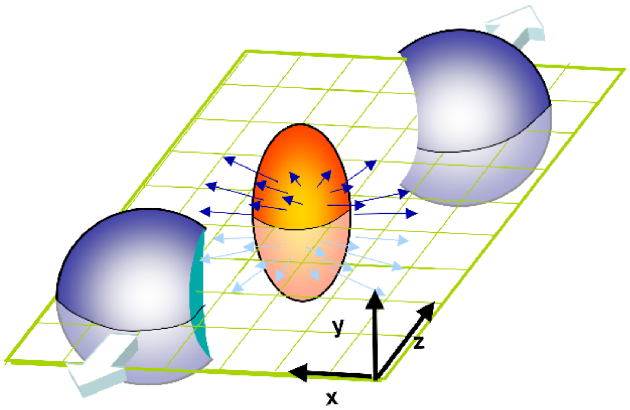

Fig. 1.9: Schematic view of a semi-central heavy-ion collision. The overlap of the two passing nuclei has asymmetrical shape which leads to rapid expansion of the QGP fireball inside the event plane (green). Taken from Ref. [51].

The motivation for such measurement is illustrated in Fig. 1.9. The two nuclei (blue spheres) collide with each other with an overlap. The plane connecting the centers of the two nuclei and parallel to the beam axis (green in Fig. 1.9) is called the reaction plane. In mid-central heavy ion collisions, the active region (orange in Fig. 1.9) has an asymmetrical shape. At sufficient collision energy and size of the overlap, the active

region is filled with the QGP which has certain non-zero pressure in the middle of its volume and zero pressure at the surface, as the collisions occur in a vacuum. For that reason, the pressure gradient inside the reaction plane is greater than in direction perpendicular to the plane. As a result, the particles emitted from the QGP fireball inside the reaction plane obtain larger momentum than particles emitted in the perpendicular direction, which then leads to $v_2 > 0$ in Eq. 1.5. The overlap of the two nuclei in the plane perpendicular to the beam axis can be reasonably approximated by an ellipse, so the observed asymmetry related to v_2 is therefore called the elliptic flow.

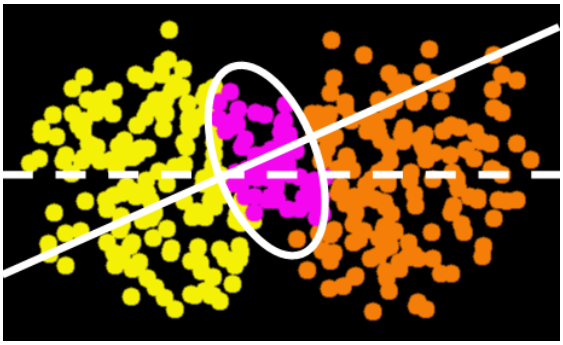

Fig. 1.10: Glauber model simulation of a heavy-ion collision. Magenta are participants of the collisions, orange and yellow are the spectators. The dashed line is the reaction plane, the solid line is the 2nd order event plane. The ellipse shows estimated elliptic asymmetry of the overlap. Taken form Ref. [51]

In the example above, several assumptions were made. The first one is that the reaction plane and the 2nd order event plane are identical and that the cross-section of the active region in plane perpendicular to the beam axis is defined simply by the overlap of the two nuclei (as can be seen in Fig. 1.3). In reality, the situation is not that straightforward, as nuclei are not perfectly spherical, uniform objects. They consist of protons and neutrons which are distributed inside the volume of the nucleus. In addition, two partons of the two colliding nuclei will interact with each other only with certain probability, even when both partons are in the overlap region. An example, how more realistic overlap region might look like can be calculated using the Glauber model as shown Fig. 1.10. The participating partons are shown in magenta and the approximate elliptic shape of the overlap is indicated. In this example the reaction plane (solid line) is very different from the 2nd order event plane (dashed line).

In addition, the overlap of the nuclei typically does not have perfectly elliptic shape. The shape fluctuates from collision to collision which leads to non-zero v_n coefficients for $n > 2$. For example in Fig. 1.11, the overlap has more triangular shape than elliptical one, which would lead to significant triangular flow v_3. In general, each heavy-ion collision can have multiple non-zero v_n coefficients, each with its own n-th order event plane Ψ_n.

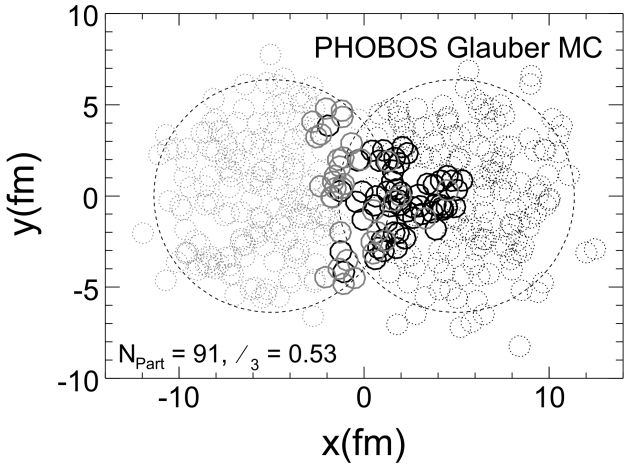

Fig. 1.11: Glauber model simulation of an Au+Au collision at $\sqrt{s_{\mathrm{NN}}} = 200\,\mathrm{GeV}$ by the PHOBOS experiment. The highlighted nucleons are the participants of the collisions, the light ones are the spectators. This example demonstrates source of non-zero higher order harmonic coefficients in heavy-ion collisions due to fluctuations of the overlap of the colliding nuclei. This specific event would generate significant v_3 due to triangular shape of the overlap. Taken from Ref. [52].

This makes experimental measurements of collective flow a challenging task. Example of such measurement is displayed in Fig. 1.12, which show the elliptic flow of light flavor hadrons measured in 0-80% (a), 40-80% (b), 10-40% (c), and 0-10% (d) central Au+Au collisions at $\sqrt{s_{\mathrm{NN}}} = 200\,\mathrm{GeV}$ by the STAR experiment [54]. All studied hadrons show significant collective elliptic flow in all centrality classes. The elliptic flow is smaller in central Au+Au collisions compared to semi-central, as gold nuclei are nearly perfectly spherical. Therefore, the overlap of the two colliding nuclei in central Au+Au collisions is close to perfect circle which has very small ellipticity. The data points are compared to ideal hydrodynamics model calculations [53]. Going from top to bottom, the lines represent predictions for π, K, p, Λ, Ξ, and Ω.

As mentioned above, it is also possible to measure higher order harmonic coefficients. One of the most extensive measurements was performed by the ATLAS experiment. Figure 1.13 shows the elliptic flow v_2 and higher order harmonics for $n = 3$–6 of charged particles measured in multiple centrality classes of Pb+Pb collisions at $\sqrt{s_{\mathrm{NN}}} = 2.76\,\mathrm{GeV}$ by the ATLAS experiment [55]. Similarly to the STAR measurement, the v_2 is significantly smaller in central Pb+Pb collisions compared to the semi-central ones. Another interesting phenomenon which can be observed in the ATLAS results is that $v_3 > v_2$ in 0-10% central Pb+Pb collisions. The explanation is similar to the ordering of v_2 with centrality. In central Pb+Pb collisions, the overlap of the two colliding nuclei is very close to circular, i.e. with small ellipticity. The measurement in 0-10% central collisions is therefore more sensitive to higher order fluctuations of the circular shape,

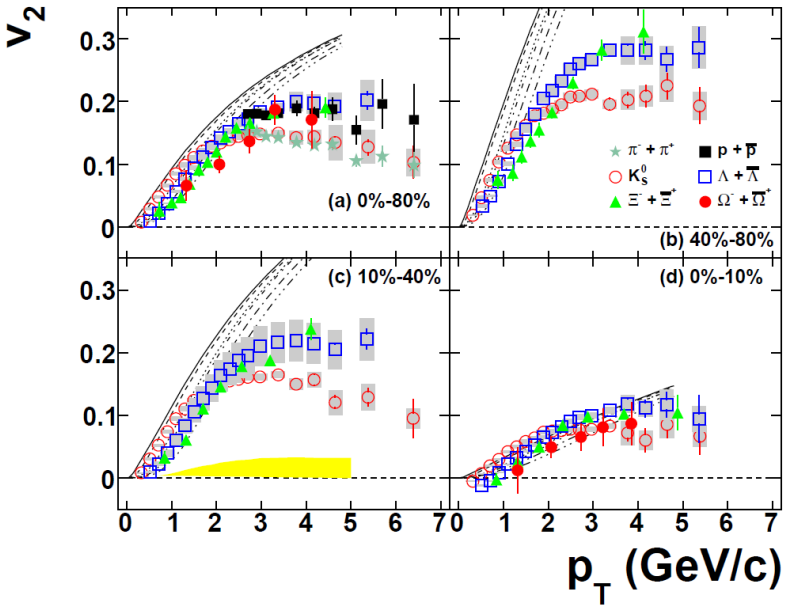

Fig. 1.12: Elliptic flow of light flavor hadrons measured in 0-80% (a), 40-80% (b), 10-40% (c), and 0-10% (d) central Au+Au collisions at $\sqrt{s_{\mathrm{NN}}} = 200\,\mathrm{GeV}$ measured by STAR. The experimental data are compared to ideal hydrodynamics model calculations [53]. Going from top to bottom, the lines represent predictions for π, K, p, Λ, Ξ, and Ω. Taken from Ref. [54].

which leads to $v_3 > v_2$. In remaining centrality classes, an ordering is observed where $v_2 > v_3 > \cdots > v_6$, which is expectable from shape of the overlap region in mid-central heavy-ion collisions. Elliptical asymmetry of the interaction region is driven primarily by the overlap of the two nuclei. Any higher order asymmetries arise mainly from fluctuations of the shape of the overlap of the nuclei and the corresponding observed higher order harmonic flow is therefore smaller than v_2.

The last harmonic coefficient that has not been discussed yet is the v_1. It is called the directed flow and it has slightly different origin and behavior than v_2 and higher order harmonic coefficients. One key difference is that v_1 is non-zero exclusively for rapidity differential measurements. In simple terms, directed flow is an asymmetry in particle production in forward-rapidity (and back-rapidity) region, with respect to the beam axis inside the reaction plane. Good point of reference are the spectators of the collision, as shown in Fig. 1.14 (a). The directed flow tells us, if there are more particles produced in the direction of the spectators (i.e. $x > 0$ and $z > 0$ for $\eta > 0$, or $x < 0$ and $z < 0$ for $\eta < 0$), or in the direction away form the spectators (i.e. $x < 0$ and $z > 0$ for $\eta > 0$, or $x > 0$ and $z < 0$ for $\eta < 0$). The asymmetry in Fig. 1.14 (a) is source of so-called rapidity odd directed flow, for which $v_1^{\mathrm{odd}}(y) = -v_1^{\mathrm{odd}}(-y)$. Similarly to the higher order flow harmonics, first order event plane will not be identical with the geometrical event

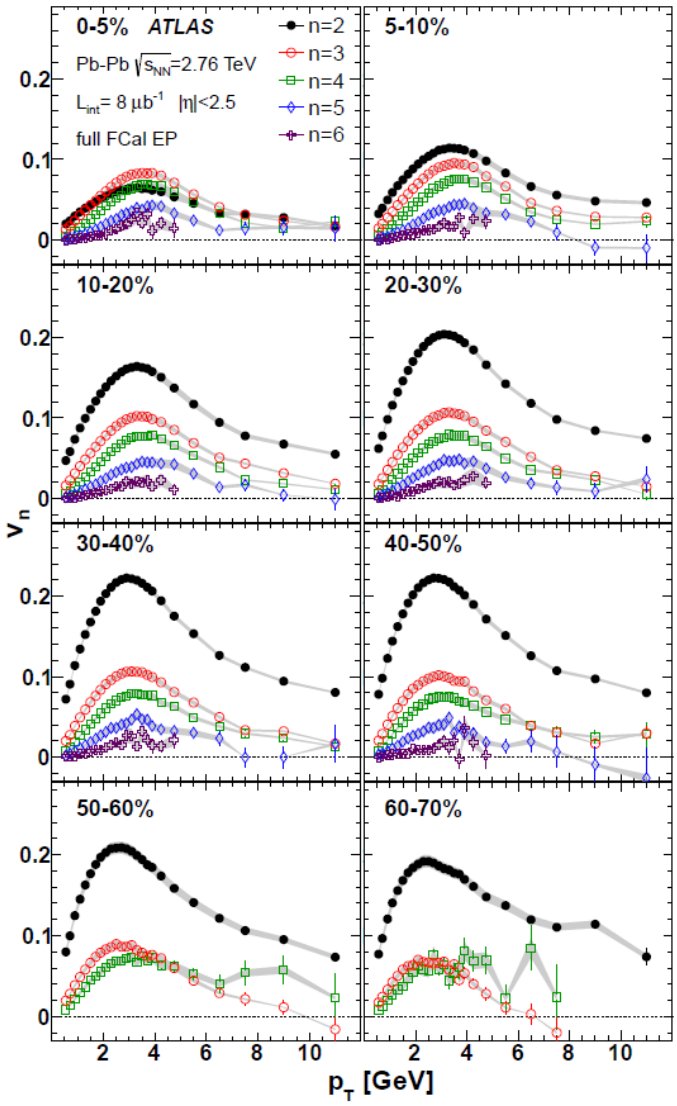

Fig. 1.13: Elliptic flow v_2 and higher order harmonics for $n = 3$–6 of charged particles measured in multiple centrality classes of Pb+Pb collisions at $\sqrt{s_{\mathrm{NN}}} = 2.76\,\mathrm{GeV}$ by the ATLAS experiment. In 0-5% central Pb+Pb collisions, $v_3 > v_2$ which is caused by that the overlap of the two nuclei is close to circular, i.e. with small ellipticity, and the measurement is therefore more sensitive to shape fluctuations. In all other presented centrality classes, the harmonic flow coefficients show ordering where $v_2 > v_3 > \cdots > v_6$. Taken from Ref. [55].

plane. The first order event plane then has its angle $\Psi_{\mathrm{PP}}^{(1)}$ (participant plane angle in Fig. 1.14). Due to fluctuations of the shapes of the colliding nuclei, it is also possible to define target and projectile spectator planes ($\Psi_{\mathrm{SP}}^{\mathrm{t}}$ and $\Psi_{\mathrm{SP}}^{\mathrm{p}}$). Because of such fluctuations the angles are generally non-zero and different for each individual heavy-ion collision and lead to a rapidity-even contribution to v_1, where $v_1^{\mathrm{even}}(y) = v_1^{\mathrm{even}}(-y)$.

Experimentally, the v_1^{odd} is often studied as a function of the collision energy. Exam-

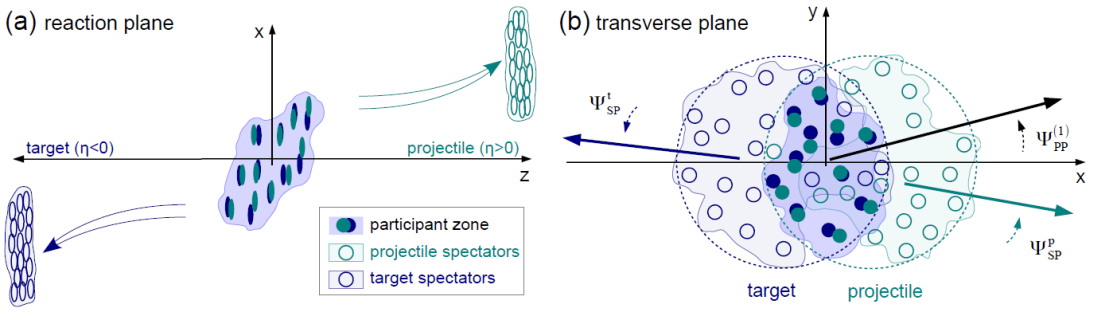

Fig. 1.14: Schematic view of a heavy-ion collision in reaction plane (a) and in transverse plane (b). The asymmetry of the interaction region in reaction plane will lead to non-zero rapidity odd directed flow $v_1^{\mathrm{odd}}(y)$. Due to fluctuations of the shape of the interaction region, several interaction planes are introduced: the participant plane, with angle $\Psi_{\mathrm{PP}}^{(1)}$, and target and projectile spectator planes ($\Psi_{\mathrm{SP}}^{\mathrm{t}}$ and $\Psi_{\mathrm{SP}}^{\mathrm{p}}$). These fluctuations then contribute to rapidity-even directed flow $v_1^{\mathrm{even}}(y)$. Taken from Ref. [56].

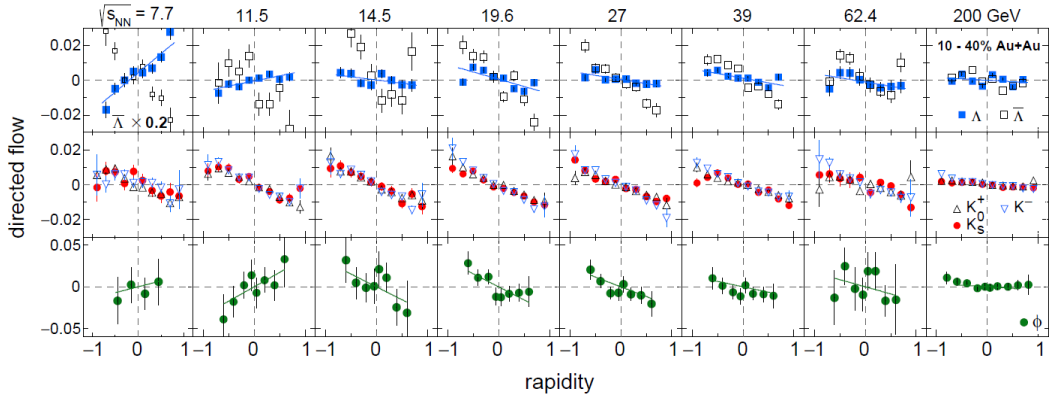

Fig. 1.15: Directed flow of identified strange baryons as a function of y measured in 10-40% central Au+Au collisions at different energies. For some of the data, there is a linear fit used to extract the directed flow slope $\mathrm{d}v_1/\mathrm{d}y$. For detailed discussion of the centrality dependence of the v_1 slope, see [57]. Taken from Ref. [57].

ple of such measurement is presented in Fig. 1.15, which shows v_1 of identified strange hadrons as a function of y in 10-40% central Au+Au collisions at different energies [57]. At high collision energies, the non-zero v_1 can be explained based on tilt of the QGP bulk within the 1st order event plane. Example of the tilt is illustrated in Fig. 1.14 (a). As with higher order harmonics, the asymmetry in the initial shape will be propagated into asymmetry of particle spectra in final state, due to pressure gradients. In this case (from Fig. 1.14), more particles will be emitted to regions with $x < 0$ and $z > 0$ for $\eta > 0$ and $x > 0$ and $z < 0$ for $\eta < 0$, which leads to negative measured v_1 slope in rapidity $\mathrm{d}v_1/\mathrm{d}y$. Detailed discussion of the collision energy dependence of the v_1 slope ($\mathrm{d}v_1/\mathrm{d}y$) is available in [57].

The discussion above applies to collective flow of light flavor hadrons, which originate

mainly from hadronization of the QGP bulk. It is also interesting and important to study collective flow of heavy quarks, which can be accessed by measurement of open heavy-flavor hadrons. The origin of collective flow for heavy flavor hadrons is slightly different than for light hadrons, as heavy quarks originate exclusively from the hard partonic scattering and therefore do not have any information about the collective motion of the medium in early stage of the collision. The details about collective flow of open-charm hadrons will be discussed in the following chapter.

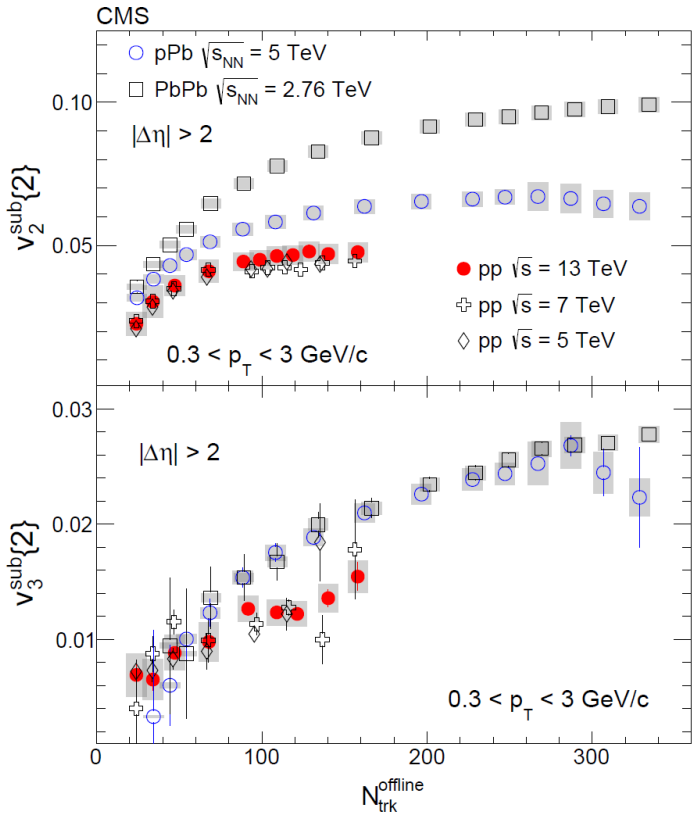

Fig. 1.16: Elliptic (top) and triangular (bottom) flow as a function of collision multiplicity ($N_{\mathrm{trk}}^{\mathrm{offline}}$) measured in p+p, p+Pb, and Pb+Pb collisions by CMS. For energy of the collisions, see the legend. The elliptic flow shows clear ordering with different collision system, where it is the largest in Pb+Pb and smallest in p+p collisions. Triangular flow, on the other hand, has similar magnitude in all studied collisions systems. The harmonic flow coefficients were extracted using two-particle correlation method. The superscript "sub" indicates that the results were corrected for back-to-back jet correlations which were estimated from low-multiplicity data. Taken from Ref. [58].

Another important thing to discuss is that collective flow is not a phenomenon observed in heavy-in collisions only. Not that long ago, it was generally accepted, that harmonic flow is a medium induced effect and should be observable exclusively in ultra-relativistic heavy-ions collisions. With development of more sophisticated experimental techniques and increased collision energies at the LHC, it was discovered, that collective

behavior can be observed in high multiplicity events of small systems (p+p, p+Pb) as well. Example of such measurement is displayed in Fig. 1.16, which shows elliptic (top) and triangular (bottom) flow as a function of collision multiplicity ($N_{\mathrm{trk}}^{\mathrm{offline}}$) measured in p+p, p+Pb, and Pb+Pb collisions by CMS. The elliptic flow clearly shows ordering based on system size, where v_2 is the largest in Pb+Pb and smallest in p+p. In case of triangular flow, the situation is a bit different as the v_3 is of similar magnitude in all collisions systems which is given by that v_3 is more sensitive to initial shape fluctuations (in A+A collisions). For that reason v_3 for all collision systems can be similar. It is also important to note, that the event plane method of v_{n} measurement, which was used for results presented above ($n \leq 2$), cannot be used in small systems, as there is no well defined geometrical overlap in p+p or p+A collisions. For that reason a different method is used for results from Fig. 1.16 which relies on measurement of multi-particle correlations which allows extraction of harmonic flow coefficients in all three collision systems. More details about this method are described in Ref. [58].

Observation of harmonic flow in small systems lead to development of new theoretical models which attempt to describe the observed flow coefficients in all collisions systems at the same time. One successful model is superSONIC [59] which uses viscous hydrodynamics to simultaneously describe the measured v_2, v_3, and v_4 in p+p, p+Pb, and Pb+Pb collisions at 5.02 TeV using the same set of fluid parameters, namely shear ($\eta/s = 0.08$) and bulk ($\xi/s = 0.01$) viscosities (over entropy s). The viscosity of the QGP based on this model is very small compared to e.g. water or liquid helium, as can be seen for example in Ref. [60]. Overall, the superSONIC model suggests that the QGP (in Pb+Pb collisions) behaves nearly as an ideal fluid and that flow-like correlations observed in small systems can be explained hydrodynamically as well, using one set of parameters.

Modification of jets

High energy collisions, regardless of the collision system (p+p, p+A, d+A, A+A, e^++e^-, etc.), are able to produce partons with high transverse momenta. In a small system, such as p+p collisions, these partons propagate through vacuum where they radiate gluons intensively which leads to creation of more partons, which then hadronize (including the primary parton). As a result, there will be a collimated shower of hadrons originating from fragmentation of the original high-p_{t} parton. Such showers are referred to as jets[5]. In the simplest case the high-p_{T} partons are produced in pairs, which then leads to two jets which are facing "back-to-back", i.e. when one jet is observed at given ϕ, the second is observed at $\phi + \pi$ due to conservation of momentum. In practice, it is also possible to observe more than two jets in one event, e.g. when one of the partons radiates very

[5]This is a theoretical definition of jet. From experimental point of view, a jet is defined by reconstruction algorithm used to reconstruct the jet.

energetic gluon, that will than have its own associated jet, or directly from 3 gluon interactions in hard partonic scattering.

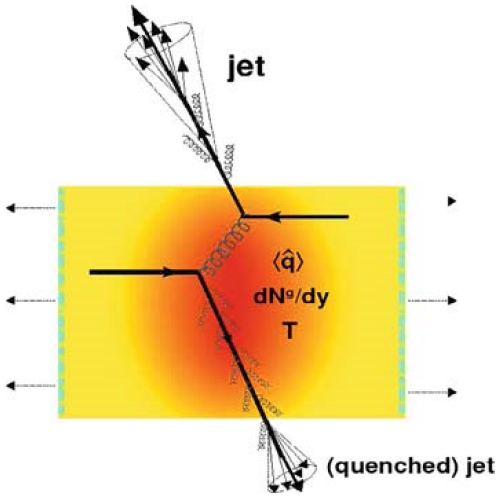

Fig. 1.17: Side view of central heavy-on collision. Indicated is a hard partonic scattering, which is origin of two high energetic partons that each travel different distance through the QGP. As a result, each parton suffers different energy loss which can be then experimentally observed in different properties of the reconstructed jets. Taken from Ref. [61].

In heavy-ion collisions, jets are induced by partons which are produced in hard partonic scattering. The key difference to p+p collisions is that the initial high-p_{T} partons have to pass through part of the volume of the QGP fireball, as shown for example in Fig. 1.17, where they loose energy and momentum. That leads to modification of jets in heavy-ion collisions with respect to p+p collisions. By convention, the jet with higher momentum is referred to as the leading jet, or the near-side jet, the one with lower momentum is called the sub-leading jet, or the away-side jet. The same terminology is used in small systems as well, where the near side jet is typically chosen as the one containing particle with the highest p_{T} (out of particles within the jets in given collision).

In case the hard partonic scattering occurs close to surface of the volume of the QGP, one of the partons can escape directly to vacuum, creating a nearly unmodified jet, but the second one has to pass through the whole volume of the QGP fireball. In some cases, the second parton can loose substantial amount of energy inside the medium, which will lead to significant modification of the away side jet. This phenomenon is called jet quenching which was first experimentally observed by the STAR experiment in Au+Au collisions at $\sqrt{s_{\mathrm{NN}}} = 200\,\mathrm{GeV}$, as shown in Fig. 1.18. The method used in this example is measurement of two particle correlations. The high-p_{T} hadron from the leading jet is chosen as the first particle and is correlated with all other particles within selected p_{T} interval. In Fig. 1.18, the two particle azimuthal distributions were extracted for trigger particles with $4 < p_{\mathrm{T}}(\mathrm{trig}) < 6\,\mathrm{GeV}/c$ and for associated particles

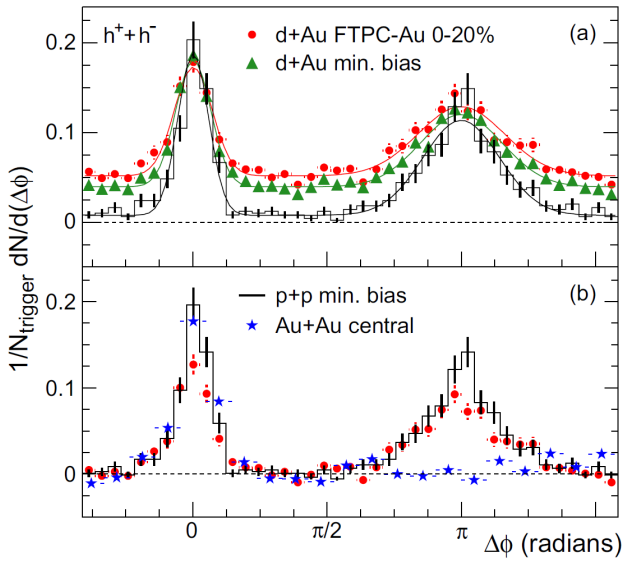

Fig. 1.18: Two-particle azimuthal distributions of charged hadrons in p+p (black), d+Au (red and green), and Au+Au (blue) collisions at $\sqrt{s_{\mathrm{NN}}} = 200\,\mathrm{GeV}$ measured by the STAR experiment. The trigger particle was required to have $4 < p_{\mathrm{T}}(\mathrm{trig}) < 6\,\mathrm{GeV}/c$, the associated particles were required to have $2 < p_{\mathrm{T}} < p_{\mathrm{T}}(\mathrm{trig})$. Taken from Ref. [62].

with $2 < p_{\mathrm{T}} < p_{\mathrm{T}}(\mathrm{trig})$. This selection of associated particles makes sure that they can originate exclusively from a hard process, i.e. from a fragmentation of high-p_{T} hadron, rather than from hadronization of the QFP bulk (in case of heavy-ion collisions). In p+p (black) and d+Au (green and red) collisions, there are such high-p_{T} associated particles in direction of the trigger particle (around $\Delta\phi = 0$) as well as on the away side (around $\Delta\phi = \pi$). In Au+Au collisions, on the other hand, the away-side high-p_{T} associated particles are completely suppressed by the medium. This does not mean that they are not present on the away-side, but they have significantly lower p_{T} due to energy loss inside the QGP.

The discussion above focused exclusively on the case, when the high-p_{T} particles created in hard partonic scattering are partons (quarks or gluons). In these measurements, both jets typically have to pass through at least part of the QGP volume. As a result, even the leading particle suffers certain energy loss inside the medium, which means that the information about energy of the initial hard partonic scattering is lost. One possibility to access this information is to measure γ-jet (or γ-hadron) correlations. There are multiple possible processes which can create such events, one of which is e.g. $qg \to q\gamma$. In this case, the leading particle is a photon, which does not interact with the QGP and the away-side particle is a high-p_{T} quark, around which a jet will be formed. Due to conservation of momentum, detecting such photon gives direct access to information about energy of the away-side quark at the time of the hard partonic scattering and so can help evaluate energy loss of the quark in the QGP medium or tu modification of

jet sub-structure with respect to p+p collisions (i.e. when the jet propagates through vacuum). Such measurement is experimentally very challenging, because there are many photons created in different processes, mainly Dalitz decays of π^0 mesons and conversion photons, created by charged particles passing through material of the detector.

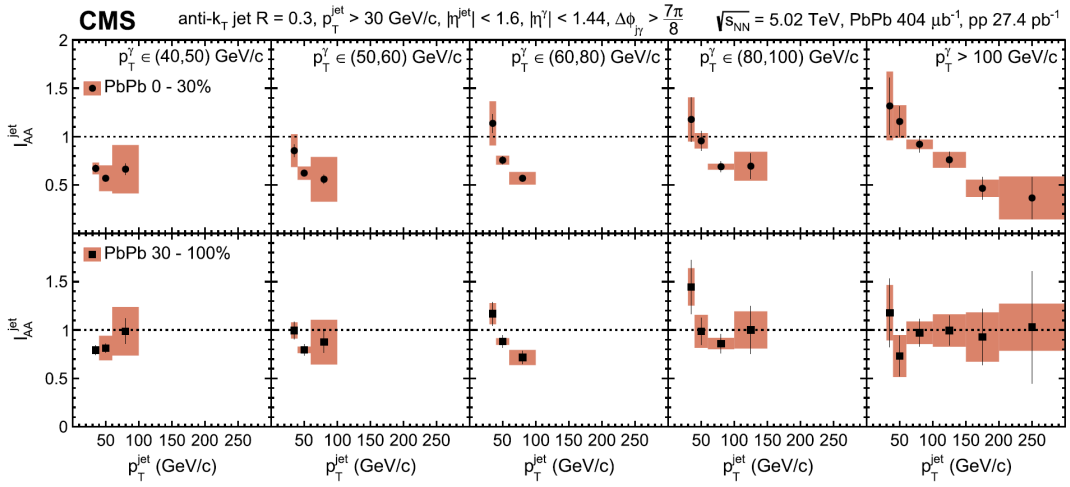

Fig. 1.19: $I_{\mathrm{AA}}^{\mathrm{jet}}$ as a function of p_{T} and collision centrality measured in Pb+Pb collisions at $\sqrt{s_{\mathrm{NN}}} = 5.02\,\mathrm{TeV}$ by the CMS experiment. The top row shows the measurement for 0-30% central Pb+Pb collisions, the bottom row for 30-100% centrality. The individual columns then correspond to various intervals of transverse momenta of photons p_{T}^{γ}. In 0-30% central Pb+Pb collisions, the high-p_{T} jets are suppressed for all intervals of photon transverse momenta, which indicates substantial energy loss of the away-side jets in the QGP. In 30-100% central Pb+Pb collisions, on the other hand, is not observed at all for high-p_{T} photons and is substantially smaller for photons with lower transverse momenta. Taken from Ref. [63].

Example of measurement of γ-jets is presented in Fig. 1.19, which shows the $I_{\mathrm{AA}}^{\mathrm{jet}}$ as a function of p_{T} measured in Pb+Pb collisions at $\sqrt{s_{\mathrm{NN}}} = 5.02\,\mathrm{TeV}$ by the CMS experiment [63]. The $I_{\mathrm{AA}}^{\mathrm{jet}}$ is defined using the following formula:

$$I_{\mathrm{AA}}^{\mathrm{jet}} = \left(\frac{1}{N_{\mathrm{PbPb}}^{\gamma}} \frac{\mathrm{d}N_{\mathrm{PbPb}}^{\mathrm{jet}}}{\mathrm{d}p_{\mathrm{T}}^{\mathrm{jet}}} \right) \Bigg/ \left(\frac{1}{N_{\mathrm{pp}}^{\gamma}} \frac{\mathrm{d}N_{\mathrm{pp}}^{\mathrm{jet}}}{\mathrm{d}p_{\mathrm{T}}^{\mathrm{jet}}} \right), \tag{1.6}$$

where N_{pp} and N_{PbPb} is number of γ, and $\mathrm{d}N_{\mathrm{pp}}^{\mathrm{jet}}/\mathrm{d}p_{\mathrm{T}}^{\mathrm{jet}}$ and $\mathrm{d}N_{\mathrm{PbPb}}^{\mathrm{jet}}/\mathrm{d}p_{\mathrm{T}}^{\mathrm{jet}}$ is number of jets observed in p+p and Pb+Pb collisions, respectively. The jets are significantly modified by the medium in central Pb+Pb collisions, as can be seen in the top row of Fig. 1.19. For given p_{T}^{γ} range, the high-p_{T} jets are suppressed in 0-30% central Pb+Pb collisions with respect to p+p collisions (upper row of Fig. 1.19), indicating significant energy loss of the away-side jet in the QGP. The excess observed at low edge of p_{T} e.g. in 0-30% central Pb+Pb collisions for p_{T}^{γ} is caused by shift of particles in jet towards lower p_{T} due to energy loss in the medium. In 30-100% central Pb+Pb collisions, no suppression

is observed for jets associated with photons with $p_{\mathrm{T}}^{\gamma} > 80\,\mathrm{GeV}/c$. For lower transverse momenta of photons, a hint of suppression of the away-side jets is still observed, but not as large as in central collisions. Possible explanation of this observation is that in mid-central and peripheral collisions the volume of the QGP fireball is smaller than in central collisions. As a result, the away-side jet in 30-100% central Pb+Pb collisions loose on average less energy than in 0-30% central collisions.

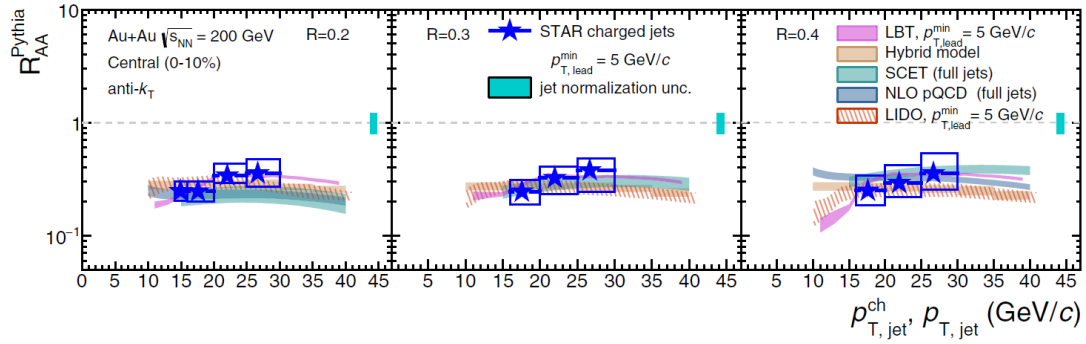

Fig. 1.20: R_{AA} of charged jets as a function of $p_{\mathrm{T,jet}}^{\mathrm{ch}}$ measured in 0-10% central Au+Au collisions at $\sqrt{s_{\mathrm{NN}}} = 200\,\mathrm{GeV}$ by the STAR experiment for three values of jet resolution parameter R. The data are compared to various model calculations which incorporate jet quenching: LBT [64–66], Hybrid model [67], SCET [68, 69], NLO pQCD [70], and LIDO [71, 72]. Taken from Ref. [73].

Modification of jets in heavy-ion collisions is not studied only via correlations between the near-side and away-side jets (or particle correlations in general). It also is possible to perform direct observations, similar to particle production measurements discussed earlier. The nuclear modification factor defined in Eq. (1.4) can be modified for jets. The only difference is that the particle spectra from Eq. (1.4) are replaced by spectra of jets with chosen properties. Figure 1.20 shows the R_{AA} of charged-particle jets as a function of $p_{\mathrm{T,jet}}^{\mathrm{ch}}$ ($p_{\mathrm{T,jet}}$ for models) measured in 0-10% central Au+Au collisions at $\sqrt{s_{\mathrm{NN}}} = 200\,\mathrm{GeV}$ by the STAR experiment [73] for three values of jet resolution parameter R. The resolution parameter is, in simple terms, a radius of a cone around the jet axis. Only part of the particles of the full jet which are inside of the cone are considered. By using small R, the core of the jet is studied, which contains primarily high-p_{T}. While increasing the R, more and more of the softer particles, further form the jet axis are considered. The measurement in Fig. 1.20 clearly indicates that charged jets are significantly suppressed in central Au+Au collisions and also that the suppression does not show strong dependence on the jet resolution parameter. The data are compared to various model calculations which incorporate jet quenching: LBT (Linear Boltzman Transport) [64–66], Hybrid model [67], SCET (Soft-Collinear Effective Theory) [68, 69], NLO (Next-to-Leading-Order) pQCD [70], and LIDO [71, 72]. Overall, the data and the models are in a good agreement within the uncertainties.

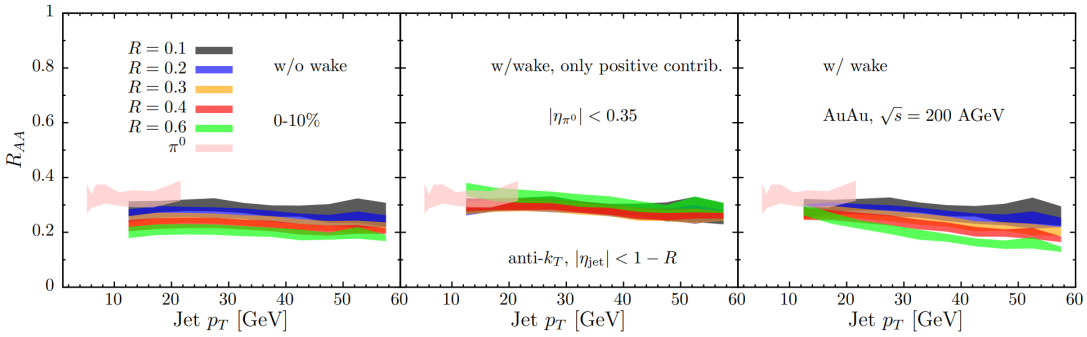

Fig. 1.21: R_{AA} of jets as a function of $p_{\text{T,jet}}$ in 0-10% central Au+Au collisions at $\sqrt{s_{\text{NN}}} = 200\,\text{GeV}$ simulated using Hybrid model for various values of jet resolution parameter. Individual panels show different setups of the model calculation, where the right panel shows the version with all contributions considered by this model. Taken from Ref. [74].

The independence of the charged jet R_{AA} on jet resolution parameter presented in Fig. 1.20 might be seen as surprising. Many jet quenching models, such as those listed above, generally predict different suppression for various values of R. One possible cause of an ordering with R is an effect called broadening of jets in heavy-ion collisions. The core idea is that as a jet is propagating through the QGP, its constituents interact with the medium, obtaining momentum transverse to the jet axis. As a result, the jet constituent particles will be "pushed" further away from the jet axis in heavy-ion collisions compared to jets in p+p collisions. In this scenario, the jet suppression should get smaller with increasing R, as more and more of the "pushed" jet constituents are included in the reconstructed jet, i.e. getting closer to the vacuum baseline from p+p. Some models, such as the Hybrid model [67], have exactly opposite ordering, i.e. jets with larger R are more suppressed, as shown in Fig. 1.21. This model contains other, more complex interactions of the jet with the medium which eventually lead to such ordering with R. This shows that it is crucial to measure properties of jets as a function of R with high precision in order to provide constraints on theoretical model calculations, which is a challenging task.

Here, it is also important to note, that STAR has also performed study of the jet broadening via measurement of dijet asymmetry A_{J} [75] which is defined as

$$A_{\text{J}} = \frac{p_{\text{T,lead}} - p_{\text{T,lead}}}{p_{\text{T,lead}} + p_{\text{T,lead}}}, \tag{1.7}$$

where $p_{\text{T,lead}}$ and $p_{\text{T,sublead}}$ are transverse momenta of the leading jet and the sub-leading (away side) jet, respectively. The measurement has been done for 0-20% central Au+Au collisions at $\sqrt{s_{\text{NN}}} = 200\,\text{GeV}$. Leading jets were required to have $p_{\text{T,lead}} > 20\,\text{GeV}/c$, and the sub-leading jets $p_{\text{T,sublead}} > 10\,\text{GeV}/c$. Two sub-sets of jets were then selected, one where the jet constituents have $p_{\text{T}} > 0.2\,\text{GeV}/c$, i.e. including soft part of the

jet, and second only with constituents with $p_{\mathrm{T}} > 2\,\mathrm{GeV}/c$, i.e. selecting only rather high-p_{T} part of the jet. The measurement was done for two values of the jet resolution parameter: $R = 0.2$ and $R = 0.4$.. For $R = 0.2$, the A_{J} is different in Au+Au and p+p collisions regardless of selection of p_{T} of the jet constituents, suggesting significant modification of the central region of the jet in heavy-ion collisions. For $R = 0.4$, on the other hand, the modification is observed only for hard jet constituents, but when the soft part of the jet is included, the measured A_{J} in Au+Au and p+p collisions is consistent within uncertainties. This observation is consistent with the broadening scenario described in the previous paragraph. Natural question is, how are the results from measurement of the full charged jets from Ref. [62] and those from measurement of A_{J} from Ref. [75] compatible. One key thing to note is that the jet selection is different in the two analyses which makes direct comparison nontrivial. A possible direction is development of theoretical framework that would be able to describe both measurements at the same time, as suggested in Ref. [62].

Chapter 2

Open-charm hadrons

This chapter provides an overview of the open-charm hadrons in the context of heavy-ion collisions and study of the QGP and it is divided into three sections. Section 2.1 provides a general overview of properties of the open charm hadrons with focus on four of their ground states: D^0, $D^{\pm}$, and $D_s^{\pm}$ mesons, and $\Lambda_c^{\pm}$ baryon. Section 2.2 describes the motivation for measurement of the open-charm hadrons in heavy-ion collisions and finally Sec. 2.3 summarizes recent results from measurements of open-charm hadrons at RHIC and the LHC.

2.1 Properties of open-charm hadrons

The Standard Model of particles contains total of six quarks, divided into three generations. The first generation contains the two lightest quarks: up (u) and down (d), which are the building blocks of nucleons. The heavier strange (s) and charm quarks (c) belong to the second generation, and the third generation consists of the two heaviest quarks - bottom (b) and top (t). Quarks are fermions with spin 1/2 that carry a fractional electric charge of $2/3e$ (u, c, t), or -1/3e (d, s, b), and also color. Quarks are therefore the only elementary particles that can interact strongly, electromagnetically or weakly. All quarks also carry their flavor specific quantum numbers. One of those is the isospin I, which is non-zero for u ($I_z = 1/2$) and d (I_z = -1/2) quarks. The s-quarks carry strangeness $S = -1$, c-quarks carry charm $C = 1$, b-quarks have bottom (or beauty) $B = -1$, and finally t-quarks have top $T = -1$. The corresponding anti-quarks have these quantum numbers with an opposite sign.

All quarks, with exception of top[1], form bound states which are called hadrons. Two main types of hadrons are mesons and (anti-)baryons. Mesons contain one quark and one anti-quark, while baryons contain three quarks (three anti-quarks in case of anti-baryons). The heavy flavor hadrons, i.e. hadrons containing either c or b (anti-)quark

[1]Due to their very low lifetime, no bound states of top quark are known.

(or both) can be then divided into two categories: hadrons with hidden charm (beauty), i.e. with $C = 0$ ($B = 0$), which are referred as quarkonia, and open charm (beauty) hadrons which have $C \neq 0$ ($B \neq 0$), which are called open heavy-flavor hadrons.

Hadron	Quark content	m [MeV/c^2]	$c\tau$ [μm]
D^0	$c\bar{u}$	1864.84 ± 0.05	122.9 ± 0.5
D^+	$c\bar{d}$	1869.66 ± 0.05	311.8 ± 2.1
D_s^+	$c\bar{s}$	1968.35 ± 0.07	151.2 ± 1.2
Λ_c^+	cud	2286.46 ± 0.14	60.7 ± 0.9

Tab. 2.1: Basic properties of four ground states of open-charm hadrons. Shown are: the quark content, the rest mass m, and the mean lifetime $c\tau$. Values are taken from Ref. [76].

In this thesis, the main focus is primarily on the four main ground states of open-charm hadrons: D^0, $D^\pm$, and $D_s^\pm$ mesons, and $\Lambda_c^\pm$ baryon. An overview of basic properties of the aforementioned hadrons is summarized in Tab. 2.1. Compared to strange hadrons, they are heavy and relatively short-lived. The short lifetime, combined with quite rich combination of possible decay channels (see Ref. [76]) makes reconstruction of the open-charm hadrons challenging.

Discovery of open-charm hadrons played an important role in confirmation of existence of charm quarks. One of the first steps to discovery of charm quarks was introduction of the quark model by Gell-Mann and Zweig in 1964 [6, 7], which in its early form contained only u, d and s quarks. This seemed to be sufficient to explain the properties of known hadrons, for some time, but relatively soon, several inconsistencies between the predictions of the quark model and experimental data appeared. Specifically, they were properties of neutral kaons, K_L^0 and K_S^0, such as branching ratios of certain decay channels, or the mass difference between the two kaons. Possible solution was proposed by Glashow, Iliopoulos, and Maiani [77] by adding a fourth quark to the quark model, which could then participate in electro-weak interactions. This helped to resolve the inconsistencies mentioned above.

Soon after that, it became clear that this new quark should be able to produce bound states with its anti-quark. That has been experimentally confirmed simultaneously by two experimental groups in 1974: one at BNL and the other at SLAC [78, 79]. The new particle with mass around 3.1 GeV/c^2 was named J/ψ. It was immediately obvious, that it is a very interesting meson. The width of the resonance peak was surprisingly narrow for such heavy resonance which indicates that the binding energy of the state is very high. In contrast to its strange counterpart, the ϕ meson, the J/ψ cannot decay strongly to the open-charm hadrons, because its mass is lower than two masses of any of the D mesons. This fact contributed to that it took additional two years to discover D^0 and $D^\pm$ mesons, which was necessary for confirmation of that J/ψ is indeed a bound

state of c quark and $\bar{c}$ anti-quark.

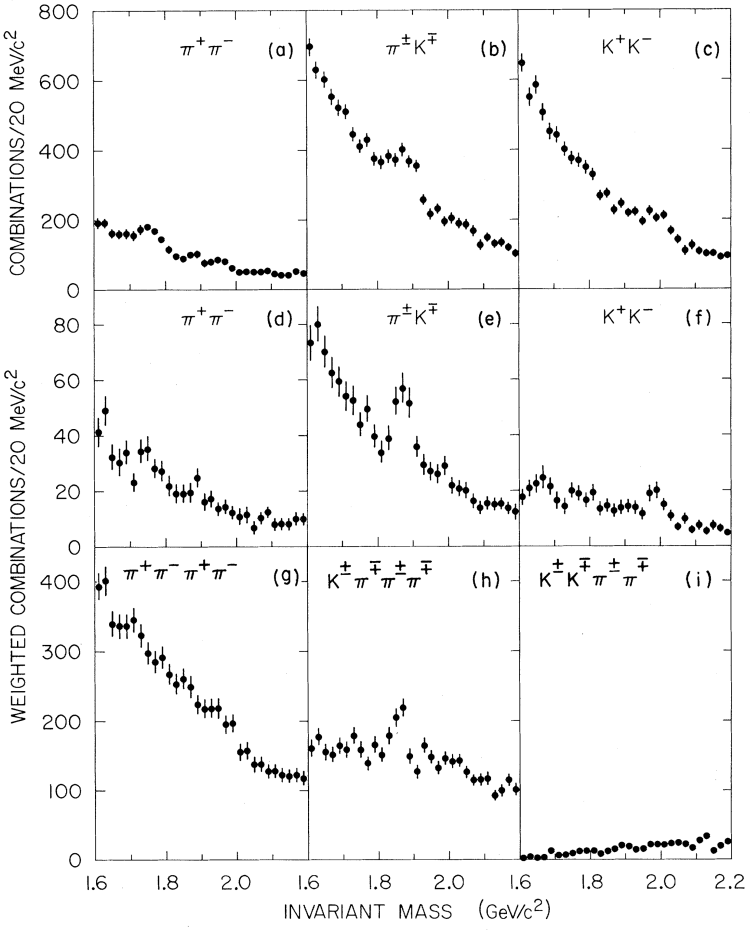

Fig. 2.1: Invariant mass spectra of different combinations of charged pions and kaons. The central column shows the invariant mass spectra for combinations expected to come from the decay of the D^0 meson, the left and right column are for other combinations and serve as a validation check of the signal observed in the central column. The top row shows the invariant mass spectra for all tacks, the bottom two for TOF identified tracks. Taken from Ref. [80].

The first open-charm hadron that was observed is the D^0 meson. It was discovered by the SLAC-LBL magnetic detector at SPEAR, by reconstruction of two hadronic decay channels of the D^0 meson: $D^0 \to K^{\pm}\pi^{\mp}$ and $D^0 \to K^{\pm}\pi^{\mp}\pi^{\pm}\pi^{\mp}$ [80]. The invariant mass spectra of the kaon-pion multiplets are shown in Fig. 2.1. Most important is the central column, which shows the invariant mass spectra for correct particle species and charge combinations. For both decay channels, there is a clear peak visible. The extracted D^0 yield is (110 ± 25) for the two-particle decay channel and (124 ± 21) for the four-particle decay channel. In both cases, the significance of the yield is above 5, which was deemed as sufficient for evidence for existence of D^0. The invariant mass distributions in the left and right columns of Fig. 2.1 are for pion and kaon combinations which should not come

from decay of D^0 mesons and are used as a control. No significant signal is observed in the control invariant mass distributions, further supporting the discovery of D^0 meson. The invariant mass of the D^0 meson was measured to be $m_{D^0} = (1865 \pm 15)\,\mathrm{MeV}/c^2$ which is very close to the latest value from Tab. 2.1.

The $D^\pm$ meson was discovered at the same facility, using essentially the same methods, using $D^\pm \to K^\mp\pi^\pm\pi^\pm$ decay channel [81]. The measured mass of $D^\pm$ is $m_{D^\pm} = (1876 \pm 15)\,\mathrm{MeV}/c^2$ which is consistent with the most recent value within the uncertainties. Discovery of the D^0 and $D^\pm$ mesons was a key step in confirmation of existence of charm quarks.

The next natural question was, if the charm quark can form mesons with strange anti-quarks. The search for, what we now know as the $D_s^\pm$ meson, took some time. There were several unsuccessful attempts, until 1983, when the $D_s^\pm$ meson was finally discovered at the CLEO detector at the Cornell Electron Storage Ring (CESR) [82]. At the time, it was called the F^+ meson. It was reconstructed using the decay channel $D_s^+ \to \phi\pi^+ \to K^-K^+\pi^+$ and its mass was measured to be $m_{D_s} = (1970 \pm 5 \pm 5)\,\mathrm{MeV}/c^2$.

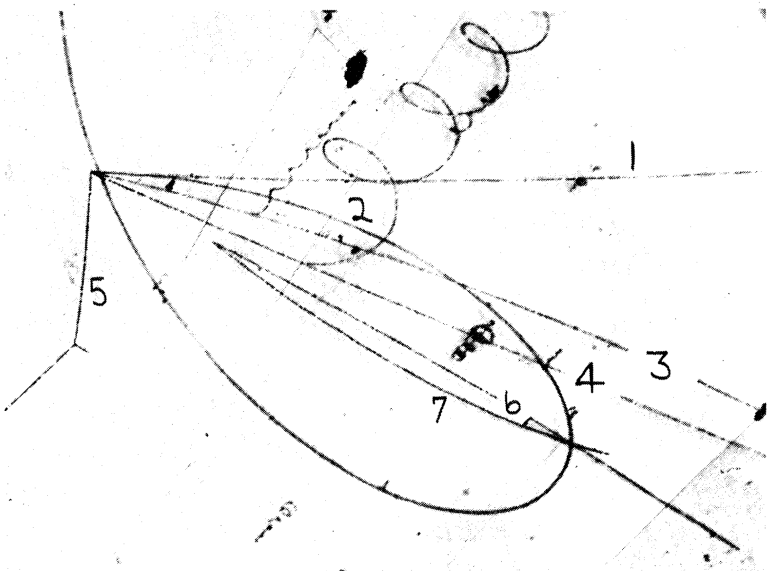

Fig. 2.2: A photo of an event from the 7-foot cryogenic bubble chamber in BNL, showing first ever recorded event of decay of the Λ_c baryon. Taken from Ref. [83].

After discovery of D mesons, the search did not focus only on finding new mesons, but also on discovery of charmed baryons. The first hint of existence of baryons containing charm quarks was actually observed before the D meson discovery. The 7-foot bubble chamber at BNL has famously taken a picture of an event measured in reaction of neutrinos with protons which is shown in Fig. 2.2. The observed final state was identified as $\Lambda 3\pi^+\pi^-$ [83] with total invariant mass $m = (2426 \pm 12)\,\mathrm{MeV}/c^2$. It was not yet clear at that time, what is the exact origin of this event, but the authors provided detailed description of possible scenarios. One of the most probable ones was deemed decay of

doubly positive charged charm baryon Σ_c^{++}:

$$\Sigma_c^{++} \rightarrow \Lambda_c^+ \pi^+ \rightarrow \Lambda 3\pi^+\pi^-$$

This was a remarkably precise explanation, which is nicely consistent with current knowledge of masses and decay channels of Σ_c^{++} and Λ_c^+ baryons. This measurement was not sufficient as an evidence for existence of the open-charm baryons. The first true observation came a bit later at Fermilab, where a decay of anti-baryon Λ_c^- was observed [84]. The Λ_c^- anti-baryons were reconstructed via decay channel $\Lambda_c^- \rightarrow \Lambda 2\pi^-\pi^+$, with measured mass $m_{\Lambda_c} = (2.26 \pm 0.01)\,\mathrm{GeV}/c^2$, again being reasonably close to the current value.

It is quite important and interesting to note that the search for more open-charm hadron species continues up to this day, primarily in the baryon sector. One of the most recent discoveries was the observation of a doubly charmed baryon Ξ_{cc}^{++} by the LHCb experiment [85]. This is the first observation of a baryon with more than one charm quark, which makes this measurement an important confirmation of predictions made by the quark model.

Overall, search for new, yet unobserved, open-heavy flavor hadron species and measurement of properties of the known ones is important for verification of prediction of the quark model and the standard model of particles. At the same time, the known open-heavy flavor hadrons turned out to a great tool to probe the properties of the QGP produced in ultra-relativistic heavy-ion collisions. A motivation for measurement of open-charm hadrons in heavy-ion collisions is described in the following section.

2.2 Open-charm hadrons in heavy-ion collisions

One of the main motivations for measurement of open-charm hadrons in heavy-ion collisions is tahat their production in p+p is reasonably well understood. This fact is demonstrated in Fig. 2.3 which shows measurement of D^0 (left) and $D^\pm$ mesons in p+p collisions at $\sqrt{s} = 7\,\mathrm{TeV}$ by ALICE [86]. The data are compared to FONLL (Fixed Order + Next to Leading Logarithm) [87–89] and GM-VFNS (General Mass Variable Flavor Number Scheme) [90, 91] theoretical model calculation. The experimental data and the models are in a good agreement which shows that p+p results are a good baseline for heavy-ion measurements.

Second important motivation is that due to their large mass, charm quarks are produced predominantly in hard partonic scatterings, at very early stages of the heavy-ion collisions. This means, that they are produced before the ignition of the QGP fireball and therefore have to pass through the volume of the QGP, where they loose energy and momentum. As in the example above from p+p collisions, the information about

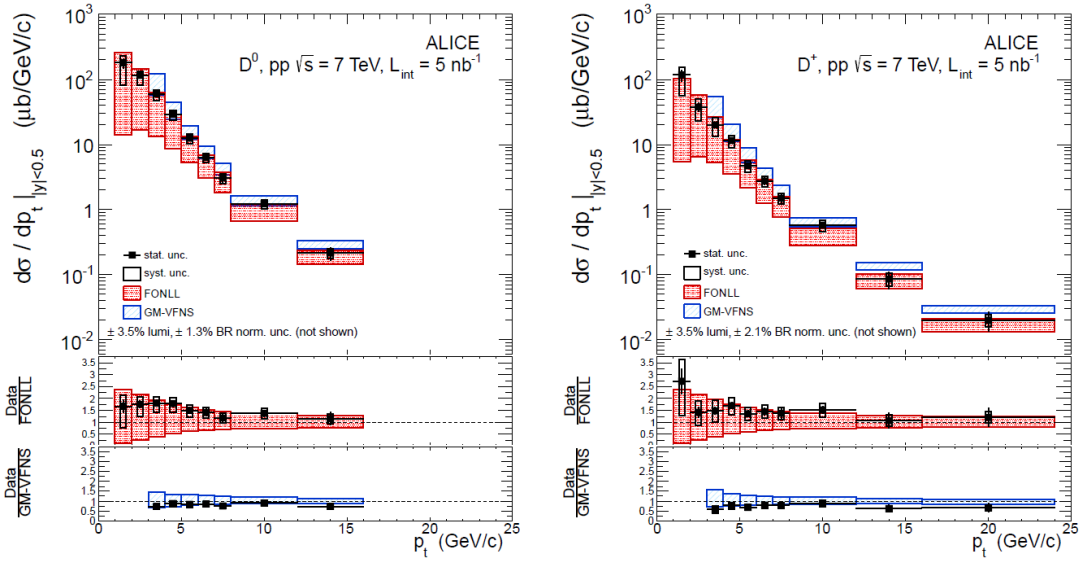

Fig. 2.3: Production cross section of D^0 (left) and $D^{\pm}$ (right) mesons measured by ALICE in p+p collisions at $\sqrt{s} = 7\,\text{TeV}$. The data are compared to FONLL [87–89] and GM-VFNS [90, 91] theoretical calculations. The data and the models are in a good agreement overall. Taken from Ref. [86].

charm quark production in heavy-ion collisions can be accessed via measurement of open-charm hadrons. At STAR, it is possible to topologically reconstruct hadronic decays of the open-charm hadrons thanks to excellent vertex resolution of the Heavy Flavor Tracker (HFT) detector [5]. More details about the HFT will be provided in Ch. 3.

The energy loss of charm quarks inside QGP can be accessed via measurement of R_{AA} of open charm hadrons. As discussed in Sec. 1.3, light flavor hadrons show significant suppression in central heavy-ion collisions compared to p+p collisions. It is therefore important to measure the R_{AA} of heavy-flavor hadrons as well in order to have good understanding of particle production modification in heavy-ion collisions. One of the main advantages of measuring the R_{AA} of open-charm hadrons over that of the light flavor hadrons is that the observed modification of production yields of the open-charm hadrons should be caused primarily by the presence of the QGP[2], as all of the observed open-charm hadrons are a result of hadronization of charm quarks originating from the hard partonic scattering, i.e. from one well defined source. The light flavor quarks can originate from multiple different sources (hard scattering, hadronization of the QGP fireball, fragmentation of jet shower) which makes any conclusions about their R_{AA} less straightforward.

Similar advantage can be found in measurement of the elliptic and higher order harmonic flow coefficients for open-charm hadrons. Again, because the charm quarks are produced before the QGP fireball, they do not have any information about the geometri-

[2]The Cold Nuclear Matter effects may play role as well.

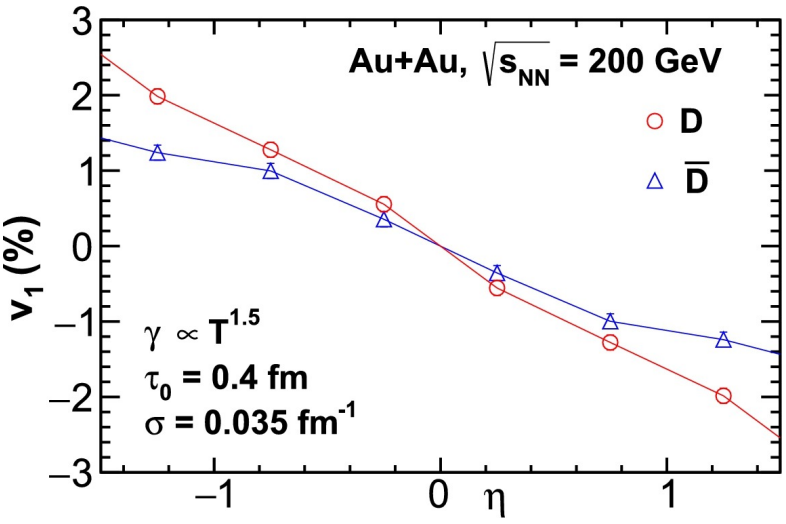

Fig. 2.4: Model calculation of the directed flow slope dv_1/dy of D^0 and $\bar{D}^0$ mesons, taking into account the initial tilt of the QGP bulk and the electromagnetic field induced by the passing spectators. Taken from Ref. [92].

cal asymmetry of the active region of the collision at the time of their creation. The only way they can acquire non-zero v_n for $n \leq 2$ is by interaction with the QGP medium. The magnitude of the harmonic flow coefficients for open-charm hadrons compared to that of the light flavor hadrons can provide access to information about how close do the charm quarks get to the thermal equilibrium with the QPG. Only simultaneous measurement of the v_2 and the R_{AA} of open-charm hadrons can give complete picture about charm quark energy loss inside the QGP medium. Good models should be able to describe both v_2 and the R_{AA} at the same time.

It is also interesting to investigate the first order harmonic flow v_1 of the open-charm hadrons. Similar to higher order harmonic flow coefficients, charm quarks are expected to have $v_1 = 0$ at the time of their creation. There are two effects that might give them a non-zero v_1: the tilt of the QGP fireball in the reaction plane (first order event plane), that would lead to a negative v_1 slope of both D^0 and $\bar{D}^0$ mesons as a function of rapidity (dv_1/dy) [93], and the strong electromagnetic field induced by the passing spectators in semi-central collisions that would lead to a negative dv_1/dy slope for D^0 and a positive for $\bar{D}^0$ [94]. In real events, both effects probably play a role. It is predicted, that combination of the two effects would lead to a negative slope dv_1/dy for both D^0 and $\bar{D}^0$, where the slope will be larger for D^0 than for $\bar{D}^0$ [92], as shown in Fig. 2.4. The open-charm mesons therefore should be able to provide insight into initial conditions of the heavy-ion collisions.

As the charm quarks are produced exclusively in hard partonic scatterings of heavy-ion collisions, they often acquire large transverse momenta and induce jets. Heavy-flavor induced jets are a useful tool to study flavor dependence of the interaction of quarks with

the QGP medium. One possibility, similar to particle production yield, is measurement of jet R_{AA} and its flavor dependence. Different more sophisticated methods focus for example on studies of jet profile with respect to its axis, such as momentum distribution[3] of particles in the jet as a function of distance from the jet axis. As it is expected that both vacuum and medium induced radiation of quarks depends on their masses, such jet profiles should be different for light flavor quark induced jets and heavy-flavor quark induced jets. In general, jet sub-structure studies use more complicated observables which compare given particle properties (e.g. momenta) from different parts of the jet. Detailed description of these methods is beyond scope of this thesis.

As was already discussed, the information about charm quark production can only be accessed via reconstruction of charmed hadrons. It is therefore important to understand charm quark hadronization process, in order to make any conclusions about the properties of the interaction of charm quarks with the medium. As in case of light quarks, which was discussed in Sec. 1.3, charm quarks produced in heavy-ion collisions can hadronize either via fragmentation or coalescence. One of the main questions then is, how important role coalescence hadronization plays for charm quarks. A possible way to study the hadronization of charm quarks is by measuring particle yield ratios of various open-charm hadrons species in heavy-ion collisions and comparing them to those measured in p+p collisions. A modification of such ratios in heavy-ion collisions can be indicative of modification of hadronization of charm quarks due to coalescence. More detailed discussion of open-charm yield ratios will be provided in Sec. 2.3.

To conclude, measurement of open-charm hadrons in heavy-ion collisions can provide deep insight into properties of the QGP, interaction of quarks with the medium, hadronization mechanisms in vacuum and inside medium, and also about conditions at very early stages of the heavy-ion collisions. Their reconstruction in heavy-ion collisions is challenging due to their relatively short lifetime and very high combinatorial background levels. Typically a detector with very good resolution of primary and secondary vertices is required in order to be able to reconstruct decays of the open-charm hadrons, such as the STAR detector at RHIC, or ALICE detector at the LHC.

2.3 Recent measurements of open-charm in heavy-ion collisions

This section provides a summary of recent results from measurements of open-heavy flavor hadrons in ultra-relativistic heavy ion collisions at RHIC and the LHC. The main focus is on results from the STAR and ALICE experiments.

[3]This can be transverse momentum of the particles with respect to the beam axis, or transverse momentum with respect to the jet axis.

2.3.1 Open heavy-flavor hadrons measured by STAR

Results presented in this section are from Au+Au collisions at $\sqrt{s_{\rm NN}} = 200$ GeV measured by the STAR experiment in years 2014 and 2016. Topological reconstruction of the decays, utilizing the Heavy-Flavor Tracker (HFT) detector [5], was used to extract the signal of the open-charm hadrons listed in Table 2.2. The branching rations BR are taken from the latest PDG tables [76]. The individual analyses may have used older versions of the tables, depending on time of publication.

Decay channel	BR [%]
$\mathrm{D}^0 \rightarrow \mathrm{K}^-\pi^+$	3.946 ± 0.030
$\mathrm{D}_\mathrm{s}^+ \rightarrow \phi\pi^+ \rightarrow \mathrm{K}^-\mathrm{K}^+\pi^+$	2.24 ± 0.08
$\Lambda_c^+ \rightarrow \mathrm{K}^-\pi^+\mathrm{p}$	6.28 ± 0.32

Tab. 2.2: List of open-charm hadrons measured at STAR using the HFT. The left column contains decay channels used for reconstruction and BR is the branching ratio of the decay. Charge conjugate particles are measured as well. Values are taken from Ref. [76].

The first open-charm hadron results with the HFT at STAR are from measurement of D^0 mesons. The nuclear modification factor $R_{\rm AA}$ of the D^0 mesons as a function of $p_{\rm T}$ in 0-10% central Au+Au collisions [2] is shown in Figure 2.5. The D^0 mesons are significantly suppressed at high-$p_{\rm T}$ region which is likely caused by significant energy loss of charm quarks inside the volume of the QGP. The data are reasonably well described by model calculations which incorporate collective flow and energy loss of charm quarks in QGP [95, 96]. The D^0 $R_{\rm AA}$ by STAR is also compared to that of the D mesons and the charged hadrons in Pb+Pb collisions at $\sqrt{s_{\rm NN}} = 2.76$ TeV measured by ALICE [97, 98], and that of the $\pi^\pm$ mesons measured by STAR in the Au+Au collisions at $\sqrt{s_{\rm NN}} = 200$ GeV [99]. The open-charm mesons show a similar level of suppression as the light-flavor mesons at both ALICE and STAR experiments.

The centrality dependence of the D^0 meson $R_{\rm AA}$ by STAR is shown in Fig. 2.6. The suppression of the D^0 mesons for $p_{\rm T} > 3\,\mathrm{GeV}/c$ decreases going from central to peripheral collisions, which supports that the suppression is caused by the QGP. The situation is different at $p_{\rm T} < 2\,\mathrm{GeV}/c$, where the suppression is significant and independent of centrality of the collision. As will be discussed in the following chapter in Sec. 4.4.4, this observation plays an important role in understanding charm quark hadronization process in heavy-ion collisions.

As already suggested above, the model calculation [95,96] predict significant collective flow of the open-charm mesons. For that reason, STAR has measured the elliptic flow of the D^0 mesons as a function of transverse momentum $p_{\rm T}$, as shown in Figure 2.7. Panel **a)** shows that the magnitude of D^0 v_2 is comparable to that of light-flavor hadrons [54] for $p_{\rm T} > 2$ GeV/c. At transverse momenta $p_{\rm T} < 2$ GeV/c there is a hint of a mass

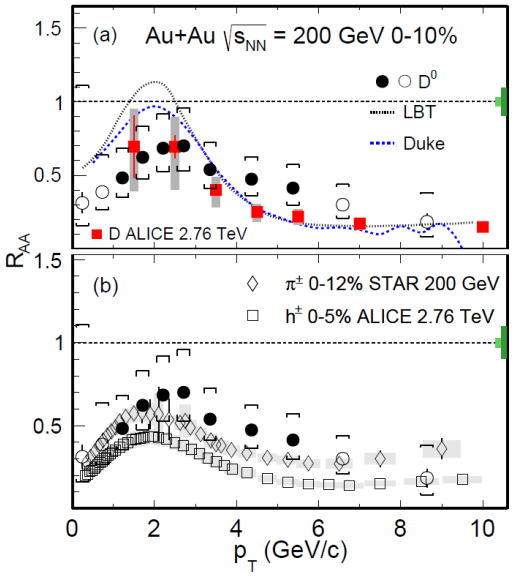

Fig. 2.5: Nuclear modification factor of D^0 mesons as a function of p_T in 0-10% central Au+Au collisions measured by the STAR experiment in Au+Au collisions at $\sqrt{s_{NN}}$ = 200 GeV [2]. The data are compared to measurement of charged pions by STAR [99], at the same collision energy, and to ALICE experiment results for D mesons and charged hadrons in Pb+Pb collisions at $\sqrt{s_{NN}}$ = 2.76 TeV [97, 98]. Taken from Ref. [2].

ordering of v_2. The observed magnitude of D^0 meson v_2 indicates that the energy loss of charm quarks inside the QGP is substantial and that they get very close to thermal equilibrium with the medium.

The measurement of D^0 v_2 can be also used to test the Number of Constituent Quarks (NCQ) scaling. Such measurement is shown in Figure 2.7 **b)**. Here, the elliptic flow v_2 is scaled by the number of constituent quarks n_q ($n_q = 2$ for mesons and $n_q = 3$ for baryons) and is plotted as a function of $(m_T - m_0)/n_q$, where m_T is the transverse mass[4] and m_0 is the rest mass of a given hadron. All hadrons, including the D^0 mesons, follow the NCQ scaling within the uncertainties. Overall, the measurement of D^0 elliptic flow v_2 by STAR suggests that the charm quarks are very close to a local thermal equilibrium with the QGP at RHIC [102].

In order to study the modification of the charm quark hadronization in the heavy-ion collisions with respect to that in the p+p collisions, STAR has measured the $(\Lambda_c^+ + \Lambda_c^-)/(D^0 + \bar{D}^0)$ yield ratio as a function of p_T and collision centrality in the Au+Au collisions at $\sqrt{s_{NN}}$ = 200 GeV, as shown in Fig. 2.8. The p_T dependence of the ratio (Figure 2.8 (**left**)) is compared to PYTHIA[5], and multiple models incorporating coa-

[4]The transverse mass is defined as: $m_T^2 = p_x^2 + p_y^2 + m_0^2$

[5]PYTHIA is a Mote Carlo generator used primarily for simulation of high energy collision events. In scope of this thesis, it is typically used to simulate production of open-charm hadrons p+p collisions in case suitable experimental data from p+p collisions are not available. As discussed above, production of open-charm hadrons in p+p collisions is in general reasonably well understood, so simulations of

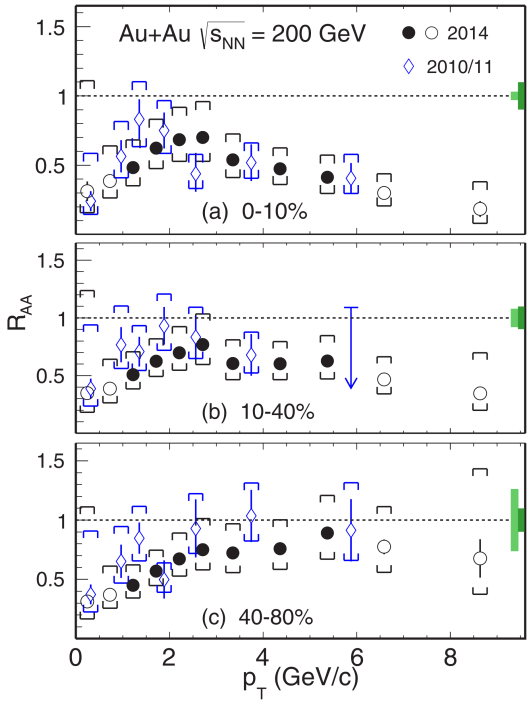

Fig. 2.6: The centrality dependence of D^0 meson $R_{AA}(p_T)$ measured by STAR in Au+Au collisions at $\sqrt{s_{NN}} = 200$ GeV with the HFT (2014) [2] and without the HFT (2010/11) [100, 101]. Taken from Ref. [2].

lescence hadronization of quarks [103–107]. The data show a significant enhancement with respect to the PYTHIA baseline and are reasonably reproduced by the coalescence models. At the same time, the ratio increases towards more central Au+Au collisions, as shown in Figure 2.8 (**right**). The observed yield ratio has a comparable magnitude to the baryon-to-meson ratios of light flavor [108] and strange hadrons [109]. The data are well reproduced by the Catania model calculation with fragmentation and coalescence hadronization [104].

A complementary measurement to the one discussed above is the measurement of the $(D_s^+ + D_s^-)/(D^0 + \bar{D^0})$ yield ratio. STAR was able to extract $D_s^\pm$ invariant yields both as a function of p_T and collision centrality thanks to topological selection selection criteria optimization utilizing the Boosted Decision Trees (BDT), similar to the $\Lambda_c^\pm$ measurement, and use them to calculate the $(D_s^+ + D_s^-)/(D^0 + \bar{D^0})$ yield ratio. Figure 2.9 shows that measured the yield ratio is enhanced with respect to the PYTHIA calculation in all studied centralities, indicating significant modification of $D_s^\pm$ mesons in Au+Au collisions compared p+p collisions. The enhancement in Au+Au collisions is also predicted by various models incorporating coalescence hadronization of quarks [104–107]. None of the models is able to describe the measured date in full measured p_T range at the

open-charm hadrons in p+p events can be used as an alternative to experimental data.

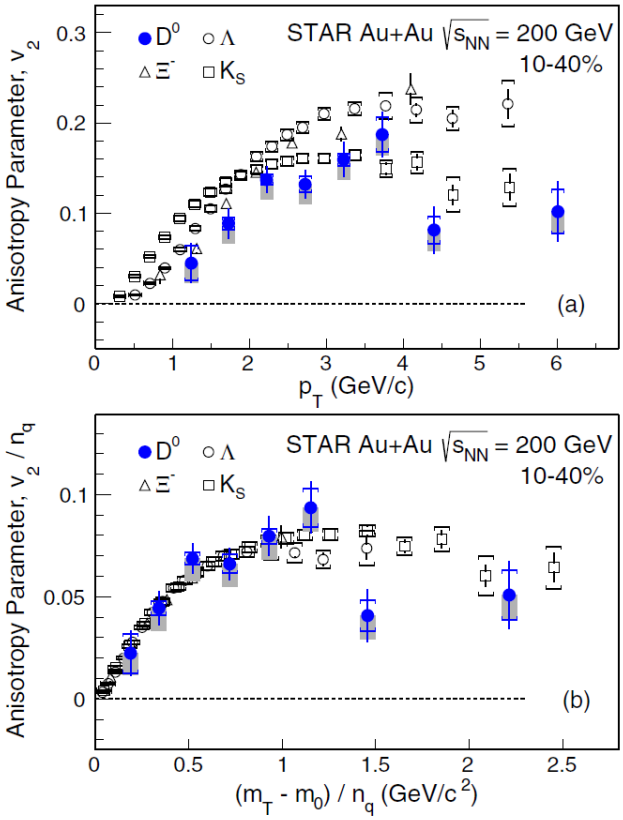

Fig. 2.7: **a)** The elliptic flow (v_2) of D^0 mesons and light-flavor hadrons [54] as a function of p_T. **b)** The elliptic flow v_2 divided by the number of constituent quarks n_q as a function of $(m_T - m_0)/n_q$, where m_T is the transverse mass and m_0 is the rest mass. Taken from Ref. [102].

moment. The STAR result has proven to be important for better understanding of the role of strangeness in hadronization process of charm quarks. Both discussed measurements, the $(\Lambda_c^+ + \Lambda_c^-)/(D^0 + \bar{D^0})$ and $(D_s^+ + D_s^-)/(D^0 + \bar{D^0})$ yield ratios, suggest that the coalescence hadronization of the charm quarks plays an important role in the Au+Au collisions at RHIC.

STAR has also measured the rapidity odd directed flow v_1 of the D^0 mesons as a function of rapidity y in 10-80% central Au+Au collisions at $\sqrt{s_{NN}} = 200\,GeV$, as shown in Figure 2.10. The D^0 data are compared to the measurement of kaons [111]. The result shows that the $v_1(y)$ slope of D^0 mesons is negative and much larger that that of kaons which is in an qualitative agreement with theoretical predictions [92, 110], both models underpredict the magnitude of the slope. Current precisions of the measurement is not sufficient to conclude about the D^0-$\overline{D^0}$ splitting caused by the electromagnetic field induced by the passing spectators of the Au+Au collision.

In addition to open-charm hadron production, STAR has also studied production of open-bottom hadrons. Important thing about open-bottom hadrons, from experi-

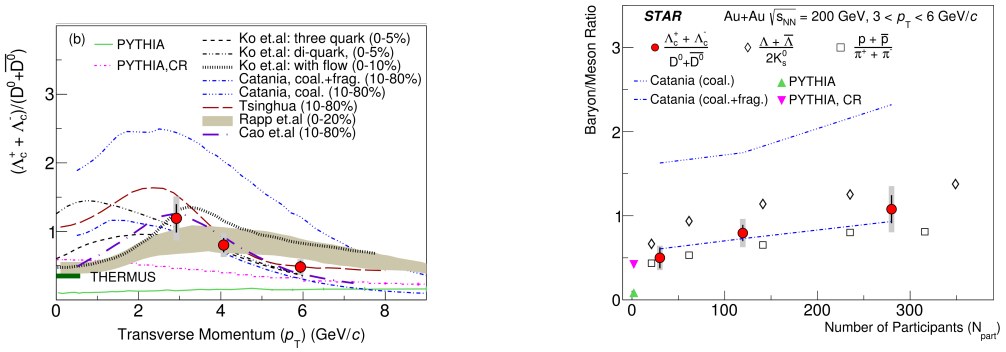

Fig. 2.8: (**left**) The $(\Lambda_c^+ + \Lambda_c^-)/(D^0 + \bar{D}^0)$ yield ratio as a function of p_T for 10-80% central Au+Au collisions at $\sqrt{s_{NN}} = 200\,\text{GeV}$. The data are compared to PYTHIA and multiple model calculations incorporating coalescence hadronization of quarks [103–107]. (**right**) The Λ_c/D^0 yield ratio as a function of centrality. The Λ_c measurement is compared to baryon-to-meson ratio for light flavor [108] and strange hadrons [109]. The data is also compared to Catania model [104] and PYTHIA calculation with and without color-reconnection (CR). Taken from Ref. [4].

mental point of view, is that they decay to open-charm hadrons, which then decay into measurable final state particles, e.g. via hadronic channel as shown in Tab. 2.2. This makes analysis of open-bottom hadrons rather challenging task. One method which was developed at collider experiments is measurement of Non-Photonic Electrons (NPE, sometimes heavy-flavor electrons) which relies on identification of electrons originating of semi-leptonic decays of the open-bottom and open-charm hadrons, separating those from electrons coming from other sources (e.g. conversion of photons in material of detector or misidentification of hadrons as electrons). This method generally only provides ratio of electrons of originating form the open-bottom and open-charm hadrons. Despite the fact that this method cannot provide spectra of open-charm or open-bottom hadrons directly, it still can be easily used to calculate ratios, and so e.g. R_{AA} or R_{CP}. Ratio of $R_{CP}^{b\to e}$ electrons originating from decay of open-bottom hadrons and $R_{CP}^{c\to e}$ of electrons originating from decay of open-charm hadrons as a function of electron p_T measured in Au+Au collisions at $\sqrt{s_{NN}} = 200\,\text{GeV}$ by the STAR experiment is shown in Fig. 2.11. The red points are for R_{CP} calculated using 0-10% and 40-80% collision centrality, while the blue points are calculated using 0-10% and 20-40% collision centrality. The red pints are significantly above unity, which suggests that the open-bottom hadrons are much less suppressed in central Au+Au collisions than open-charm hadrons. The difference in the bottom and charm modification is less visible while comparing central and mid-central Au+Au collisions. The data are compared to Duke model [113] and parton-hadron-string-dynamics (PHSD) [114,115] theoretical calculations. This measurement is a clear evidence of mass ordering of energy loss of heavy quarks in the QGP at RHIC.

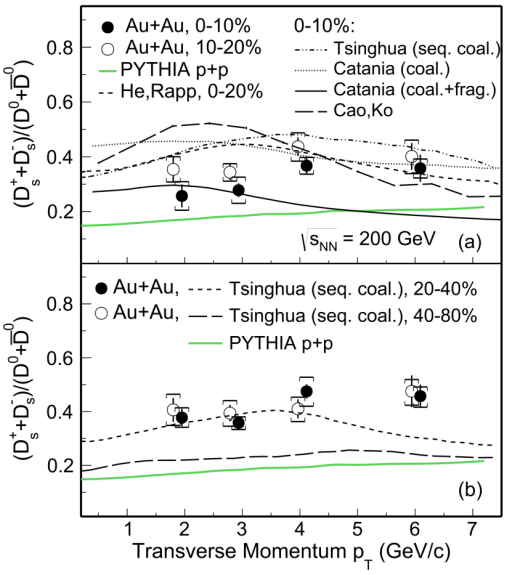

Fig. 2.9: $(D_s^+ + D_s^-)/(D^0 + \bar{D^0})$ yield ratio as a function of p_T for four centralities of Au+Au collisions at $\sqrt{s_{NN}} = 200$ GeV. The data are compared to combined PYTHIA and multiple model calculations incorporating coalescence hadronization of quarks [104–107]. Taken from Ref. [3].

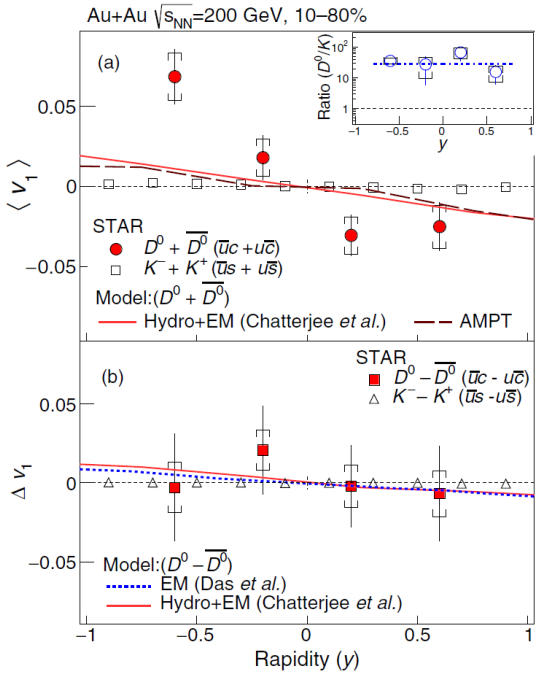

Fig. 2.10: Directed flow of D^0 and $\overline{D^0}$ mesons as a function rapidity y in 10-80% central Au+Au collisions at $\sqrt{s_{NN}} = 200$ GeV. Panel **(a)** shows the average v_1 of D^0+$\overline{D^0}$, panel **(b)** shows the difference between v_1 of D^0 and $\overline{D^0}$. The data are compared to multiple model calculations [92, 94, 110] and to the same measurement for charged kaons in the same collision system at the same energy [111]. Taken from Ref. [112].

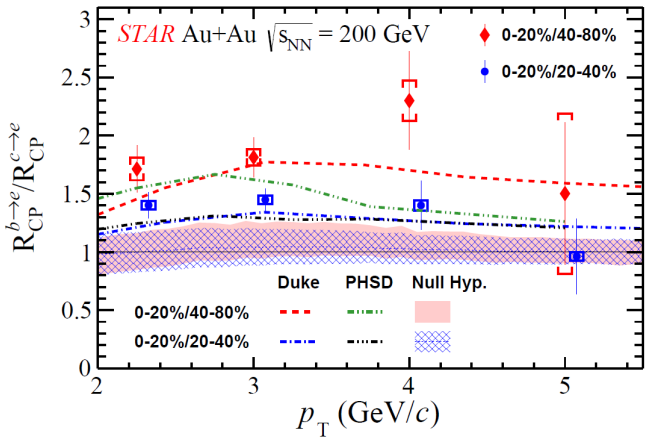

Fig. 2.11: Ratio of $R_{\mathrm{CP}}^{b\to e}$ of electrons originating from decay of open-bottom hadrons and $R_{\mathrm{CP}}^{c\to e}$ of electrons originating from decay of open-charm hadrons as a function of electron p_{T} measured in Au+Au collisions at $\sqrt{s_{\mathrm{NN}}} = 200\,\mathrm{GeV}$ by the STAR experiment. The red markers are for centrality ratio 0-20%/40-80% and the blue circles are for 0-20%/20-40%. The open-bottom hadrons are clearly less suppressed in central to peripheral Au+Au collisions which is consistent with mass ordering of energy loss of heavy quarks in the QGP. The data are compared to Duke [113] and PHSD [114, 115] model calculations. Taken from Ref. [116].

2.3.2 Open-heavy flavor hadrons measured by ALICE

The ALICE experiment at the LHC has very rich open-heavy flavor program as well. Similar to STAR, ALICE is capable of topological reconstruction of hadronic decays of open-charm hadrons. This section provides a brief overview of open-charm hadron measurements by ALICE in Pb+Pb collisions at $\sqrt{s_{\rm NN}} = 2.76\,\text{TeV}$ and $\sqrt{s_{\rm NN}} = 5.02\,\text{TeV}$.

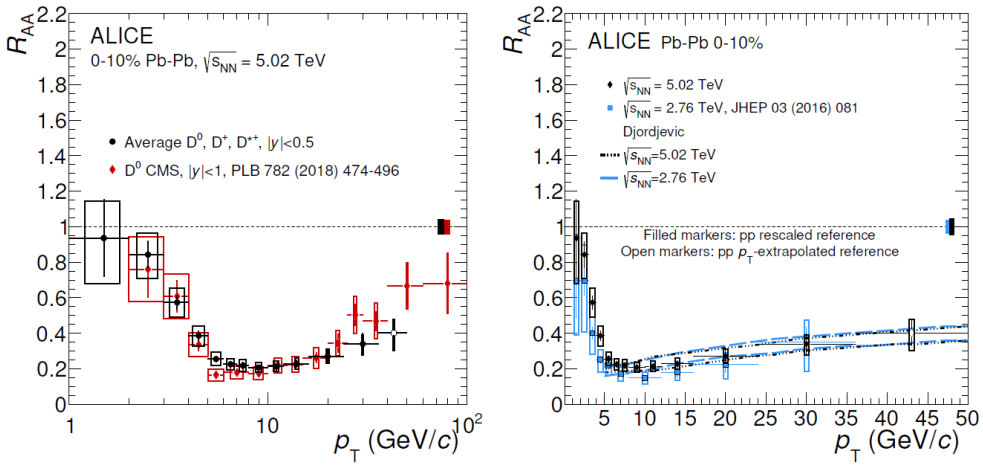

Fig. 2.12: $R_{\rm AA}$ of D mesons ($\rm D^0$, $\rm D^+$, and $\rm D^{*+}$ average) measured by ALICE [117] and $\rm D^0$ mesons by the CMS [118] in 0-10% Pb+Pb collisions at $\sqrt{s_{\rm NN}} = 5.02$ TeV. ALICE data from Pb+Pb collisions at $\sqrt{s_{\rm NN}} = 2.76$ TeV [97] are shown for comparison. The data are also compared to Djordjevic model calculations [119]. Taken from Ref. [117].

Figure 2.12 shows the $R_{\rm AA}$ of D mesons ($\rm D^0$, $\rm D^+$, and $\rm D^{*+}$ average) measured by ALICE in $\sqrt{s_{\rm NN}} = 5.02\,\text{TeV}$ [117]. The left panel shows comparison to the measurement of $\rm D^0$ mesons by CMS in the same collision system at the same energy [118]. The two measurements are in a good agreement and both show substantial suppression of open-charm mesons with $p_{\rm T} > 4\,\text{GeV}/c$, with maximum suppression around 10 GeV/c. The right panel shows comparison to the previous ALICE measurement of D mesons ($\rm D^0$, $\rm D^+$, and $\rm D^{*+}$ average) in $\sqrt{s_{\rm NN}} = 2.76\,\text{TeV}$ [97] and Djordjevic model calculations [119]. The observed suppression is similar, within the uncertainties, for both collision energies and is consistent with the model calculation. This result shows that c quarks loose significant portion of their energy at LHC energies as well.

This significant energy loss indicates, that open-charm mesons at the LHC could have significant elliptic flow. As shown in Fig. 2.13 in the left panel, this is the case for D mesons ($\rm D^0$, $\rm D^+$, and $\rm D^{*+}$ average) with $2 < p_{\rm T} < 10\,\text{GeV}/c$ in 30-50% central Pb+Pb collisions at $\sqrt{s_{\rm NN}} = 5.02\,\text{TeV}$. The measured D meson v_2 is compared to several model calculations. Right panel of Fig. 2.13 shows comparison of the D meson $R_{\rm AA}$ in in 0-10% central Pb+Pb collisions to the same model calculations [120–125]. As discussed in Sec. 2.2, the goal of the models is to describe both $R_{\rm AA}$ and v_2.

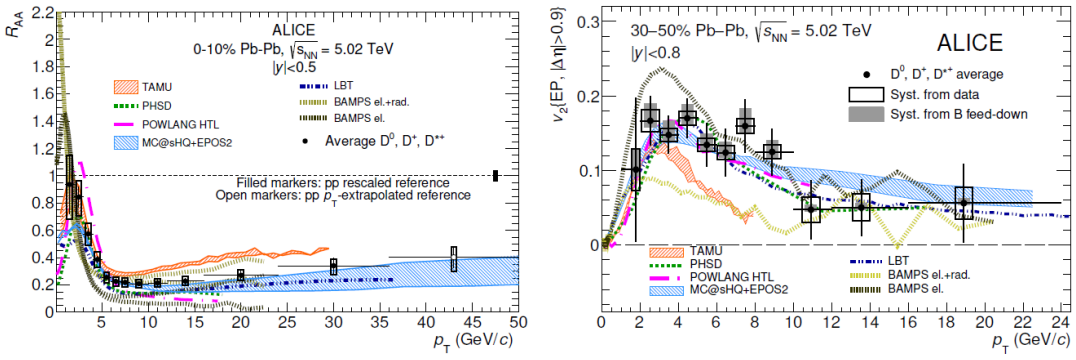

Fig. 2.13: The D mesons (D^0, D^+, and D^{*+} average) R_{AA} (**left**) and elliptic flow v_2 (**right**) measured by ALICE in 0-10% (R_{AA}) and 30-50% (v_2) central Pb+Pb collisions at $\sqrt{s_{NN}} = 5.02$ TeV compared to various model calculations [120–125]. Taken from Ref. [117].

In order to understand the charm quark hadronization process at LHC energies, ALICE has also measured the Λ_c^+/D^0 yield ratio. Left panel of Fig. 2.14 shows the Λ_c^+/D^0 yield ratio measured by ALICE in 0-80% central Pb+Pb collisions [126] and p+Pb collisions at $\sqrt{s_{NN}} = 5.02$ TeV, and in p+p collisions at $\sqrt{s_{NN}} = 7$ TeV. The Pb+Pb data are clearly enhanced with respect to the p+Pb and p+p data indicating significant modification of Λ_c baryon production in Pb+Pb collisions at LHC energies. Similar to STAR, this modification is likely caused by coalescence hadronization of charm quarks, which is also supported by models shown in the right panel of Fig. 2.14. There are two important notes to be made. Firstly, there is a key difference between the STAR and ALICE result. The STAR measurement is consistent with the Catania model calculation [104] which incorporates both fragmentation and coalescence, ALICE result is consistent with the Catania model with coalescence only. This gives a hint that the hadronization mechanism of charm quarks at RHIC and the LHC is probably significantly different. The second note is regarding the Shao-Song model [127, 128], in which the baryon to meson ratio ($R_{B/M}$) is an input parameter. The two curves represent calculation for two different choices of the $R_{B/M}$, where $R_{B/M} = 0.425$ is the value for a good description of the result from p+p and p+Pb collisions [126] and $R_{B/M} = 1.2$ was chosen to achieve a better description of the measured data. Measurement at lower p_T is needed to make any meaningful conclusions and constraints on the models.

Since ALICE has measured the Λ_c^+ in p+p and p+Pb collisions as well, it has also calculated the nuclear modification factor of Λ_c^+ baryons, as shown in Fig. 2.15. Due to insufficient coverage in p_T of the p+p measurement (see Fig. 2.14, left panel), the reference for the R_{AA} calculation is taken from measurement in p+Pb collisions. The left panel of Fig. 2.15 shows comparison to multiple setups of the Catania model [104]. The best description of the measured data is for coalescence+fragmentation hadroniza-

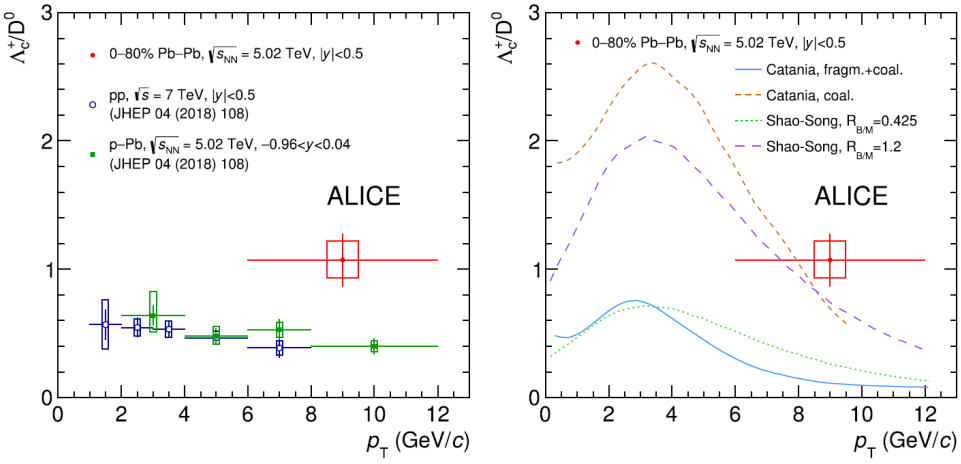

Fig. 2.14: Λ_c^+/D^0 yield ratio measured by ALICE in 0-80% central Pb+Pb collisions [126] and p+Pb collisions at $\sqrt{s_{NN}} = 5.02$ TeV, and in p+p collisions at $\sqrt{s_{NN}} = 7$ TeV. The right panel show comparison of the measurement in Pb+Pb collisions to various model calculations [104, 127, 128]. Taken from Ref. [126].

tion in Pb+Pb collisions and only fragmentation hadronization in p+p collisions. The difference between individual setups shows that it is also important to understand the hadronization process of charm quarks in p+p and p+Pb collisions as well [126]. The right panel of Fig. 2.15 shows comparison of the Λ_c^+ R_{AA} to the measurements of charged particles [129], D mesons (D^0, D^+, and D^{*+} average), and D_s^+ mesons [117]. The data suggest a mass ordering of the suppression, where lighter particles are more suppressed than heavier particles. The difference between the Λ_c^+ and D^0 R_{AA} is in qualitative agreement with coalescence hadronization of charm quarks in the QPG medium [126].

Similar to STAR, ALICE has also measured production of open-bottom hadrons in heavy-ion collisions. Compared to STAR, ALICE has used a different approach, by reconstructing D^0 mesons which likely originate from decays of open-bottom hadrons (non-prompt D^0 mesons). This analysis is based on selection of D^0 mesons which decay far from the primary vertex. The D^0 mesons which are result of hadronization of charm quarks from hard partonic scattering (prompt D^0 mesons) will decay much closer to the primary vertex than the non-prompt D^0 mesons due to combination of large decay length of open-bottom hadrons (ca. 500 μm) and the decay length of the D^0 mesons themselves (ca. 120 μm). The non-prompt D^0 mesons can be therefore used to access information about open-bottom hadron production. Figure 2.16 shows ratio of R_{AA} of non-prompt and prompt [130] D^0 mesons measured by ALICE in 0-10% central Pb+Pb collisions at $\sqrt{s_{NN}} = 5.02$ TeV. The top panel shows comparison of the data to various models [**?**, 120, 131, 132]. The bottom panel shows central values of the LGR model [131, 133] for various setups. Overall, the models provide good description of the experimental data. The different modifications of the LGR model indicate that the measured shape of the

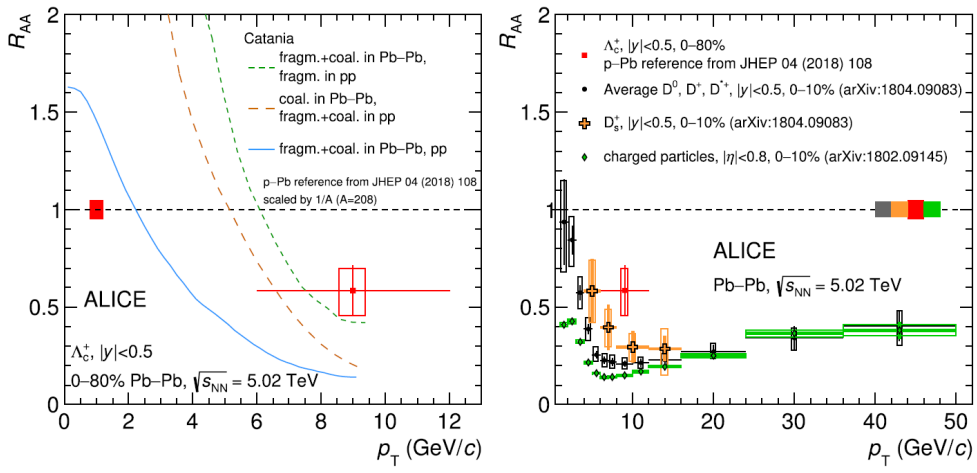

Fig. 2.15: R_{AA} of Λ_c baryons measured by ALICE in 0-80% central Pb+Pb collisions at $\sqrt{s_{NN}} = 5.02$ TeV [126]. The data are compared to various setups of the Catania model calculation [104] (**left** and to measurements of D mesons (D^0, D^+, and D^{*+} average), D_s^+ mesons [117], and charged particles [129]. Taken from Ref. [126].

ratio is driven by different energy loss of charm and bottom quarks in the medium due to their different masses and due to significant contribution of coalescence hadronization of charm quarks inside the QGP. It is important to note that ALICE has also performed a measurement of NPE in Pb+Pb collisions at $\sqrt{s_{NN}} = 5.02$ TeV [135], but these results are only for electrons originating from decays of both open-charm and open-bottom hadrons.

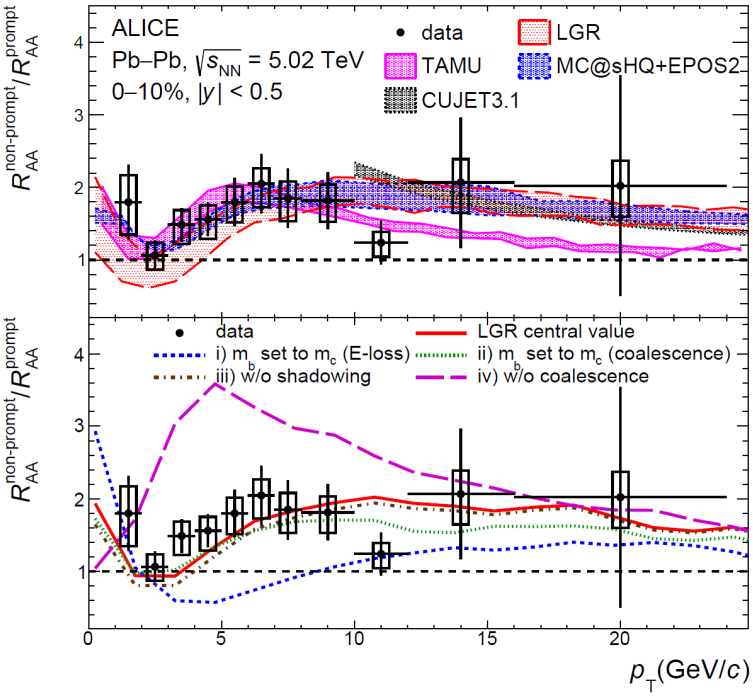

Fig. 2.16: Ratio of R_{AA} of non-prompt and prompt [130] D^0 mesons measured by ALICE in 0-10% central Pb+Pb collisions at $\sqrt{s_{\mathrm{NN}}} = 5.02$ TeV. The top panel shows comparison of the data to various models [?, 120, 131, 132]. The bottom panel shows central values of the LGR model [131,133] for various setups. Overall, the models provide good description of the experimental data. The different modifications of the LGR model indicate that the measured shape of the ratio is driven by different energy loss of charm and bottom quarks in the medium due to their different masses and due to significant contribution of coalescence hadronization of charm quarks inside the QGP. Taken from Ref. [134].

Chapter 3

The STAR experiment

This chapter provides a general overview of the RHIC accelerator complex and of the STAR detector with focus on sub-systems used in analysis presented in Ch. 4.

3.1 Relativistic Heavy-Ion Collider

Relativistic Heavy-Ion Collider (RHIC) at Brookhaven National Laboratory (BNL) is a versatile collider which is designed to collide large variety of atomic nuclei, ranging from protons, up to uranium. There are in total six interaction points (IP) over its 3.8 km circumference, out of which four have been used for experimental measurements. Three of those experiments have already finished their program: BRAHMS (Broad Range Hadron Magnetic Spectrometer), PHOBOS, and PHENIX (Pioneering High Energy Nuclear Interaction Experiment). The fourth experiment - STAR (Solenoidal Tracker at RHIC) is therefore the only currently active experiment at RHIC and is scheduled to continue taking data until year 2025. From 2023, STAR will be accompanied by the sPHENIX experiment, which will be located at the former PHENIX interaction point. After that RHIC is about to be transformed into the Electron Ion Collider (EIC), and so the STAR detector will be decommissioned and later replaced by a dedicated detector for the EIC physics. Total of three detectors were proposed as the main EIC detector: ATHENA, ECCE, and CORE. Recently, ECCE has been chosen as a core of the design for detector 1 for the EIC, but certain level of merging with ATHENA proposal is likely due to similarity of both designs. The exact design of the EIC first detector is currently being discussed.

The map of the BNL accelerator complex is shown in Fig. 3.1. Both protons and nuclei start their journey to RHIC in the building 930. Gold (^{1}97Au) ions are produced by the Laser Ion Source (LION) [137, 138]. In LION, a laser pulse hits a gold plate which produces a cloud of Au^{1+} gold ions, which are subsequently transferred in the Electron Beam Ion Source (EBIS) [139]. In EBIS, an electron beam is used to produce

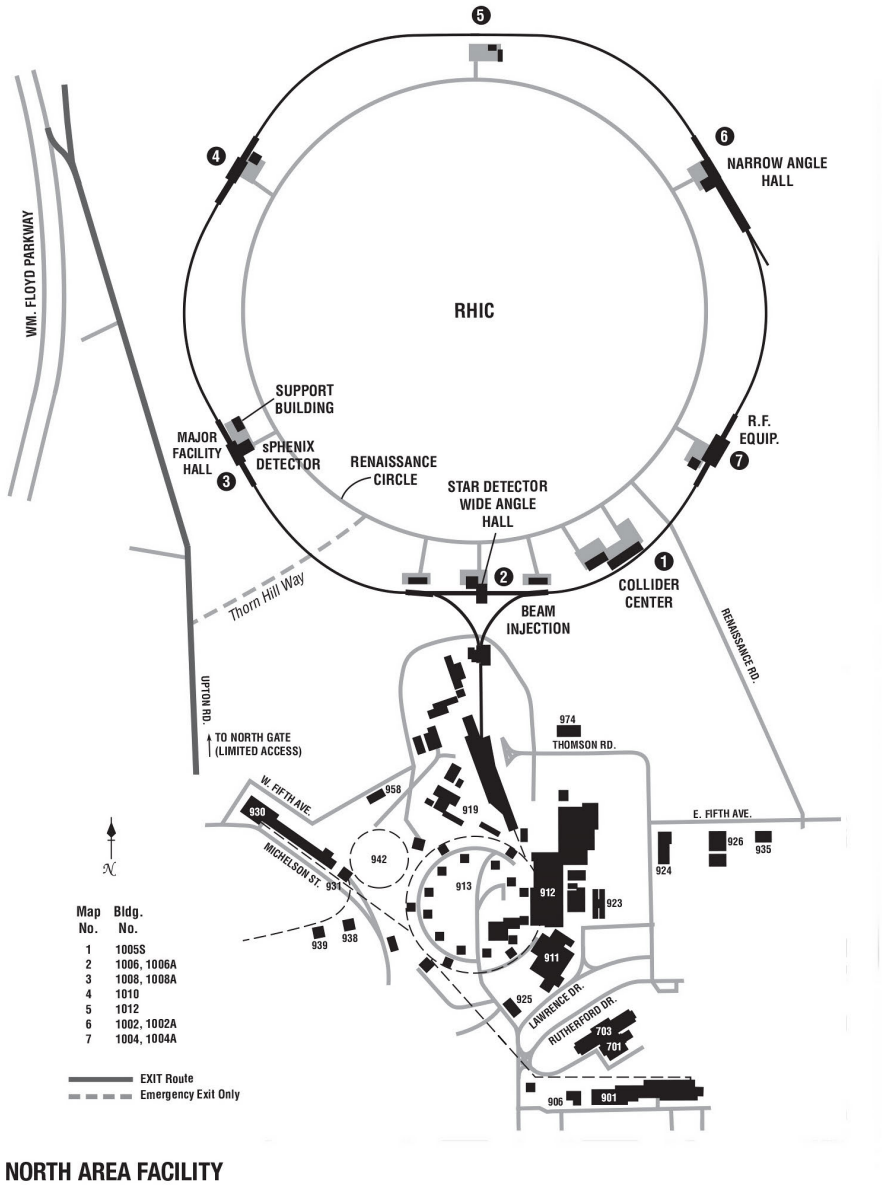

Fig. 3.1: Map of BNL accelerator complex. Both ions and protons start their path in the building 930 from which they are transferred to Booster (942). Their journey continues to the AGS (913), before they are injected into RHIC. Taken from ref. [136].

Au^{32+} ions which are then accelerated from 17 keV to 2 MeV[1] by RFQ (Radio Frequency Quadrupole) and the Inter-digital H-mode drift tube linear accelerators [140]. In Booster, the ions are grouped into 24 bunches and are accelerated to 95 MeV. After that they are injected into the Alternating Gradient Synchrotron (AGS) through a stripper to

[1]Energies are per one nucleon.

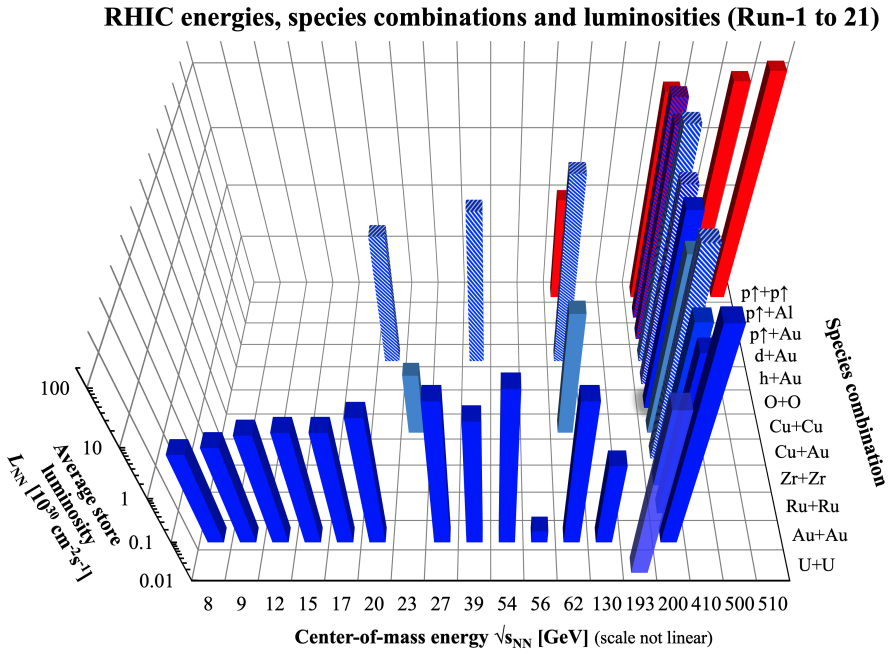

Fig. 3.2: An overview of collision systems and their energies used at RHIC. Taken from Ref. [141].

Au^{77+}. The AGS regroups the ions into 4 bunches and accelerates the gold ions to 9.8 MeV. At this stage, the ions pass through the last stripper, creating bare gold nuclei Au^{79+}, and are moved into one of the RHIC rings. Typically, 112 bunches are filled into each of the RHIC rings, which are then accelerated to desired energy. The maximum operating energy for gold ions is 100 GeV, leading to maximum collision energy of $\sqrt{s_{\mathrm{NN}}} = 200\,\mathrm{GeV}$.

Other particle species can be injected and accelerated by RHIC as well. Historically, RHIC has collided many different particle species at large variety of collision energies, as shown in Fig. 3.2. This enables a very rich physics program to be carried out at RHIC. A few notable examples are studies of internal spin structure of protons studied in collisions of polarized protons at energy up to $\sqrt{s} = 510\,\mathrm{GeV}$, study of Cold Nuclear Effects in asymmetrical collisions systems, or the Beam Energy Scan in Au+Au collisions which aims to probe the phase diagram of nuclear matter. In this thesis, the main focus is on Au+Au collisions at the top energy of $\sqrt{s_{\mathrm{NN}}} = 200\,\mathrm{GeV}$ which are used primarily for study of properties of the QGP.

3.2 STAR detector

STAR is a multipurpose detector which is located at the southern interaction point of RHIC (number 2 in Fig. 3.1). The STAR detector consists of many sub-detectors, making it a very versatile detector. A cutaway view of the central barrel of the STAR

detector as it was between years 2014 and 2016 is shown in Fig. 3.3. The brief description of the STAR detector which follows is for the subsystems present in the aforementioned period of time. Upgrades and changes to the STAR detector from this era until present day are summarized in Sec. 3.2.5.

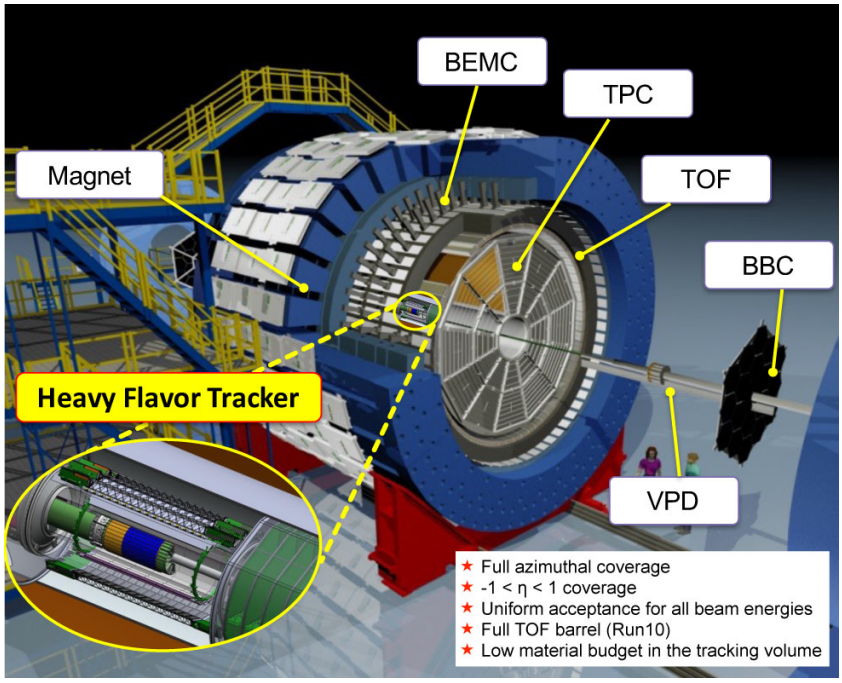

Fig. 3.3: A schematic view of the STAR detector. For the open-charm hadron measurements, the most important sub-systems are the Heavy Flavor Tracker (HFT), Time Projection Chamber (TPC), the Time Of Flight (TOF), the Vertex Position Detector (VPD) and the Zero Degree Calorimeter (ZDC, not shown).

As the name of the experiment suggests, the core part of the STAR detector is large cylindrical solenoidal magnet (blue in Fig. 3.3) which provides 0.5 T magnetic field, that is crucial for determination of momentum of charged particles. Closest to the beam axis was the Heavy Flavor Tracker (HFT) detector which was a 4-layer silicon tracker designed specifically to improve pointing resolution of the Time Projection Chamber (TPC) in order to be able to reconstruct decays of open-heavy flavor hadrons. The TPC itself is used to determine charged particle momentum, as suggested above, and also to identify the species of the charged particles based on their energy loss in the TPC gas. In order to improve the particle identification (PID), STAR is also equipped with the Time-of-Flight (TOF) detector. These three sub-detectors are the most important for reconstruction of open-charm hadrons.

Other sub-detectors in the central barrel, used by different analyses include the Barrel Electromagnetic Calorimeter (BEMC) which is used for example for di-electron studies (i.e. quarkonium reconstruction), or for jet analyses, and the Muon Telescope Detector (MTD, not highlighted in Fig. 3.3) which is used primarily for reconstruction of di-

muon decays of quarkonia. All of the central barrel detectors have acceptance $|\eta| < 1$ and $0 < \phi < 2\pi$.

STAR also has three trigger detector systems which are placed close to the beam axis on both sides from the center of the central barrel. Closest to the interaction point are the Beam-Beam Counters (BBC) which are used primarily while running p+p collisions. Further along the beam axis are the Vertex Position Detectors (VPD) which are used to trigger on collisions, determine the position of the primary vertex along the beam axis, and also provide starting time for the TOF system. Furthest from the interaction point are the Zero Degree Calorimeters (ZDC) which are also used to trigger on Au+Au collisions and are a core part of luminosity monitoring of RHIC.

More detailed description of the individual sub-detectors is provided in the following sections.

3.2.1 Heavy Flavor Tracker

The Heavy Flavor Tracker (HFT) [5,142] is a 4-layer silicon detector which was installed into the STAR detector between year 2014 and 2016. It was designed primarily in order to enable STAR to measure open-heavy flavor hadrons. Thanks to the HFT, STAR is capable of precise topological reconstruction of hadronic decays of open-charm hadrons and at the same time is able to identify electrons originating from semi-leptonic decays of open-charm and open-bottom mesons.

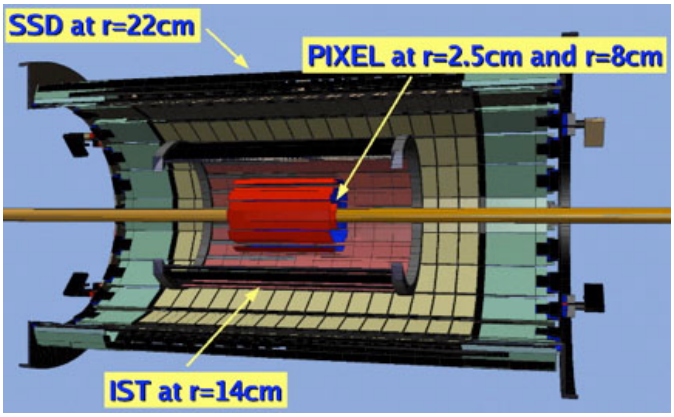

Fig. 3.4: Schematic view of the STAR Heavy Flavor Tracker detector. Closest to the beam pipe are two layers of pixel sensors (PIXEL), followed by the Intermediate Silicon Tracker (IST) and the Silicon Strip Detector (SSD). Taken from Ref. [142].

A schematic view of the HFT is shown in Fig. 3.4 and its position within the STAR detector is indicated in Fig. 3.3. The most important part of the HFT are the two layers that are closest to the beam axis which consist of 400 MAPS (Monolithic Active Pixel Sensor) sensors which were made using the CMOS (Complementary Metal-Oxide Semiconductor) technology. Each of the sensors contains 928×960 individual pixels,

which leads to total of 365.352 M individual pixels in both of the pixel layers. The HFT was the first detector to use CMOS technology at a large physics experiment. The main advantage of using this technology is that the pixel sensors are just 50 μm thick, which is about tree times thinner than more conventional hybrid pixel sensors. As a result, the HFT pixel layers have very low material budget and therefore do not produce substantial background from conversion.

The third layer of the HFT is the Intermediate Silicon Tracker (IST), which is a silicon pad detector. Its main purpose is to improve tracking between the pixel layers and the TPC (2014) or the fourth layer of the HFT - the Silicon Strip Detector (SSD, 2016)[2]. The IST consists of 864 sensors which have combined total of 110, 592 channels.

As mentioned above, the fourth layer of the HFT is the SSD. It is the oldest part of the HFT, as it was also part of the HFT predecessor - the Silicon Vertex Tracker (SVT). The readout electronics has been updated for the HFT era in order to keep up with the higher demands on the readout frequency. The SSD is built up from 320 two-sided strip sensors, where each has 1, 536 channels (768 per each side), which gives total of 491, 520 channels for the whole SSD.

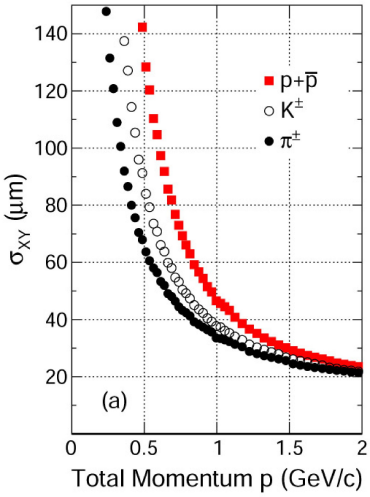

Fig. 3.5: Spatial resolution of the STAR HFT in the plane perpendicular to the beam axis for identified light hadrons. Taken from Ref. [102]

The achieved pointing resolution of the HFT (together with the TPC) in the $x - y$ plane for identified hadrons is shown in Fig. 3.5. For all particle species with $p_{\mathrm{T}} > 1\,\mathrm{GeV}/c$ the pointing resolution is better than 50 μm, which is sufficient even for short lived open-charm hadrons, such has the Λ_{c} baryons (see Tab. 2.1).

[2]The SSD was included in data-taking only in the year 2016.

3.2.2 Time Projection Chamber

The most important sub-detector of STAR is the Time Projection Chamber (TPC) [143], which is a large cylindrical gas filled detector designed to determine charged particle momentum and species. The momentum is determined based on radius of the curved ionization trail created by passing charged particle in the magnetic field. The charged particle are identified based on energy loss inside the TPC gas ($\mathrm{d}E/\mathrm{d}x$) using the following formula:

$$\mathrm{n}\sigma_{\mathrm{a}} = \ln\left[\frac{\left(\frac{\mathrm{d}E}{\mathrm{d}x}\right)_{\mathrm{a}}}{B_{\mathrm{a}}}\right]/\sigma_{\mathrm{a}}, \tag{3.1}$$

where $(\mathrm{d}E/\mathrm{d}x)_{\mathrm{a}}$ is the measured energy loss of particle a, B_{a} is the Bischel formula (modified Bethe-Bloch forumla) which is the theoretical prediction of the energy loss for particle a, and the σ_{a} is the energy loss resolution for particle a. Figure 3.6 shows an example of TPC measured $\mathrm{d}E/\mathrm{d}x$ as a function of track momentum together with predicted energy loss by Bischel formula for multiple particle species. In addition, the TPC provides precise information about the 3-dimensional geometry of each track, which is important for reconstruction of primary and secondary vertices. In addition, the multiplicity of charged tracks in the TPC is used to determine centrality of heavy-ion collisions.

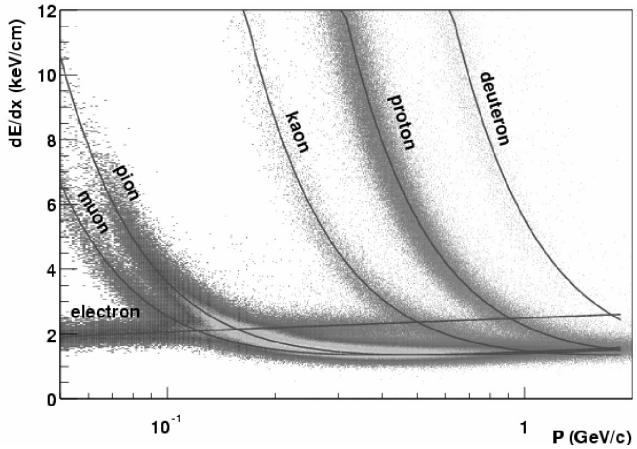

Fig. 3.6: Energy loss of charged tracks inside STAR TPC ($\mathrm{d}E/\mathrm{d}x$) as a function of particle momentum. Expected energy loss of various particles based on Bishel formula is also indicated in the figure. Taken from Ref. [143].

A schematic view of the TPC is shown in Fig. 3.7. It is a 4.2 m long cylinder, with inner diameter of 1 m and outer diameter of 4 m. It is filled with P10 gas (90% argon, 10% methane). In the middle of its length (at $z = 0$), there is a high voltage cathode made of mylar foil. During data-taking, the cathode is operated at -28 kV, which provides 140 Vcm^{-1} electric field through the volume of the TPC. The uniformity

of the electric file is ensured by a field cage, which covers the whole cylindrical surface of the TPC (both inner and outer). On both sides of the TPC there are total of 48 read out modules (12 inner and 12 outer modules at each side).

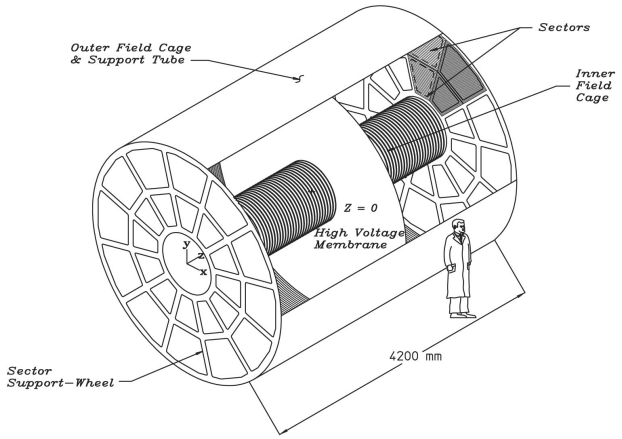

Fig. 3.7: Cutaway schematic view of the STAR TPC. Taken from Ref. [143].

The modules are Multi-Wire Proportional Counters (MWPC) with pad readout. A cross-section view of the outer readout module is shown in Fig. 3.8. When a collision occurs at STAR, charged particles produced in the collision pass through the TPC gas where they leave ionization trail. The electrons from the trails are then transported by the electric field towards the MWPC modules and the ions are transported towards the cathode. If the collision is evaluated as good by the trigger electronics, the gated grid "opens" and lets the electrons from the main volume of the TPC pass into the MWPC modules. The electrons then pass around the shield wires, whose main purpose to collect ions produced inside the MWPC modules and so prevent them to enter the main volume of the TPC. The electrons are then accelerated while moving towards the anode wires and producing an avalanche of electrons in the process. The signal is then readout by pads at the very end of the TPC, which "feel" the electric field induced by the avalanche (i.e. no electrons are directly collected by the pads).

As the name of the modules already suggests, they work in so called proportional mode, which means that the size of the signal extracted from the pads is directly proportional to the number of electrons which enters them. This is crucial for particle identification inside the TPC, as it is done based on energy loss of the charged particles inside the TPC gas, as discussed above. At the same time, the TPC provides a 3D spatial information about each track. The information in $x - y$ plane (perpendicular to beam axis) is determined from the pad grid in the MWPC modules. The outer sectors each have $3,942$ pads organized in 32 rows, while the inner sectors have $1,750$ pads in 13 rows. This gives total of $5,692$ readout pads per one TPC super-module organized in

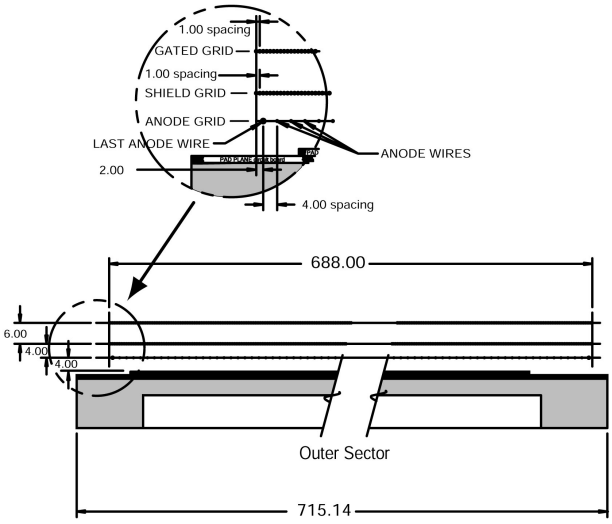

Fig. 3.8: A schematic view of STAR TPC outer readout module. Type and spacing of individual wire layers of the MWPC is indicated int the figure. Taken from Ref. [144].

45 rows[3]. The MWPC readout sectors are therefore able to provide detailed information about track geometry in the $x - y$ plane. The z information is then determined based on drift time and known drift velocity of the electrons from the volume of the TPC into the readout modules. The nominal drift velocity of electrons in the STAR TPC is 5.45 cm/μs, but in practice, a measured value of the velocity is used. The drift velocity is measured using the STAR TPC laser system [145]. This provides accurate value of the drift velocity throughout the data-taking period, which may vary for example due to differences in the pressure of the TPC gas, which has to always be at +2 mbar over the atmospheric pressure, or the slight variation in the composition of the fill gas. The drift velocity of electrons and ions, combined with the size of the TPC and properties the readout electronics is what limits the maximum STAR detector readout rate, which is around 1.8 kHz (for events with the TPC)[4] [146].

The setup described above was available at STAR until year 2018. Overall, the performance of the TPC in this setup was very good for the high energy measurements. For the physics program at STAR from 2019 and forward, all the inner sectors were upgraded with the so called iTPC ("i" stands for inner). The new inner sectors now have 40 pad rows, which significantly improves the resolution of the inner half of the TPC. As a result, the geometrical acceptance is now extended to $|\eta| < 1.5$ (compared to $|\eta| < 1$) and the TPC has now better ability to reconstruct tracks in the inner half of the TPC. This is very important for example for the STAR Beam Energy Scan (BES) program, where the improved resolution is used for precise collective flow measurements.

[3]This is where nHitsMax comes from in the following chapter.

[4]In case the TPC is not required, the rate can be increased to approximately 3 kHz [146].

Additional benefit of the upgrade is that STAR can now better explore production of particles in forward direction, which is important for the STAR fixed target which was part of BES, and more recently for forward physics in collisions of polarized protons (more on other forward upgrades for p+p in Sec. 3.2.5). In summary, the STAR iTPC opened many opportunities for STAR's physics program which would not be accessible with the original setup. At the same time, it is necessary to highlight that the old setup has proven to be very good for physics before BES or forward upgrades.

3.2.3 Time-Of-Flight detector

In order to improve particle identification in the TPC, STAR is also equipped by Time-of-Flight system [144, 147], which measures velocity of charged particles produced in the studied collisions. It consists of two parts. The first one are the Vertex Position Detectors (VPD) [148] which are used to determine time of the collision that is used as a time creation of the detected particels (more details on the VPD is in Sec. 3.2.4). The velocity of a given particle is then determined from the path length[5] and the time it takes it to reach the barrel TOF modules, which are placed just outside the volume of the TPC.

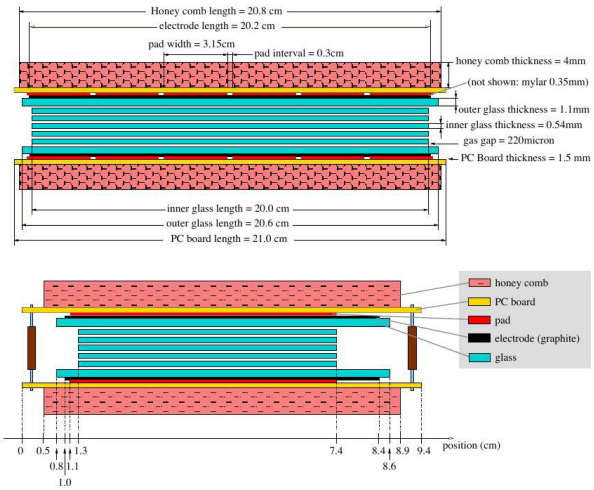

Fig. 3.9: A cutaway view of one STAR barrel TOF MRPC module. Taken from Ref. [144].

The barrel TOF consists of 120 trays (60 pairs arranged in full azimuth ϕ, covering $|\eta| < 1$), where each contains 32 Multi-gap Resistive Plate Chamber (MRPC) modules. A cross-section of one of the TOF MRPC modules is shown in Fig. 3.9. It consists of 7

[5]The tracks of charged particles are curved due to magnetic field. The distance a given particle travels is therefore different and it is not simply a distance from the beam axis to the barrel TOF modules.

glass plates with 220 micron gas filled gaps between them. The glass sandwich is placed between two graphite electrodes which provide high voltage electric field. Outside of the electrodes, on both sides, there are mylar foil insulated readout pads (6 on each side). The gas used in the MRPC is a mixture of 90% R134a, 5% isobutane, and 5% SF_6.

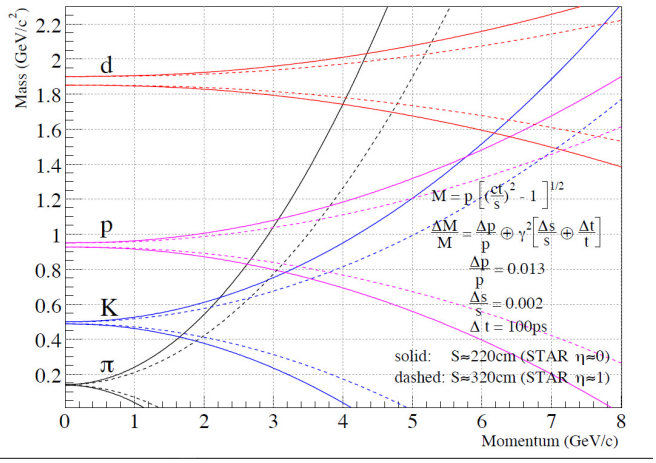

Fig. 3.10: Resolution of particle mass as a function of particle momentum identified using the STAR TOF with 100 ps time resolution. The solid line is the resolution at mid-rapidity ($\eta \approx 0$), the dashed line is for $\eta \approx 1$. Taken from Ref. [144].

The charged particles are detected inside of the MRPC chambers by leaving an ionization trail in the small gaps. The ionization electrons are immediately accelerated in the strong electric field causing strong avalanches. The readout pads then can "sense" the electric field induced by the electron clouds. The main advantage of the MRPC technology is that these detectors are extremely fast. As a result the whole STAR TOF system has time resolution of $\approx$ 100 ps, which provides good particle identification, mainly for particles with $p_{\mathrm{T}} < 1.5\,\mathrm{GeV}/c$. As shown in Fig. 3.10, the STAR TOF is able to reliably distinguish between light hadrons up to about quoted $p_{\mathrm{T}} \approx 1.5\,\mathrm{GeV}/c$. Identification of particles with higher momenta is generally difficult with TOF systems, as all particle species become relativistic and their (relativistic) velocity β is close to unity.

The PID using the TOF at STAR is done by comparing the inverse relativistic velocity measured by TOF ($1/\beta_{\mathrm{TOF}}$) to expected value of the inverse velocity ($1/\beta_{\mathrm{th}}$) utilizing the following formula:

$$\Delta|1/\beta - 1/\beta_{\mathrm{th}}|,$$

where $\beta_{\mathrm{th}} = p/E = p/\sqrt{p^2 + m^2}$ and is calculated from particle momentum measured by the TPC (p) and assumed rest mass (m).

3.2.4 Trigger detectors

One of the most important trigger detectors, which are also a part of the TOF system, are the Vertex Position Detectors (VPD) [148], which consist of two modules, each located 5.7 m from the center of the STAR detector. Each of the modules contains 19 assemblies consisting of Pb converter, followed by Eljen EJ-204 scintillator and fast Hamamatsu R-5946 photomultiplier. Rapidity coverage of the VPD is $4.24 \leq \eta \leq 5.10$. Coincidence of both VPD modules is used to trigger on good collision events. In addition, the position of the primary vertex is determined using the VPD based on time difference of signal detected in the two modules. As discussed in the previous section, the VPD is also used for determination of starting time for the STAR TOF system. It is therefore a crucial subsystem of the STAR detector.

In addition to the VPD, heavy-ion collisions are also selected using coincidence in the Zero Degree Calorimeters (ZDC) [149,150]. The ZDC consists of two super-modules which are located 18 m from the center of the STAR, inside the RHIC tunnel. Each ZDC super-module is further divided into three individual towers, where each contains a sandwich of tungsten plates and plastic optical fibers. The plates are tilted by 45° with respect to the beam axis and the fibers are all connected into a single bundle which is then readout by a single photomultiplier (i.e. one photomultiplier per ZDC tower). The ZDC detects spectator neutrons from collision of heavy nuclei, which convert in the tungsten plates, causing a spray of charged particles. These particles are faster than light in the optical fibers, causing a flash of Cherenkov light in the process, which is then detected by the photomultipliers. In addition to triggering on heavy-ion collisions, the ZDC also plays important role in monitoring RHIC luminosity during data-taking periods.

As the ZDC is designed to detect neutrons, it is not very efficient during RHIC runs with p+p collisions. For that reason STAR is equipped with Beam Beam Counters (BBC) [151], which are two large scintillator detectors, which were placed 3.75 m from the center of star (see also Fig. 3.3). Its main purpose is to trigger on p+p events and also is used as a polarimeter in polarized p+p collisions.

3.2.5 Other STAR detector systems

In addition to the systems described in the previous sections, STAR is equipped with multiple other sub-detectors, which are not needed for the analysis described in Ch. 4, but are important for other studies. In the main barrel there is the Barrel Electromagnetic Calorimeter (BEMC) [152], which is important for example for identification of electrons and photons. Second one is the Muon Telescope Detector (MTD) [153] which is designed to identify muons, which is mainly useful in reconstruction of quarkonia.

STAR has also a variety of detectors in forward rapidity. One of them is the Endcap

Electromagnetic Calorimeter (EEMC) [154] which serves as an extension of the BEMC into pseudorapidity region of $1.086 \leq \eta \leq 2.00$. More modern addition to the STAR detector is the Event Plane Detector (EPD) [155], which consists of two large scintillator discs, located approximately in the same location as the BBC used to be mounted. Main purpose of the EPD is determination of the event plane in heavy-ion collisions and is also included in the trigger system of STAR.

The latest additions to the STAR detector are sub-systems designed for currently ongoing polarized p+p run. In general, their main purpose was to extend STAR acceptance in forward-rapidity which is important for studies of internal structure of proton. The new systems for Run22 are the Forward Silicon Tracker (FST), small-strip Thin Gap Chambers (sTGC) [156, 157], and the Forward Calorimeter System (FCS) [158].

Chapter 4

Reconstruction of $D^{\pm}$ mesons in Au+Au collisions at $\sqrt{s_{NN}} = 200$ GeV

This chapter provides a summary of a reconstruction of $D^{\pm}$ mesons in Au+Au collisions at $\sqrt{s_{NN}} = 200$ GeV measured by the STAR experiment in the year 2016. A topological reconstruction, enabled by outstanding spatial resolution of the HFT, of the hadronic decay listed in Tab. 4.1, was used for the signal extraction. The Feynman diagram of the decay channel is shown in Fig. 4.1 for illustration.

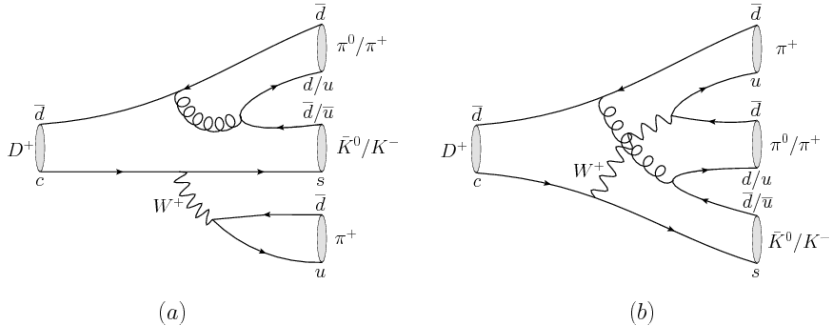

Fig. 4.1: Feynman diagram of two hadronic decay of $D^{\pm}$ mesons: $D^{\pm} \to K^{\mp}\pi^{\pm}\pi^{\pm}$ and $D^{+} \to K^{0}\pi^{0}\pi^{+}$ (and charge conjugate). The decay channel to charged kaons and pions is used in this analysis. Taken from Ref. [159].

Decay channel	M_{inv} [MeV/c^2]	$c\tau$ [μm]	BR [%]
$D^{\pm} \to K^{\mp}\pi^{\pm}\pi^{\pm}$	$1\,869.65 \pm 0.05$	311.8 ± 2.1	9.46 ± 0.24

Tab. 4.1: Decay channel of $D^{\pm}$ mesons used in this analysis and its basic properties. Values are taken from Ref. [76].

The $D^{\pm}$ signal is extracted in four centrality classes of the Au+Au collisions defined

by the percentage of total geometric cross section as given in Tab. 4.2. Also shown are the corresponding charged particle multiplicities in STAR TPC (N_{ch}), mean number of participants ($\langle N_{\mathrm{part}} \rangle$), and mean number of binary collisions $\langle N_{\mathrm{coll}} \rangle$ matched to the charged particle multiplicities using the Glauber model [23].

Centrality [%]	N_{ch} [-]	$\langle N_{\mathrm{part}} \rangle$ [-]	$\langle N_{\mathrm{coll}} \rangle$ [-]
0-10	> 373	324.3 ± 3.7	959 ± 28
10-40	$372 > 116$	172.5 ± 10.0	401 ± 31
40-80	$115 > 10$	41.9 ± 7.8	59 ± 14

Tab. 4.2: List of centrality classes of the Au+Au collisions used in this analysis. Also shown are the corresponding charged particle multiplicities in STAR TPC (N_{ch}), mean number of participants ($\langle N_{\mathrm{part}} \rangle$), and mean number of binary collisions $\langle N_{\mathrm{coll}} \rangle$ matched to the charged particle multiplicities using the Glauber model [23]. The values are taken from Galuber model centrality calculation done for Run14 and Run16 Au+Au data-sets (not publicly available).

and in 10 differential p_{T} bins which edges are defined in Tab. 4.3.

p_{T} [GeV/c]	0.0, 0.5, 1.0, 1.5, 2.0, 2.5, 3.0, 4.0, 5.0, 6.0, 8.0, 10.0

Tab. 4.3: List of p_{T} bin edges used for extraction of $\mathrm{D}^{\pm}$ raw yields in this analysis. This binnig was selected to match the one used in the published D^0 measurement [2].

4.1 Data-set and event selection

As mentioned at the beginning of this chapter, the data-set used for this part of the analysis are the Run16 Au+Au collisions at $\sqrt{s_{\mathrm{NN}}} = 200\,\mathrm{GeV}$. This data-set has three independent parts that are suitable for this analysis. First is the *st_physics* stream, which contains the majority of usable events. Next two sub-sets are the *st_sst* and *st_nosst* streams which were collected later in Run16 and contain less good events than the *st_physics* stream, but are still a very good addition to the total event statistics. For exact statistics in each sub-data set, see Figs. 4.2 in the following section.

The data were used in the form of centrally produced PicoDst files. The SL16ij production was used for all three sub-sets where the *st_physics* stream was running under the SL16j STAR library used and the *st_sst* and *st_nosst* were running under the SL20j STAR library.

The events are selected in three main steps. First, all runs from a bad run list are rejected. The bad run list used for this analysis was created based on Run16 QA described in Appendix A. Next, the trigger ID is checked. For this analysis, the main Minimum Bias (MB) trigger was used. For the *st_physics* stream a "VPDMB-5-p-sst"

trigger was used, for the *st_sst* stream it was "VPDMB-5-sst", and for the *st_nosst* stream "VPDMB-5-nosst". A list of specific trigger IDs can be found in Tab. 4.4.

st_physics	52001 52011 52021 52031 52041 52051
st_sst	57001
st_nosst	57002

Tab. 4.4: Summary of trigger IDs from Run16 Au+Au collisions at $\sqrt{s_{NN}} = 200\,GeV$ data-set used in this analysis.

The final step in event selection is applying a cut on position of the primary vertex along the beam axis. This is necessary due to dimensions and geometrical acceptance of the HFT. The selection criteria on $|V_z|$ and $|V_z - V_{z(VPD)}|$ are listed in Tab. 4.5. These are standard event cuts used in multiple HFT analyses.

Event selection	$\|V_z\| < 6$ cm $\|V_z - V_{z(VPD)}\| < 3$ cm

Tab. 4.5: Summary of event selection criteria used for extraction of $D^{\pm}$ candidates from the data-set.

How the event selection criteria affect the number of events is shown in Fig. 4.2. The upper panel shows event statistics for the *st_physics* stream and the bottom panel for combined *st_sst*+*st_nosst* streams. The total number of good events used in this analysis is approximately 1.5B events, where 1.1B is from the *st_physics* stream and 400M is from the *st_sst*+*st_nosst* streams.

The next step after the event selection is the extraction of the $D^{\pm}$ raw yield. The procedure used for the $D^{\pm}$ meson signal extraction is described in the following section.

4.1.1 Selection criteria

The next step after the event selection described in Section 4.1 is track selection and subsequent particle identification (PID). Because of long lifetime of the $D^{\pm}$ mesons, all global tracks are used for the analysis. Multiple selection criteria are applied to the tracks to ensure their good quality, which are listed in Tab. 4.6. The lower cut on p_T for all tracks is used in order to reduce the combinatorial background in the low p_T region. This is very important because of the three body decay used for the $D^{\pm}$ reconstruction. The cut on η is given by the STAR detector geometry. The following two cuts on number

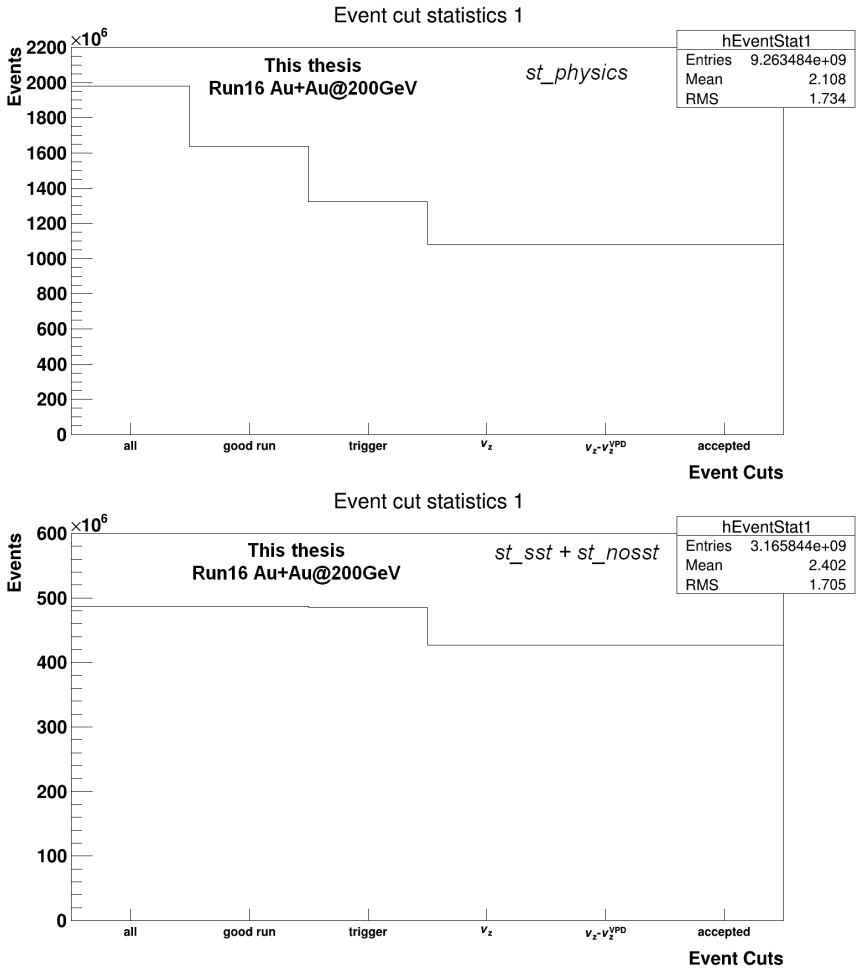

Fig. 4.2: Number of events after individual event selection criteria for *st_physics* stream (top) and for *st_sst* and *st_nosst* streams (bottom) of the Run16 Au+Au at $\sqrt{s_{\mathrm{NN}}} = 200\,\mathrm{GeV}$ data-set.

of hits in the TPC ensure that only good quality TPC tracks are analyzed. And finally it is required, that each track has properly matched signal in the HFT which for Run16 means that there is a hit in at least three layers of the HFT: one hit in the PXL1, one hit in the PXL2 and at least one hit in the IST or SSD.

Next, the tracks are identified using standard procedures at STAR. The kaons and pions are identified in the TPC based on a cut on their energy loss $\mathrm{d}E/\mathrm{d}x$ in the TPC gas by cutting on the $\mathrm{n}\sigma$. The TOF is used to help with the PID based on a cut on $|1/\beta - 1/\beta_{\mathrm{TOF}}|$, where β is particle velocity measured determined from its momentum and β_{TOF} is a velocity measured by the TOF. Figure 4.3 shows the $\mathrm{d}E/\mathrm{d}x$ (left) and $1/\beta$ (right) distributions from the TPC and TOF for Run16 data-set.

Values of the selection criteria used in this analysis are summarized in Tab. 4.7. In order to preserve as many tracks as possible, the TOF selection criteria are required only for tracks that have valid TOF information. For tracks without the TOF information,

Track selection	$p_T > 300\,\mathrm{MeV}/c$
	$\lvert\eta\rvert < 1$
	nHitsFit > 20
	nHitsFit/nHitsMax > 0.52
	PXL1+PXL2+(IST or SSD)

Tab. 4.6: Summary of charged track selection criteria used for extraction of $D^{\pm}$ candidates from the data. For more details, see the text.

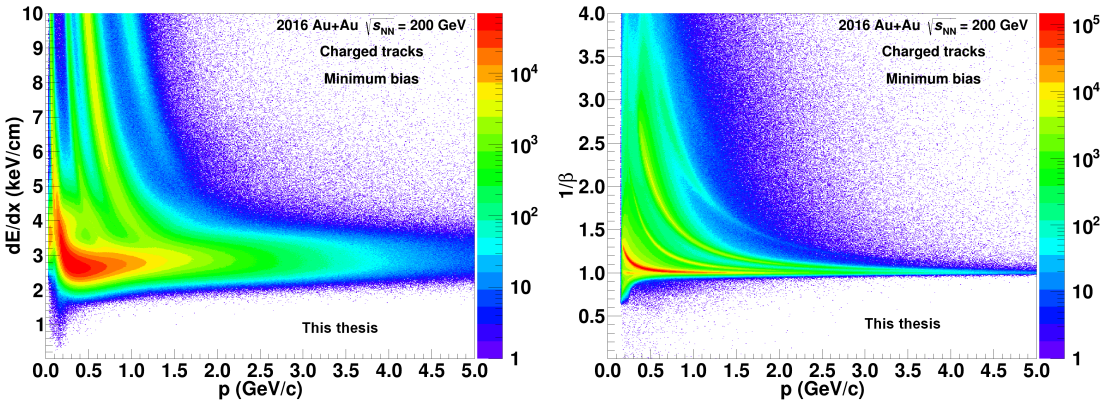

Fig. 4.3: The $\mathrm{d}E/\mathrm{d}x$ (left) and $1/\beta$ (right) distributions from the TPC and TOF for minimum bias Run16 Au+Au collisions at $\sqrt{s_{NN}} = 200\,\mathrm{GeV}$.

only the TPC is used for PID. This method is usually referred to as a *Hybrid TOF PID*.

Particle identification	TPC	$\lvert n\sigma_\pi\rvert < 3$
		$\lvert n\sigma_K\rvert < 2$
	TOF	$\lvert 1/\beta - 1/\beta_\pi\rvert < 0.03$
		$\lvert 1/\beta - 1/\beta_K\rvert < 0.03$

Tab. 4.7: Summary of particle identification selection criteria used for extraction of charged pions and kaons from Run16 Au+Au collisions at $\sqrt{s_{NN}} = 200\,\mathrm{GeV}$. For more details, see the text.

The identified pions and kaons are subsequently combined into $K\pi\pi$ tripets. Thanks to an exceptional spatial resolution of the HFT, it is possible to constrain the topology of the three tracks in order to improve the raw yield significance. There are six topological variables used and they are listed in Tab. 4.8 and also shown in Fig. 4.4. Going from top to bottom row, DCA_{pair} is the distance of closest approach between track pairs, $ct_{D^{\pm}}$ is decay length of the $D^{\pm}$ meson, $\cos(\theta)$ is cosine of the pointing angle, i.e. an angle between $D^{\pm}$ momentum and a vector connecting primary and secondary vertex, Δ_{max} is the maximum distance between the secondary vertices of track pairs, and $DCA_{\pi-\mathrm{PV}}$ and $DCA_{K-\mathrm{PV}}$ are distances of closest approach to the primary vertex of pions and kaons, respectively.

Decay topology	$DCA_{\text{pair}} < 80$ µm
	30 µm $< ct_{\text{D}^\pm} < 2\,000$ µm
	$\cos(\theta) > 0.998$
	$\Delta_{\text{max}} < 200$ µm
	$DCA_{\pi-\text{PV}} > 100$ µm
	$DCA_{\text{K}-\text{PV}} > 80$ µm

Tab. 4.8: Summary of topological selection criteria used for extraction of decay vertices of $\text{D}^\pm$ candidates from the data. The values are used as a reference for the TMVA optimized topological selection criteria.

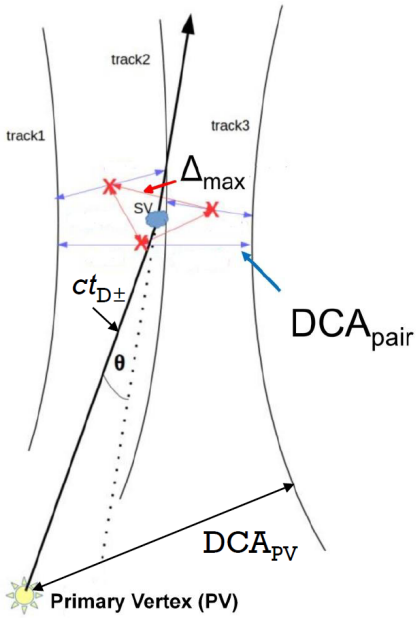

Fig. 4.4: Topology of a three body decay with topological variables from Tab. 4.8.

The values of the topological selection criteria were optimized manually and were used to extract raw yields in early stages of the analysis. For final results, the criteria were optimized using ROOT package TMVA [1]. The following section describes the procedure used for the optimisation.

TMVA optimization of topological cuts

The topological selection criteria were optimized using the TMVA in order to increase the statistical precision of the $\text{D}^\pm$ signal in all p_{T} and centrality bins. Rectangular criteria optimization was chosen as it was proven to be efficient and the optimized criteria can be easily implemented in calculation of the reconstruction efficiency. At the same time, it is simple to correct the raw yields extracted with help of this TMVA method for reconstruction efficiency.

Generally the main goal of this optimization is to find a set of topological criteria which has good separation power between signal, i.e. $K\pi\pi$ triplets with correct charge combination, and background, i.e. $K\pi\pi$ triplets with wrong charge combination. For that reason the TMVA needs to "learn" how do the topological variable distributions look like for the signal and for the background.

The background sample was extracted directly from the data by selecting the wrong-sing $K\pi\pi$ triplets using the event, track and PID selection criteria listed in Table 4.7. The signal sample was obtained using the data-driven fast-simulator (see Section 4.2.1 for details), in which 160 millions of $D^{\pm} \to K^{\mp}\pi^{\pm}\pi^{\pm}$ decays were simulated. The same set of pre-criteria was applied to the simulated triplets and the topological variables were stored. An example of the distributions for one centrality and p_T bin is shown in Figure 4.5.

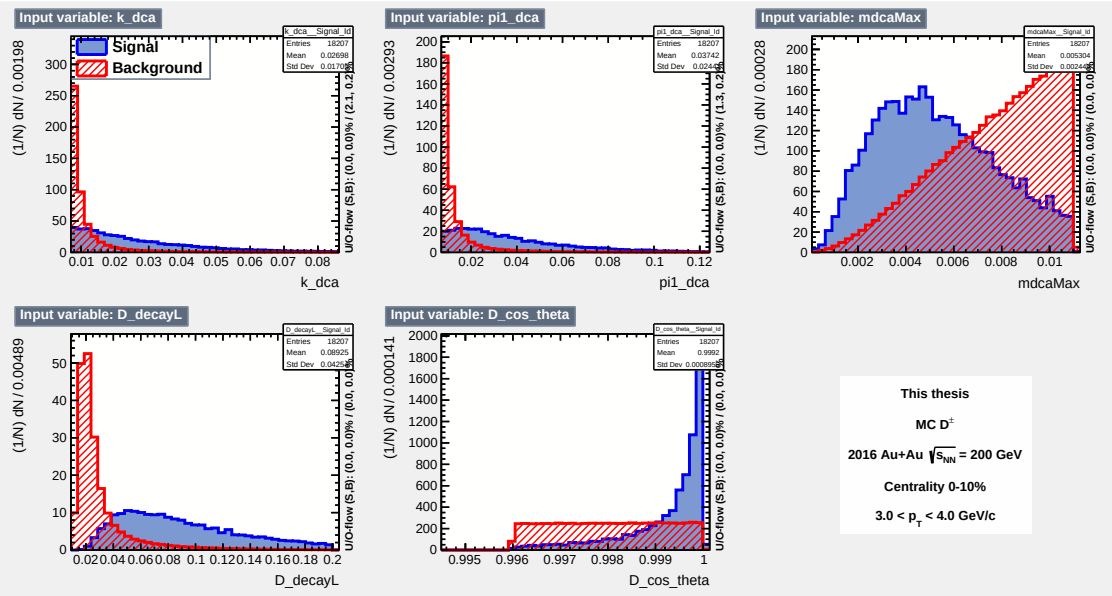

Fig. 4.5: Signal (blue histograms) and background (red histograms) topological variable distributions for centrality $0-10\%$ and transverse momentum of the $D^{\pm}$ in range $3 < p_T < 4$ GeV/c. The names of the variables in the plots correspond to the notation in Tab. 4.8 as follows: k_dca = DCA_{K-PV}, pi1_dca = $DCA_{\pi-PV}$, mdcaMax = DCA_{pair}, D_decayL = $ct_{D^{\pm}}$, D_cos_theta = $\cos(\theta)$.

The procedure itself starts by requesting the TMVA algorithm to look for either maximal or minimal value[1] of each of the trained variables. Then, the topological variable phase-space is sampled in 100 iterations, going from signal efficiency $\epsilon_S = 0$ to $\epsilon_S = 1$ and the corresponding background efficiency ϵ_B is matched to each ϵ_S and significance Σ is calculated:

[1]Maximal value = everything in the range from 0 to the maximal value will be chosen. Minimal value = everything in the range from the minimal value up to ∞ will be selected.

$$\Sigma = \frac{\epsilon_{\mathrm{S}} N_{\mathrm{S}}}{\sqrt{\epsilon_{\mathrm{S}} N_{\mathrm{S}} + \epsilon_{\mathrm{B}} N_{\mathrm{B}}}}, \tag{4.1}$$

where N_{S} (N_{B}) is number of expected signal (background) counts in the studied real data sample before applying the optimized criteria.

The N_{B} can be easily determined directly from the data by counting the wrong-sign K$\pi\pi$ triplets near the expected $\mathrm{D}^{\pm}$ invariant mass peak. The N_{S} can be understood as an expected raw yield of $\mathrm{D}^{\pm}$ mesons in the real data extracted using the pre-criteria, which were used to generate the inputs into the TMVA. For this analysis, it was calculated from measured spectrum of D^0 mesons in the 2014 Au+Au data at $\sqrt{s_{\mathrm{NN}}} = 200\,\mathrm{GeV}$ [2].

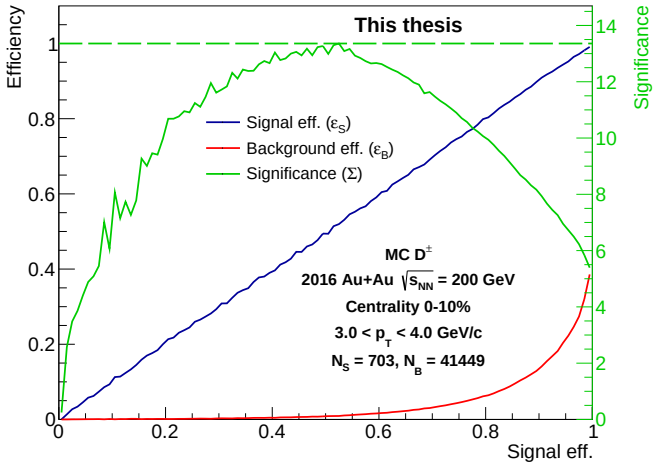

Fig. 4.6: The output distributions from the TMVA training plotted as a function of signal efficiency for Au+Au centrality $0-10\%$ and transverse momentum of the $\mathrm{D}^{\pm}$ in the range $3 < p_{\mathrm{T}} < 4\,\mathrm{GeV}/c$. The blue line is the signal efficiency, the red one is the background efficiency and the green one is the significance calculated using the formula (4.1) for $N_{\mathrm{S}} = 703$ and $N_{\mathrm{B}} = 41\,448$.

The ideal set of the topological selection criteria is then chosen based on maximal significance calculated according to Eq. (4.1) using the corresponding N_{S} and N_{B}. An example of a significance distribution used to determine the ideal criteria is shown in Figure 4.6 for collision centrality $0-10\%$ and transverse momentum of the $\mathrm{D}^{\pm}$ in the range $3 < p_{\mathrm{T}} < 4\,\mathrm{GeV}/c$. In this plot $N_{\mathrm{S}} = 703$ and $N_{\mathrm{B}} = 41\,448$.

In addition to the TMVA tuned topological cuts, two manually tuned topological cuts were introduced to improve the raw yield significance. One is an upper limit on the DCA_{PV} of both pions and kaons. The DCA_{PV} was set to a rather loose value of $DCA_{\mathrm{PV}} < 2$ mm, which helps reducing background coming from not correctly reconstructed secondary vertices, mainly in the 40–80% centrality bin. The second one is for $\Delta_{\mathrm{max}} < 250\,\mu\mathrm{m}$. This cut is based on the manually tuned value from Tab. 4.8 with a slightly more open value. The reason, why it was not included in the TMVA training is

that the rectangular cuts TMVA optimisation works better with lower number of optimized variables. Inclusion of the Δ_{max} into the training made the optimisation rather unstable due to relatively large correlations of the individual topological variables. This manually tuned value improves the significance in all centrality classes and proves to be important in combinatorial background suppression.

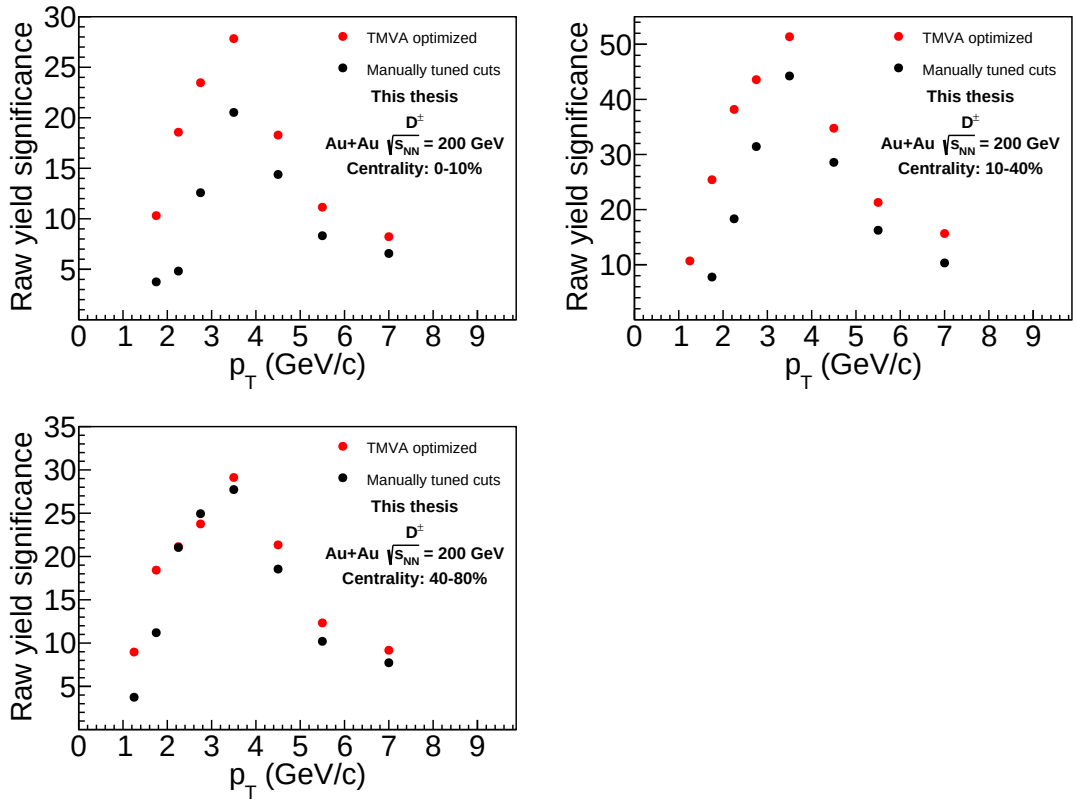

Fig. 4.7: Significance of $D^{\pm}$ raw yields extracted using topological selection criteria from Tab. 4.8 (black circles) and using the criteria from the TMVA training (red circles). The TMVA optimization significantly improves raw yield significance and enables to signal extraction at low transverse momenta.

The TMVA optimized criteria can be then applied to the real data. As can be seen in Figure 4.7, the optimized criteria give better significance of $D^{\pm}$ meson raw yield in most of the p_T bins in all studied centrality classes. The performance is the best in the region with $p_T < 3$ GeV/c, where the TMVA helps significantly with the background suppression. In the high p_T region, the improvement is not that visible, since the combinatorial background is low there even with relatively open topological selection criteria. The fact that the significance is lower for the TMVA optimized criteria in several bins, can be probably explained by statistical fluctuations an quality of the fit used for raw yield extraction.

The performance of the TMVA can be also demonstrated on the invariant mass $M_{inv}^{K\pi\pi}$ spectrum of the $K\pi\pi$ triplets. Comparison of the $M_{inv}^{K\pi\pi}$ spectrum reconstructed using

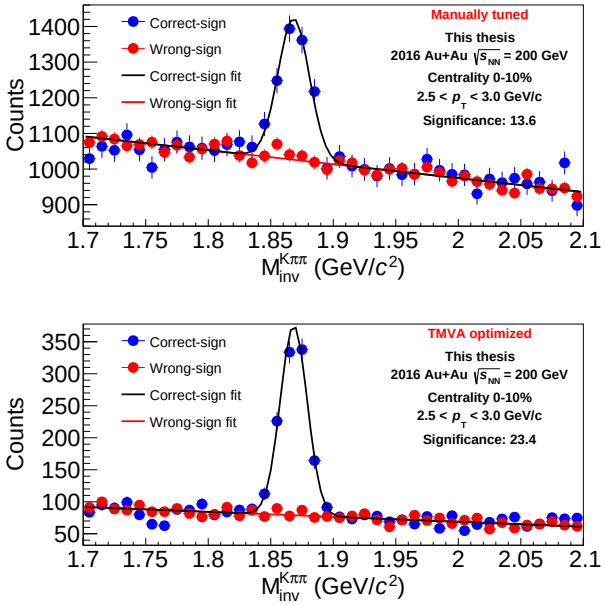

Fig. 4.8: Comparison of K$\pi\pi$ triplets invariant mass $M_{\mathrm{inv}}^{\mathrm{K}\pi\pi}$ spectra with manually tuned rectangular topological selection criteria from Tab. 4.8 (**up**) and with TMVA optimized topological selection criteria (**bottom**).

the selection criteria from Table 4.8 and using the TMVA optimized selection criteria is shown in Figure 4.8 for $\mathrm{D}^{\pm}$ with $2.5 < p_{\mathrm{T}} < 3.0$ GeV/c in 0-10% central Au+Au collisions. The background is significantly suppressed using the TMVA selection criteria (Figure 4.8, (**bottom**)) with respect to the criteria from Table 4.8 (Figure 4.8, (**up**)).

The raw yield of $\mathrm{D}^{\pm}$ mesons has been extracted using the TMVA optimized topological selection criteria for combined st_physics+st_sst+st_nossst streams using the binning 2 from Table 4.3. The raw yield has been extracted using the topological criteria from Table 4.8 as well for comparison. All raw yield values and corresponding significance are listed in Tables 4.9, 4.10, and 4.11. Only raw yields with $\Sigma > 3$ for the TMVA optimized selection criteria are shown.

Centrality: 0-10%				
	Non-optimized criteria		**TMVA criteria**	
p_T [GeV/c]	Y_{raw} [−]	Σ [−]	Y_{raw} [−]	Σ [−]
1.5 – 2.0	1210 ± 320	3.8	594 ± 58	10
2.0 – 2.5	1020 ± 210	4.9	844 ± 45	19
2.5 – 3.0	1241 ± 99	13	908 ± 39	23
3.0 – 4.0	1240 ± 60	21	1147 ± 41	28
4.0 – 5.0	346 ± 24	14	432 ± 24	18
5.0 – 6.0	108 ± 13	8.3	178 ± 16	11
6.0 – 8.0	53 ± 8	6.6	95 ± 12	7.9

Tab. 4.9: Raw yield Y_{raw} and corresponding significance Σ of $D^{\pm}$ mesons in 0-10% central Au+Au collisions for binning 2 from Table 4.3. Values extracted using non-optimized and TMVA optimized topological selection criteria are compared.

Centrality: 10-40%				
	Non-optimized criteria		**TMVA criteria**	
p_T [GeV/c]	Y_{raw} [−]	Σ [−]	Y_{raw} [−]	Σ [−]
1.0 – 1.5	0 ± 0	0	1363.0 ± 127.6	10.7
1.5 – 2.0	2270 ± 290	7.8	1991 ± 78	26
2.0 – 2.5	2860 ± 160	18	2263 ± 59	38
2.5 – 3.0	2664 ± 84	32	2736 ± 63	43
3.0 – 4.0	3014 ± 68	44	3336 ± 65	51
4.0 – 5.0	1025 ± 35	29	1445 ± 42	34
5.0 – 6.0	334 ± 21	16	585 ± 28	21
6.0 – 8.0	154 ± 15	10	325 ± 20	15

Tab. 4.10: Raw yield Y_{raw} and corresponding yield significance Σ of $D^{\pm}$ mesons in 10-40% central Au+Au collisions for binning 2 from Table 4.3. Values extracted using non-optimized and TMVA optimized topological selection criteria are compared.

Centrality: 40-80%				
	Non-optimized criteria		**TMVA criteria**	
p_{T} [GeV/c]	Y_{raw} [−]	Σ [−]	Y_{raw} [−]	Σ [−]
1.0 – 1.5	239 ± 63	3.8	308 ± 34	9.1
1.5 – 2.0	512 ± 46	11	742 ± 40	19
2.0 – 2.5	721 ± 34	21	874 ± 41	21
2.5 – 3.0	731 ± 29	25	1020 ± 43	24
3.0 – 4.0	855 ± 31	28	1228 ± 42	29
4.0 – 5.0	372 ± 20	19	584 ± 27	22
5.0 – 6.0	116 ± 11	11	200 ± 16	13
6.0 – 8.0	72.5 ± 9.4	7.7	136 ± 15	9.1

Tab. 4.11: Raw yield Y_{raw} and corresponding significance Σ of $\mathrm{D}^{\pm}$ mesons in 40-80% central Au+Au collisions for binning 2 from Table 4.3. Values extracted using non-optimized and TMVA optimized topological selection criteria are compared.

4.1.2 Raw yield extraction

After all selection criteria are applied to the events, tracks and Kππ triplets, the raw yield can be extracted from the data. This is done from invariant mass spectra of the Kππ triplets. As can be seen in Tab. 4.1, there are two combinations of the Kππ triplets with correct charge combination. Those are filled into a "correct-sign" spectrum which contains the $D^{\pm}$ signal and a combinatorial background. All other combinations are filled into a "wrong-sign" spectrum which is used to estimate the combinatorial background.

For combinatorial reasons, there are approximately three times as many wrong-sign combinations as the correct-sign ones. For that reason, the wrong sign spectrum needs to be scaled. This is done as follows: an integral of the wrong-sign and correct-sign spectrum outside the $D^{\pm}$ invariant mass peak is calculated. The range outside of the peak was chosen manually and is divided into two regions: $1.0 < M_{\mathrm{inv}} < 1.8\,\mathrm{GeV}/c^2$ and $1.95 < M_{\mathrm{inv}} < 2.1\,\mathrm{GeV}/c^2$. The two integral are subsequently divided giving the scaling factor of the wrong-sign spectrum. As can be seen in Fig. 4.9 and figures in Appendix B, the wrong-sign spectrum reproduces the combinatorial background well.

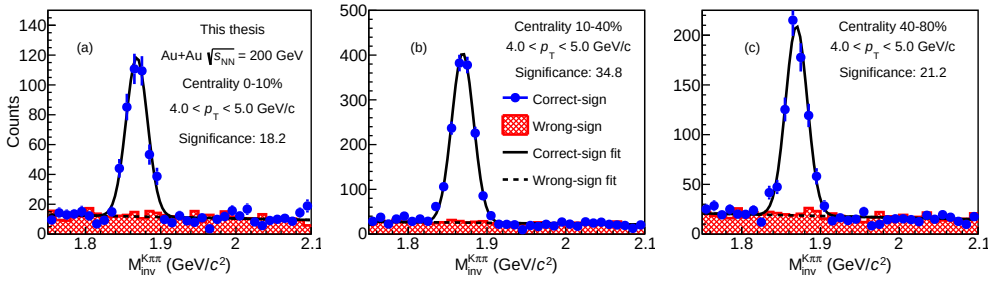

Fig. 4.9: Invariant mass spectra of the Kππ triplets for $D^{\pm}$ candidates with $4 < p_{\mathrm{T}} < 5\,\mathrm{GeV}/c$ in three centrality classes of the Au+Au collisions at $\sqrt{s_{\mathrm{NN}}} = 200$ GeV.

In order to extract the raw yield, the correct-sign is fitted with Gauss+linear function. First, the linear part of the fit is determined by fitting a linear function to the scaled wrong-sign spectrum in the area of the $D^{\pm}$ mass peak ($1.80 < M_{\mathrm{inv}} < 1.95\,\mathrm{GeV}/c^2$). The advantages of fitting the wrong-sign spectrum for background estimation are that it is possible to directly estimate the shape of the background under the mass peak and that the wrong-sign spectrum has smaller statistical uncertainties which makes the fit more reliable.

Next, the correct-sign spectrum is fitted with Gauss+linear function, where the parameters of the linear part are fixed from the fit of the wrong-sign spectrum and the parameters of the Gauss are left free. The raw yield is subsequently calculated in $\pm 3\sigma$ interval around the Gauss mean using two methods: directly from parameters of the fit (from the Gaussian part) and from bin counting.

The value from fit is used for the calculation of the invariant spectra and the value from bin counting is used for estimation of systematic uncertainty from raw yield ex-

traciton. More details about the systematic uncertainty calculation are available in Chapter 4.3.

4.2 $D^{\pm}$ reconstruction efficiency

This chapter provides a description of the calculation of the reconstruction efficiency of $D^{\pm}$ meson in Run16. This efficiency has two main parts. The first one is the HFT+TPC efficiency which is determined using the data-driven fast simulator. The second contribution is the PID efficiency.

4.2.1 Data-driven fast-simulator

The data-driven fast-simulator which was used, is based on the same data-driven fast-simulator that was implemented for efficiency study for D^0 spectra with the HFT. The core of this simulation is the EvtGen event generator [160], that is used to generate $D^{\pm}$ mesons with preset kinematics. More specifically, the $D^{\pm}$ mesons are simulated uniformly in full azimuthal angle, with uniform distribution in pseudorapidity where $|\eta| < 1$. The position of the primary vertex along the beam axis (V_z) is randomly generated based on distribution from data. The p_T is also simulated as flat, in the range $0 < p_T < 10\,\mathrm{GeV}/c$. Such p_T distribution is not realistic, so a weight is assigned to each generated $D^{\pm}$ meson which is taken from the measured D^0 meson spectra in Run12. The efficiency is calculated separately for the *st_physics* stream and the *st_sst+st_nosst* streams as there are some key differences between the two sub-sets (e.g. luminosity was different).

The generator on its own does not contain any information about the STAR detector, so distributions from data and TPC embedding are used to smear information about the decay daughters. Total of five different inputs are used in this analysis:

- TPC transverse momentum resolution (embedding)
- TPC tracking efficiency (embedding)
- HFT matching efficiency (data)
- DCA resolution (data)
- Primary vertex position along the beam axis (data)

More detailed description of the individual inputs and procedures used to obtain them is given in the two following sections.

The way the fast-simulator works is as follows: the EvtGen generates a $D^{\pm}$ meson with random kinematics within the range stated above and decays it into a $K\pi\pi$ triplet.

First, momentum of each of the daughters is smeared using momentum resolution distributions. Next, each of the tracks is shifted with respect to the simulated secondary vertex. The magnitude of the shift is randomly generated based on the DCA distributions from data. After that, the smeared kinematics and topology of the decay is calculated the same way as it is done in real data.

Next information needed for the efficiency calculation is the HFT and TPC matching (tracking) efficiency of each track. The method is essentially the same for both detectors. The HFT and TPC matching (tracking) efficiency distributions are simple p_T dependent distributions which tell us how likely it is that a pion or kaon with given kinematics is correctly reconstructed by the HFT or TPC. This means that the values of these distributions are always between 0 and 1. To simulate the HFT and TPC matching, it is sufficient to randomly generate a number between 0 and 1 for each particle (and detector) and compare this generated value to the one from the reference distribution. When the generated value is smaller than the reference one, the particle is correctly matched to the detector, if it is larger, then the track is not matched.

When the smearing and matching is done, the simulated $D^{\pm}$ mesons can be reconstructed using the same selection criteria as were used for extraction of the raw yield. The HFT+TPC efficiency is then given by a ratio of number of the $D^{\pm}$ mesons that passed the selection criteria and all generated ones. For reference, for this efficiency study, about 35M $D^{\pm}$ mesons were generated for the *st_physics* stream and about 37M for the *st_sst+st_nosst* streams.

As discussed above, there are two sources of the inputs to the data-driven fast-simulator: TPC embedding and the data. All of the inputs, except the momentum resolution, are created separately for *st_physics* stream and the *st_sst+st_nosst* streams and all of them contain information about identified particles, i.e. about pions and kaons. This section provides a detailed description of the individual inputs and the procedures used to generate them.

Inputs from TPC embedding

The inputs from embedding are used in order to take into account the performance of the TPC, specifically the momentum resolution and the tracking efficiency. A centrally produced, single particle (π^+, π^-, K^+, K^-) TPC embedding was used for this study. For both momentum resolution and tracking efficiency, a set of selection criteria was applied to the simulated (MC) and reconstructed tracks. The criteria are listed in Tab. 4.12.

The only requirement on the MC tracks is that they are inside the pseudorapidity acceptance. The cuts for reconstructed tracks in Tab. 4.12 are set to the same values as for tracks used in the analysis. The only embedding specific selection cut is on $nHitsCom$

$\lvert\eta_{\mathrm{MC}}\rvert < 1$
$\lvert\eta_{\mathrm{reco}}\rvert < 1$
$nHitsFit > 20$
$nHitsFit/nHitsMax > 0.52$
$nHitsCom > 10$ $DCA < 1.5\,\mu\mathrm{m}$

Tab. 4.12: Selection criteria applied to charged pions and charged kaons in embedding which were used for momentum resolution and TPC tracking efficiency calculation.

which is set to the same value as was used in $\mathrm{D_s}$ and $\mathrm{D^0}$ analyses. For the momentum resolution calculation, a PID cut is applied on track's nσ in addition to the cuts listed in Tab. 4.12. The values of the PID cuts are the same as were used in the analysis and are listed in Tab. 4.7.

The transverse momentum resolution ($\sigma_{p_{\mathrm{T}}}$) is determined from the embedding by comparing the transverse momentum of the embedded (simulated) track ($p_{\mathrm{T(MC)}}$) to its transverse momentum after it was reconstructed by the tracking algorithm ($p_{\mathrm{T(reco)}}$) using the following formula:

$$\Delta_{p_{\mathrm{T}}} = \frac{p_{\mathrm{T(MC)}} - p_{\mathrm{T(reco)}}}{p_{\mathrm{T(MC)}}}, \tag{4.2}$$

which is then fitted with a Gaussian function. The resolution $\sigma_{p_{\mathrm{T}}}$ is given as the width of the Gaussian function. The distribution (4.2) is filled in 120 bins covering $0 < p_{\mathrm{T}} < 12\,\mathrm{GeV}/c$. The momentum resolution as a function of p_{T} is plotted in Fig. 4.10. The data are fitted with a following function:

$$\sigma_{p_{\mathrm{T}}} = a + \frac{b}{p_{\mathrm{T}}} + \frac{c}{p_{\mathrm{T}}^2} + d \cdot p_{\mathrm{T}} + e \cdot p_{\mathrm{T}}^2, \tag{4.3}$$

where a, b, c, d, and e are free parameters of the fit.

The same calculation is repeated for π^-, K^+, and K^- mesons. The momentum resolutions of these mesons are plotted in Figs. 4.11, 4.12, and 4.13, respectively. The momentum resolution was extracted from embedding for the *st_physics* stream without the HFT. The reason is that at the time of the efficiency calculation, it was the only version of the embedding that was available.

The calculation was also done for newer versions of the embedding which included the HFT, for both *st_physics* and *st_sst+st_nosst* streams. The momentum resolution turned out to be significantly better (up to by a factor of 4 smaller) for this version of the embedding than for the older one, without the HFT. It was not clear whether the HFT can actually improve the momentum resolution this much, so it was decided that the version without the HFT will be used for a conservative estimate of the resolution. This step was also verified by calculating the total reconstruction efficiency with both versions of the momentum resolution (with and without the HFT) and there was no

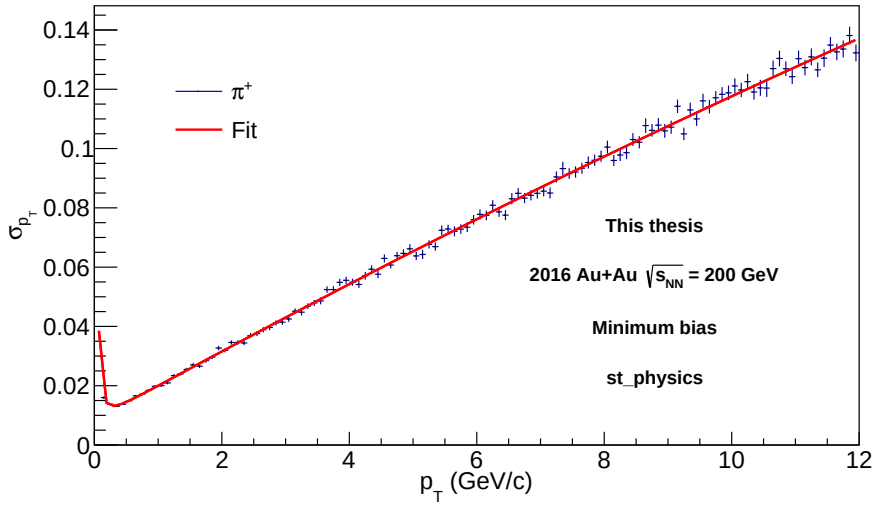

Fig. 4.10: Momentum resolution of π^+ mesons as a function of p_T for Run16 minimum bias Au+Au collisions at $\sqrt{s_{NN}} = 200$ GeV. The data are fitted with function defined using Eq. 4.3.

significant difference observed.

The TPC tracking efficiency is determined by calculating ratio of reconstructed tracks (N_{reco}) over the number of simulated tracks (N_{MC}, both passing the corresponding selection criteria in Tab. 4.12. In this case, no PID cuts are applied as PID efficiency is treated separately. This study was done separately for π^+, π^-, K^+, and K^- mesons and for *st_physics* and *st_sst* + *st_nosst* streams. In this case it was possible, as the HFT is not required in the track reconstruction for TPC tracking efficiency calculation.

The TPC tracking efficiency is calculated in 9 centrality bins, following the same binning as is used in the StRefMultCorr class used for centrality determination in the analysis. The TPC tracking efficiency of π^+ and K^+ in the *st_physics* stream as a function of $p_{T,MC}$ and collision centrality is shown in Fig. 4.14 and in Fig. 4.15, respectively. Figures for π^- and K^- and for *st_sst* + *st_nosst* stream are shown in Appendix D.

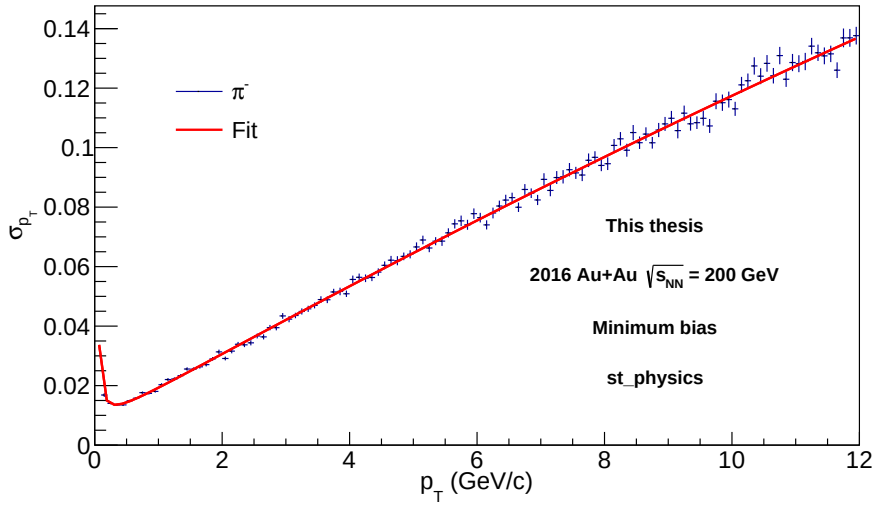

Fig. 4.11: Momentum resolution of π^- mesons as a function of p_{T} for Run16 minimum bias Au+Au collisions at $\sqrt{s_{\mathrm{NN}}} = 200\,\mathrm{GeV}$. The data are fitted with function defined using Eq. 4.3.

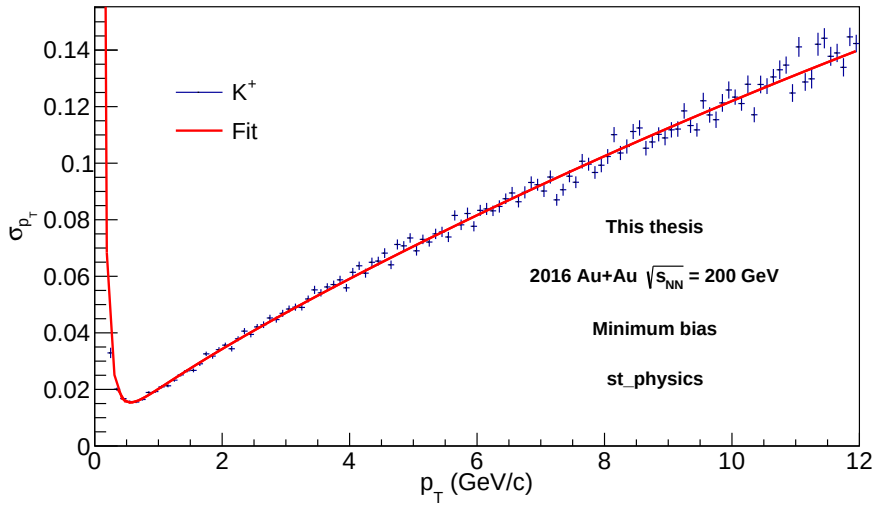

Fig. 4.12: Momentum resolution of K^+ mesons as a function of p_{T} for Run16 minimum bias Au+Au collisions at $\sqrt{s_{\mathrm{NN}}} = 200\,\mathrm{GeV}$. The data are fitted with function defined using Eq. 4.3.

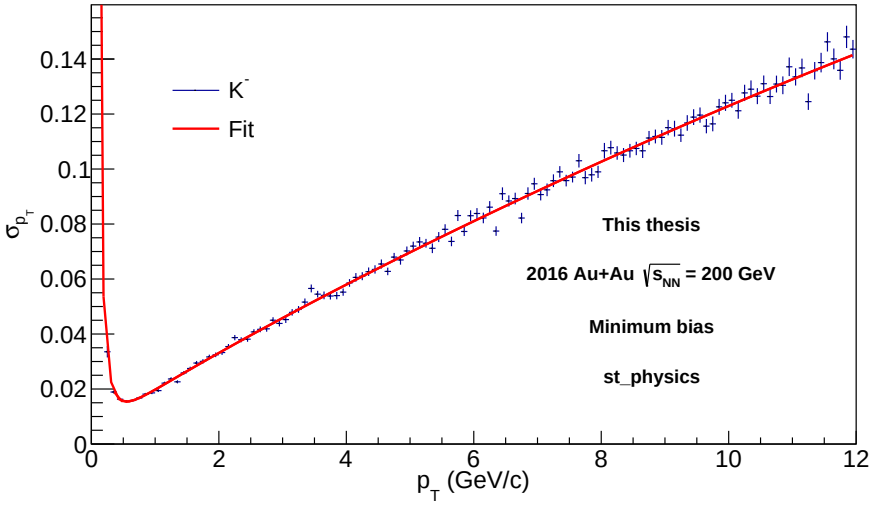

Fig. 4.13: Momentum resolution of K^- mesons as a function of p_T for Run16 minimum bias Au+Au collisions at $\sqrt{s_{NN}} = 200$ GeV. The data are fitted with function defined using Eq. 4.3.

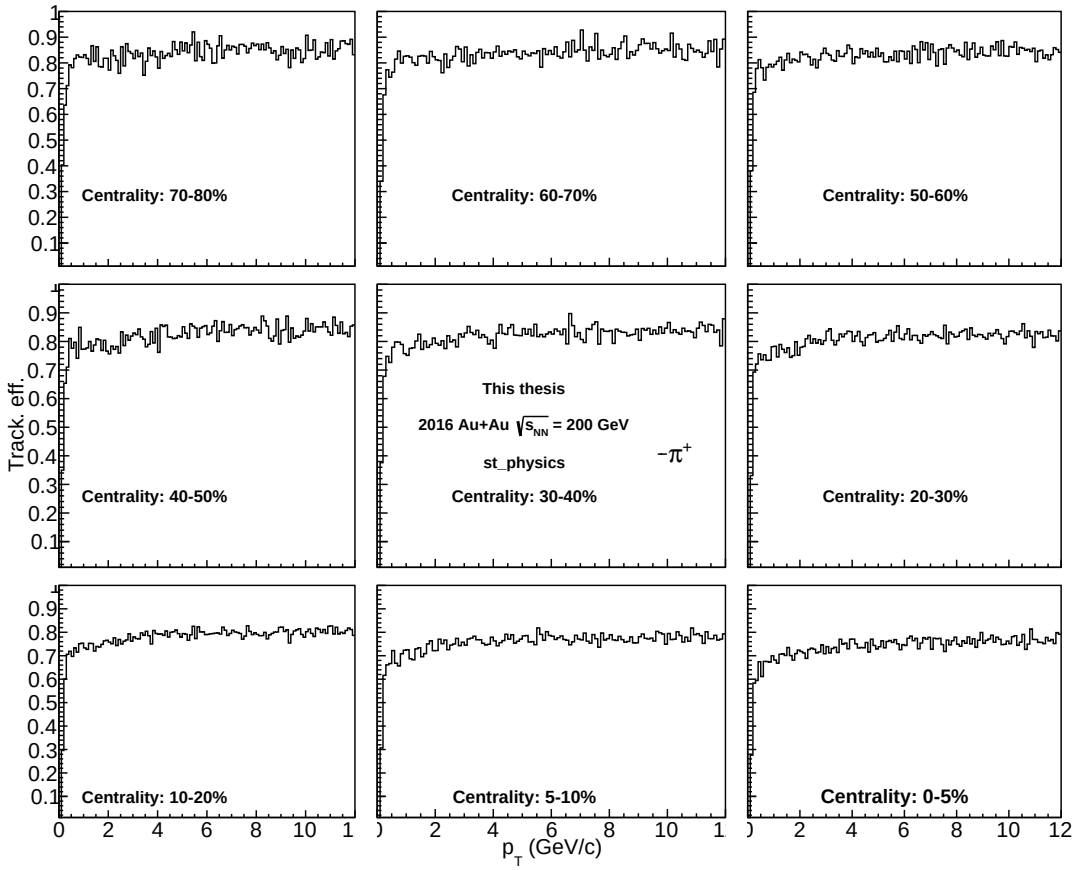

Fig. 4.14: TPC tracking efficiency of π^+ in the *st_physics* stream for different centralities of Au+Au collisions at $\sqrt{s_{NN}} = 200$ GeV.

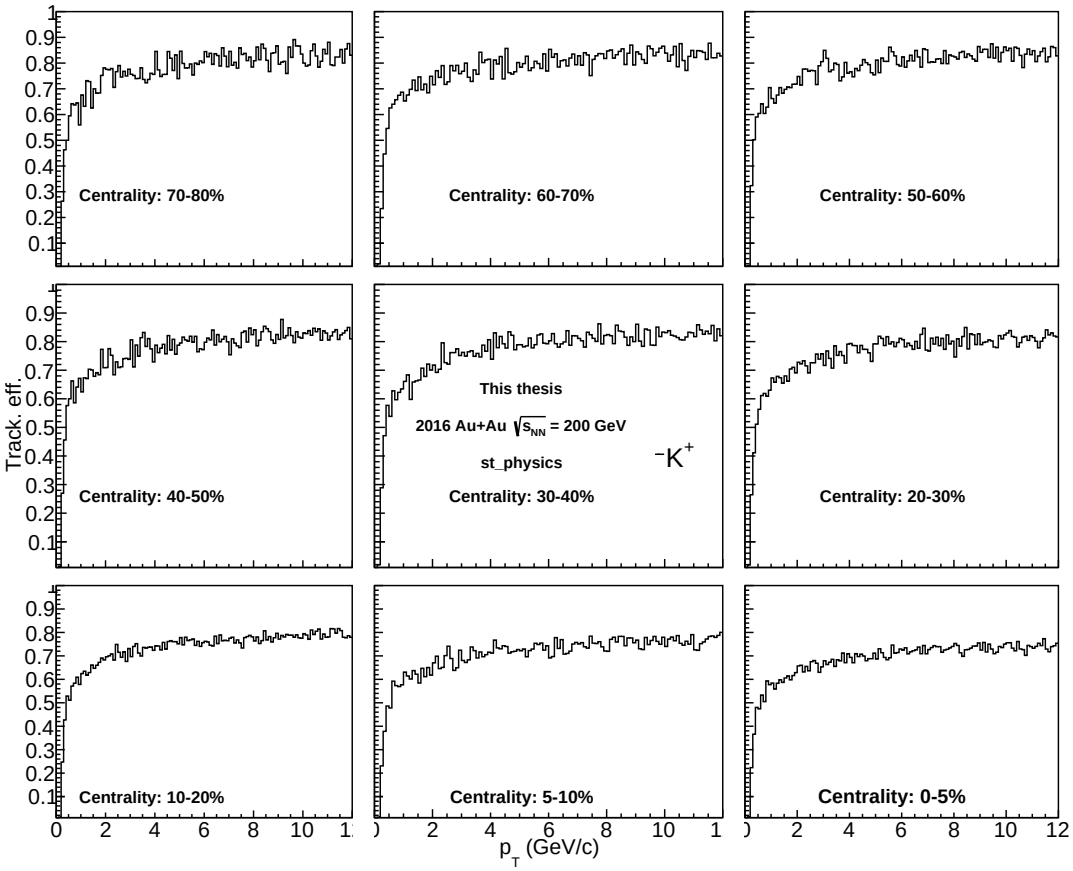

Fig. 4.15: TPC tracking efficiency of K^+ in the *st_physics* stream for different centralities of Au+Au collisions at $\sqrt{s_{\mathrm{NN}}} = 200\,\mathrm{GeV}$.

Inputs from data

One of the inputs from data to the fast simulation are the DCA distributions of pions and kaons. In this case, a DCA distribution is a histogram with the DCA_{xy} on one axis and the DCA_z on the second axis. Each axis is divided into 144 bins, covering the range of $-1 < DCA < 1$ cm, with finer binning near the center of the distribution (i.e. around $DCA = 0\,\mu$m). The distributions are filled separately in multiple bins in p_T, η, ϕ, v_z, and collision centrality. More details about the binning are listed in Tab. 4.13. The binning in centrality is the same as for the TPC tracking efficiency (see e.g. Fig. 4.14).

$0.3 < p_T < 12.0$ GeV/c	19 bins
$\lvert\eta\rvert < 1$	5 bins
$-\pi < \phi < \pi$	11 bins
$-6 < v_z < 6$ cm	4 bins

Tab. 4.13: Binning of space used for filling of DCA distributions which were then used as an input to the data-driven fast-simulator.

The track and event selection criteria and the PID are the same as in the analysis to get real picture of the DCA distributions from the data. The values of the cuts used are listed in Tabs. 4.5, 4.6, and 4.7.

In order to calculate the HFT matching ratios, two sets of tracks are selected. The first one are all tracks passing selection criteria listed in Tabs. 4.5, 4.6, and 4.7, i.e. tracks with properly matched HFT and with the same selection as was used for the $D^{\pm}$ candidates. The second one is nearly the same, but it is not required for the tracks to be matched to the HFT. We refer to such tracks as TPC tracks. The HFT matching ratio is then simply a ratio of the HFT matched tracks over the TPC tracks. The ratio is filled as a function of track p_T in 36 bins covering the range of $0.3 < p_T < 12.0$ GeV/c. Similarly to the DCA distributions, the HFT matching ratios are calculated in multiple in η, ϕ, v_z, and collision centrality bins. More details about the binning are listed in Tab. 4.14. Again, the binning in centrality is the same as for the TPC tracking efficiency (see e.g. Fig. 4.14).

$\lvert\eta\rvert < 1$	10 bins
$-\pi < \phi < \pi$	11 bins
$-6 < v_z < 6$ cm	6 bins

Tab. 4.14: Binning of space used for filling of HFT matching ratios which were then used as an input to the data-driven fast-simulator.

The last input from data are the distributions of the primary vertex position along the beam axis v_z. As shown above, the other two inputs from data depend on v_z. In real data, the v_z distribution is not flat, so the real shape of the distribution needs to

$0 < p_{\mathrm{T}} < 11$ GeV/c
$\lvert y \rvert < 1$
$0 < \phi < 2\pi$

Tab. 4.15: Intervals of p_{T}, y, and ϕ in which the simulated $\mathrm{D}^{\pm}$ mesons were generated by the EvtGen particle generator. All distributions (p_{T}, y, and ϕ) were generated as uniform.

be taken into account during the efficiency calculation. The distributions are filled in 9 centrality classes, following the same binnig as all previous distributions.

All inputs from data are created separately for *st_physics* and *st_sst* + *st_nosst* streams to capture any differences between the two Run16 sub-sets.

EvtGen data-driven fast-simulator

The core of the data-driven fast-simulator is the EvtGen particle generator [160], which was developed primarily for simulation of decays of open-heavy flavor hadrons. It is used to generate D^{+} and D^{-} mesons with given kinematics, which is randomly chosen within pre-set parameters listed in Tab. 4.15. All of the kinematic variables are generated with a uniform distribution. This is not realistic for p_{T}, so a weight is associated with each generated $\mathrm{D}^{\pm}$ meson. The weight is taken from the Levy fit to Run12 D^{0} invariant spectrum measured in p+p collisions at $\sqrt{s} = 200\,\mathrm{GeV}$ (not published).

After a $\mathrm{D}^{\pm}$ meson is generated, it is decayed by the EvtGen into a $\mathrm{K}^{\mp}\pi^{\pm}\pi^{\pm}$ triplet. Position of the primary vertex along the beam axis v_{z} is randomly generated from distributions from data described in the previous section. As EvtGen has no information about the STAR detector, the information about the decay daughters is subsequently smeared using the inputs from data and embedding.

For each daughter separately, the transverse momentum is smeared using the momentum resolution, the daughter's position is randomly shifted with respect to the MC secondary vertex according to the DCA distributions from data, and is matched to the TPC and the HFT. The matching procedure is similar for the TPC and the HFT. First, a random number is generated between 0 and 1 (separately for the TPC and HFT). Next, this number is compared to a value from the TPC tracking efficiency (HFT matching efficiency) distribution. If the random number is larger than the value from the distribution, the track is not properly matched. If it is smaller than the value from the input distribution, it is matched.

The HFT+TPC reconstruction efficiency ($\varepsilon_{\mathrm{HFT+TPC}}$) can be then determined as a ratio of simulated $\mathrm{D}^{\pm}$ mesons which passed the analysis topological selection criteria, over all generated $\mathrm{D}^{\pm}$ mesons.

4.2.2 PID efficiency

To get the total reconstruction efficiency, it is necessary to calculate the PID efficiency. By using the PID selection criteria from Tab. 4.7, a part of $\pi^{\pm}$ and $K^{\pm}$ mesons was rejected from the analysis, which decreases the measured raw yield. The PID efficiency compensates for this drop in the raw yield. The general strategy in PID efficiency calculation is to obtain a pure sample of π (K) mesons and look at their $n\sigma_{TPC}$ and $|1/\beta - 1/\beta_{\pi(K)}|$ distributions and determine the fraction of π (K) mesons outside the PID cut.

A pure sample of $\pi^{\pm}$ mesons can be easily obtained via reconstruction of decay of K^0_s mesons which decay into a $\pi^+\pi^-$ pair, with $BR = (69.20 \pm 0.05)\%$ [76]. Another advantage of the K^0_s mesons si that they have a long decay length of $c\tau = 2.7$ cm, so they can be reconstructed with the HFT only using the topological selection criteria and track selection criteria (i.e. PID can be avoided). The event and track selection is the same as in the analysis, so the vales used are summarized in Tabs. 4.5 and 4.6. The topological selection criteria for K^0_s reconstruction are listed in Tab. 4.16.

Decay topology	$DCA_{pair} < 100\ \mu m$
	$0.5\ \mu m < ct_{D^{\pm}} < 100.0\ cm$
	$\cos(\theta) > 0.995$
	$DCA_{\pi-PV} > 0.5\ cm$

Tab. 4.16: Summary of topological selection criteria used for extraction of K^0_s mesons. Pions from decay of the selected K^0_s mesons were then used to determine the PID efficiency of $\pi^{\pm}$ mesons in the Run16 Au+Au collisions at $\sqrt{s_{NN}} = 200\,GeV$.

The K^0_s candidates are reconstructed in a similar way as the $D^{\pm}$ mesons. The invariant mass spectrum of the $\pi\pi$ meson pairs is filed for unlike-sign (US) and like-sign (LS) charge combinations. The LS is then subtracted from the US, leaving only the K^0_s without the combinatorial background. The invariant mass peak is fitted with a Gaussian function in order to determine its width. The K^0_s invariant mass distributions ($M^{\pi\pi}_{inv}$) before and after combinatorial background subtraction are plotted in Fig. 4.16.

The $n\sigma_{\pi}$ and $|1/\beta - 1/\beta_{\pi}|$ distributions are filled for LS and US for pions which are coming from $\pi\pi$ meson pairs which have $M^{\pi\pi}_{inv}$ within $\pm 3\sigma$ from the mean of the peak. Again the LS is subtracted from the US, leaving $n\sigma_{\pi}$ and $|1/\beta - 1/\beta_{\pi}|$ distributions for signal only. The PID distributions are filled in 16 bins covering $0 < p_T < 4\,GeV/c$ and fitted with a Gaussian function. The fitted distributions are shown in Fig. 4.17 ($n\sigma_{\pi}$) and Fig. 4.18 ($|1/\beta - 1/\beta_{\pi}|$), respectively.

The PID efficiency is then determined as a ratio of integral of the fit function within the PID cut region (see Tab. 4.7) and of the integral in the full range (in this case full range of x-axis in Fig. 4.17 or 4.18). The PID efficiency of the TPC and TOF as a function of p_T is plotted in Fig. 4.19. The data are fittet by a constant function which

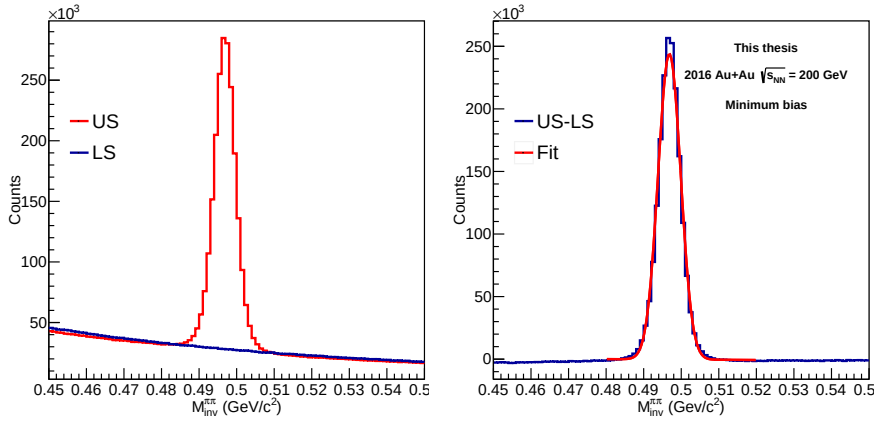

Fig. 4.16: (left) The invariant mass spectrum of the $\pi^+\pi^-$ meson pairs is filed for unlike-sign (US) and like-sign (LS) charge combinations. (right) The LS is then subtracted from the US, leaving only the K^0_s without the combinatorial background. The K^0_s mass peak is fitted with a Gaussian function in order to determine the $\pm 3\sigma$ signal region.

is then used to determine the final value of the PID efficiency.

In case of the TPC PID efficiency, it was decided to use a constant function to fit the PID efficiency data points despite the shape of the p_T dependency in order to simplify the procedure. The reason why this should not pose serious problems is that majority of pions coming from decays of $D^\pm$ mesons in this analysis have $p_T < 2\,\mathrm{GeV}/c$. In that region, the TPC PID efficiency is practically constant in p_T, so the constant fit captures the shape well. Another argument is, that PID plays an important role in the low-p_T region. For $p_T > 2\,\mathrm{GeV}/c$, the topological selection will play much more significant role in $D^\pm$ reconstruction.

The general strategy for $K^\pm$ meson PID efficiency is the same as for π. The only difference is in the way the pure $K^\pm$ was obtained. There is a suitable decay, which can be used, specifically decay of $\phi \to K^+K^-$, but its reconstruction using just decay topology and PID on one of the decay daughters was not successful in the Run16 data-set. For that reason a different strategy was implemented.

For determination of the TPC PID efficiency, the pure sample of $K^\pm$ mesons was selected using a strict PID cut in the TOF and vice versa for the TOF PID efficiency. Specifically, the strict TOF cut used is $|1/\beta - 1/\beta_K| < 0.01$ and the strict TPC cut is $|n\sigma_K| < 0.5$. The rest of the calculation is the same as for $\pi^\pm$ mesons, i.e. the $n\sigma_K$ and $|1/\beta - 1/\beta_K|$ distributions are filled in 16 bins, this time covering $0 < p_T < 2\,\mathrm{GeV}/c$. The reasons, why it should not be a problem to use this more limited p_T range are the same as for the fit of the TPC PID efficiency of $\pi^\pm$ mesons, as discussed above.

The fitted PID distributions for $K^\pm$ mesons are shown in Fig. 4.20 and 4.21. The $n\sigma_K$ distributions look quite similar to those of $n\sigma_\pi$. On the other hand, the $|1/\beta - 1/\beta_K|$ show clearly significant level of contamination with other hadrons (pions and protons,

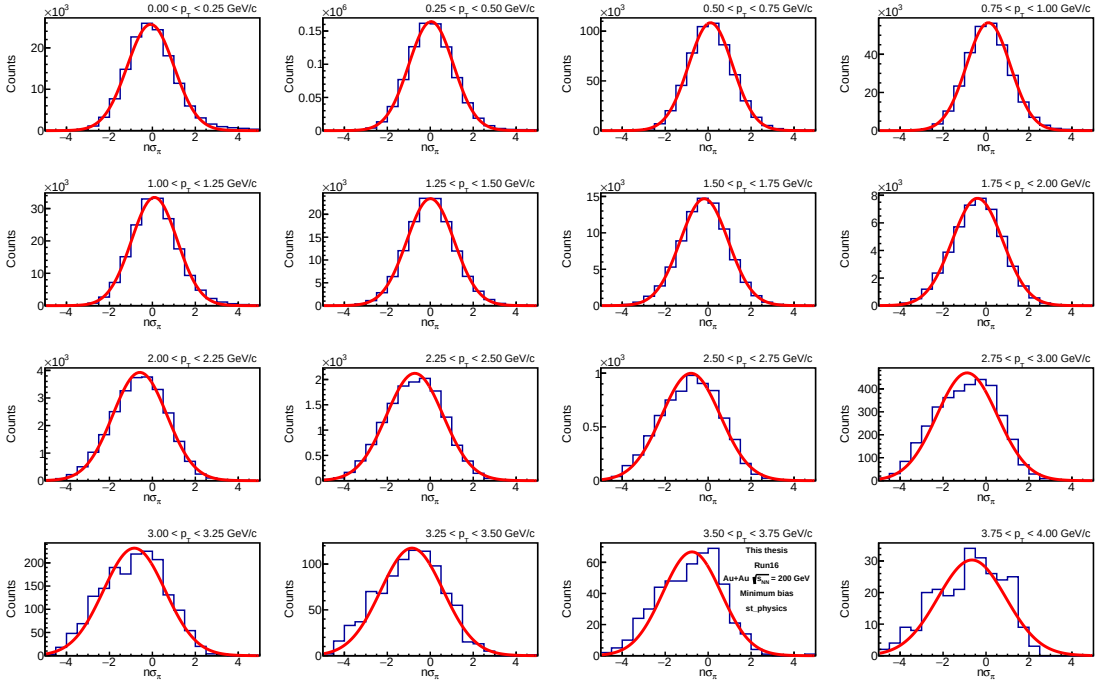

Fig. 4.17: Fitted $n\sigma_{\pi}$ distributions which were used in determination TPC PID efficiency of pions in Run16 Au+Au collisions at $\sqrt{s_{NN}} = 200$ GeV. The $n\sigma_{\pi}$ distributions are plotted for 16 bins in p_T. The data are fitted with a Gaussian function.

most likely) with increasing p_T. For that reason the $|1/\beta - 1/\beta_K|$ distribution is fitted with single, double or triple Gaussian function, depending on the level of contamination. The PID efficiency of the TOF is then determined only from the $K^{\pm}$ peak.

The p_T dependency of the TPC and TOF PID efficiency of $K^{\pm}$ mesons is plotted in Fig. 4.22. Again, the data are fitted with a constant function in order to determine the final PID efficiency. In this case, the constant fit gives good approximation for both the TPC and TOF.

The total PID efficiency of $\pi^{\pm}$ and $K^{\pm}$ mesons is then given by the following formula:

$$\varepsilon_{\mathrm{PID}}^{\pi(\mathrm{K})}(p_T) = P_{\mathrm{TOF}}^{\pi(\mathrm{K})}(p_T)\varepsilon_{\mathrm{TOF}}^{\pi(\mathrm{K})}\varepsilon_{\mathrm{TPC}}^{\pi(\mathrm{K})} + (1 - P_{\mathrm{TOF}}^{\pi(\mathrm{K})}(p_T))\varepsilon_{\mathrm{TPC}}^{\pi(\mathrm{K})}, \tag{4.4}$$

where $P_{\mathrm{TOF}}^{\pi(\mathrm{K})}$ is the TOF matching efficiency of pions or kaons. The TOF matching efficiency is calculated as a ratio of number of tracks that are properly matched to TOF over those only reconstructed by the HFT+TPC, both groups passing event and track selection cuts from Tabs. 4.5 and 4.6, and a strict TPC PID cut $|n\sigma_{\pi(\mathrm{K})}| < 1$. The TOF matching efficiency is plotted in Fig. 4.23 and the total single particle PID efficiency is plotted in Fig. 4.24.

The single particle PID efficiency is practically constant in p_T for both $\pi^{\pm}$ and $K^{\pm}$ mesons. The final value is extracted from a constant fit to the data. The total PID efficiency of the reconstructed $D^{\pm}$ mesons is then given by the following formula:

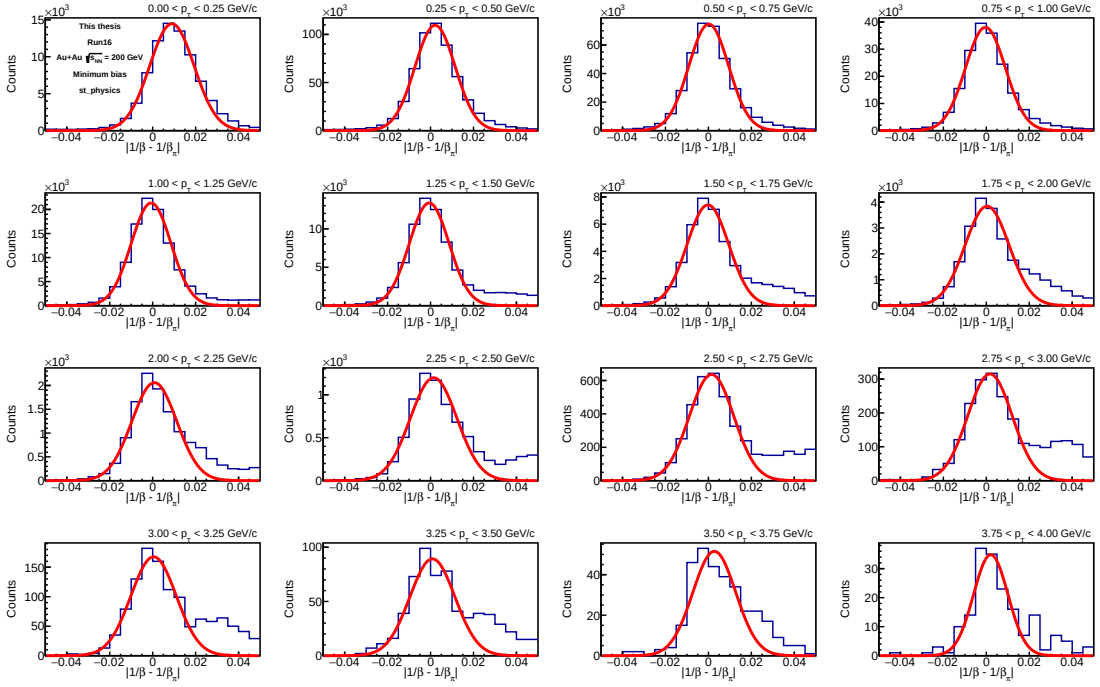

Fig. 4.18: Fitted $|1/\beta - 1/\beta_\pi|$ distributions which were used in determination TOF PID efficiency of pions in Run16 Au+Au collisions at $\sqrt{s_{\mathrm{NN}}} = 200\,\mathrm{GeV}$. The $|1/\beta - 1/\beta_\pi|$ distributions are plotted for 16 bins in p_{T}. The data are fitted with a Gaussian function.

$$\varepsilon_{\mathrm{PID}}(p_{\mathrm{T}}) = \varepsilon^{\pi}_{\mathrm{PID}}(p_{\mathrm{T}})\varepsilon^{\pi}_{\mathrm{PID}}(p_{\mathrm{T}})\varepsilon^{\mathrm{K}}_{\mathrm{PID}}(p_{\mathrm{T}}). \tag{4.5}$$

All the plots above are for the *st_physics* stream. The calculation was done for the *st_sst* + *st_nosst* streams as well and the final value of the PID efficiency is nearly identical. The values from *st_physics* stream were used for both sub-sets of the data in order to simplify the application of the PID efficiency.

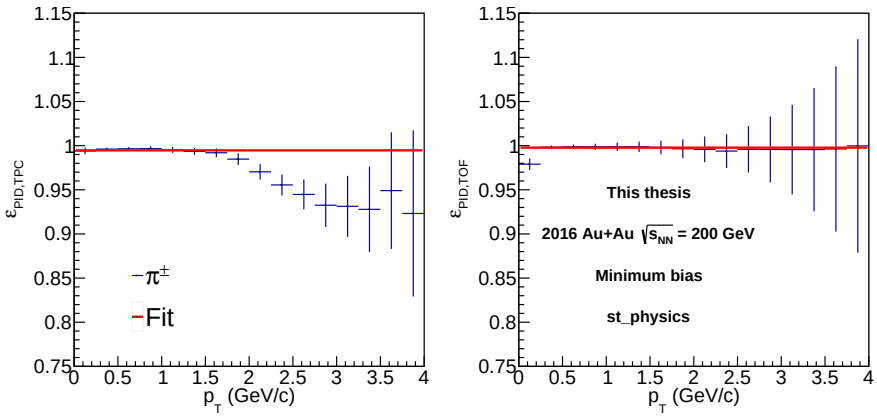

Fig. 4.19: PID efficiency of the TPC (left) and TOF (right) for $\pi^{\pm}$ mesons.

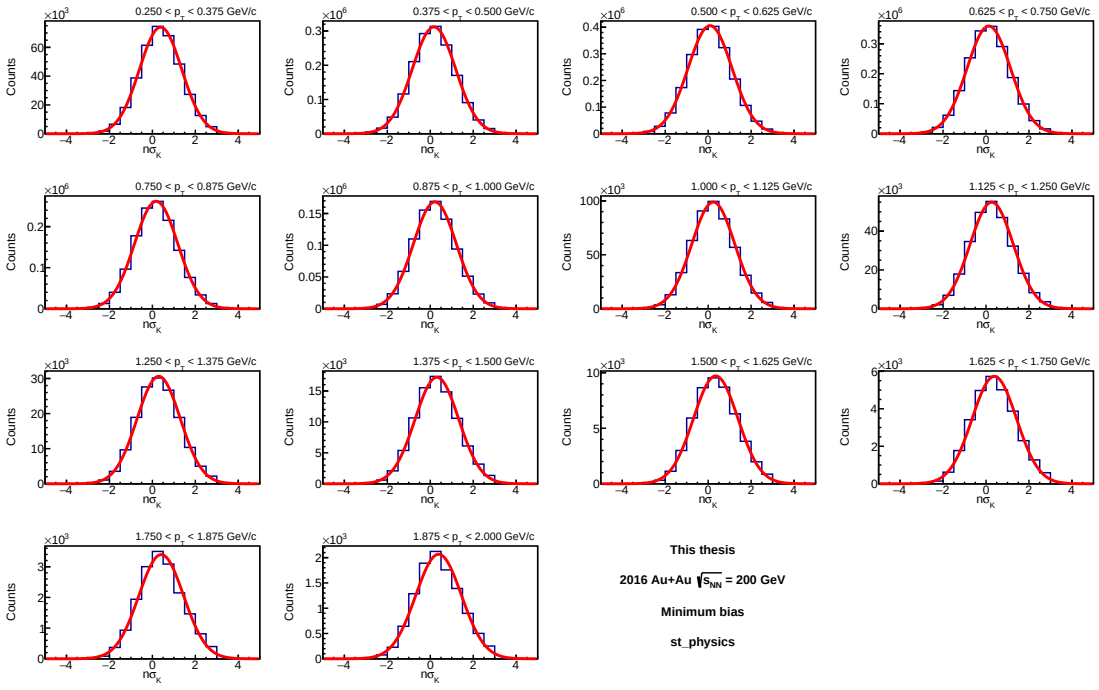

Fig. 4.20: Fitted $n\sigma_K$ distributions which were used in determination TPC PID efficiency of kaons in Run16 Au+Au collisions at $\sqrt{s_{NN}} = 200$ GeV. The $n\sigma_\pi$ distributions are plotted for 14 bins in p_T. The data are fitted with a Gaussian function.

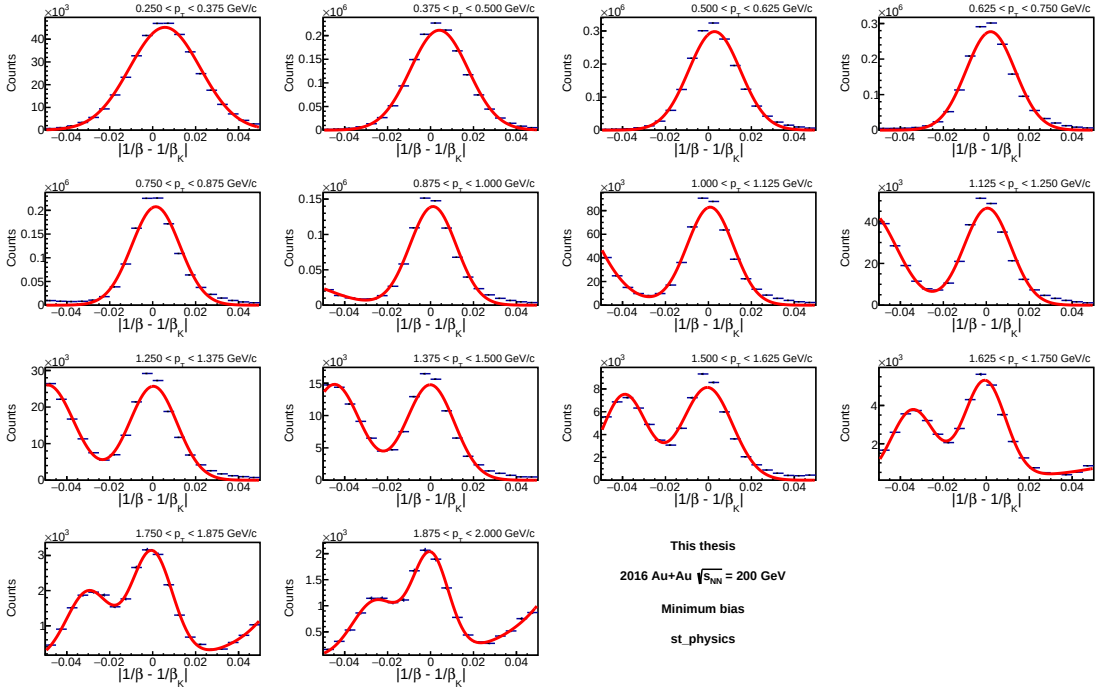

Fig. 4.21: Fitted $|1/\beta - 1/\beta_{\mathrm{K}}|$ distributions which were used in determination TOF PID efficiency of kaons in Run16 Au+Au collisions at $\sqrt{s_{\mathrm{NN}}} = 200\,\mathrm{GeV}$. The $|1/\beta - 1/\beta_{\mathrm{K}}|$ distributions are plotted for 14 bins in p_{T}. The data are fitted with a single Gaussian function for $p_{\mathrm{T}} < 0.875\,\mathrm{GeV}/c$, by a double-Gaussian function for $0.857 < p_{\mathrm{T}} < 1.625\,\mathrm{GeV}/c$., and by a tripple-Gaussian function for $1.625 < p_{\mathrm{T}} < 2.000\,\mathrm{GeV}/c$. The multi-Gaussian functions were used to capture the contribution from contamination of the kaon sample by pions and protons.

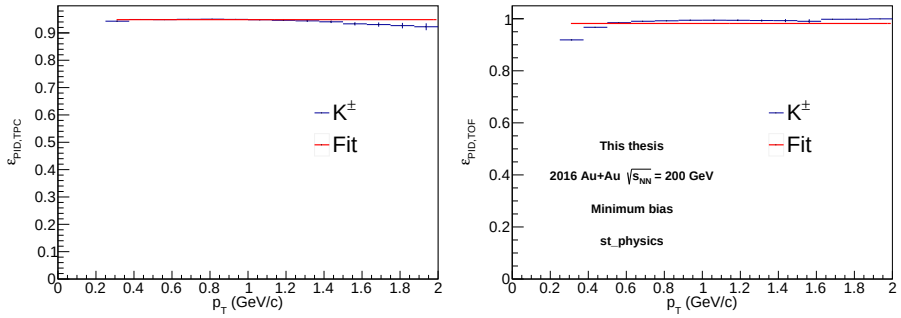

Fig. 4.22: Calculated total PID efficiency of the TPC (left) and TOF (right) for $\mathrm{K}^{\pm}$ mesons in Run16 Au+Au collisions at $\sqrt{s_{\mathrm{NN}}} = 200\,\mathrm{GeV}$.

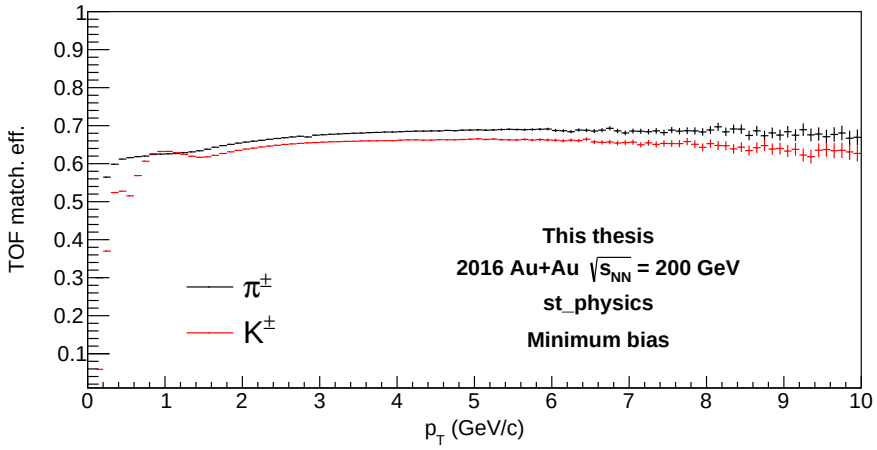

Fig. 4.23: TOF matching efficiency of $\pi^{\pm}$ and $K^{\pm}$ mesons in Run16 Au+Au collisions at $\sqrt{s_{NN}} = 200\,GeV$.

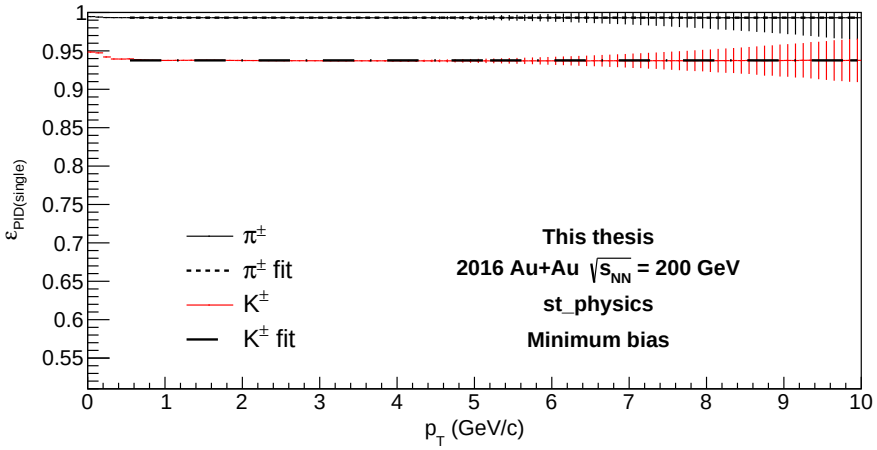

Fig. 4.24: Total single particle PID efficiency of $\pi^{\pm}$ and $K^{\pm}$ mesons in Run16 Au+Au collisions at $\sqrt{s_{NN}} = 200\,GeV$.

4.2.3 Total reconstruction efficiency

The total $D^{\pm}$ meson reconstruction efficiency is first determined separately for the *st_physics* and *st_sst* + *st_nosst* streams using:

$$\varepsilon(p_{\mathrm{T}}) = \varepsilon_{\mathrm{HFT+TPC}}(p_{\mathrm{T}})\varepsilon_{\mathrm{PID}}(p_{\mathrm{T}}). \tag{4.6}$$

The efficiencies for the two subsets are then combined as a weighted average, where the weights are numbers of good events in the *st_physics* and *st_sst* + *st_nosst* streams.

The total reconstruction efficiency of $D^{\pm}$ meson in Run16 Au+Au at $\sqrt{s_{\mathrm{NN}}} = 200\,\mathrm{GeV}/c$ as a function p_{T} and collision centrality is plotted in Fig. 4.25.

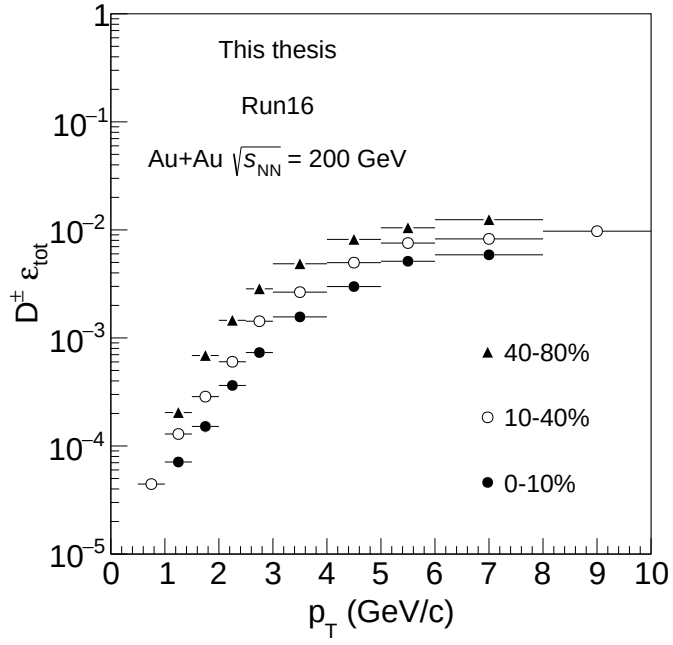

Fig. 4.25: Total reconstruction efficiency of $D^{\pm}$ mesons in Run16 for three centrality classes of the Au+Au collisions at $\sqrt{s_{\mathrm{NN}}} = 200\,\mathrm{GeV}$.

4.3 Systematic uncertainties

4.3.1 Invariant spectra

Systematic uncertainties of the invariant spectra were calculated independently for Run14 and Run16 data-set. This section provides description of the systematic uncertainty studies primarily for Run16 and method used to combine Run14 a nd Run16 systematic uncertainties.

The first systematic uncertainty source taken into account is the one associated with the raw yield extraction method. As mentioned in Section 4.1.2, the raw yield is extracted from the fit function. An alternative method is to use the invariant mass

spectrum, after subtraction of the combinatorial background, and count the $D^{\pm}$ candidates directly from the histogram in the $\pm 3\sigma$ range. The value of σ is the width of the invariant mass peak, which is determined using the same fit as is used for the raw yield determination. This direct method is usually referred to as "bin-counting".

The systematic uncertainty ($\sigma_{RawYield}$) is calculated simply by comparing the raw yield determined from the fit (Y_{fit}) and by using the bin-counting (Y_{bin}) using the following formula:

$$\sigma_{RawYield} = \frac{|Y_{\text{fit}} - Y_{\text{bin}}|}{Y_{\text{fit}}}. \tag{4.7}$$

The values of this systematic uncertainty are plotted in Fig. 4.26 as red open circles. The σ_{RawYield} does not exceed 20% and is the largest in p_{T} bins with low significance, which is expectable.

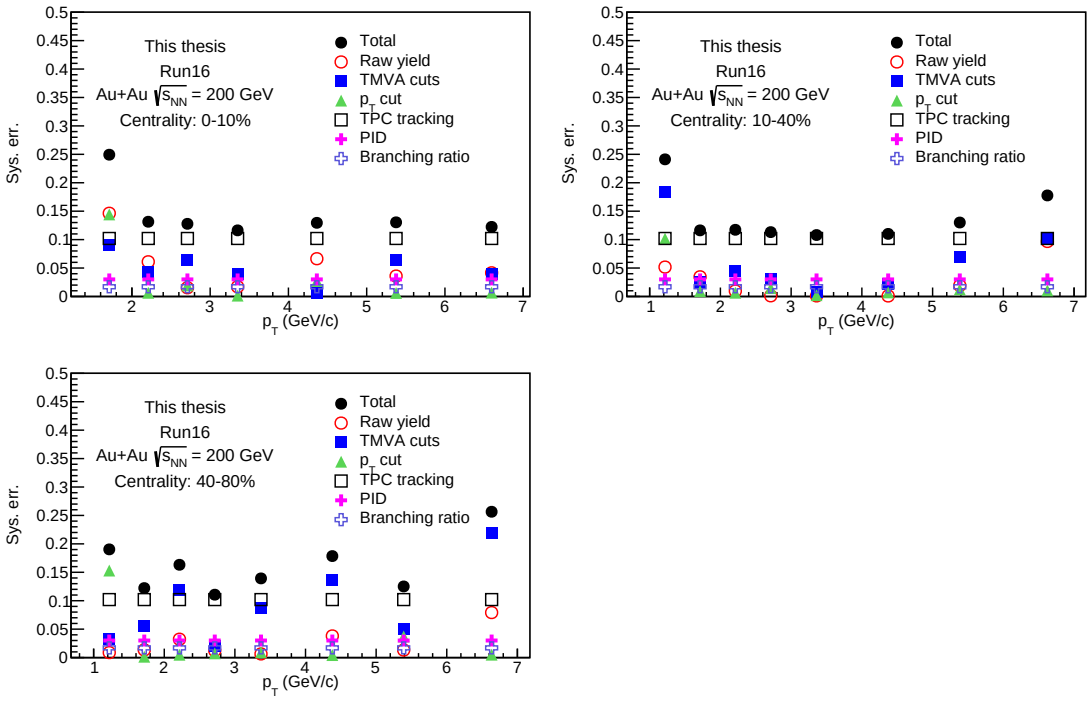

Fig. 4.26: Systematic uncertainties of invariant spectra of $D^{\pm}$ mesons in the Run16 dataset. Individual sources of systematic uncertainties are plotted separately, together with the total systematic uncertainty. Each panel corresponds to one centrality bin.

Next systematic uncertainty considered in this analysis is associated with the data-driven fast simulator. It is evaluated by varying the TMVA signal efficiency by $\pm 30\%$. As described in Section 4.1.1, the analysis topological selection criteria are chosen from the TMVA based on maximum significance. For such set of cuts, there is a corresponding TMVA signal efficiency ε_{s} (one point on the blue line in Fig. 4.6 and in figures in Appendix C). For this study, two additional sets of TMVA cuts are selected with signal

efficiency $0.7\varepsilon_{\mathrm{s}}$ and $1.3\varepsilon_{\mathrm{s}}$. Like this, we have three sets of TMVA topological cuts: analysis, loose, and tight[2].

Invariant spectrum ($\mathrm{d}N/\mathrm{d}y$), i.e. including reconstruction efficiency correction, is calculated for all three cut sets and the systematic uncertainty is then calculated using the following formula:

$$\sigma'_{\mathrm{loose/tight}} = \frac{|(\mathrm{d}N/\mathrm{d}y)_{\mathrm{ana}} - (\mathrm{d}N/\mathrm{d}y)_{\mathrm{loose/tight}}|}{(\mathrm{d}N/\mathrm{d}y)_{\mathrm{ana}}}. \tag{4.8}$$

The formula (4.8) does not take into account statistical precision of the yields in individual p_{T} bins. The statistical fluctuation associated with the formula (4.8 can be calculated using a following formula

$$\Delta^{\mathrm{stat}}_{\mathrm{loose/tight}} = \sqrt{|(\sigma^{\mathrm{stat}}_{\mathrm{ana}})^2 - (\sigma^{\mathrm{stat}}_{\mathrm{loose/tight}})^2|}, \tag{4.9}$$

where $\sigma^{\mathrm{stat}}_{\mathrm{ana}}$ and $\sigma^{\mathrm{stat}}_{\mathrm{loose/tight}}$ are statistical uncertainties of invariant yield for analysis and loose/tight cuts. The $\Delta^{\mathrm{stat}}_{\mathrm{loose/tight}}$ is then subtracted from $\sigma'_{\mathrm{loose/tight}}$ to obtain the corrected systematic uncertainty $\sigma_{\mathrm{loose/tight}}$ for loose and tight cuts. This corrected systematic uncertainty is plotted in Fig. 4.27.

When the value of $\sigma_{\mathrm{loose/tight}}$ turns out to be negative (i.e. after the statistical uncertainty correction), it is set to a value without the correction. The larger value of the two (for loose or tight cuts) is then quoted as the systematic uncertainty from TMVA cuts variation σ_{TMVA}. The values are plotted in Fig. 4.26 as blue solid squares.

Similar approach as described above is used to evaluate the systematic uncertainty of p_{T} cut variation. The cut on daughter p_{T} is varied from 300 MeV/c (used for raw yield extraction) to 500 MeV/c. The efficiency corrected invariant spectra are calculated for both cuts and compared using a formula similar to Eq. (4.8. Again, this value needs to be corrected for the statistical fluctuation in a given p_{T} bin, which is achieved by using a formula similar to Eq. (4.9). This systematic uncertainty is shown in Fig. 4.26 as full green triangles.

Another systematic uncertainty comes from the TPC embedding and is evaluated using a standard procedure used at STAR by variation of $nHitsFit$. This method relies on comparing ratio of number of TPC tracks with $nHitsFit > 25$ (N_{25}) and $nHitsFit > 20$ (N_{20}), i.e. with cut used in analysis, for data and embedded (simulated) tracks. As a result, there are two ratios: r_{data} and r_{embed} which are calculated according to

[2]In case the signal efficiency would exceed 100%, the loose TMVA topological selection criteria are chosen for $\varepsilon_{\mathrm{s}} = 100\%$.

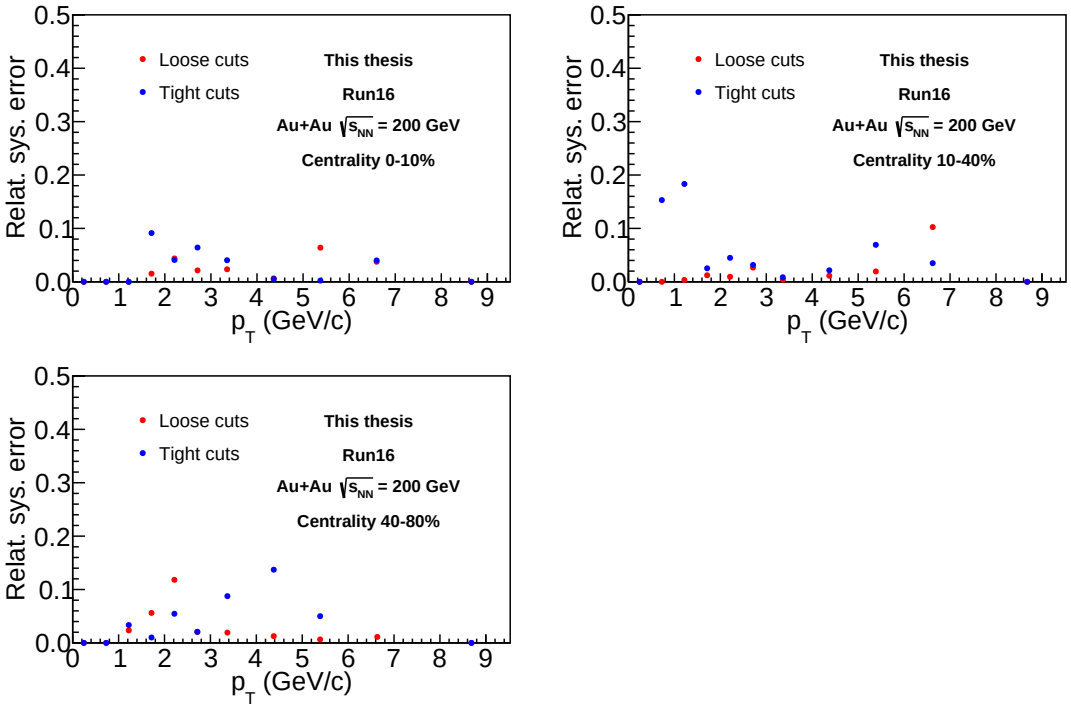

Fig. 4.27: Systematic uncertainties from cuts variation for loose (red) and tight (blue) TMVA topological selection criteria after statistical uncertainty correction. Missing points mean that the value is negative and is fixed at value of 0 later in the systematic uncertainty calculation.

$$r_{\text{data}} = \frac{N_{25}^{\text{data}}}{N_{20}^{\text{data}}}, \tag{4.10}$$

$$r_{\text{embed}} = \frac{N_{25}^{\text{embed}}}{N_{20}^{\text{embed}}}. \tag{4.11}$$

The data and embedding are then compared as a double ratio (r_{double}), i.e. as a ratio of r_{data} and r_{embed}:

$$r_{\text{double}} = \frac{r_{\text{data}}}{r_{\text{embed}}}. \tag{4.12}$$

This double ratio turns out to be constant in p_{T} and very close to unity in all centrality classes. In order to extract the p_{T} integrated value of the double ratio, r_{double} is fitted by a constant. The parameter of the fit is then used to calculate the systematic uncertainty. This procedure is done using charged tracks from data and π^+ from embedding. The double ratios with the fits are plotted in Fig. 4.28.

In an ideal case, the double ratio would be equal to unity, so the systematic uncertainty of the TPC tracking efficiency for a single track $\sigma_{\text{TPC(single)}}$ can be calculated using the following formula

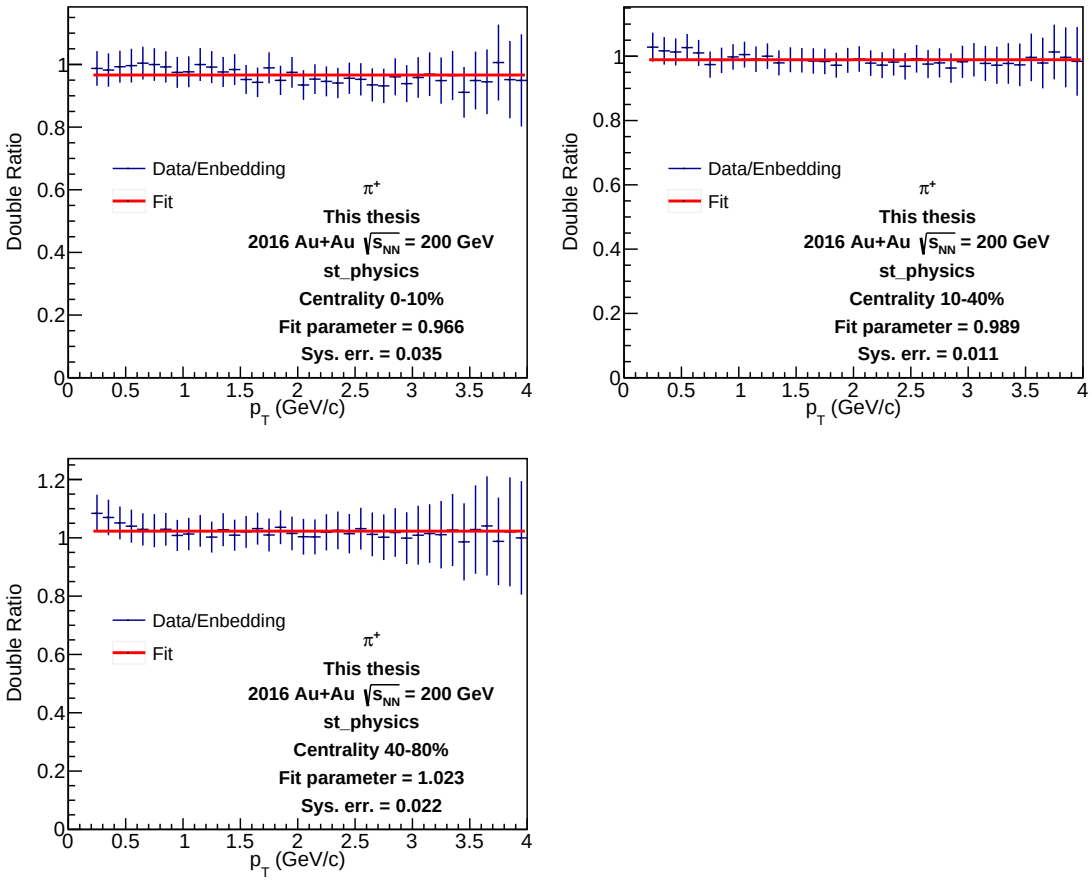

Fig. 4.28: Double ratio used for the TPC tracking efficiency systematic uncertainty of π^+ for three centrality classes of Au+Au collisions. The double ratio is constant in p_{T} so it is fitted by a constant function. The parameter of the fit and corresponding systematic uncertainty, calculated using formula (4.12) are shown in individual panels.

$$\sigma_{\mathrm{TPC(single)}} = \frac{1 - r_{\mathrm{double}}}{r_{\mathrm{double}}}. \tag{4.13}$$

To obtain the total TPC tracking systematic uncertainty for $\mathrm{D}^{\pm}$ mesons σ_{TPC}, the single track contributions are simply added together, as they are assumed to be largely correlated:

$$\sigma_{\mathrm{TPC}} = 3\sigma_{\mathrm{TPC(single)}}. \tag{4.14}$$

In general, all single particle TPC tracking systematic uncertainties should be calculated separately for π^+, π^-, K^+, and K^- mesons in each centrality class. During study of Run16, it turned out that the single particle uncertainties do not strongly depend on centrality or particle species. Therefore, it was possible to simplify the calculation by using a conservative value for single particle uncertainty $\sigma_{\mathrm{TPC(single)}} = 3.4\,\%$ which gives the total uncertainty of $\sigma_{\mathrm{TPC}} = 10.2\,\%$. For reference, σ_{TPC} is plotted in Fig. 4.26 as

open black squares.

There are two more systematic uncertainties sources for the invariant yields. One of them is the systematic uncertainty of PID. This uncertainty is relatively small compared to the other sources. The value is taken from the analysis of D^0 mesons, i.e. 1 % per track. To get the PID systematic uncertainty for the $D^{\pm}$ mesons, the same approach is applied as was used in the D_s analysis. This way, the final PID systematic uncertainty quoted in this analysis is $\sigma_{\mathrm{PID}} = 3\,\%$. In Fig. 4.26, this uncertainty is plotted as blue open crosses.

The last systematic uncertainty taken into account is coming from the uncertainty on the branching ratio of $D^{\pm}$ mesons. For this analysis a value from 2021 PDG was used: $BR = (9.38 \pm 0.16)\,\%$ [76], which gives relative systematic uncertainty of $\sigma_{\mathrm{BR}} = 1.7\,\%$. In Fig. 4.26, this uncertainty is plotted as the magenta full crosses.

For invariant p_{T} spectra, all aforementioned systematic uncertainties are combined as follows

$$\sigma_{\mathrm{tot}} = \sqrt{\sigma^2_{\mathrm{RawYield}} + \sigma^2_{\mathrm{TMVA}} + \sigma^2_{\mathrm{TPC}} + \sigma^2_{\mathrm{PID}} + \sigma^2_{\mathrm{BR}}}. \tag{4.15}$$

In Fig. 4.26, the total uncertainty is plotted as black solid circles.

This total systematic uncertainty is for Run16 data-set only. For the final results, it needs to be combined with the systematic uncertainty of Run14 $D^{\pm}$ spectra. As the two data-sets (Run14 and Run16) are very similar, the systematic uncertainties are correlated. For that reason they are combined as a weighted average, where the weights are $1/\sigma^2_{\mathrm{stat}}$.

4.3.2 Nuclear modification factor

The systematic uncertainty of the R_{AA} of $D^{\pm}$ mesons is calculated in nearly identical way as for the spectra. The only difference is that the systematic uncertainty which comes from the branching ratio is included in the global systematic uncertainty (blue box around unity in Fig. 4.36). The contribution to the systematic uncertainty plotted on the points of R_{AA} from Run16 is plotted in Fig. 4.29.

The global systematic uncertainty has three contributions. One of them is the branching ratio, as mentioned above, and its value is the same as quoted in the previous section ($\sigma_{\mathrm{BR}} = 3.1\,\%$). The second contribution comes from uncertainty of the N_{part} (σ_{Npart}) which was defined in Chapter 4.1, and the last one if from fragmentation function of D^0 $\sigma_{\mathrm{ff}} = 1.2\,\%$ which is based on the value of fragmentation function from Ref. [161]. The total global uncertainty is then given as $\sigma_{\mathrm{glob}} = \sqrt{\sigma^2_{\mathrm{BR}} + \sigma^2_{\mathrm{Npart}} + \sigma^2_{\mathrm{ff}}}$. The individual contributions and the total global systematic uncertainties per centrality are summarized in Tab. 4.17.

The last and very significant systematic uncertainty of the R_{AA} comes from the p+p

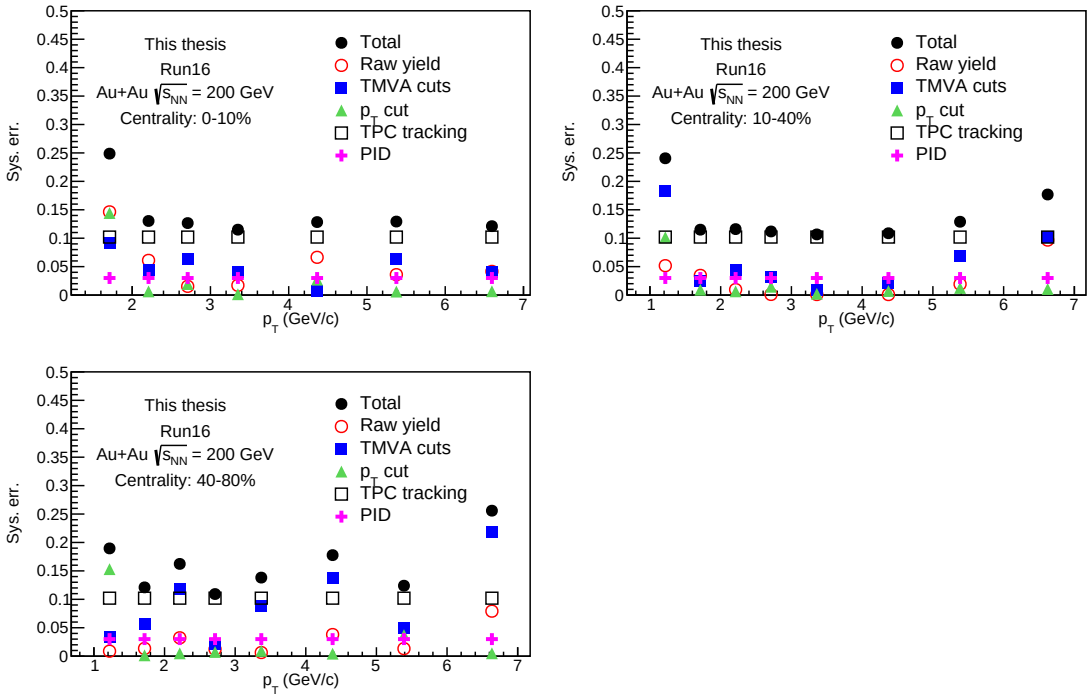

Fig. 4.29: Systematic uncertainties of R_{AA} of $D^{\pm}$ mesons in the Run16 data-set. Individual sources of systematic uncertainties are plotted separately, together with the total systematic uncertainty. Each panel corresponds to one centrality bin.

reference data. As the p+p reference has smaller coverage and binning in p_T than the $D^{\pm}$ data, the systematic uncertainties from the p+p reference need to be interpolated and extrapolated properly. This study has already been done for reference used in the D^0 meson R_{AA} calculation from Ref. [2]. For that reason, the same systematic uncertainties of the p+p reference are used for this analysis.

The way the uncertainty from the p+p reference is propagated to the R_{AA} is relatively straightforward. The R_{AA} is first calculated directly using the Levy fit to the p+p reference. Next it is calculated from the Levy fit shifted by the systematic uncertainty of the p+p reference up and down. This way we obtained three values of the R_{AA}: the measured experimental value, and the upper and lower limit for the R_{AA} based on the p+p systematic uncertainty.

4.3.3 $D^{\pm}/D^0$ yield ratio

Compared to the R_{AA}, the systematic uncertainty calculation for the $D^{\pm}/D^0$ yield ratio is a bit more complex. It is necessary to take into account any correlations of systematic uncertainties between the $D^{\pm}$ and D^0 data. As both analyses share many procedures, some systematic uncertainties will, at least partially, cancel out and other can be largely correlated. For that reason, the systematic uncertainty of the yield ratio is calculated as

σ_{BR} [%]	σ_{Ncoll} [%]	σ_{ff} [%]	σ_{glob} [%]
1.7	1.9	1.2	3.9
1.7	4.5	1.2	5.9
1.7	11.1	1.2	11.6

Tab. 4.17: Global uncertainties of R_{AA} of $D^{\pm}$ mesons for all three studied centrality classes. There are two sources of global systematic uncertainty: branching ratio (σ_{BR}), number of binary collisions (σ_{Ncoll}), and from fragmentation function of D^0 (σ_{ff}) which are used to calculate the total global uncertainty σ_{glob}.

described below. All the steps are done separately for Run14 and Run16 and the total systematic uncertainty is then obtained by combining values for Run14 and Run16.

The systematic uncertainty from raw yield extraction and from p_T cut variation of the yield ratio is directly propagated from the $D^{\pm}$ measurement. This method was chosen as it gives a conservative estimate of the uncertainty. This systematic uncertainty is plotted in Fig. 4.30 for Run14 and in Fig. 4.31 as red open circles.

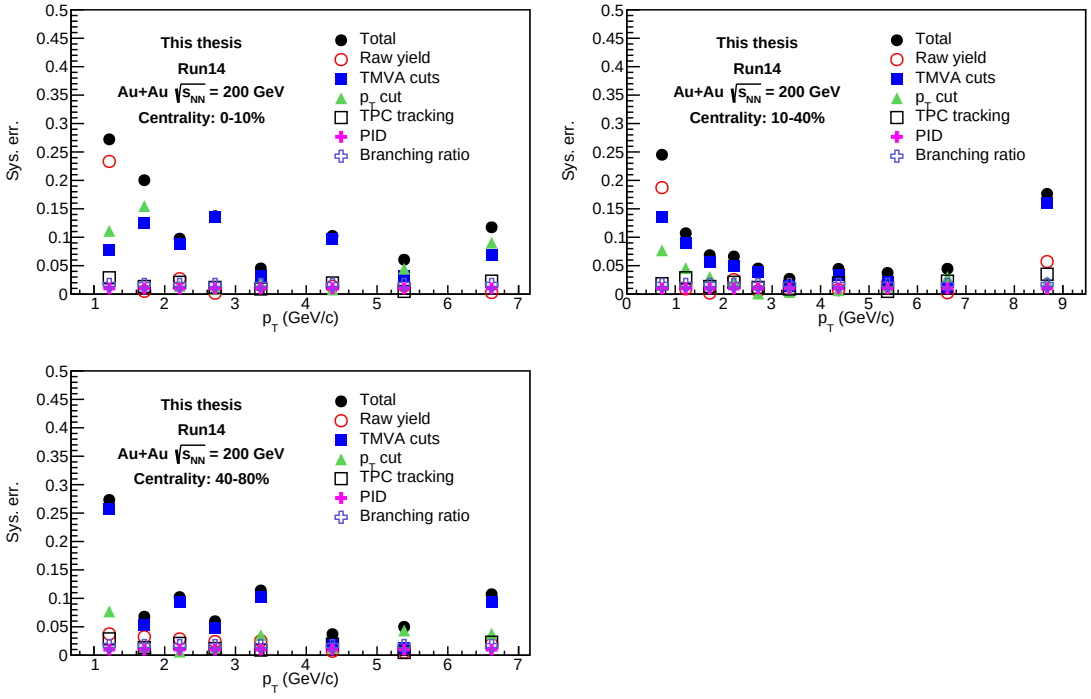

Fig. 4.30: Systematic uncertainties of $D^{\pm}/D^0$ yield ratio as a function of p_T of $D^{\pm}$ mesons in the Run14 data-set. Individual sources of systematic uncertainties are plotted separately, together with the total systematic uncertainty. Each panel corresponds to one centrality bin.

The contribution from variation of the TMVA cuts was done by comparing the $D^{\pm}/D^0$ yield ratio value for analysis set (R_{ana}) of topological selection criteria to the value for

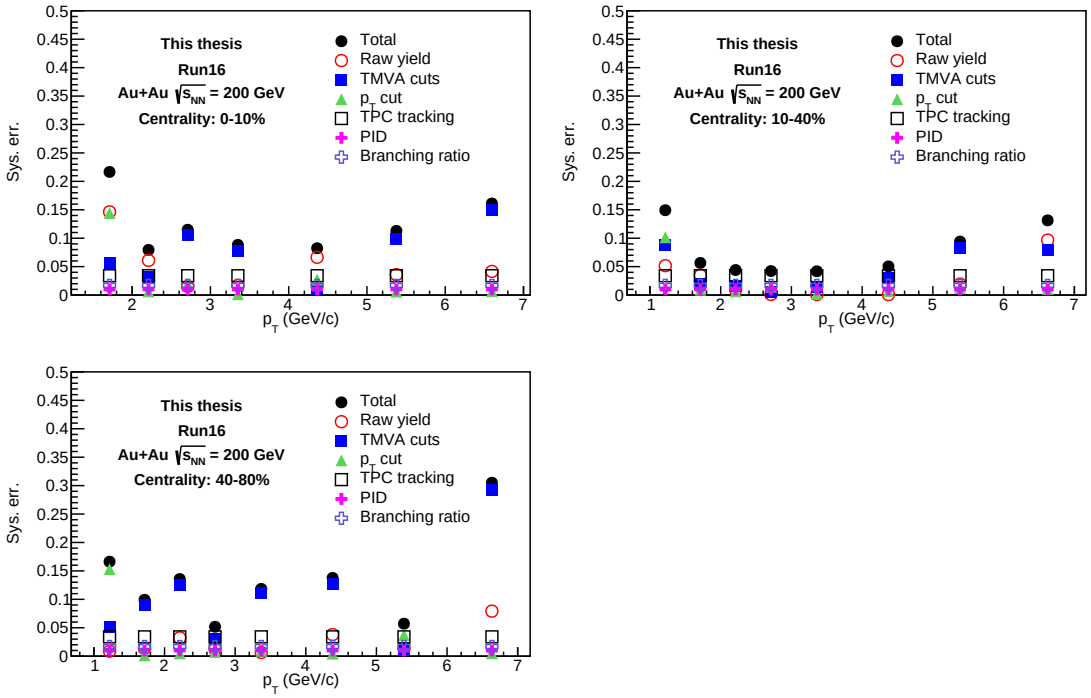

Fig. 4.31: Systematic uncertainties of $D^{\pm}/D^{0}$ yield ratio as a function of p_{T} of $D^{\pm}$ mesons in the Run16 data-set. Individual sources of systematic uncertainties are plotted separately, together with the total systematic uncertainty. Each panel corresponds to one centrality bin.

loose (R_{loose}) and tight (R_{tight}) cuts[3]. Then, the standard procedure is used to determine the systematic uncertainty:

$$\sigma'_{\mathrm{TMVA}} = \frac{|R_{\mathrm{ana}} - R_{\mathrm{loose(tight)}}|}{R_{\mathrm{ana}}}, \tag{4.16}$$

which is subsequently corrected for the statistical precision using a modification of Eq. (4.9). In this case, the statistical uncertainties of the ratios are used. After the correction, the larger of the two values (for loose or tight cuts) is quoted as the final systematic uncertainty σ_{TMVA}. This systematic uncertainty is plotted in Fig. 4.30 for Run14 and in Fig. 4.31 as blue solid squares.

In case of systematic uncertainty of TPC tracking and the PID, the contribution from the D^{0} will get cancelled out with the part of the $D^{\pm}$ contribution. The reason is that D^{0} is reconstructed in two-body decay channel and $D^{\pm}$ in a three-body decay. For that reason, the contributions from kaons and one of the pions will cancel each other out. For that reason, the systematic uncertainty of the ratio coming from TPC tracking and PID can be estimated as $\sigma_{\mathrm{TPC}}/3$ and $\sigma_{\mathrm{PID}}/3$, where σ_{TPC} and σ_{PID} are systematic uncertainties of $D^{\pm}$ invariant spectra defined in Section 4.3.1. These two systematic

[3]All three sets of invariant spectra (analysis, loose, and tight) for both D^{0} and $D^{\pm}$ were used in this study.

uncertainties are plotted in Fig. 4.30 for Run14 and in Fig. 4.31 as black open squares (TPC) and magenta full crosses (PID).

The last contribution to the total systematic uncertainty of the yield ratio comes from the branching ratios of D^0 and $D^{\pm}$ mesons. As mentioned in Section 4.3.1, this uncertainty for $D^{\pm}$ mesons is $\sigma_{BR}(D^{\pm}) = 1.7\,\%$. For D^0, the systematic uncertainty is calculated from the following value of the branching ratio: $BR(D^0) = (3.89 \pm 0.04)\,\%$ which is taken form 2018 PDG [162] and gives a systematic uncertainty of $\sigma_{BR}(D^0) = 1.0\,\%$. The two contributions are combined as a square root of the sum of squares which leads to the total global systematic uncertainty of the ratio from the branching ratios $\sigma_{BR,tot} = 1.97\,\%$. This systematic uncertainty is plotted in Fig. 4.30 for Run14 and in Fig. 4.31 as blue open crosses.

The total systematic uncertainty is calculated as a square root of the sum of squares of all the individual sources and is plotted as black solid circles in Fig. 4.32 and Fig. 4.33. The systematic uncertainty of for the combined Run14+Run16 yield ratio is calculated as a weighted average, where the weights are $1/\sigma^2_{stat}$.

All systematic uncertainties discussed above are for the p_T dependence of the $D^{\pm}/D^0$ yield ratio. In case of the centrality dependence, a few changes are needed. One of the most significant changes is for the systematic uncertainty from raw yield extraction and p_T cut variation. Here, the yield ratio is calculated from the integrated invariant yields in a given p_T range. In order to calculate this systematic uncertainty, the central values of the $D^{\pm}$ points in the p_T spectrum are each randomly shifted within the systematic uncertainty[4]. Then, the integrated yield from this p_T spectrum with shifted points is calculated and divided by the integrated yield of D^0. This is repeated 100 times, which gives 100 different values of the p_T integrated yield ratio R_i. All the "shifted" ratios are then compared to the value calculated with experimental (unshifted) $D^{\pm}$ spectrum (R_{ana}) using the following formula:

$$\sigma_{RawYield,i} = \frac{|R_i - R_{ana}|}{R_{ana}}. \tag{4.17}$$

The largest value is then quoted as the final systematic uncertainty $\sigma_{RawYield}$ and σ_{p_T}. This calculation is performed only in p_T covered by the $D^{\pm}$ data points (i.e. without any extrapolation). The $\sigma_{RawYield}$ is plotted as red open circles and σ_{p_T} is shown as full green triangles in Fig. 4.32 for Run14 and in Fig. 4.33 for Run16.

The approach to calculate the systematic uncertainty of TMVA cuts variation for centrality dependence of the yield ratio is basically the same as for the p_T dependence. The ratio is calculated from integrated invariant yields of $D^{\pm}$ and D^0 mesons for analysis, loose, and tight TMVA cuts. The key difference is that all $D^{\pm}$ spectra are extrapolated

[4]Each point is shifted independently up or down. It is **not** a systematic shift of the whole spectrum up or down.

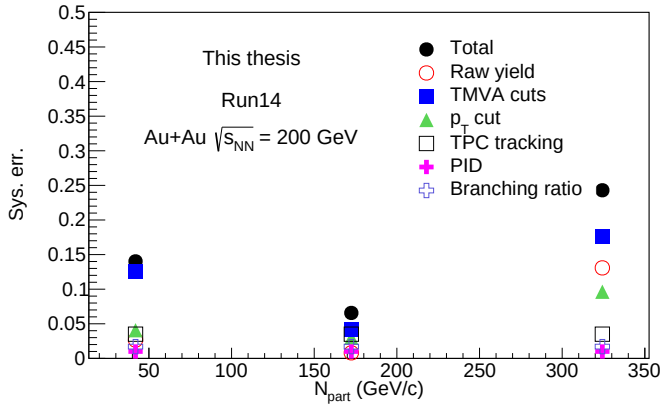

Fig. 4.32: Systematic uncertainties of $D^{\pm}/D^{0}$ yield ratio as a function of N_{part} of $D^{\pm}$ mesons in Run14 data-set. Individual sources of systematic uncertainties are plotted separately, together with the total systematic uncertainty.

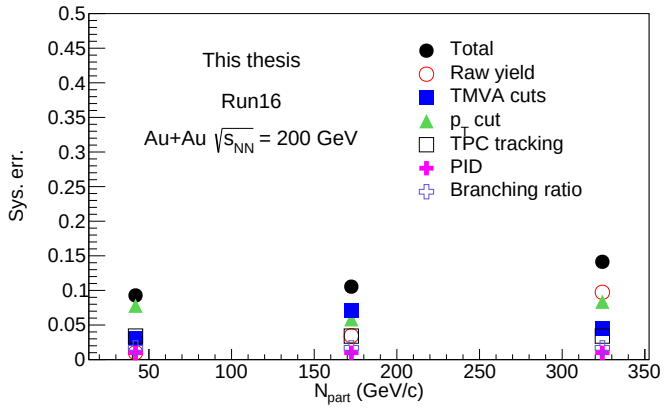

Fig. 4.33: Systematic uncertainties of $D^{\pm}/D^{0}$ yield ratio as a function of N_{part} of $D^{\pm}$ mesons in Run16 data-set. Individual sources of systematic uncertainties are plotted separately, together with the total systematic uncertainty.

to 0 GeV/c and the integrated yields are calculated on region $0 < p_{\mathrm{T}} < 8$ GeV/c. The systematic uncertainty itself is then calculated using formula (4.16), but with ratios calculated from the integrated yields. Again, this value is corrected for statistical precision. The larger of the two values (for loose and tight cuts) is then quoted as the final one. This systematic uncertainty is plotted in Fig. 4.32 for Run14 and in Fig. 4.33 as blue solid squares.

Systematic uncertainties from TPC tracking, PID and branching ratio are directly propagated to the uncertainty of centrality dependence of the ratio at they all do not depend on p_{T}. All three contributions are plotted in Fig. 4.32 for Run14 and in Fig. 4.33, resepctively.

The way the systematic uncertainties were combined for Run14 and Run16 is the same as for the p_{T} dependence, i.e. a square root of the sum of squares of the individual

contributions. The Run14 and Run16 systematic uncertainty is then combined as a weighted average, again with weights which are given as $1/\sigma^2_{\text{stat}}$.

4.4 Results

This section provides a summary of the combined results from the measurement of $D^{\pm}$ mesons in Run14 and Run16 Au+Au collisions $\sqrt{s_{NN}} = 200$ GeV. Each of the following sub-sections describes procedures used to calculate individual observables.

4.4.1 Invariant spectrum of $D^{\pm}$ mesons

The invariant spectra of $D^{\pm}$ mesons in Run16 Au+Au collisions at $\sqrt{s_{NN}} = 200\,\text{GeV}$ are calculated from the raw yields (Y_{raw}) listed in Tabs. 4.9, 4.10, and 4.11 and using reconstruction efficiency ($\varepsilon_{\text{reco}}$) from Fig. 4.25 using the following formula

$$\frac{\mathrm{d}^2N}{2\pi p_{\mathrm{T}}\mathrm{d}p_{\mathrm{T}}\mathrm{d}y} = \frac{Y_{\text{raw}}}{2\pi p_{\mathrm{T}}\Delta p_{\mathrm{T}}\Delta y \cdot BR \cdot \varepsilon_{\text{reco}}}, \tag{4.18}$$

where $BR = (9.38 \pm 0.16)\,\%$ [76] is the branching ratio, Δp_{T} is the bin width, and Δy is the rapidity window. The $D^{\pm}$ mesons were reconstructed in $|y| < 1$ and consequently $\Delta y = 2$.

The Run16 invariant spectrum is subsequently combined with the Run14 spectrum. This is done as a weighted average for each point in p_{T}, where the weights are $w_{\text{Run14}} = 1/\sigma^2_{\text{stat,Run14}}$ and $w_{\text{Run16}} = 1/\sigma^2_{\text{stat,Run16}}$. The statistical uncertainty of the combined spectrum is calculated as follows

$$\sigma_{\text{stat,tot}} = \sqrt{\frac{1}{w_{\text{Run14}} + w_{\text{Run16}}}}. \tag{4.19}$$

The combined invariant spectrum of $D^{\pm}$ mesons is plotted in Fig. 4.34 for three centrality classes of Au+Au collisions. The $10-40\%$ and $40-80\%$ spectra are scaled by a constant for plotting. The data are fitted with the Levy function:

$$\frac{\mathrm{d}^2N}{2\pi p_{\mathrm{T}}\mathrm{d}p_{\mathrm{T}}\mathrm{d}y} = \frac{1}{2\pi}\frac{\mathrm{d}N}{\mathrm{d}y}\frac{(A-1)(A-2)}{AB(AB+m_0(A-2))}\left[1 + \frac{\sqrt{p_{\mathrm{T}}^2+m_0^2}-m_0}{AB}\right]^{-A}, \tag{4.20}$$

where $\mathrm{d}N/\mathrm{d}y$, A and B are free parameters of the fit and m_0 is the rest mass of the $D^{\pm}$ meson. The fits are plotted as dashed lines.

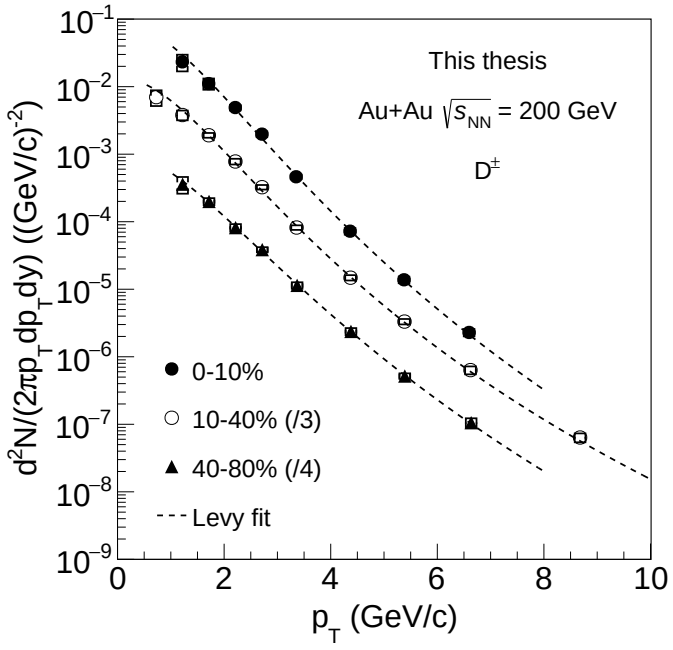

Fig. 4.34: Invariant spectra of $D^{\pm}$ mesons measured in 0-10%, 10-40%, and 40-80% central Au+Au collisions at $\sqrt{s_{\mathrm{NN}}} = 200$ GeV. The data are fitted with tge Levy function.

4.4.2 Nuclear modification factor

The combined invariant spectrum of $D^{\pm}$ mesons described in the previous section is used to calculate the nuclear modification factor R_{AA}, defined using Eq. (1.4). No measurement of $D^{\pm}$ mesons in p+p collisions by STAR is currently available, so the measurement of $c\bar{c}$ cross section in p+p collisions at $\sqrt{s} = 200\,\mathrm{GeV}$ [163] was used instead. The $c\bar{c}$ is first scaled to the invariant yield of D^0 which is achieved by using a scaling factor $f(c \to D^0)/\sigma_{\mathrm{pp}}^{\mathrm{inel}}$, where $f(c \to D^0) = 0.6086$ is the D^0 fragmentation function and $\sigma_{\mathrm{pp}}^{\mathrm{inel}}$ is the total inelastic p+p cross section.

Next, this invariant spectrum of D^0 in p+p is scaled by the $D^{\pm}/D^0$ yield ratio from PYTHIA. As shown in Fig. 4.35, three different PYTHIA versions were chosen based on discussion within the STAR Heavy Flavor Physics Working Group. In general, all three versions use a tune for heavy flavor production at RHIC energies. PYTHA 6.4 Perugia 2012 and PYTHIA 8.1 were both thoroughly tuned on STAR p+p data in order to ensure good description of various observables measured in p+p collisions at STAR (not only heavy favor production, but also jets). The tune for PYTHA 8.2 was a bit simpler, focusing primarily on description of open-charm production in p+p collisions. An average of the three PYTHIA versions from Fig. 4.35 was used for the scaling of the p+p reference. Like this, the $D^{\pm}$ invariant spectrum in p+p collisions is estimated and is used for the R_{AA} calculation. The reason to use this procedure is that in the first step, the $c\bar{c}$ is scaled to D^0 invariant spectrum, which was used as a reference in the published D^0 R_{AA} measurement [2]. In the next step the D^0 invariant spectrum in p+p

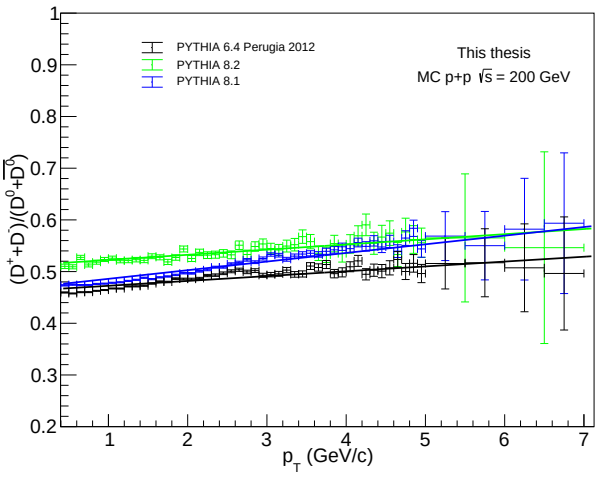

Fig. 4.35: $(D^+ + D^-)/(D^0 + \overline{D^0})$ yield ratio calculated using three different versions of PYTHIA. The data are fitted by a linear function which is then used for scaling of the p+p reference for the R_{AA} and as a reference for the $(D^+ + D^-)/(D^0 + \overline{D^0})$ yield ratio.

collisions is scaled to $D^{\pm}$ invariant spectrum using $D^{\pm}/D^0$ yield ratio from PYTHIA, taking into account difference in shape of $D^{\pm}$ and D^0 p_T spectra. Finally, the mean number of binary collisions $\langle N_{coll} \rangle$ is taken from Tab. 4.2.

The R_{AA} of $D^{\pm}$ mesons is plotted in Fig. 4.36. The data are compared to the D^0 measurement in Au+Au collisions at $\sqrt{s_{NN}} = 200$ GeV from STAR [2] and to $D^{\pm}$ mesons measured by ALICE in $0-10\%$ central Pb+Pb collisions at $\sqrt{s_{NN}} = 5.02$ TeV [117]. All data-sets are in a good agreement and they all show a significant suppression of open-charm mesons in central and mid-central heavy-ion collisions in the high-p_T region.

As expected, the p_T and centrality dependence of the $D^{\pm}$ mesons is essentially the same as for previously measured D^0 mesons. The suppression at high transverse momenta is the largest in central Au+Au collisions and gets weaker when going to mid-central and peripheral collisions. In $40-80\%$ centrality class, there is no suppression observed at high p_T within the uncertainties.

The low p_T D-mesons exhibit a significant suppression as well, but in this case independent of collision centrality. As shown in several STAR open-charm studies [3, 4], this observation can be likely contributed to redistribution of c-quarks among open-charm hadron species due to coalescence hadronization of c-quarks in the QGP.

4.4.3 $D^{\pm}/D^0$ yield ratio

The $(D^+ + D^-)/(D^0 + \overline{D^0})$ yield ratio is calculated as a function of p_T and collision centrality. The p_T dependence calculation is straightforward, as binning in p_T is the same for $D^{\pm}$ and D^0 meson invariant spectra. The ratio can be therefore calculated directly from central values of $D^{\pm}$ and D^0 spectra. The result is shown in Fig. 4.37

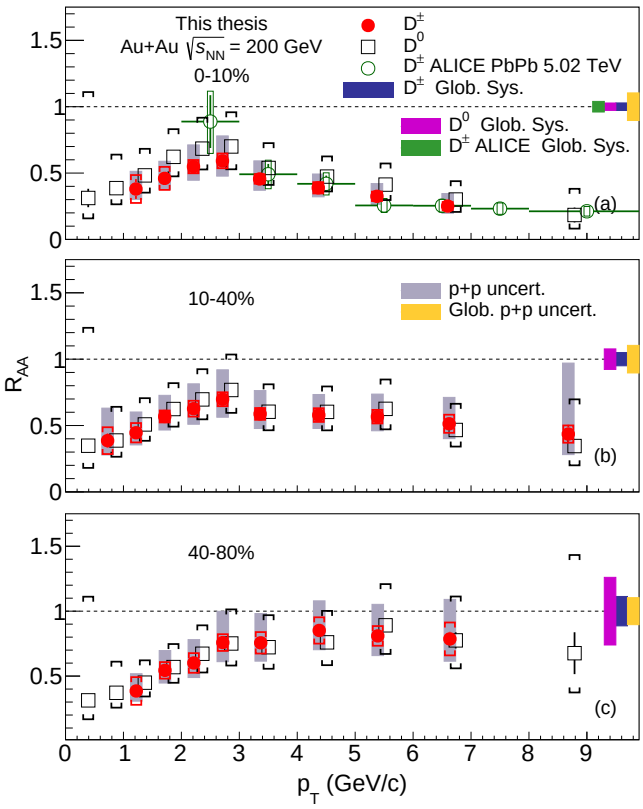

Fig. 4.36: R_{AA} of D^0 [2] and $\mathrm{D}^{\pm}$ mesons measured in 0-10%, 10-40%, and 40-80% central Au+Au collisions at $\sqrt{s_{\mathrm{NN}}} = 200$ GeV as measured by STAR. Measurement of $\mathrm{D}^{\pm}$ mesons in Pb+Pb collisions at $\sqrt{s_{\mathrm{NN}}} = 5.02$ TeV by ALICE experiment is shown for comparison [117].

together with two PYTHIA calculations for p+p at $\sqrt{s} = 200\,\mathrm{GeV}$ and for the ALICE measurement in $0-10\%$ central Pb+Pb collisions at $\sqrt{s_{\mathrm{NN}}} = 5.02\,\mathrm{TeV}$.

The STAR measurement is in a reasonable agreement with the PYTHIA calculations. The ratio in Au+Au at $\sqrt{s_{\mathrm{NN}}} = 200\,\mathrm{GeV}$ collisions seems to have a weak dependence on p_{T} and its value is the same as predicted for p+p collisions at the same energy. This indicates, that there is no significant modification of the $\mathrm{D}^{\pm}/\mathrm{D}^0$ yield ratio in Au+Au collisions with respect to p+p collisions.

The general approach to the calculation of the centrality dependence of the yield ratio is to calculate integrated invariant yields of $\mathrm{D}^{\pm}$ and D^0 mesons in a given p_{T} range and then divide those integrated yields. The integral can be calculated simply by adding the central values of the points in the p_{T} spectra together. For that reason, the centrality dependent yield ratio was calculated for D mesons with $1 < p_{\mathrm{T}} < 8\,\mathrm{GeV}/c$, as shown in Fig. 4.38. The STAR data are compared to data from several other experiments, covering various collision systems and energies. Overall, all the experimental data are consistent with each other, within the uncertainties. The solid line represents an average value from all the plotted data points and was obtained as a constant fit to the data. The

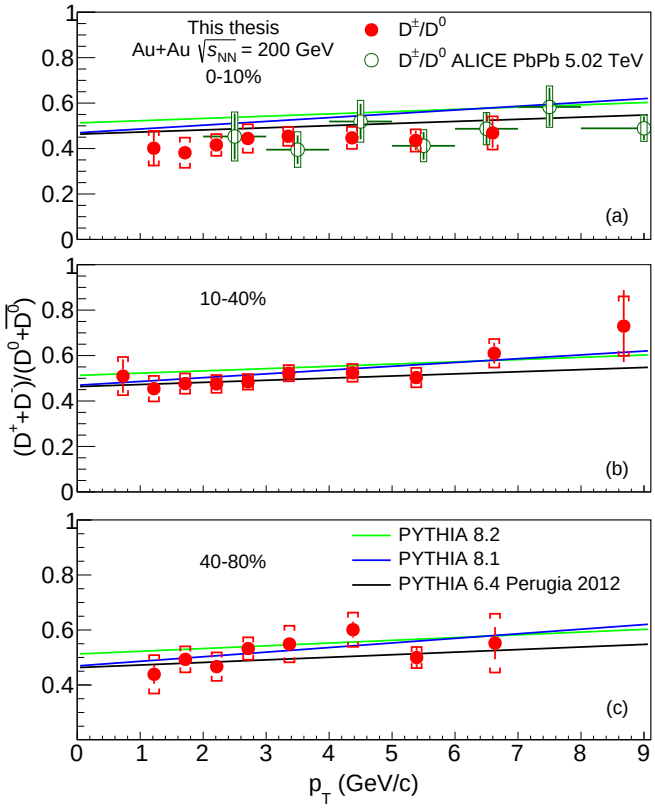

Fig. 4.37: $(D^+ + D^-)/(D^0 + \overline{D^0})$ yield ratio as a function of p_T measured in 0-10%, 10-40%, and 40-80% central Au+Au collisions at $\sqrt{s_{NN}} = 200$ GeV. Theoretical PYTHIA calculations for p+p collisions at $\sqrt{s} = 200$ GeV and a measurement of $D^{\pm}$ mesons in Pb+Pb collisions at $\sqrt{s_{NN}} = 5.02$ TeV by the ALICE experiment is shown for comparison [117].

dashed lines represent 1σ uncertainty band given by the uncertainty of the fit parameter. For the fit, the statistical and systematic uncertainties for each individual result were combined together in order to get the total uncertainty of the fit.

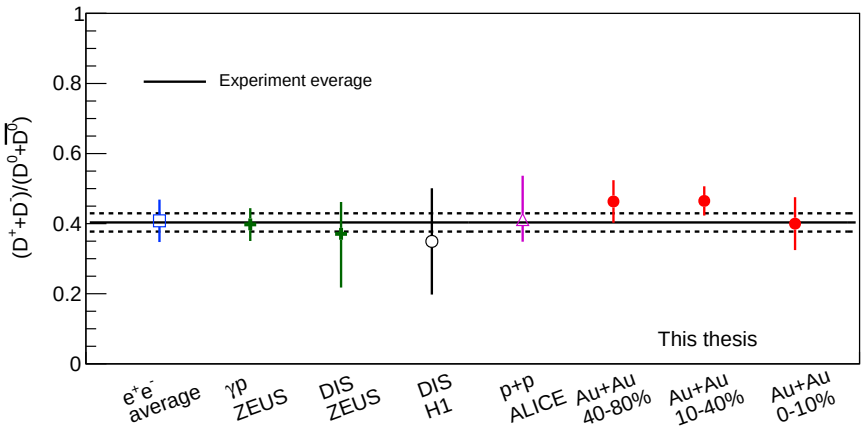

Fig. 4.38: $(D^+ + D^-)/(D^0 + \overline{D^0})$ yield ratio as a function of centrality of Au+Au collisions at $\sqrt{s_{NN}} = 200$ GeV. The data are compared to measurements from HERA, e^+e^- collisions [164], and to the ALICE data from p+p collisions at $\sqrt{s} = 5.02$ TeV [165].

4.4.4 Total charm cross section

The invariant yield of $D^\pm$ mesons has been used together with spectra of D^0 and $D_s^\pm$ mesons, and $\Lambda_c^\pm$ baryons to calculate the total charm hadron production cross section per nucleon pair in 10-40% central Au+Au collisions at $\sqrt{s_{NN}} = 200$ GeV. The p_T interval used for all the mentioned open-charm hadron species is $0 < p_T < 8\,\mathrm{GeV}/c$. Only spectra of D^0 mesons cover this p_T with experimental data [2]. The other three spectra had to be therefore extrapolated. This was done using a set of appropriate theoretical predictions. In case of $D_s^\pm$ mesons and $\Lambda_c^\pm$ baryons, theoretical models shown in the Refs. [3, 4] which describe the data well were used. In case of $D^\pm$ mesons, the p_T shape of the $D^\pm$ meson spectrum from three versions of PYTHIA was fitted to the measured Au+Au spectrum and subsequently used for the extrapolation. Difference between the cross section calculated the different modes, or versions of PYTHIA then contributes to the quoted systematic uncertainty. It is important to note, that all of the aforementioned calculations were done by one of members of STAR Heavy Flavor Physics Working Group and not by me. It is still important to explain the procedure in order to properly discuss the results.

The extracted total cross sections and the cross sections of the individual open-charm hadrons in 10-40% central Au+Au collisions at $\sqrt{s_{NN}} = 200$ GeV is shown in Tab. 4.18 and compared to the value measured in p+p collisions at $\sqrt{s} = 200$ GeV. The invariant spectra of D^0 [2], $D^\pm$ (this analysis), and $D_s^\pm$ [3] mesons, and $\Lambda_c^\pm$ baryons [4] measured in 10-40% central Au+Au collisions at $\sqrt{s_{NN}} = 200$ GeV have been used. The p+p reference was calculated using the $c\bar{c}$ cross section from Ref. [163]. The total cross section measured in Au+Au collisions is consistent with that measured in p+p collisions, within the uncertainties. This observation suggests, that the charm quark

Collision system	Hadron	$d\sigma/dy$ [μb]
Au+Au at 200 GeV Centrality: 10-40%	D^0	$39.0 \pm 0.6(\text{stat}) \pm 1.1(\text{sys})$
	$D^{\pm}$	$19.2 \pm 0.9(\text{stat}) \pm 3.1(\text{sys})$
	D_s	$15.4 \pm 1.7(\text{stat}) \pm 3.6(\text{sys})$
	Λ_c	$39.7 \pm 5.8(\text{stat}) \pm 26.7(\text{sys})$
	Total:	$113.3 \pm 6.2(\text{stat}) \pm 27.2(\text{sys})$
p+p at 200 GeV	Total:	$130 \pm 30(\text{stat}) \pm 26(\text{sys})$

Tab. 4.18: Total open charm hadron production cross section per binary collision as measured in 10-40% central Au+Au collisions at $\sqrt{s_{NN}} = 200$ GeV and in p+p collisions at $\sqrt{s} = 200$ GeV. The invariant spectra of D^0 [2], $D^{\pm}$ (this analysis), and $D_s^{\pm}$ [3] mesons, and $\Lambda_c^{\pm}$ baryons [4] measured in 10-40% central Au+Au collisions at $\sqrt{s_{NN}} = 200$ GeV have been used. The p+p reference was calculated using $c\bar{c}$ cross section from Ref. [163].

production cross section per nucleon pair follows number of binary collisions scaling. The cross sections of the individual open-charm hadron species, on the other hand, are significantly modified in Au+Au compared to p+p collisions due to coalescence hadronization of charm quarks in the QGP, which leads to re-distribution of charm quarks among the open-charm hadron species.

Summary and discussion

The STAR experiment has extensively studied production of open-charm hadrons in Au+Au collisions at $\sqrt{s_{\mathrm{NN}}} = 200\,\mathrm{GeV}$. Until now, STAR has measured invariant yields of D^0 [2], $\mathrm{D}_\mathrm{s}^\pm$ [3] mesons, and $\Lambda_\mathrm{c}^\pm$ [4] baryons. The only remaining ground state open-charm hadrons which remained to be measured were the $\mathrm{D}^\pm$ mesons. This thesis provides a description of analysis of the $\mathrm{D}^\pm$ mesons measured in Au+Au collisions at $\sqrt{s_{\mathrm{NN}}} = 200\,\mathrm{GeV}$ by STAR in the year 2016.

The analysis described in Chapter 4 was done from the very very beginning by me, if not stated othrwise. The first step of the analysis was extraction of $\mathrm{D}^\pm$ signal, which involved TMVA optimization of topological selection criteria. The candidates for $\mathrm{D}^\pm$ signal were extracted from centrally produced PicoDst files, which already included some basic event selection criteria. The $\mathrm{D}^\pm$ mesons were reconstructed via a hadronic decay $\mathrm{D}^\pm \to \mathrm{K}^\mp\pi^\pm\pi^\pm$, from invariant mass spectra of the $\mathrm{K}\pi\pi$ triplets. The raw yield extracted this way has to be corrected for geometrical acceptance and reconstruction efficiency of the STAR detector. This was done using a data-driven fast simulator, which was developed at STAR for open-charm hadron measurements with the HFT. In this analysis, the EvtGen particle generator has been employed to generate decays of $\mathrm{D}^\pm$ mesons with pre-set kinematics. The information about the decay daughters is then smeared using information from data and TPC embedding[5].

The calculated total reconstruction efficiency was then used to calculate the invariant yields of $\mathrm{D}^\pm$ mesons in 0-10%, 10-40%, and 40-80% central Au+Au collisions at $\sqrt{s_{\mathrm{NN}}} = 200\,\mathrm{GeV}$ measured by STAR in the year 2016. The 2016 invariant yields were subsequently combined with those measured in the 2014 data-set. The combined $\mathrm{D}^\pm$ meson invariant yield was then used to calculate the R_{AA} as a function of p_{T}, the $\mathrm{D}^\pm/\mathrm{D}^0$ yield ratio as a function of p_{T} and collision centrality, and most importantly for calculation of the total charm production cross section in Au+Au collisions at $\sqrt{s_{\mathrm{NN}}} = 200\,\mathrm{GeV}$. Results of this analysis are currently being reviewed by the STAR Collaboration for publication in Physics Letters B journal.

One of the most important aspects of the measured $\mathrm{D}^\pm$ invariant spectrum is that

[5]TPC embedding is a centrally produced simulation used to evaluate performance of the STAR TPC. For more information about the fast simulation inputs, see Sec. 4.2.1.

it was obtained using topological reconstruction of a three-body hadronic decay of the $D^{\pm}$ mesons. That was not possible at STAR until installation of the HFT which allows substantial suppression of combinatorial background by constraining the decay topology using a set of TMVA optimized topological selection criteria. As a result, a good statistical precision (raw yield significance larger than 3) can be achieved from as low as $p_{\mathrm{T}} > 0.5\,\mathrm{GeV}/c$, up to $p_{\mathrm{T}} < 10\,\mathrm{GeV}/c$. Compared to D^0 mesons, which were reconstructed via a two-body hadronic decay, it is not as easily possible to access the lowest transverse momenta for $D^{\pm}$ mesons, as the combinatorial background levels for three body decays rise very quickly toward $p_{\mathrm{T}} \to 0\,\mathrm{GeV}/c$. This is given by the fact, that most of the background in this p_{T} region comes from thermally produced hadrons ($\pi^{\pm}$ and $K^{\pm}$ in this case), which have exponential p_{T} spectra. This will lead to enormous number of random $K\pi\pi$ combinations (with the correct charge combinations and invariant mass close to that of $D^{\pm}$ meson) which will completely hide any $D^{\pm}$ signal. At high transverse momenta, the challenge is somewhat opposite. From open-charm hadron measurements in p+p collisions, or from theoretical calculations, e.g. using the FONLL calculation [87–89], we know that open-charm hadron spectra are steeply falling with rising p_{T}. The low abundance of $D^{\pm}$ mesons, combined with detector efficiency make it challenging to obtain a significant signal at high transverse momenta. For that reason, the precise pointing resolution enabled by the HFT, together with the TMVA topological selection criteria optimization is vital part of all recent open-charm hadron production studies at STAR. In case of $D^{\pm}$ mesons, it was possible to achieve p_{T} coverage which is close to that of D^0 mesons.

As shown in Sec. 4.3, there are multiple sources of systematic uncertainties of the invariant $D^{\pm}$ yield. The dominant systematic uncertainty source depends on specific collision centrality class and p_{T} bin. The systematic uncertainty sources can be divided into two general classes. The first one is for systematic uncertainties that are calculated separately for individual p_{T} bins. These uncertainties are in general reasonably small in all p_{T} bins except for the lowest and highest p_{T}. This is expected, as in this "mid-p_{T}" interval, the combinatorial levels are under good control thanks to the optimized topological selection of the $D^{\pm}$ candidates and, at the same time, the number of $D^{\pm}$ candidates is sufficient to observe a clear peak in the invariant mass spectrum of the $K\pi\pi$ triplets. As a result, changing the TMVA selection criteria, or the daughter p_{T} cut will not significantly affect the calculated invariant yield, and the raw yield extraction will be reliable thanks to well defined invariant mass peak. The variation of the daughter p_{T} cut has the largest influence in the first p_{T} bin, it is more likely that at least one of the decay daughters of a low-p_{T} $D^{\pm}$ will fall below the varied p_{T} cut. The variation of TMVA selection criteria and the raw yield extraction play role in both the first and last p_{T} bins. At low-p_{T} this is again given by high combinatorial background levels and their large changes with variation of topological selection criteria. At high p_{T}, it

is again due to small abundance of $D^{\pm}$, combined with the reconstruction efficiency. The second class of uncertainties are those, which are the same for all p_T bins and independent of centrality. The TPC tracking and PID systematic uncertainty turned out to be constant in p_T for both $\pi^{\pm}$ and $K^{\pm}$ and could be treated as a global systematic uncertainty. The single-particle values of both systematic uncertainties are consistent with previous STAR analyses[6]. The last uncertainty is that from the branching ratio which is simply propagated from the uncertainty of the BR value used in his analysis, which was taken from Ref. [76]. Despite all the challenges, the systematic uncertainties of the $D^{\pm}$ invariant spectrum are under good control.

The good precision of the invariant $D^{\pm}$ yields allowed to calculate the R_{AA} of $D^{\pm}$ mesons in the full measured p_T range and in all three studied collision centrality classes. The measured suppression of $D^{\pm}$ mesons in Au+Au collisions is of the same magnitude as that of D^0 mesons, which confirms the observations and physics conclusions of the D^0 measurement. The $D^{\pm}$ measurement is therefore compatible with energy loss of charm quarks in the QGP for $p_T > 3\,GeV/c$ and with suppression at low transverse momenta due to re-distribution of charm quarks among open-charm hadron species due to coalescence hadronization of charm quarks.

The systematic uncertainties of the R_{AA} originating from the $D^{\pm}$ measurement are the same as for the $D^{\pm}$ invariant yields. There are two additional systematic uncertainty sources which both contribute to the global systematic uncertainty. The first one is the uncertainty of D^0 fragmentation function[7] and from uncertainty of $\langle N_{coll} \rangle$ in given collision centrality. Another source of systematic uncertainty of the $D^{\pm}$ R_{AA} originates from the p+p reference. This is the dominating systematic uncertainty in both $D^{\pm}$ and D^0 R_{AA} measurements, as the only currently available reference is the combined measurement of D^0 and $D^{\star}$ in p+p collisions at $\sqrt{s} = 200\,GeV$. At that time, the HFT was not available yet which limited the statistical and systematic precision of the measurement. The p+p reference could be improved by using p+p collision $\sqrt{s} = 200\,GeV$ data-sets collected by STAR in years 2012 and 2015. Neither of these data-sets has usable HFT information therefore it would not be possible to obtain $D^{\pm}$ reference directly, but the large combined statistics available in 2009, 2012, and 2015 data-sets would improve the statistical and systematic precision of the existing p+p reference which uses of D^0 and $D^{\star}$ meson measurement.

The $D^{\pm}$ invariant spectra were also directly compared to those of D^0 mesons via $(D^+ + D^-)/(D^0 + \overline{D^0})$ yield ratio. In 10-40% and 40-80% central Au+Au collisions, the

[6]The PID systematic uncertainty was actually taken from other open-charm analyses. This is a standard procedure at STAR, as certain single particle detector performance can shared by many analyses. In case of PID, it is justified, as the PID selection criteria were the same for many of the open-charm analyses.

[7]The p+p reference has been fist scaled to D^0 invariant yield and then re-scaled to $D^{\pm}$ using $(D^+ + D^-)/(D^0 + \overline{D^0})$ yield ratio from PYTHIA.

PYTHIA model calculation is consistent with the measured yield ratio. In 0-10% there is a hint of systematic shift, $D^{\pm}$ mesons being slightly suppressed compared to D^0 mesons, but the shift is not significant within combined statistical and systematic uncertainty. The measured $(D^+ + D^-)/(D^0 + \overline{D^0})$ yield ratio is measured to be unmodified in Au+Au collisions at $\sqrt{s_{\rm NN}} = 200\,\text{GeV}$ compared to PYTHIA prediction for p+p collisions at $\sqrt{s} = 200\,\text{GeV}$. This observation is further supported by a good agreement of the STAR $p_{\rm T}$-integrated Au+Au measurement of the yield ration with results from other experiments. This observation provides more details about charm quark energy loss and hadronization, suggesting that production of both $D^{\pm}$ and D^0 mesons is modified the same way in heavy-ion collisions.

The systematic uncertainty sources for the $(D^+ + D^-)/(D^0 + \overline{D^0})$ are similar to those of the $D^{\pm}$ invariant yields, but there are several key differences. Firstly, it is important to note that the contribution from Run14 and Run16 data-sets was calculated independently, in order to capture any differences between the two data sets. The two contributions were then combined the same way as in case of the invariant yield systematic uncertainties, i.e. as a weighted average, where the weights are $1/\sigma^2_{\rm stat}$. Another important thing is that the systematic uncertainty from TMVA cuts variation was calculated directly using invariant yields of $D^{\pm}$ and D^0 for loose, tight and analysis sets of TMVA optimized topological selection criteria. The calculation was done independently for the Run14 and Run16 $D^{\pm}$ invariant spectra. This way, any potential correlations between the systematic uncertainties from variation of TMVA topological selection criteria of $D^{\pm}$ and D^0 were taken into account. Second important difference is that the systematic uncertainty from the branching ratio has contribution from both $D^{\pm}$ and D^0. As the uncertainty of branching ratio of D^0 mesons is small (1%), it is not large contribution to the total systematic uncertainty. Remaining systematic uncertainties were propagated directly from the invariant yields of $D^{\pm}$ in given sub-data-set (Run14 and Run16).

Probably the most important physics result the $D^{\pm}$ meson invariant yields were used for is the total charm quark production cross section per nucleon-nucleon collision in 10-40% central Au+Au collisions at $\sqrt{s_{\rm NN}} = 200\,\text{GeV}$. The cross section was calculated measured invariant yields of D^0, $D^{\pm}$, and $D_s^{\pm}$ mesons and $\Lambda_c^{\pm}$ baryons[8]. The measured value of $113.3 \pm 6.2(\text{stat}) \pm 27.2(\text{sys})\,\mu\text{b}$ is consistent with that measured in p+p collisions at the same energy: $130 \pm 30 \pm 26\,\mu\text{b}$. The overall precision of the Au+Au measurement is much better than that of in p+p collisions, which is a result of precise topological reconstruction of hadronic decays of the studied open-charm hadrons. As can be seen in Tab. 4.18, both the statistical and systematic uncertainties of the Au+Au measurement are dominated by those from the $\Lambda_c^{\pm}$ measurement, as it is the most experimentally challenging of the four, due to combination of relatively small fragmentation ratio $c \to \Lambda_c^{\pm}$, small decay length and used decay channel. Despite these challenges, the $\Lambda_c^{\pm}$ has

[8]The $\Lambda_c^{\pm}$ was calculated from the $(\Lambda_c^+ + \Lambda_c^-)/(D^0 + \overline{D^0})$ yield ratio.

unprecedented precision and coverage in p_T and collision centrality. Overall, the STAR charm quark production cross section in Au+Au collisions has an excellent statistical precision. The systematic uncertainty has a reasonable value and is dominated primarily by uncertainties originating from extrapolation of the $D^{\pm}$, and $D_s^{\pm}$ meson and $\Lambda_c^{\pm}$ baryon invariant yields to $p_T \to 0\,GeV/c$.

To conclude, the $D^{\pm}$ measurement presented in this thesis is a vital contribution to open-charm hadron production studies in Au+Au collisions at $\sqrt{s_{NN}} = 200\,GeV$ by the STAR experiment. All of the STAR open-charm results from Au+Au collisions have excellent statistical and systematic precision and provide detailed insight into charm quark energy loss and charm quark hadronization process inside the QGP. Main possible improvement for all of the STAR measurements would be a better p+p reference for the R_{AA} calculation. As suggested above, one possible way would be combining all available p+p at $\sqrt{s} = 200\,GeV$ data-sets measured by STAR. As none of the data-sets has useful HFT information available, this method would most likely provide a combined D^0 and $D^{\star}$ invariant yield with higher precision. An alternative way is to obtain invariant yields of D^0, $D^{\pm}$, and $D_s^{\pm}$ mesons and $\Lambda_c^{\pm}$ baryons in p+p collisions independently which should be possible using the sPHENIX experiment which is scheduled to start taking data at RHIC in year 2023 [166]. In order to have a full understanding of open-charm hadron production, it is also important to compare the STAR (RHIC) results to those measured at the LHC in Pb+Pb collisions. The leading experiment at the LHC in open-charm production studies is the ALICE experiment. At the moment ALICE has reasonably precise invariant spectra of various D meson species both at $\sqrt{s_{NN}} = 2.76\,TeV$ and $\sqrt{s_{NN}} = 5.02\,TeV$, but the spatial resolution of the ALICE silicon tracker, the ITS, did not allow to probe the lowest p_T region (ca. $p_T < 2\,GeV/c$), or to measure spectra $\Lambda_c^{\pm}$ baryons as a function of p_T and collision centrality. This is about to change with current updates to the ALICE detector, which include for example much better ITS, which should provide sufficient vertex resolution needed for reconstruction of low-p_T D mesons, or for measurement spectra $\Lambda_c^{\pm}$ baryons. This version of the ALICE detector is currently being commissioned and will start taking experimental data soon. There are also plans for more upgrades of the ALICE detector, which is supposed to rely heavily on MAPS based silicon trackers, instead of using the TPC [167]. This should improve the spatial resolution even more, allowing e.g. reconstruction multi-charmed baryons which will provide much more complete picture of production of open-charmed hadrons at the LHC.

Appendices

Appendix A

Data-set quality assurance

Before the main analysis, it was necessary to perform a QA of the Run16 Au+Au at $\sqrt{s_{\mathrm{NN}}} = 200\,\mathrm{GeV}$ data-set. The main goal of the QA was to create a list of "bad runs", which e.g. have missing or bad detector information and thus are not worth analyzing. After discussion within STAR Heavy Flavor Physics Working Group three parameters/observables were chosen for evaluation of individual runs.

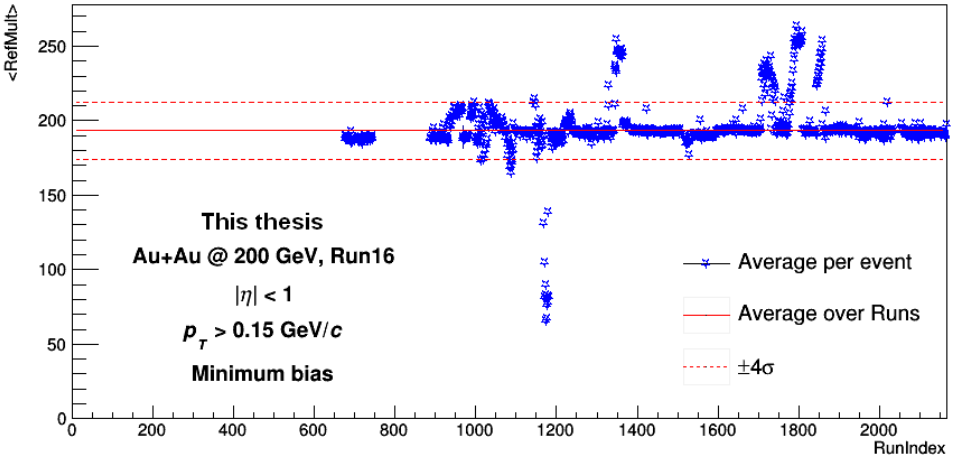

Fig. A.1: Mean multiplicity of charged particles measured by the STAR TPC ($\langle RefMult \rangle$) per event in Run16 Au+Au at $\sqrt{s_{\mathrm{NN}}} = 200\,\mathrm{GeV}$ data-set. Each point represents the average value in a single run. The solid red line is fit to the data points, the dashed lines indicate $\pm 4\sigma$ band. Any runs outside of the indicated band were marked as bad.

The first parameter which was examined is the mean multiplicity of charged particles measured by the STAR TPC ($\langle RefMult \rangle$) per event. The reason is that $RefMult$ plays key role in collision centrality determination and any events or runs which significantly deviate from average, or expected, behavior may cause issues with division of the data-

set into collision centrality classes. Figure A.1 shows the $\langle RefMult \rangle$ per event in Run16 Au+Au at $\sqrt{s_{\mathrm{NN}}} = 200\,\mathrm{GeV}$ data-set. Each point represents the mean mesured in a single run. The solid red line is fit to the data points, the dashed lines indicate $\pm 4\sigma$ band. Any runs outside of the indicated band were marked as bad. Before marking all those runs as bad, the individual $RefMult$ distributions were checked and compared to the same distribution from a good run. All the $RefMult$ distributions from runs which were marked as bad significantly deviated from expected behavior and were therefore removed from the analysis in order to prevent problems with centrality determination.

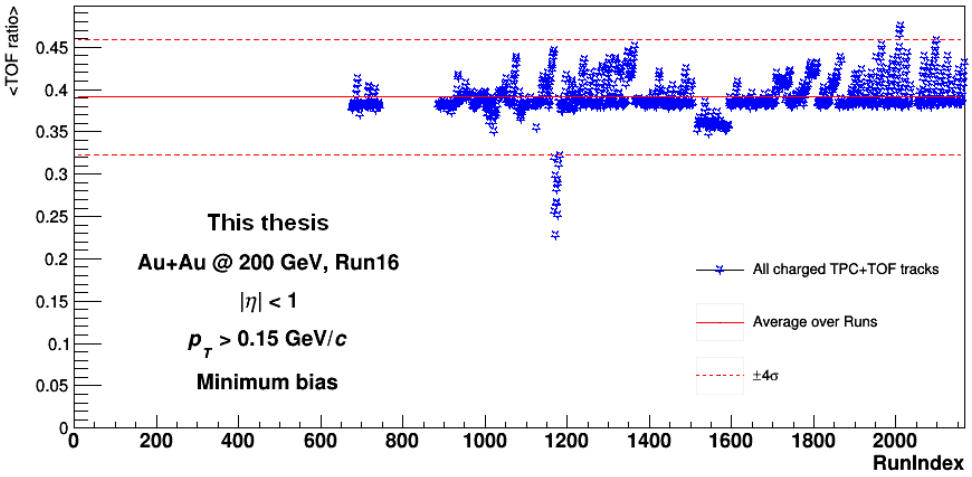

Fig. A.2: Mean TOF matching ratio per run $\langle \mathrm{TOFratio} \rangle$ of charged particles in Run16 Au+Au at $\sqrt{s_{\mathrm{NN}}} = 200\,\mathrm{GeV}$ data-set. The solid red line is fit to the data points, the dashed lines indicate $\pm 4\sigma$ band. Any runs outside of the indicated band were marked as bad.

The other two observables which were used are the mean TOF matching ratio per run $\langle \mathrm{TOFratio} \rangle$ and the mean HFT matching ratio per run $\langle \mathrm{HFTratio} \rangle$. The $\langle \mathrm{TOFratio} \rangle$ of charged tracks in Run16 Au+Au at $\sqrt{s_{\mathrm{NN}}} = 200\,\mathrm{GeV}$ data-set is shown in Fig. A.2 and the $\langle \mathrm{HFTratio} \rangle$ is shown in Fig. A.3. The three panels in the HFT plot are for different p_{T} intervals of the charged particles. As in case of $\langle RefMult \rangle$, all runs which are outside of the $\pm 4\sigma$ band were added to the bad run list. Low matching ratio of HFT or TOF generally indicates, that the performance of the STAR detector, or the RHIC was poor at that period and it would not be efficient to analyze those data, as the reconstruction efficiency of $\mathrm{D}^{\pm}$ mesons in such runs would be very low compared to good runs.

Overall, a run was marked as bad when at least one of the criteria described above has been met. Using this procedure, 132 runs containing about 93M events have been rejected from the analysis. In addition, runs from the beginning of Run16 have been rejected as well (large gaps in Figs. A.1, A.2, and A.3). These runs were marked as bad

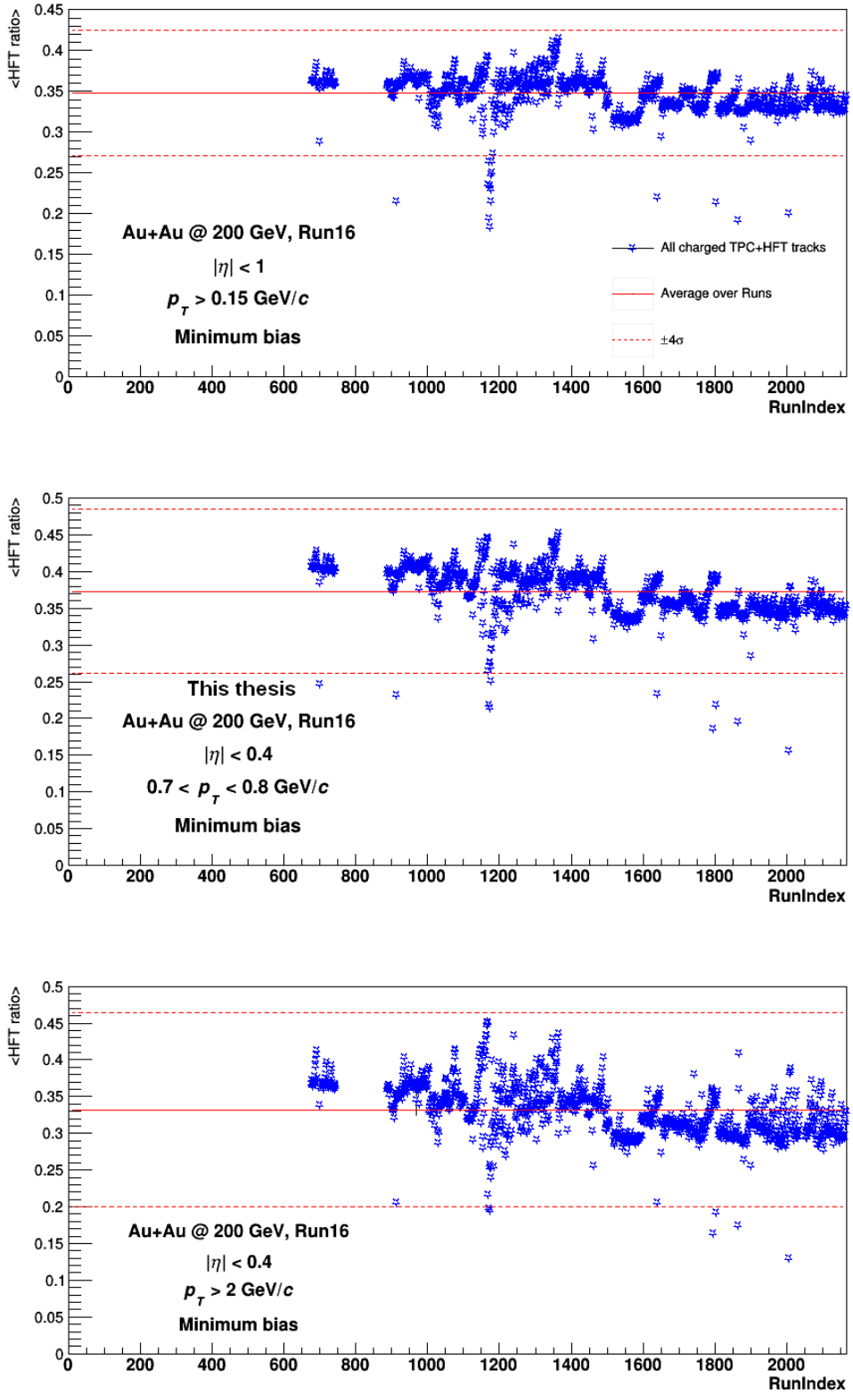

Fig. A.3: Mean HFT matching ratio per run ⟨HFTratio⟩ of charged particles in Run16 Au+Au at $\sqrt{s_{\mathrm{NN}}} = 200\,\mathrm{GeV}$ data-set. The solid red line is fit to the data points, the dashed lines indicate $\pm 4\sigma$ band. The upper panel is for all charged tracks with $p_{\mathrm{T}} > 0.15\,\mathrm{GeV}/c$, the middle panel for tracks with $0.7 < p_{\mathrm{T}} < 0.8\,\mathrm{GeV}/c$, and the bottom panel for tracks with $p_{\mathrm{T}} > 2\,\mathrm{GeV}/c$. Any runs outside of the indicated band were marked as bad.

due to issues with firmware of the HFT. These runs were rejected by all HFT analyses which used Run16 data-set. As can be seen in Fig. 4.2, the total number of events rejected based on bad run list from this QA and the list of runs with bad HFT firmware is about 400M out of 2B minimum bias Au+Au events available in Run16 data-set.

Appendix B

Invariant mass spectra

This appendix contains a summary of invariant mass spectra of the K$\pi\pi$ triplets used for recontruction of the $D^{\pm}$ mesons. Only p_T bins with significance of the raw yield greater than three are shown. The left plots show the correct-sign spectra (blue circles) and properly scaled wrong-sign spectra (red circles). The wrong-sign spectrum is used to estimate the background by fitting it by a linear function. The correct-sign spectra are subsequently fitted with Gauss+linear function, where the parameters of the linear part are fixed by the aforementioned fit of the combinatorial background.

The plots on the right are the correct-sign spectra after subtraction of the wrong-sign spectra. The Gaussian function plotted in these figures if from the fit described above. These figures, without the background, serve as a cross-check of the fit.

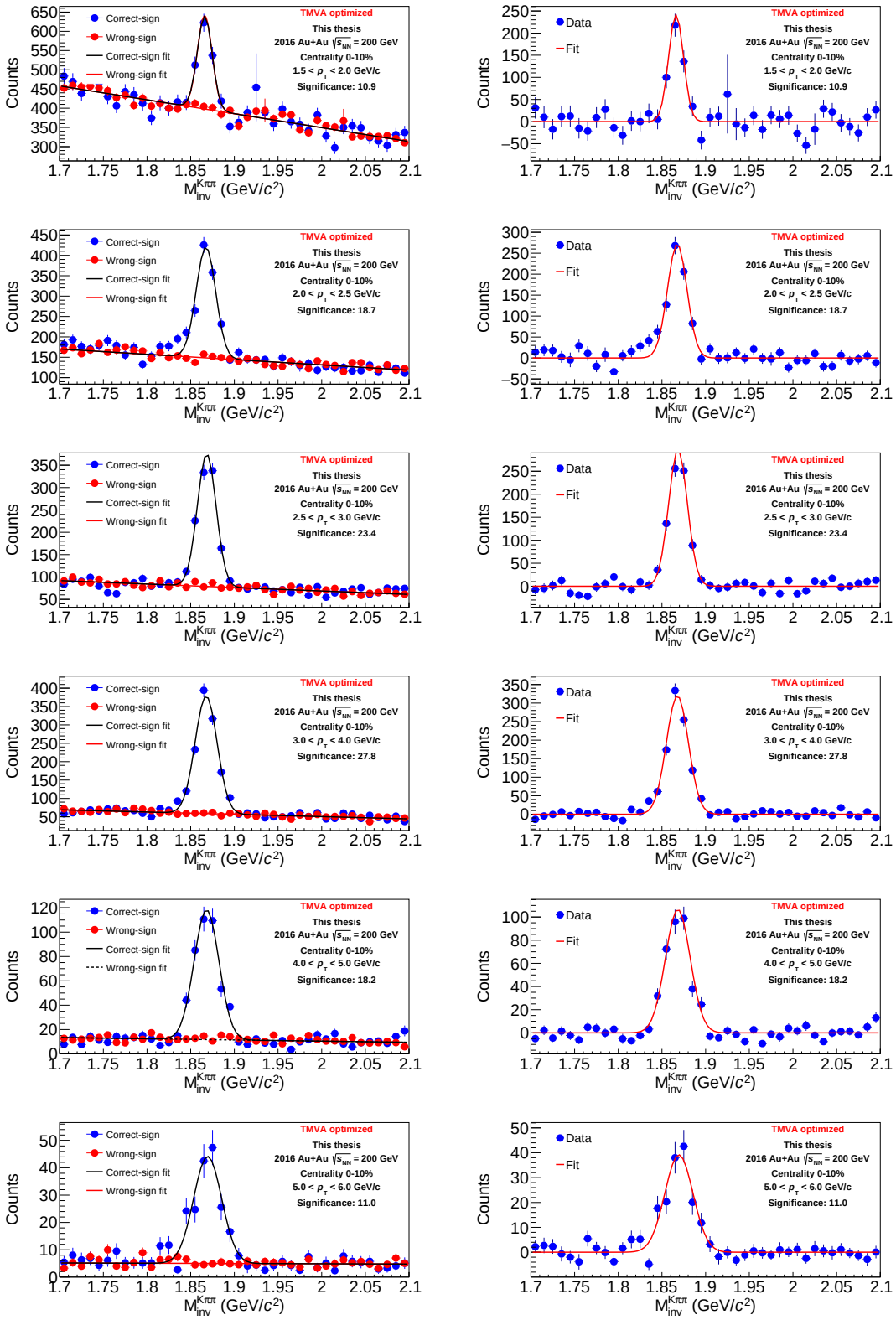

Fig. B.1: Invariant mass spectra of the Kππ triplets for 0-10% central Au+Au collisions for each significant p_T bin.

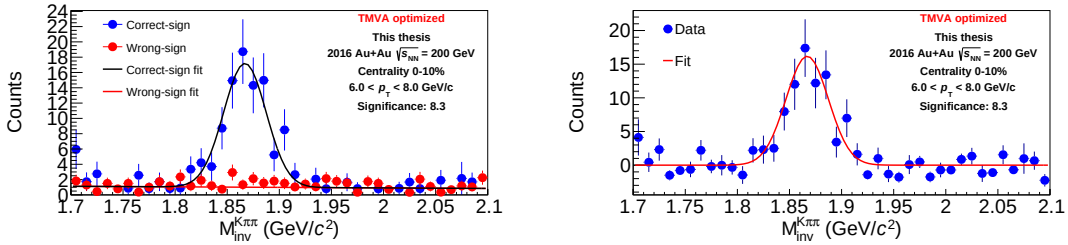

Fig. B.2: Invariant mass spectra of the Kππ triplets for 0-10% central Au+Au collisions for each significant p_{T} bin (continued).

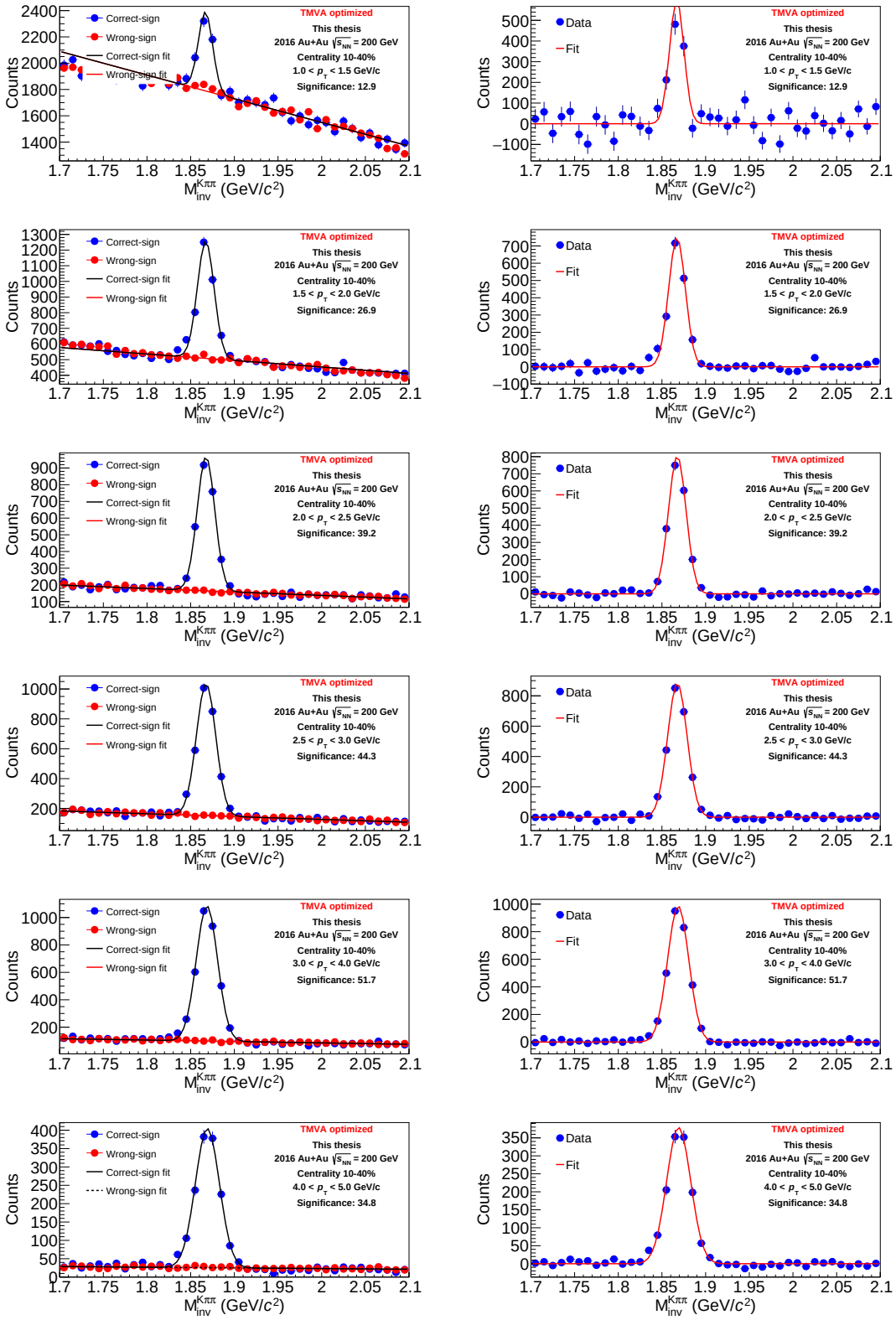

Fig. B.3: Invariant mass spectra of the Kππ triplets for 10-40% central Au+Au collisions for each significant p_T bin.

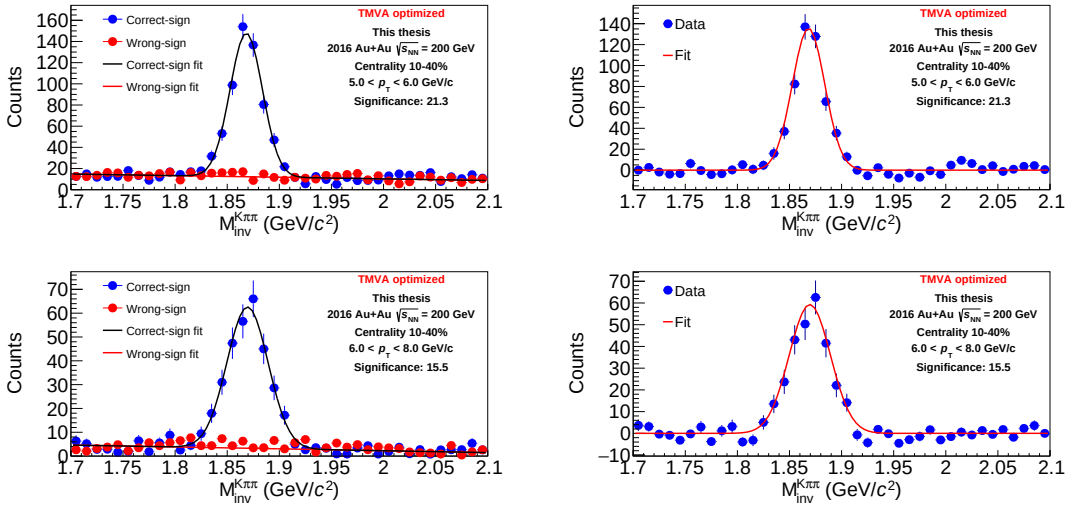

Fig. B.4: Invariant mass spectra of the Kππ triplets for 10-40% central Au+Au collisions for each significant p_T bin (continued).

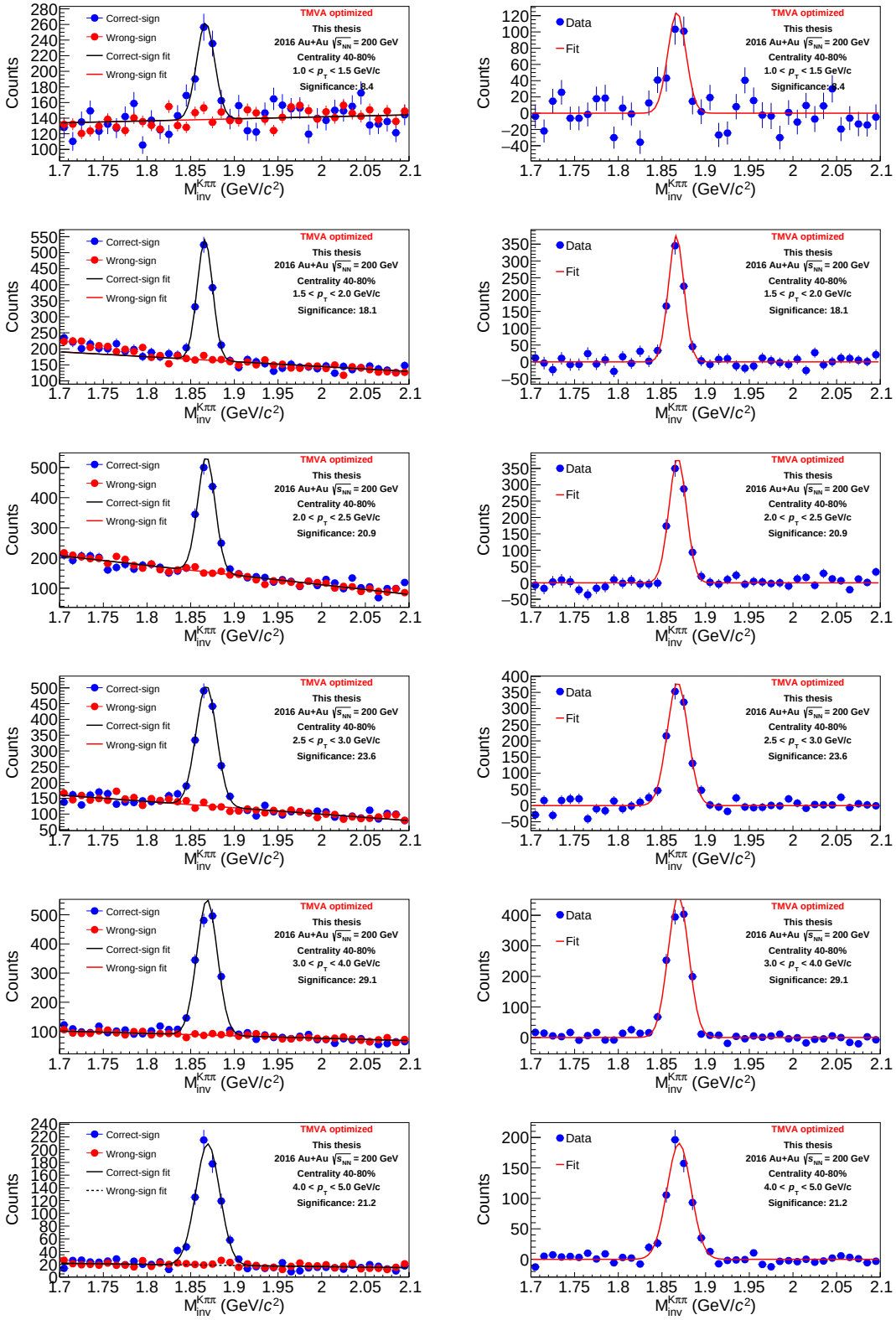

Fig. B.5: Invariant mass spectra of the Kππ triplets for 40-80% central Au+Au collisions for each significant p_T bin.

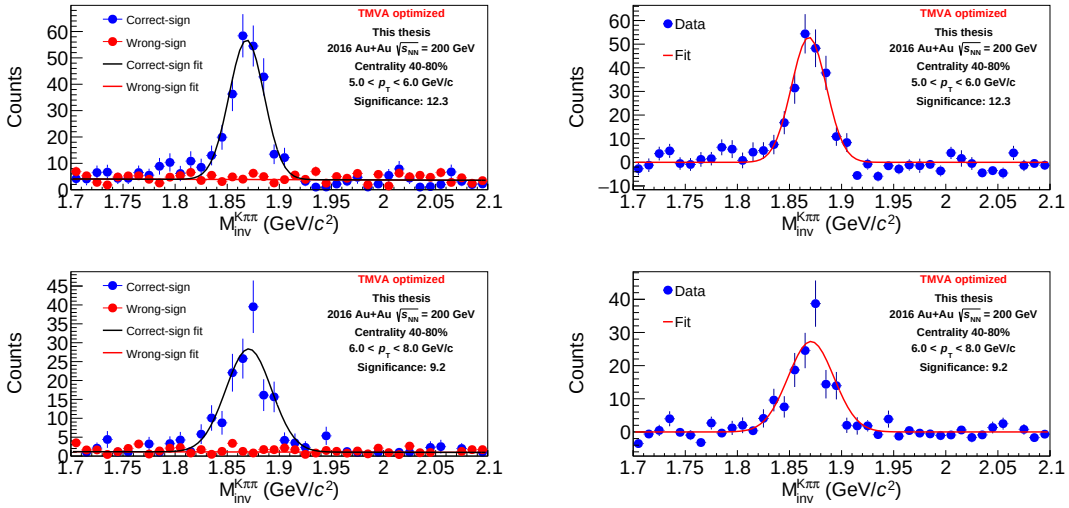

Fig. B.6: Invariant mass spectra of the Kππ triplets for 40-80% central Au+Au collisions for each significant p_{T} bin (continued).

Appendix C

TMVA selection criteria optimization

This appendix contains plots related to the TMVA optimization of topological selection criteria. On the left, there are plots of TMVA efficiencies and of corresponding significance, on the right, there are input topological distributions for signal (from fast-simulator) and for background (from data, wrong sign K$\pi\pi$ triplets). Only p_{T} bins with significant signal in data are shown.

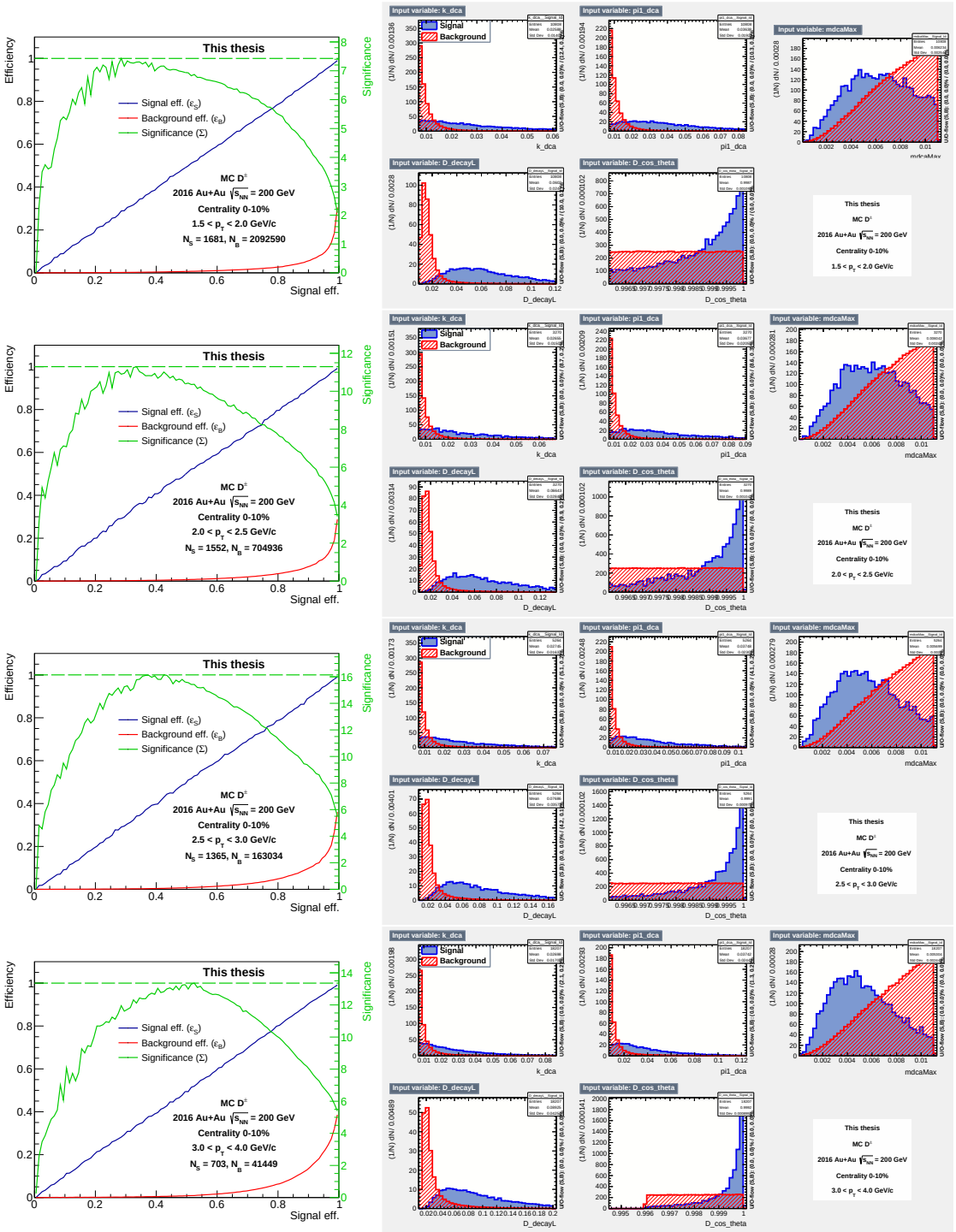

Fig. C.1: TMVA distributions for 0-10% centrality: (left) TMVA signal (blue) and background (red) efficiency with corresponding significance (green). (right) Signal and background topological distributions used for TMVA optimization.

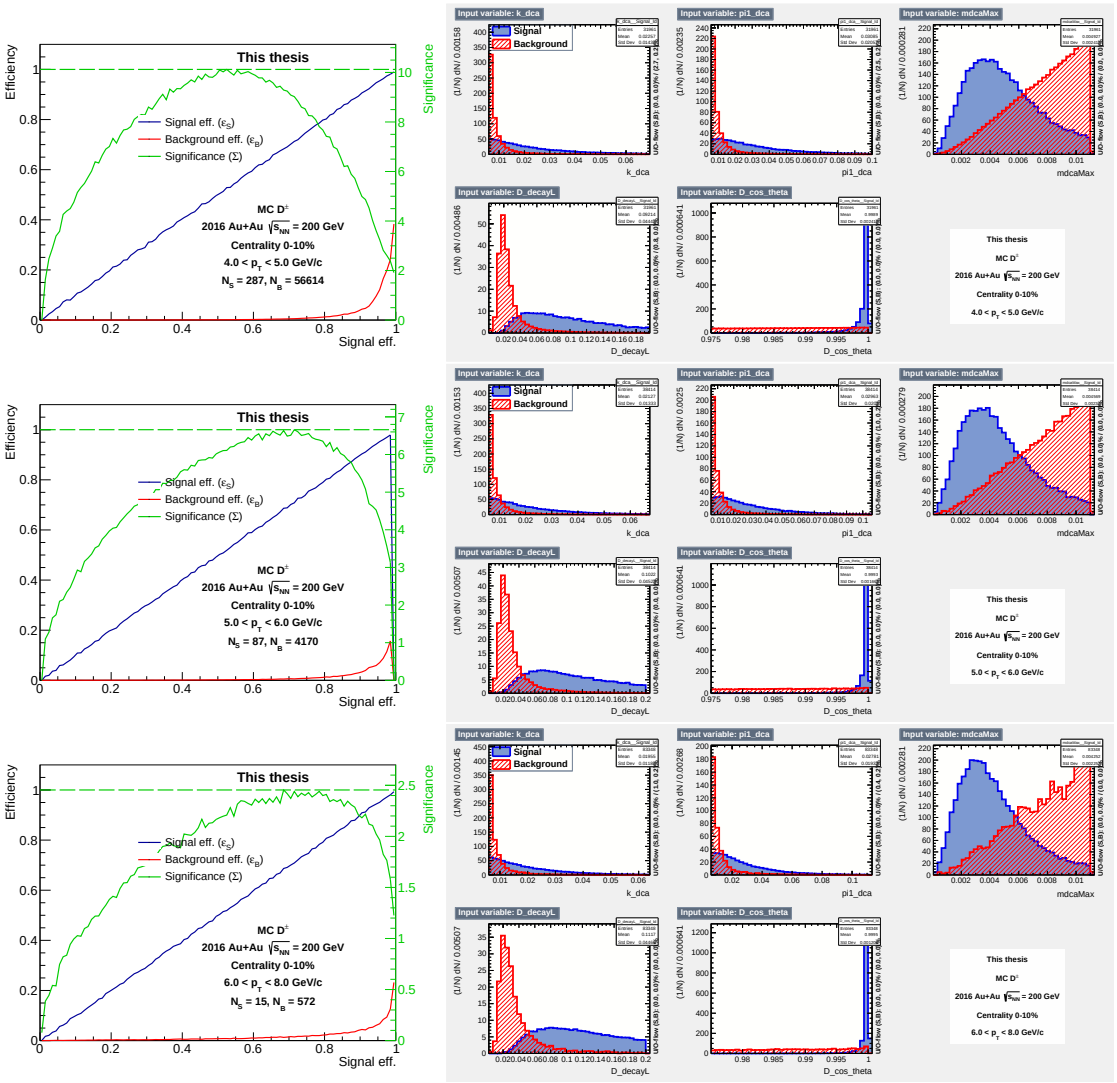

Fig. C.2: TMVA distributions for 0-10% centrality: (left) TMVA signal (blue) and background (red) efficiency with corresponding significance (green). (right) Signal and background topological distributions used for TMVA optimization. (continued)

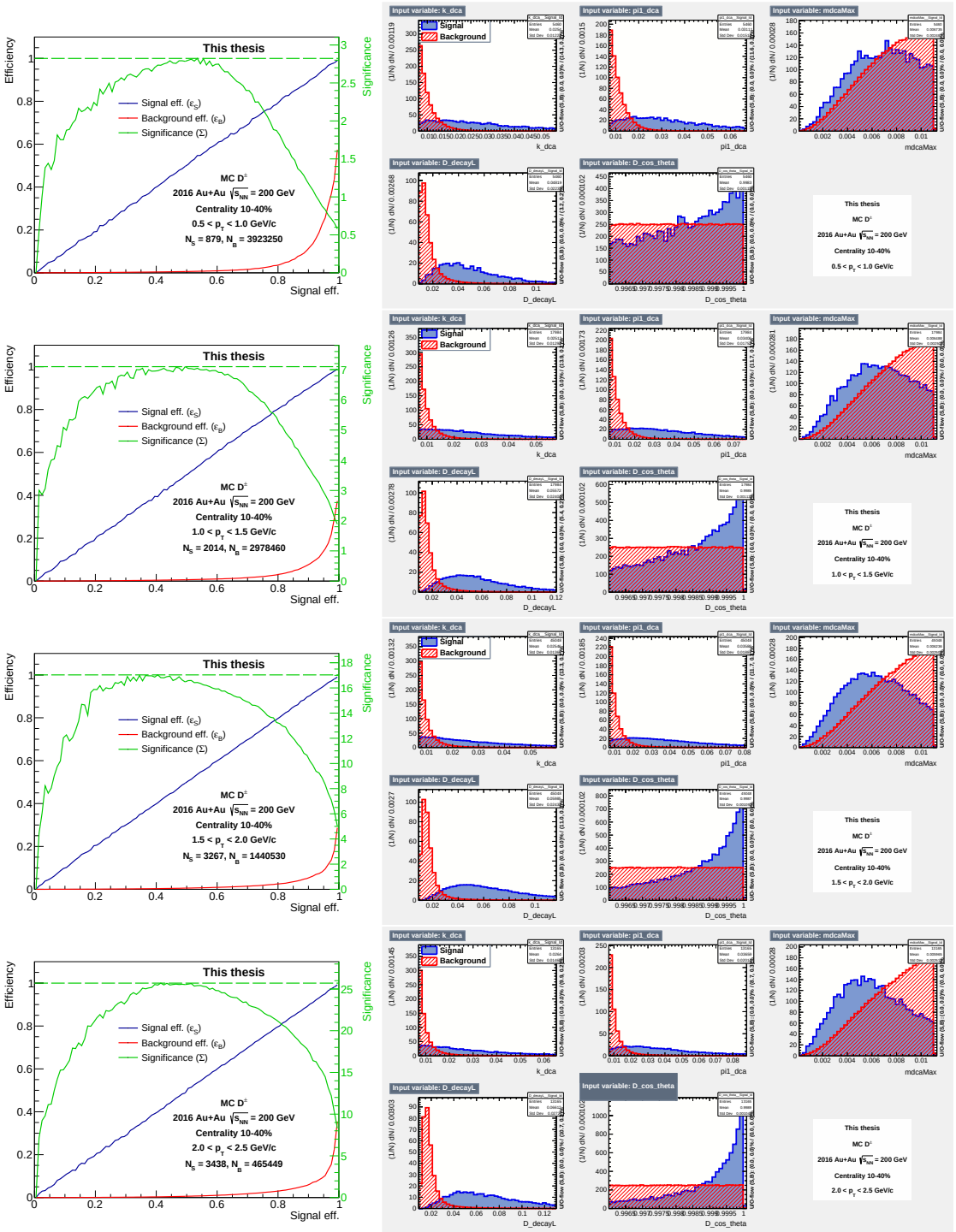

Fig. C.3: TMVA distributions for 10-40% centrality: (left) TMVA signal (blue) and background (red) efficiency with corresponding significance (green). (right) Signal and background topological distributions used for TMVA optimization.

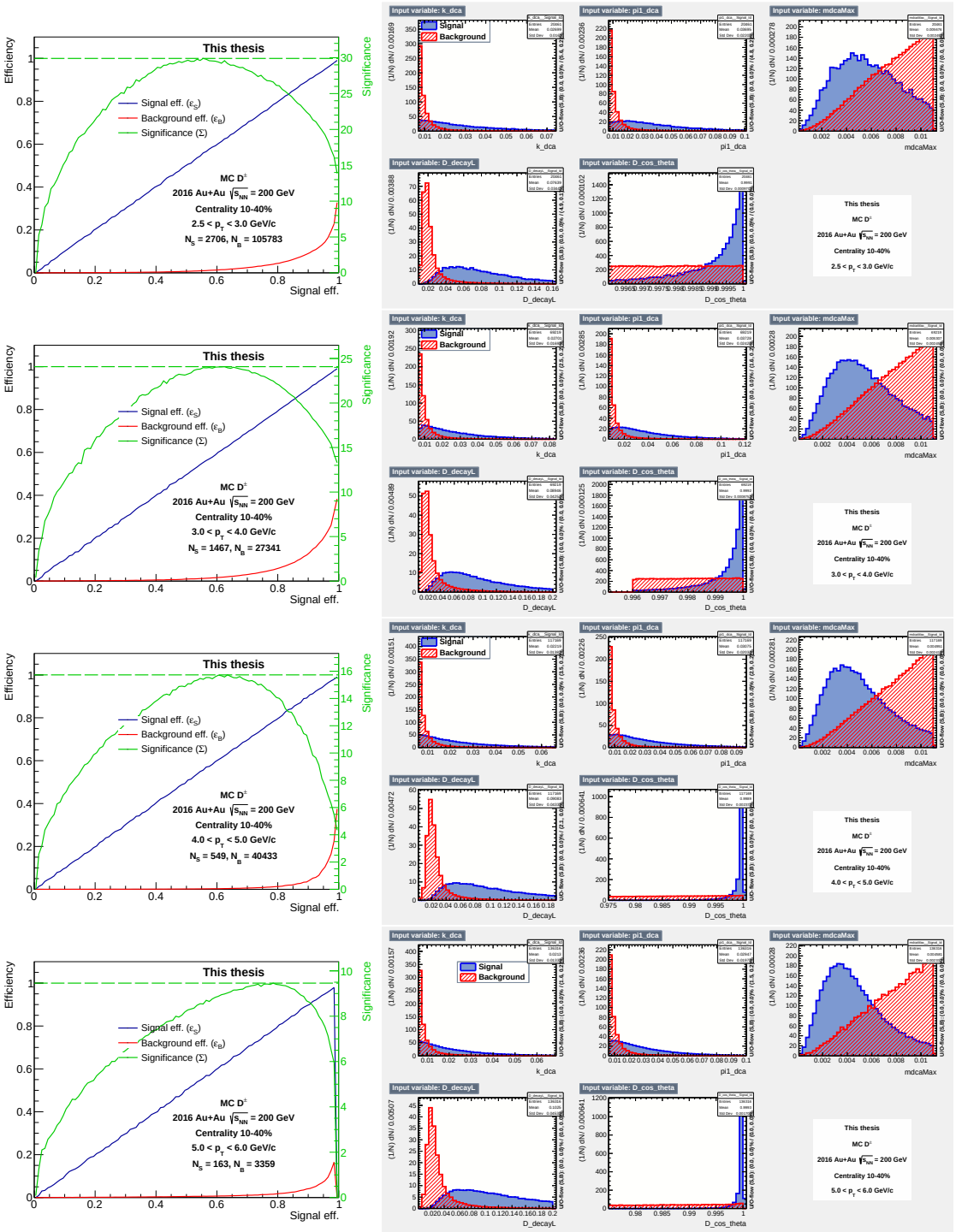

Fig. C.4: TMVA distributions for 10-40% centrality: (left) TMVA signal (blue) and background (red) efficiency with corresponding significance (green). (right) Signal and background topological distributions used for TMVA optimization. (continued)

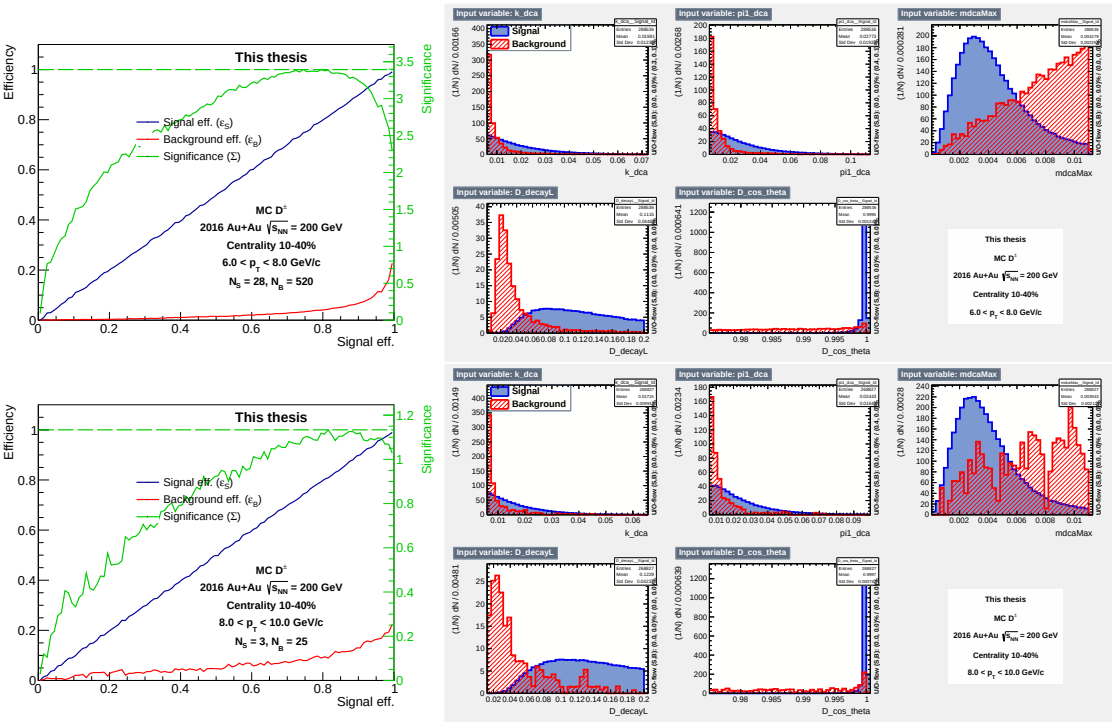

Fig. C.5: TMVA distributions for 10-40% centrality: (left) TMVA signal (blue) and background (red) efficiency with corresponding significance (green). (right) Signal and background topological distributions used for TMVA optimization. (continued 2)

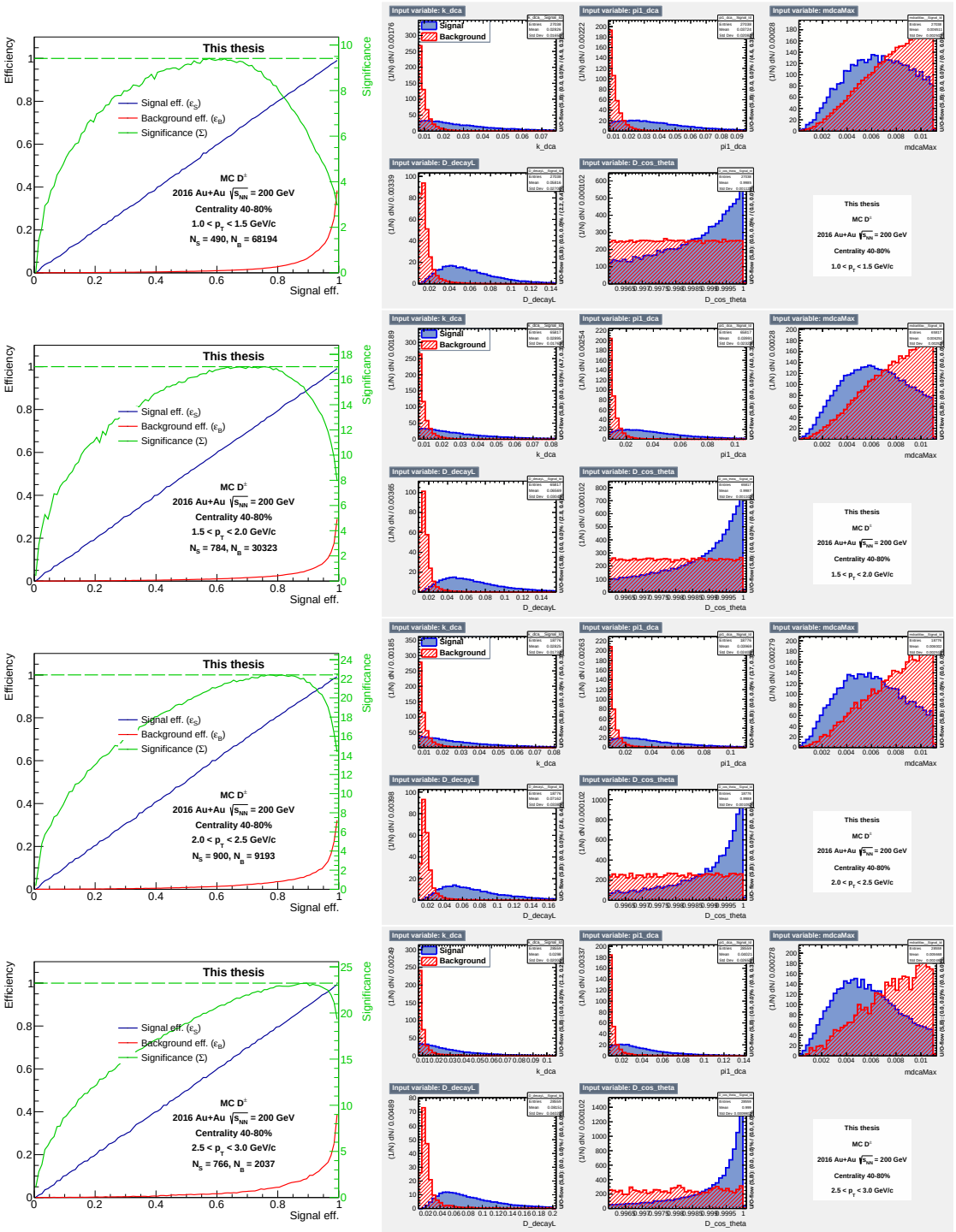

Fig. C.6: TMVA distributions for 40-80% centrality: (left) TMVA signal (blue) and background (red) efficiency with corresponding significance (green). (right) Signal and background topological distributions used for TMVA optimization.

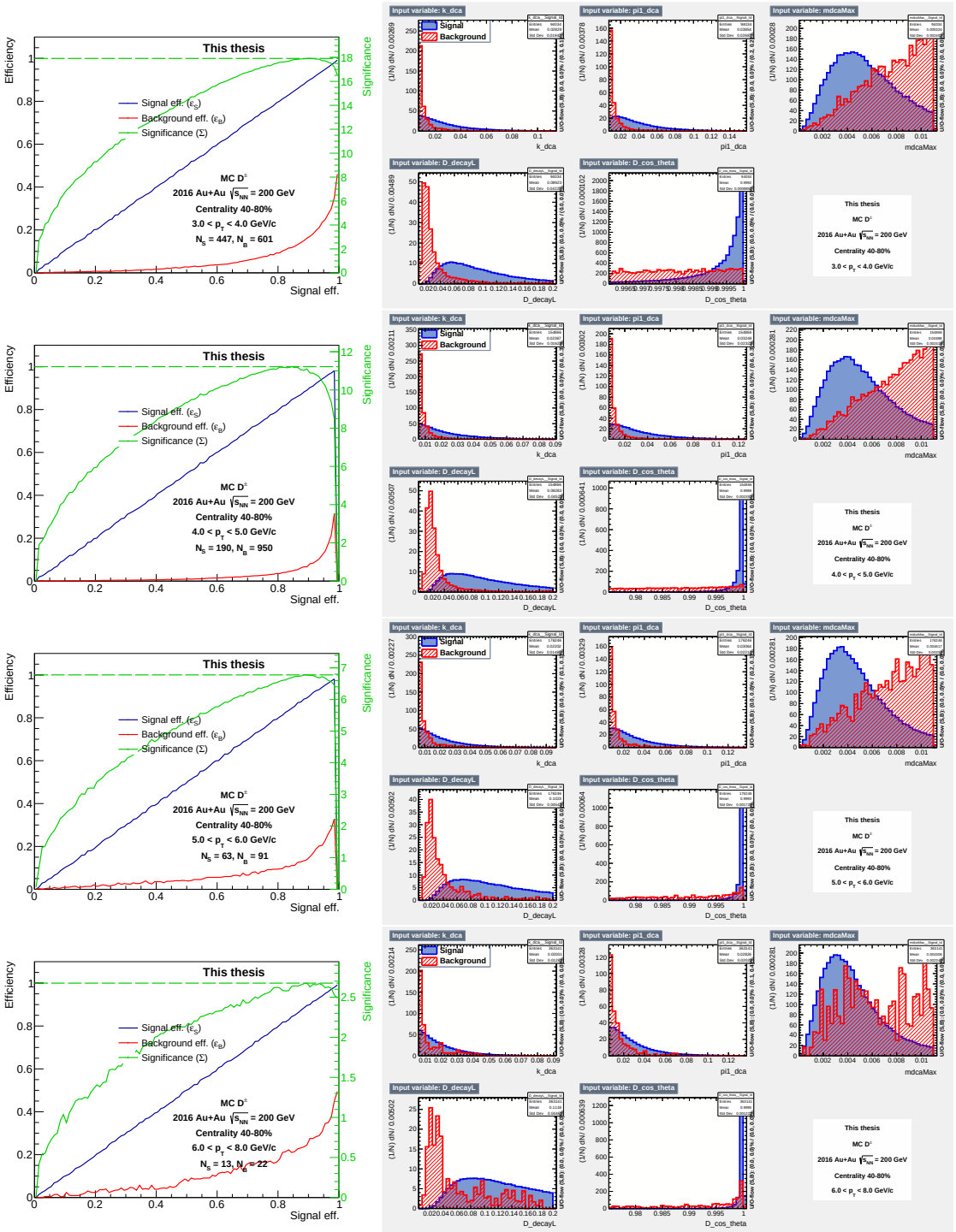

Fig. C.7: TMVA distributions for 40-80% centrality: (left) TMVA signal (blue) and background (red) efficiency with corresponding significance (green). (right) Signal and background topological distributions used for TMVA optimization. (continued)

Appendix D

TPC tracking efficiency

This appendix provides a summary of TPC tracking efficiencies of π^+, π^-, K^+, and K^- mesons for *st_physics* and *st_sst* + *st_nosst* streams as a function of p_T and collision centrality. Only figures that were not presented in Sec. 4.2.1 are shown.

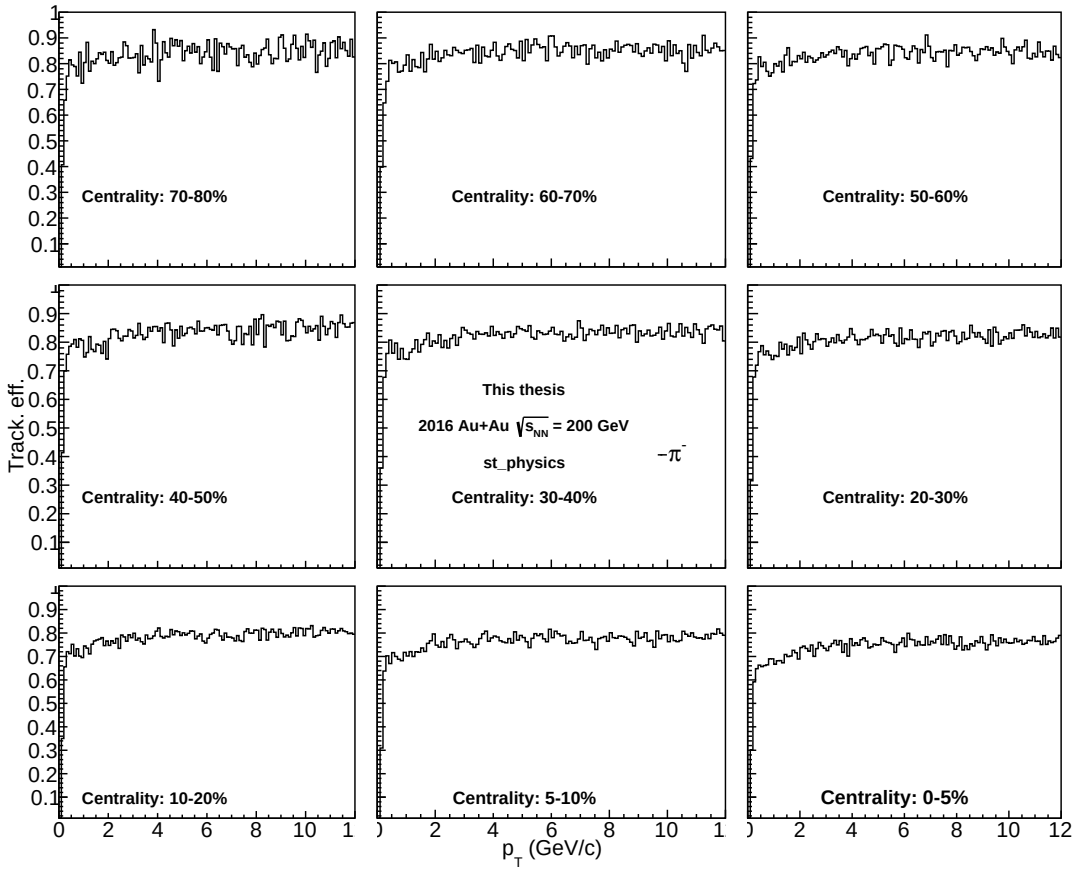

Fig. D.1: TPC tracking efficiency of π^- in *st_physics* stream for different centralities of Au+Au collisions at $\sqrt{s_{NN}} = 200\,\text{GeV}$.

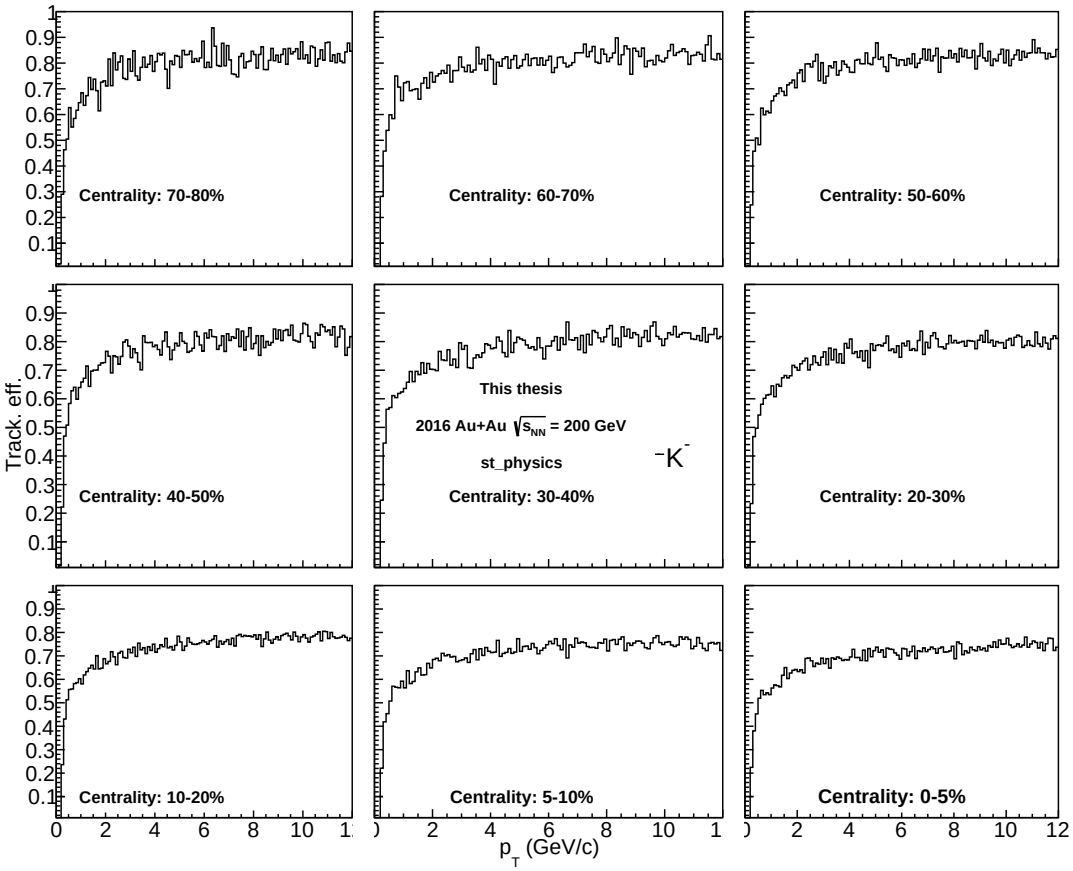

Fig. D.2: TPC tracking efficiency of K^- in *st_physics* stream for different centralities of Au+Au collisions at $\sqrt{s_{\mathrm{NN}}} = 200\,\mathrm{GeV}$.

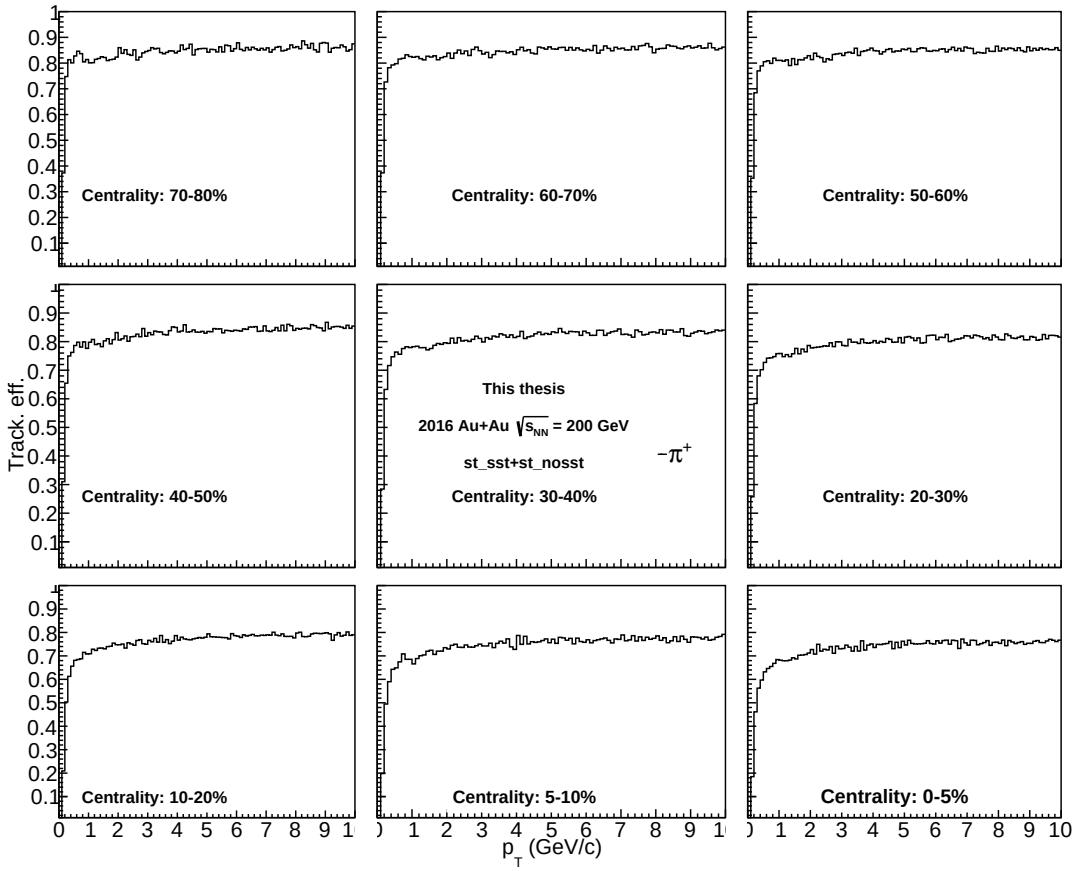

Fig. D.3: TPC tracking efficiency of π^+ in $st\_sst + st\_nosst$ stream for different centralities of Au+Au collisions at $\sqrt{s_{\mathrm{NN}}} = 200\,\mathrm{GeV}$.

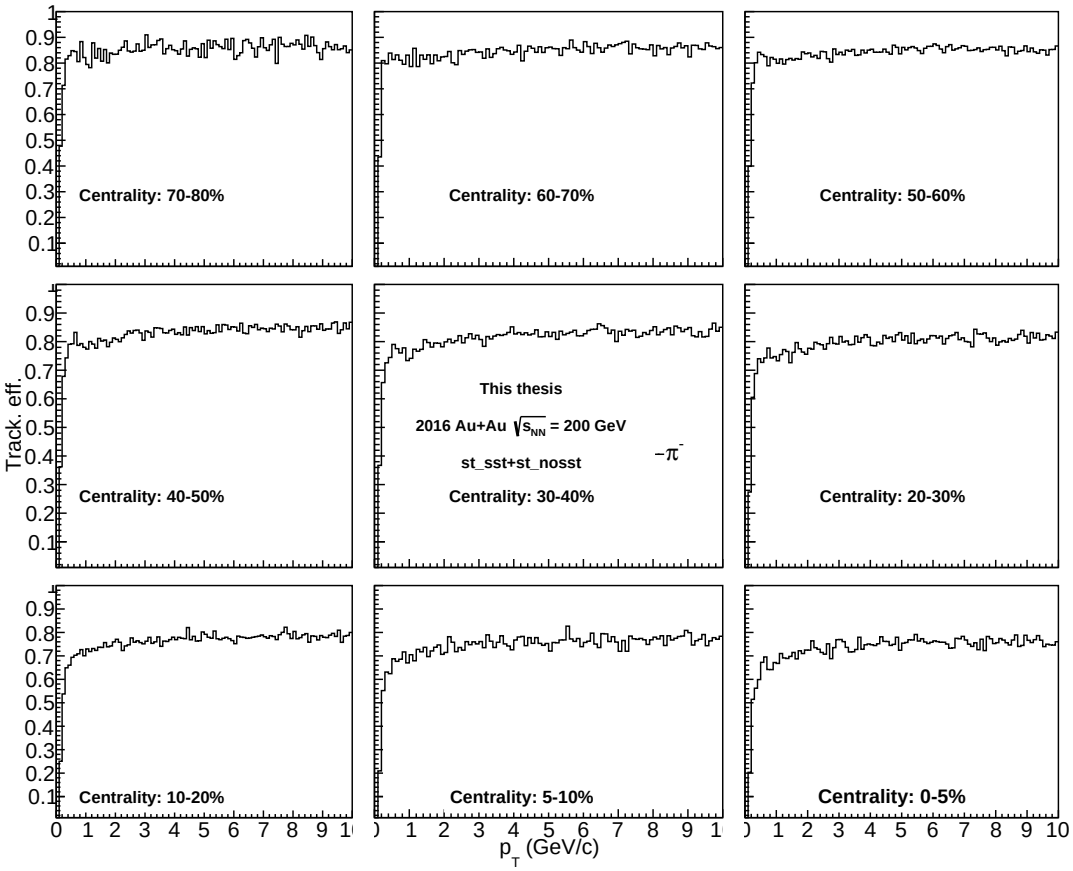

Fig. D.4: TPC tracking efficiency of π^- in $st\_sst + st\_nosst$ stream for different centralities of Au+Au collisions at $\sqrt{s_{\mathrm{NN}}} = 200\,\mathrm{GeV}$.

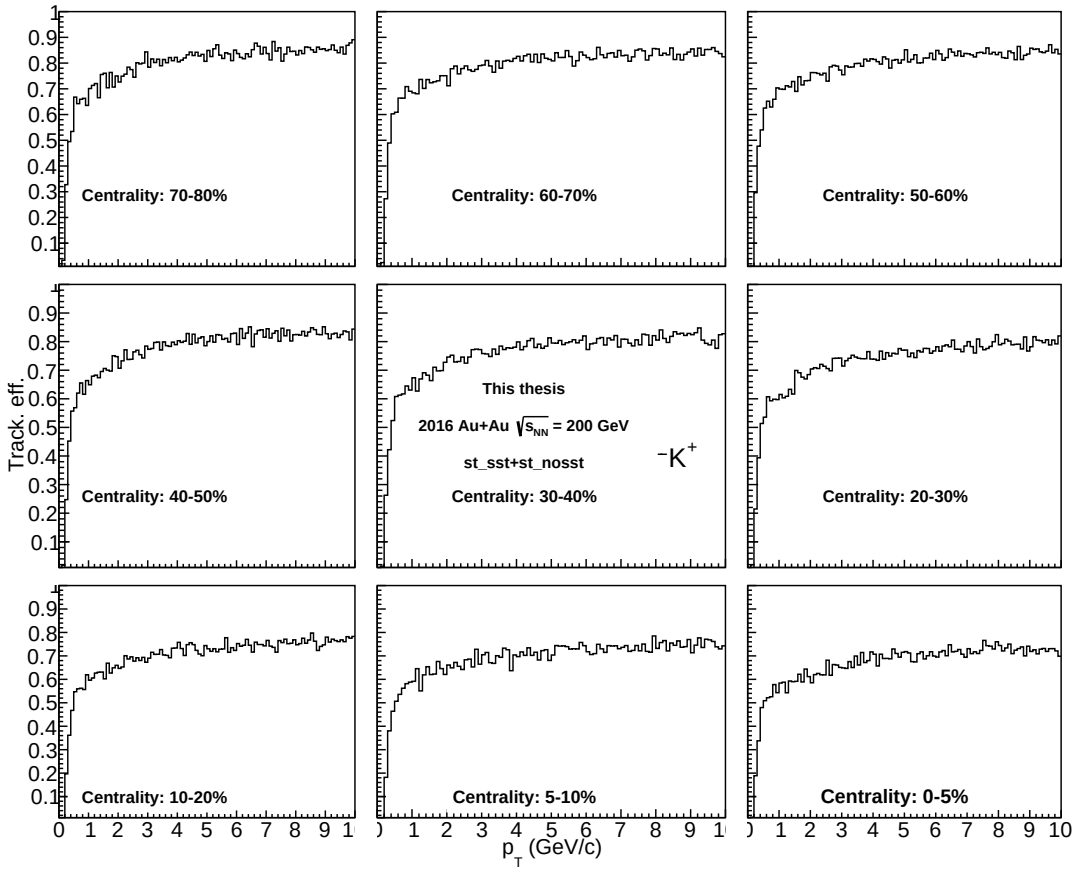

Fig. D.5: TPC tracking efficiency of K^+ in $st\_sst + st\_nosst$ stream for different centralities of Au+Au collisions at $\sqrt{s_{\mathrm{NN}}} = 200\,\mathrm{GeV}$.

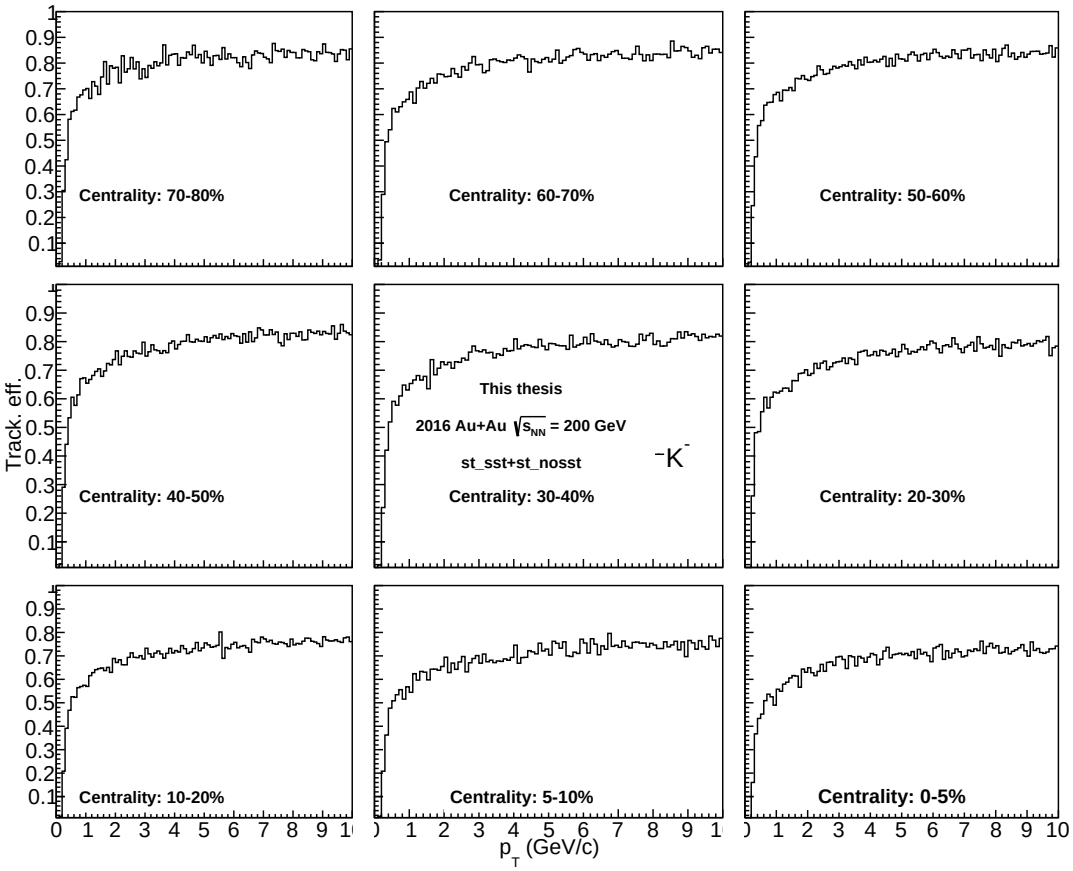

Fig. D.6: TPC tracking efficiency of K^- in $st\_sst + st\_nosst$ stream for different centralities of Au+Au collisions at $\sqrt{s_{\mathrm{NN}}} = 200\,\mathrm{GeV}$.

Appendix E

Other research activities

Service tasks:

- 2017: Calibration of STAR Barrel ElectroMagnetic Calorimeter (BEMC) before data-production of Au+Au collisions at $\sqrt{s_{\mathrm{NN}}} = 54$ GeV measured by STAR in 2017.
- 2018-2022: Maintenance and calibration of the STAR ZDC.

Shifts:

- 2016-2022: Summary of shifts during data-acquisition (including only those taken during my doctoral studies):
  - 2018: two weeks as a detector operator, Isobars (Ru+Ru and Zr+Zr) at $\sqrt{s_{\mathrm{NN}}} = 200$ GeV
  - 2019: two weeks as a detector operator, Au+Au at $\sqrt{s_{\mathrm{NN}}} = 19.6$ GeV
  - 2020: two weeks as an online shift crew (online only due to covid restrictions)
  - 2021: equivalent of two weeks - creation of HEPdata tables for multiple older STAR analyses
  - 2022: three weeks, one as a detector operator and two as a shift leader

Other activities:

- 2017: Quality assurance of Au+Au at $\sqrt{s_{\mathrm{NN}}} = 200$ GeV data from 2016.
  - Check of the original production of the data-set, before the start of the analysis of $\mathrm{D}^{\pm}$ mesons. The main goal was to identify bad runs in the data-set and exclude those from the main analysis. A run can be marked as bad, for example, when one of the required sub-systems, such as the HFT, did not work.

- 2018-2019: Quality assurance of reproduction of the of Au+Au at $\sqrt{s_{\mathrm{NN}}} = 200\,\mathrm{GeV}$ data from 2016.
  - Check of same data-set as listed above, but produced with a new STAR library. This production contains updates such as changes of types of certain variables and slightly different momentum calculation.
- 2018-2019: Quality assurance of the new TPC embedding for Au+Au at $\sqrt{s_{\mathrm{NN}}} = 200\,\mathrm{GeV}$ data from 2016.
  - Check of a simulation used to determine the performance of the STAR TPC. The new version of the embedding includes the HFT tracking for the first time. It is therefore necessary to validate the performance of the simulation.
- 2021-2022: Trigger efficiency studies for analysis of D mesons in p+p collisions at $\sqrt{s} = 500\,\mathrm{GeV}$ measured by STAR in 2011.
- 2022: Implementation of barrel hadronic calorimeter for ATHENA detector, originally planned to be built at the EIC, using DD4hep framework.

Appendix F

Internships

This appendix contains a summary of internships taken during my doctoral studies:

- 08/02 - 08/30/2017, Rice University, Houston, Texas, USA
  - Quality assurance of Run16 Au+Au at $\sqrt{s_{\mathrm{NN}}} = 200\,\mathrm{GeV}$ data-set.
- 10/28 - 11/22/2017, Brookhaven National Laboratory, New York, USA
  - Maintenance of the STAR ZDC and presentation at STAR Collaboration meerting
- 02/14 - 03/15/2018, Brookhaven National Laboratory, New York, USA
  - Calibration and maintenance of the STAR ZDC at the beginning of data-acquisition in 2018. I have also served two weeks of shifts during the data-acquisition as a detector operator.
- 07/12 - 09/18/2018, Lawrence Berkeley National Laboratory, Berkeley, California, USA
  - Optimization of topological selection criteria using the TMVA; implementation of EvtGen into the data-driven fast-simulator; $\mathrm{D}^{\pm}$ candidates extraction from second production of the analyzed data-set (st_sst and st_nosst streams). Discussion of the analysis with experts on HFT related analyses.
- 02/10 - 03/06/2019, Brookhaven National Laboratory, New York, USA
  - Calibration and maintenance of the STAR ZDC at the beginning of data-acquisition in 2019. I have also served two weeks of shifts during the data-acquisition as a detector operator.
- 09/01 - 10/13/2019, Lawrence Berkeley National Laboratory, Berkeley, California, USA

  - Discussion of my analysis with experts from LBNL. Finalization of results for Quark Matter conference in Wuhan, China.

- 11/15 - 12/06/2019, Brookhaven National Laboratory, New York, USA

  - Maintenance and calibration of STAR ZDC at the beginning of data-acquisition in 2020.

- 02/23 - 02/29/2020, Warsaw University of Technology, Warsaw, Poland

  - Introduction to STAR framework and open-heavy flavor analyses for new postdoctoral fellow at WUT.

- 01/17 - 03/26/2022, rookhaven National Laboratory, New York, USA

  - Shifts at STAR during data taking period, finalization of results for Quark Matter conference in Krakov, Poland, and help with development of Barrel Hadronic Calorimeter for ATHENA experiment to be built at the EIC.

Appendix G

Public presentations

This appendix contains a list of publications and public presentations (talks and posters) given by the author since the beginning of the doctoral studies until finishing this thesis. Attached are also poster presentations and published publications with my primary authorship.

- Quark Matter, Venice, Italy, 05/13 - 05/19/2018
  - Poster: Production of $D^{\pm}$ Mesons in Au+Au Collisions at $\sqrt{s_{NN}} = 200$ GeV Measured by the STAR Experiment
- Hot Quarks, Texel, Netherlands, 09/07 - 09/15/2018
  - Talk: Production of Open-charm Hadrons in Au+Au Collisions at $\sqrt{s_{NN}} = 200$ GeV Measured by the STAR Experiment
- Joliot-Curie School, La Grande Motte, France, 10/07 - 10/12/2018
  - Poster: Production of $D^{\pm}$ Mesons in Au+Au Collisions at $\sqrt{s_{NN}} = 200$ GeV Measured by the STAR Experiment
- Zimániy School, Budapest, Hungary, 12/03 - 12/07/2018
  - Talk: Production of Open-charm Hadrons in Au+Au Collisions at $\sqrt{s_{NN}} = 200$ GeV Measured by the STAR Experiment
- 57. International Winter Meeting on Nuclear Physics, Bormio, Italy, 01/21/ - 01/25/2019
  - Poster: Production of Open-charm Hadrons in Heavy-ion Collisions Measured by the STAR Experiment
- Strangeness in Quark Matter, Bari, Italy, 05/10 - 05/15/2019

  - Talk: Measurements of Open-charm hadrons in Au+Au Collisions at $\sqrt{s_{\mathrm{NN}}}$ = 200 GeV by the STAR Experiment

- GDRI 2019 - International Research Network Meeting, Nantes, France, 07/17 - 07/21/2019
  - Talk: Reconstruction of $\mathrm{D}^{\pm}$ Mesons in Au+Au Collisions at $\sqrt{s_{\mathrm{NN}}} = 200\,\mathrm{GeV}$ by the STAR Experiment

- Quark Matter 2019, Wuhan, China, 11/02 - 11/10/2019
  - Poster: Production of $\mathrm{D}^{\pm}$ Mesons in Au+Au Collisions at $\sqrt{s_{\mathrm{NN}}} = 200$ GeV Measured by the STAR Experiment

- Hard Probes 2020, Austin, Texas, USA, 05/31 - 06/05/2020
  - Talk: Measurement of $\mathrm{D}^{\pm}$ Mesons Production in Au+Au Collisions at $\sqrt{s_{\mathrm{NN}}}$ = 200 GeV with the STAR Experiment

- ICHEP 2020, Prague, Czech Republic, 07/28 - 08/06/2020
  - Poster: Production of $\mathrm{D}^{\pm}$ Mesons in Au+Au Collisions at $\sqrt{s_{\mathrm{NN}}} = 200$ GeV at the STAR Experiment

- Conference of Czech and Slovak Physicists 2020, Prague, Czech Republic, 09/07 - 07/10/2020
  - Talk: Measurements of Open-charm Hadrons in Au+Au Collisions at $\sqrt{s_{\mathrm{NN}}}$ = 200 GeV by the STAR Experiment

- 10th International Conference on New Frontiers in Physics, Kolymbari, Crete, Greece, 08/23 - 09/03/2021
  - Talk: Measurements of Open-charm Hadrons in Au+Au Collisions at $\sqrt{s_{\mathrm{NN}}}$ = 200 GeV by the STAR Experiment

- Particles and Nuclei International Conference, Lisbon, Portugal, 09/05 - 09/10/2021
  - Talk: Measurements of $\mathrm{D}^{\pm}$ Meson Production and total charm quark production yield at midrapidity in Au+Au Collisions at $\sqrt{s_{\mathrm{NN}}} = 200$ GeV by the STAR Experiment

- Quark Matter 2021, Krakov, Poland, 04/04 - 04/10/2021
  - Poster: Measurements of open-charm hadron production and total charm cross section in Au+Au collisions at $\sqrt{s_{\mathrm{NN}}} = 200\,\mathrm{GeV}$ by the STAR experiment

In addition I regularly present my analysis progress at weekly online meetings of the STAR heavy-flavor physics working group and on STAR collaboration and analysis meetings which are organized regularly through the year at institutions involved in the STAR experiment.

Below are attached my poster presentations:

Production of D± Mesons in Au+Au Collisions at $\sqrt{s_{NN}}$ = 200 GeV Measured by the STAR Experiment

Jan Vaněk, *for the STAR Collaboration*

Nuclear Physics Institute of the Czech Academy of Sciences
Faculty of Nuclear Sciences and Physical Engineering, CTU in Prague

Venezia 2018 Quark Matter

Abstract

Charm quarks are primarily produced at early stages of ultra-relativistic heavy ion collisions and can be used to probe the properties of the quark-gluon plasma (QGP) created in these collisions. Final-state open charm mesons are usually used experimentally to study the charm quark interaction with the medium. For example, suppression of D-meson production in heavy-ion collisions is sensitive to the energy loss of charm quarks in the QGP. In this poster, the production of D± mesons in Au+Au collisions at $\sqrt{s_{NN}}$ = 200 GeV measured by the STAR experiment using data taken in 2016 is presented. Precise topological reconstruction of secondary decay vertices enabled by the STAR Heavy Flavor Tracker through the hadronic decay channel, $D^{\pm} \rightarrow K^{\mp}\pi^{\pm}\pi^{\pm}$, is used in this analysis. The nuclear modification factor of D± meson is presented as a function of transverse momentum in 0-10% central collisions.

Physics Motivation

- Suppression of high-p_T D^0 is observed in central Au+Au collisions and is comparable to that of pions [1].
- The study of D± production in Au+Au collisions is complementary to the study of D^0 and light mesons production in the effort to better understand properties of the QGP.
- New precision measurements of open charm mesons with the HFT by STAR will bring significant constraints on model calculations.

$$R_{AA}(p_T) = \frac{\frac{dN^{AA}}{dp_T}}{\langle N_{coll} \rangle \frac{dN^{pp}}{dp_T}}$$

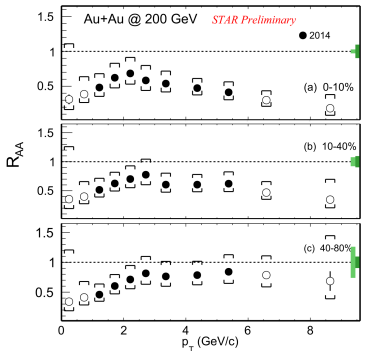

Fig. 1: R_{AA} of D^0 measured by STAR.

Raw Yield Extraction

- D± signal is extracted from Kππ invariant mass $M_{inv}^{K\pi\pi}$ spectrum.
- The wrong-sign distribution, an estimate of combinatorial background, is scaled using the side-band method and subtracted from the correct-sign spectrum.
- The raw yield Y_{raw} is calculated by the bin-counting method.
- Comparable significance to 2014 data.
- Comparison of Y_{raw} to signal extracted from the fit function is quoted as one of the systematic uncertainty sources.

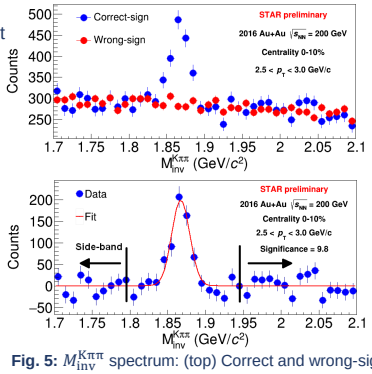

Fig. 5: $M_{inv}^{K\pi\pi}$ spectrum: (top) Correct and wrong-sign combinations, (bottom) After background subtraction.

STAR Detector

- STAR is an experiment designed primarily to study properties of strongly-interacting matter and proton spin structure.
- Heavy Flavor Tracker (HFT) is a 4-layer silicon detector used for precise topological reconstruction of heavy-flavor hadrons, such as D±.
  - Pixel detectors – 2 layers, Strip detectors – 2 layers.
- Time Projection Chamber (TPC) and Time Of Flight (TOF).
  - Particle momentum (TPC) and identification (TPC and TOF).

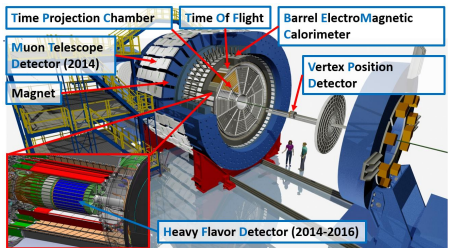

Fig. 2: The STAR detector and its sub-detectors.

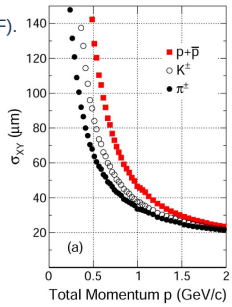

Fig. 3: HFT spatial resolution [2].

Detector Efficiency and Acceptance

- HFT+TPC efficiency determined by data-driven fast-simulator.
- D± decays are generated by PYTHIA.
- Detector efficiency and resolution effects are applied to the D decayed daughters according to inputs from embedding and data:
  - TPC momentum resolution (embedding)
  - TPC tracking efficiency (embedding)
  - HFT matching efficiency (data)
  - DCA resolution (data)
  - Primary vertex position along beam axis (data)
- Efficiency $\varepsilon(p_T)$ obtained from fraction of simulated D± passing the analysis cuts.
- PID efficiency of TPC and TOF.
  - Enriched K sample at low p_T from data using strict TOF PID cuts.
  - Pure π sample obtained by reconstruction of K^0_S.

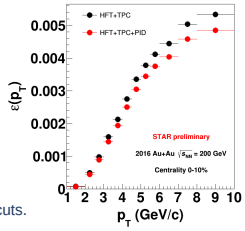

Fig. 6: D± reconstruction efficiency.

Event and Track Selection

- Analyzed 1.03 billion events of Au+Au collisions at $\sqrt{s_{NN}}$ = 200 GeV taken in 2016.
- $D^{\pm} \rightarrow K^{\mp}\pi^{\pm}\pi^{\pm}$ decay channel at mid-rapidity $|y| < 1$, BR = (8.98 ± 0.28)%.
- Particle identification (PID): HFT+TPC+(TOF).
  - TOF used only for tracks which have valid TOF information.

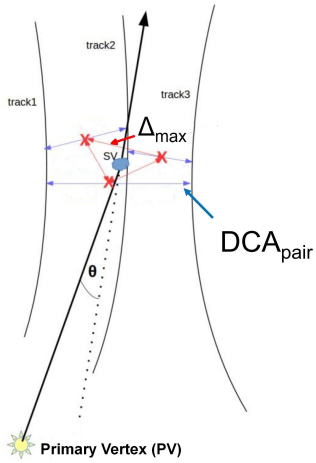

Fig. 4: Topology of the $D^{\pm} \rightarrow K^{\mp}\pi^{\pm}\pi^{\pm}$ decay.

Event selection	$\lvert v_{z(TPC)} \rvert$ < 6 cm	
	$\lvert v_{z(TPC)} - v_{z(VPD)} \rvert$ < 3 cm	
Track selection	p_T > 500 MeV/c	
	$\lvert\eta\rvert$ < 1	
	nHitsFit > 20	
	nHitsFit/nHitsMax > 0.52	
PID cuts	TPC	$\lvert n\sigma_\pi \rvert$ < 3
		$\lvert n\sigma_K \rvert$ < 2
	TOF	$\lvert 1/\beta - 1/\beta_\pi \rvert$ < 0.03
		$\lvert 1/\beta - 1/\beta_K \rvert$ < 0.03
Topological cuts	DCA_{pair} < 80 μm	
	30 μm < $c\tau_{D+/-}$ < 2000 μm	
	cos(θ) > 0.998	
	Δ_{max} < 200 μm	
	$DCA_{\pi\text{-}PV}$ > 100 μm	
	$DCA_{K\text{-}PV}$ > 80 μm	

D± Nuclear Modification Factor

- Invariant yield is calculated according to:

$$\frac{d^2N}{2\pi p_T \, dp_T dy} = \frac{Y_{raw}}{2\pi N_{evt} BR \, p_T \Delta p_T \Delta y \, \varepsilon(p_T)}$$

- Number of events N_{evt}.
- Reference: combined D^0 and D* measurement in 200 GeV p+p collisions [3].
- High-p_T D± and D^0 suppressed in central Au+Au collisions.
- 2016 D± suppression comparable to that of 2014 D^0.
- Other centralities are currently being studied.

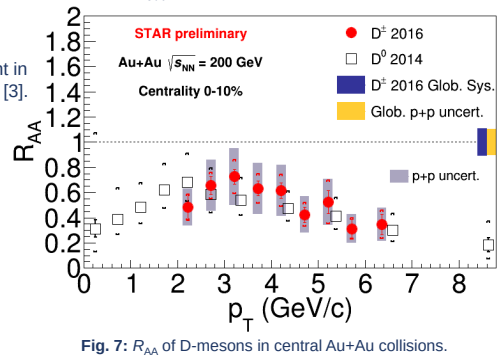

Fig. 7: R_{AA} of D-mesons in central Au+Au collisions.

Conclusion

- D± has been measured in central Au+Au collisions at $\sqrt{s_{NN}}$ = 200 GeV by STAR using data taken in 2016.
- A significant suppression of the high-p_T D± production is observed in central Au+Au collisions at $\sqrt{s_{NN}}$ = 200 GeV and is comparable to that of D^0.
- These high precision measurements can provide stringent constraints on model calculations.

References

[1] G. Xie, for the STAR Collaboration, Nucl. Phys. A, 956, 473-476
[2] Adamczyk L. *et al.* (STAR) 2017 Phys. Rev. Lett. **118** 212301
[3] Adamczyk L. et al. (STAR) 2012 Phys. Rev. D **86** 072013

This work is supported by OPVVV grant CZ.02.1.01/0.0/0.0/16_013/0001569 of Ministry of Education, Youth and Sports of the Czech Republic.

EUROPEAN UNION
European Structural and Investment Funds
Operational Programme Research, Development and Education

MINISTRY OF EDUCATION, YOUTH AND SPORTS

The STAR Collaboration
drupal.star.bnl.gov/STAR/presentations

Nuclear Physics Institute of the CAS
public research institution

Production of D± Mesons in Au+Au Collisions at $\sqrt{s_{NN}}$ = 200 GeV Measured by the STAR Experiment

Jan Vaněk, *for the STAR Collaboration*

Nuclear Physics Institute of the Czech Academy of Sciences

EJC2018 école Joliot-Curie school

Abstract

Charm quarks are primarily produced at early stages of ultra-relativistic heavy ion collisions and can be used to probe the properties of the quark-gluon plasma (QGP) created in these collisions. Final-state open charm mesons are usually used experimentally to study the charm quark interaction with the medium. For example, suppression of D-meson production in heavy-ion collisions is sensitive to the energy loss of charm quarks in the QGP. In this poster, the production of D± mesons in Au+Au collisions at $\sqrt{s_{NN}}$ = 200 GeV measured by the STAR experiment using data taken in 2016 is presented. The secondary decay vertices of D± mesons through the hadronic decay channel, $D^{\pm} \rightarrow K^{\mp}\pi^{\pm}\pi^{\pm}$, are reconstructed topologically utilizing the STAR Heavy Flavor Tracker. The nuclear modification factor of D± meson is presented as a function of transverse momentum in 0-10% central collisions.

Physics Motivation

- Heavy-ion collisions are used to explore the phase diagram of the nuclear matter.
- Charm quarks are created dominantly at early stages of a A+A collision, before ignition of the QGP fireball.
- Charm quarks pass through the volume of the QGP where they loose energy.
- The energy loss can be quantified by using the **nuclear modification factor:**

$$R_{AA}(p_T) = \frac{dN^{AA}/dp_T}{\langle N_{coll}\rangle\ dN^{pp}/dp_T}$$

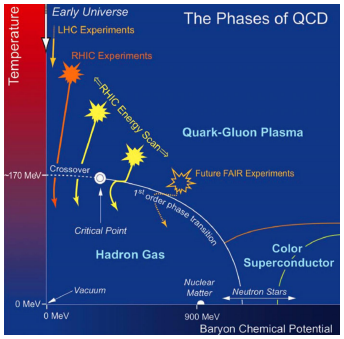

Raw Yield Extraction

- D± is measured through the hadronic decay channel: $D^{\pm} \rightarrow K^{\mp}\pi^{\pm}\pi^{\pm}$.
- D± signal is extracted from Kππ invariant mass $M_{inv}^{K\pi\pi}$ spectrum.
- Background: wrong-sign spectrum scaled using regions outside the D± mass peak.
- The raw yield Y_{raw} is calculated by the bin-counting method in ±3σ region.

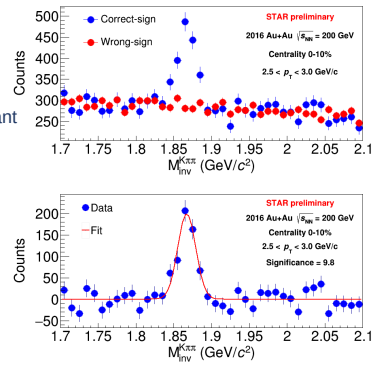

STAR Detector

- STAR is an experiment designed primarily to study properties of strongly-interacting matter and proton spin structure.
- **Time Projection Chamber** (TPC) and **Time Of Flight** (TOF)
  - Particle momentum (TPC) and identification (TPC and TOF)
- **Heavy Flavor Tracker** (HFT) is a 4-layer silicon detector used for precise topological reconstruction of heavy-flavor hadrons, such as D± [1].
  - Pixel detectors – 2 layers, Strip detectors – 2 layers

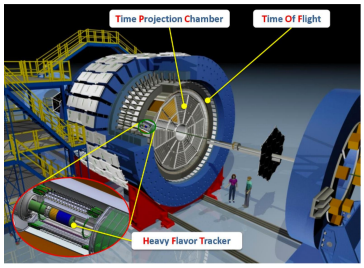

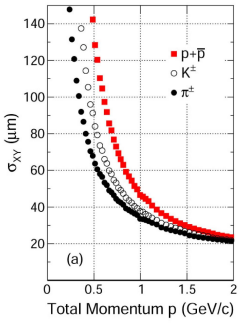

Detector Efficiency and Acceptance

- **HFT+TPC efficiency** determined by **data-driven fast-simulator** with inputs from data and TPC embedding.
  - D± decays are generated by PYTHIA [2].
    - EvtGen [3] will be used for the 3-body decay.
  - Detector efficiency and resolution effects are applied to the D±-decayed daughters according to inputs from embedding and data:
    - TPC momentum resolution (embedding)
    - TPC tracking efficiency (embedding)
    - HFT matching efficiency (data)
    - DCA resolution (data)
    - Primary vertex position along the beam axis (data)
  - Efficiency $\varepsilon(p_T)$ is obtained from fraction of simulated D± passing the analysis cuts.
- **PID efficiency** of TPC and TOF
  - Enriched K sample at low p_T from data using strict TOF PID cuts.
  - Pure π sample obtained by reconstruction of K_s^0.

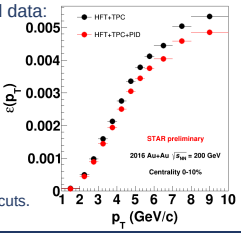

Event and Track Selection

- STAR 2016 Au+Au collisions at $\sqrt{s_{NN}}$ = 200 GeV
- Event selection cuts
  - $|v_z|$ < 6 cm – position of primary vertex along the beam axis
- Track cuts
  - p_T > 300 MeV/c – suppresses combinatorial background from low p_T particles
  - Pseudorapidity $|\eta|$< 1 – detector acceptance
  - Full coverage in azimuthal angle φ.
  - Number of hits in TPC > 20 – good track quality
- Topological cuts
  - Constrain topology of the secondary vertex
    - Decay length, distance among daughter tracks, pointing angle, distance of closest approach to the primary vertex of daughter tracks
  - Suppress combinatorial background
- Particle identification (PID)
  - TPC – energy loss of charged particles in the TPC gas
  - TOF – velocity of the charged particles

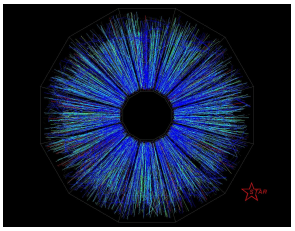

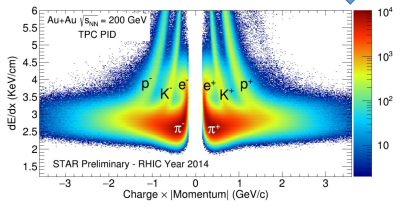

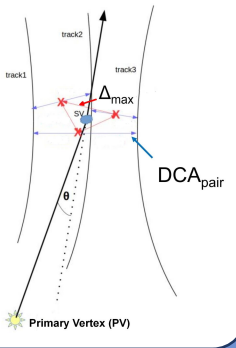

D± Nuclear Modification Factor

- Invariant yield is calculated according to:

$$\frac{d^2N}{2\pi\, p_T\, dp_T dy} = \frac{Y_{raw}}{2\pi\, N_{evt}\, BR\, p_T \Delta p_T \Delta y\, \varepsilon(p_T)}$$

- Number of events N_{evt}, branching ratio BR, rapidity y.
- Reference: combined D^0 and D* measurement in 200 GeV p+p collisions [4].
- D± and D^0 suppressed in central Au+Au collisions.
- D± suppression comparable to that of D^0.
- Other centralities are currently being studied.

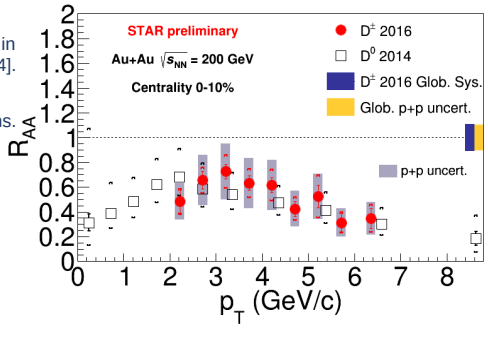

Conclusion

- D± has been measured in central Au+Au collisions at $\sqrt{s_{NN}}$ = 200 GeV by STAR using data taken in 2016.
- A significant suppression of the high-p_T D± production is observed in central Au+Au collisions at $\sqrt{s_{NN}}$ = 200 GeV and is comparable to that of D^0.
- These high precision measurements can provide stringent constraints on model calculations.

References

[1] Adamczyk L., *et al.* (STAR) 2017 Phys. Rev. Lett. **118** 212301 [2] PYTHIA: http://home.thep.lu.se/~torbjorn/Pythia.html
[3] EvtGen: https://evtgen.hepforge.org [4] Adamczyk L., *et al.* (STAR) 2012 Phys. Rev. D **86** 072013

This poster is supported by grant Inter-Excellence of the Ministry of Education, Youth and Sports of the Czech Republic.

EUROPEAN UNION
European Structural and Investment Funds
Operational Programme Research, Development and Education

MINISTRY OF EDUCATION, YOUTH AND SPORTS

The STAR Collaboration
drupal.star.bnl.gov/STAR/presentations

Nuclear Physics Institute of the CAS
public research institution

Measurements of open-charm hadrons in heavy-ion collisions by the STAR Experiment

Jan Vaněk, *for the STAR Collaboration*

Nuclear Physics Institute of the Czech Academy of Sciences

Abstract

Charm quarks are primarily produced at early stages of ultra-relativistic heavy-ion collisions and can therefore probe the Quark-Gluon Plasma (QGP) throughout its whole evolution. Transverse momentum spectra and azimuthal anisotropies of open-charm hadrons are commonly used to experimentally study the charm quark interaction with the QGP. Thanks to the precise vertex reconstruction provided by the Heavy Flavor Tracker (HFT), STAR is able to directly reconstruct $D^{\pm}$, D^0, $D_s^{\pm}$, and $\Lambda_c^{\pm}$ via their hadronic decay channels. The topological cuts for signal extraction are optimized using multivariate analysis and supervised machine learning techniques. In this poster, we show an overview of recent open charm results from the STAR experiment. In particular, the nuclear modification factors of open-charm mesons, together with $D_s^{\pm}/D^0$ and $\Lambda_c^{\pm}/D^0$ ratios as functions of transverse momentum and collision centrality are presented.

Physics Motivation

- Heavy-ion collisions are used to explore the phase diagram and properties of the nuclear matter.
- Charm quarks are created dominantly at early stages of A+A collisions at RHIC, before creation of the QGP fireball.
- Charm quarks lose energy and gain collective flow as they pass through and interact with the QGP medium
- They are an ideal probe of the QGP.

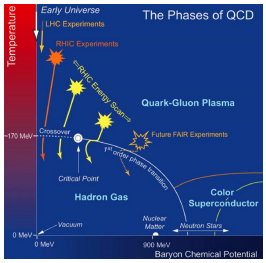

STAR Detector

- STAR is an experiment designed primarily to study properties of strongly-interacting matter and proton spin structure.
- **Time Projection Chamber** (TPC) and **Time Of Flight** (TOF)
  - Particle momentum (TPC) and identification (TPC and TOF)
- **Heavy Flavor Tracker** (HFT) is a 4-layer silicon detector used for precise topological reconstruction of heavy-flavor hadrons decays [1].
  - Pixel detectors – 2 layers, Strip detectors – 2 layers

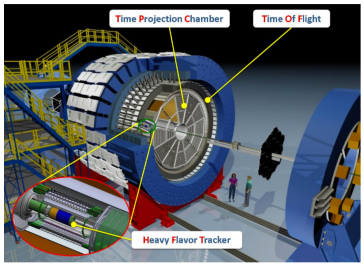

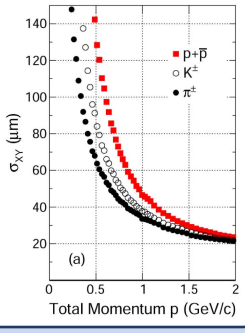

D⁰ and D± Nuclear Modification Factor

- Decay channels used:
  - $D^+ \rightarrow K^-\pi^+\pi^+$ $c\tau$ = (311.8 ± 2.1) μm, BR = (8.98 ± 0.28) %
  - $D^0 \rightarrow K^-\pi^+$ $c\tau$ = (122.9 ± 0.4) μm, BR = (3.93 ± 0.04) %
- Nuclear modification factor:

$$R_{AA}(p_T) = \frac{dN^{AA}/dp_T}{\langle N_{coll}\rangle\, dN^{pp}/dp_T}$$

$\langle N_{coll}\rangle$ is the mean no. of binary collisions from Glauber model

- dN^{pp}/dp_T from combined D^0 and D^* measurement in 200 GeV p+p collisions [2].
- **$D^{\pm}$ and D^0 [3] suppressed in central Au+Au collisions.**
- Similar level of suppression for $D^{\pm}$ and D^0.

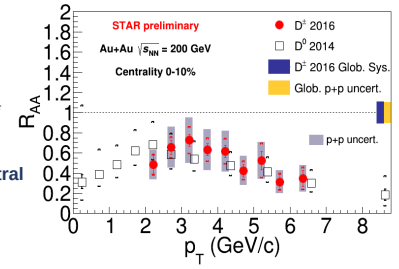

D⁰ Elliptic Flow

- Large elliptic flow (v_2) of D^0
  - Comparable to that of light-flavor hadrons
- Charm quarks follow the Number of Constituent Quarks (NCQ) scaling
- **Suggests strong interactions of the charm quarks with the QGP and that charm quarks acquire similar flow as light flavor quarks**

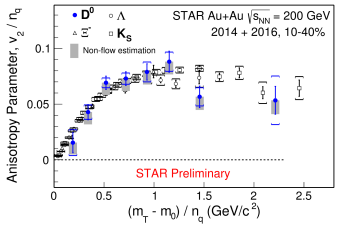

D⁰ Directed Flow

Phys. Rev. Lett. **120**, 192301

- Predicted contributions:
  - Hydrodynamics
    - Mismatch between the tilt of the bulk and the longitudinal density profile of charm quark production
    - Predicts significantly larger v_1 for charm hadrons than for light-flavor hadrons [4]
  - Initial EM field from passing spectators
    - May lead to opposite slopes for D^0 and $\overline{D^0}$ [5] with respect to rapidity
- First evidence of large directed flow (v_1) of D^0 and $\overline{D^0}$
  - Negative v_1 slope for both D^0 and $\overline{D^0}$ with respect to rapidity
  - **Approximately 20 times larger v_1 for D^0 than for kaons [6].**
  - Insufficient precision to conclude about the EM induced splitting

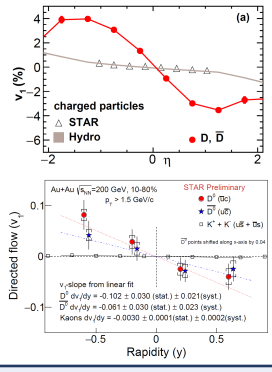

Open-charm Baryon/Meson Ratio

Decay channel used:

- $\Lambda_c^+ \rightarrow K^-\pi^+p$, $c\tau$ = (59.9 ± 1.8) μm, BR = (6.35 ± 0.33) %

Centrality Dependence:

- Enhancement of the $\Lambda_c^{\pm}/D^0$ ratio increases towards central collisions
- The value in peripheral collisions is close to p+p measurement at $\sqrt{s}$ = 7 TeV by ALICE [6]

Transverse momentum dependence:

- Strong enhancement of the $\Lambda_c^{\pm}/D^0$ ratio compared to PYTHIA calculations
- Coalescence model calculations [7,8] closer to data
- Statistical Haronization Model (SHM) [9] underpredicts data
- **Λ_c/D^0 ratio shows significant enhancement in Au+Au collisions with respect to PYTHIA**

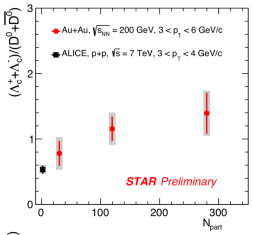

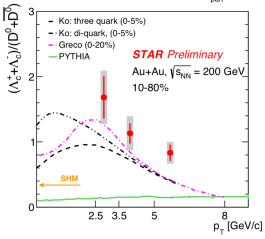

D_s/D^0 Enhancement

- Decay channel used:
  - $D_s^+ \rightarrow \phi\pi^+$, $\phi \rightarrow K^-K^+$, $c\tau$ = (149.9 ± 2.1) μm BR = (2.27 ± 0.08) %
- Enhancement of D_s/D^0 ratio in Au+Au collisions with respect to PYTHIA and elementary collisions (ee/pp/ep) [10]
  - TAMU [11] underpredicts measurements
  - Reasonable agreement with the SHM [9]
- **D_s/D^0 is enhanced in Au+Au collisions possibly due to strangeness enhancement and coalescence hadronization**

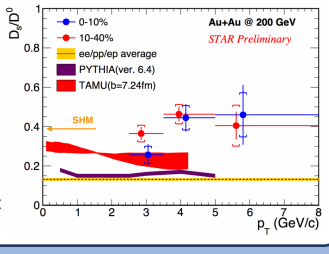

Conclusion

- STAR has extensively studied production of open-charm hadrons in heavy-ion collisions.
- D^0 and $D^{\pm}$ mesons are significantly suppressed in central Au+Au collisions.
- D^0 mesons have large v_1 with negative slope.
- D^0 mesons have v_2 comparable to light-flavor hadrons and seem to follow the NCQ scaling.
- Λ_c/D^0 and D_s/D^0 enhancements in Au+Au collisions with respect to p+p collisions.

References

[1] L. Adamczyk, *et al.* (STAR), 2017, Phys. Rev. Lett. **118** 212301
[2] L. Adamczyk, *et al.* (STAR), 2012, Phys. Rev. D **86** 072013
[3] J. Adam, *et al.* (STAR), 2018, arXiv:1812.10224v1
[4] S. Chatterjee, P. Bozek, 2018, Phys. Rev. Lett. **120**, 192301
[5] Santosh K. Das, *et al.*, 2017, Phys Lett B **768**, 260-264
[6] S. Acharya, *et al.*, (ALICE), 2018, JHEP 04 108
[7] M. Ko, *et al.*, 2009, Phys.Rev.C **79** 044905
[8] V. Greko, *et al.*, 2018, Eur.Phys.J.C 78:348
[9] Y. Oh, et al., 2009, Phys.Rev.C **79** 044905
[10] M. Lisovyi, et al., 2016, Eur. Phys. J. C **76**: 397
[11] M. He, et al., 2013, Phys. Rev. Lett. **110** 112301

This poster is supported by grant LTT18022 Inter-Excellence of the Ministry of Education, Youth and Sports of the Czech Republic.

The STAR Collaboration
drupal.star.bnl.gov/STAR/presentations

Production of D± Mesons in Au+Au Collisions at $\sqrt{s_{NN}}$ = 200 GeV at the STAR Experiment

Jan Vaněk *for the STAR Collaboration*

Nuclear Physics Institute of the Czech Academy of Sciences

Abstract

Charm quarks are a unique probe of the QGP created in heavy-ion collisions as they are produced at very early stages of these collisions and subsequently experience the whole evolution of the system. Information on charm quark production and dynamics in the QGP medium can be accessed through open charm hadrons. At STAR, measurement of the open charm hadrons is enabled by the Heavy Flavor Tracker which allows their direct topological reconstruction, thanks to its excellent track pointing resolution. In this poster, we present a measurement of D± meson production in Au+Au collisions at $\sqrt{s_{NN}}$ = 200 GeV by the STAR using data collected in year 2016. In particular, we focus on optimization of topological selection criteria using a machine learning technique from the Toolkit for Multivariate Data Analysis (TMVA) which has been done separately for each studied p_T bin of D± and each collision centrality class. The optimization uses 160M simulated D± meson decays as a signal sample and wrong-sign Kππ triplets from data as a background. The TMVA-optimized topological criteria help to significantly suppress the combinatorial background for p_T < 4 GeV/c and improve the significance of the D± raw yield.

Physics Motivation

- Suppression of high-p_T D^0 is observed in central Au+Au collisions and is comparable to that of pions [1]

$$R_{AA}(p_T) = \frac{dN^{AA}/dp_T}{\langle N_{coll}\rangle dN^{pp}/dp_T}$$

- The study of D± production is complementary to that of D^0 and also provides constraints on the total charm cross-section in heavy-ion collisions
- Precise measurements of open-charm mesons with the HFT by STAR will provide constraints for model calculations

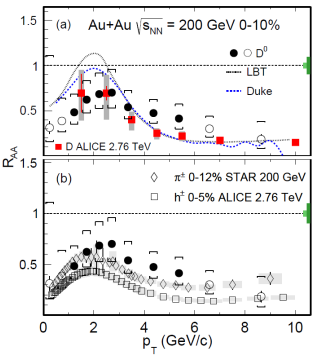

STAR Experiment

- **Heavy Flavor Tracker** (HFT): 4-layer silicon detector used for precise topological reconstruction of heavy-flavor hadrons, such as D±
  - MAPS-based pixel detectors – 2 layers, Strip detectors – 2 layers
- **Time Projection Chamber** (TPC) and **Time Of Flight** (TOF) detector
  - Particle momentum (TPC) and identification (TPC and TOF)

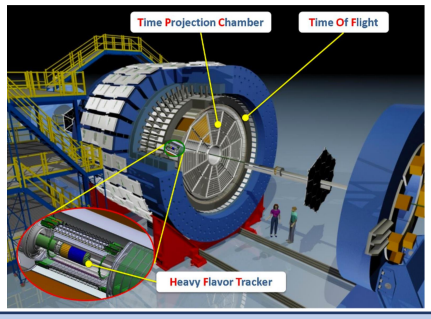

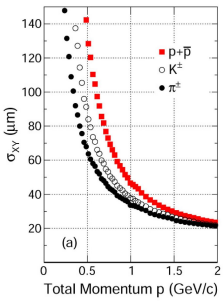

Event and Track Selection

- Analyzed 1.3 billion Au+Au events at $\sqrt{s_{NN}}$ = 200 GeV taken in 2016 with the HFT
  - 1 billion events used previously for the Preliminary
- D±→$K^{\mp}\pi^{\pm}\pi^{\pm}$ decay channel at mid-rapidity:
  - |y| < 1, *BR* = (8.98 ± 0.28)%, *cτ* = (311.8 ± 2.1) μm
- Particle selection and identification: HFT+TPC+(TOF)
  - TOF used only for tracks which have valid TOF information
- Precise topological reconstruction utilizing excellent vertex resolution of the HFT
  - Topological selection criteria tuned using TMVA rectangular cuts optimization

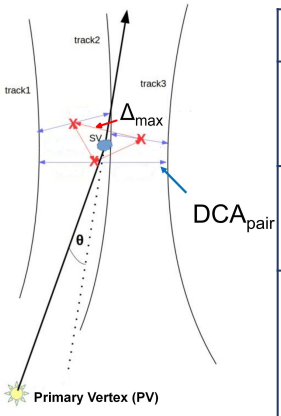

Δ_{max} = maximum distance between the secondary vertices of track pairs

Event selection	$\lvert v_{z(TPC)}\rvert$ < 6 cm	
	$\lvert v_{z(TPC)} - v_{z(VPD)}\rvert$ < 3 cm	
Track selection	p_T > 300 MeV/c	
	$\lvert\eta\rvert$ < 1	
	nHitsFit > 20	
	nHitsFit/nHitsMax > 0.52	
Particle identification	TPC	$\lvert n\sigma_\pi\rvert$ < 3
		$\lvert n\sigma_K\rvert$ < 2
	TOF	$\lvert 1/\beta - 1/\beta_\pi\rvert$ < 0.03
		$\lvert 1/\beta - 1/\beta_K\rvert$ < 0.03
Topological variables (Optimized)	DCA$_{pair}$	
	$L_{D+/-}$ < 2 mm	
	cos(θ)	
	Δ_{max}	
	DCA$_{π1\text{-}PV}$	
	DCA$_{π2\text{-}PV}$	
	DCA$_{K\text{-}PV}$	

TMVA Topological Selection Criteria Optimization

- Rectangular cuts optimization method from the Toolkit for Multivariate Data Analysis [3]
- **Inputs to TMVA**
  - Background sample
    - From data
    - Wrong-sign Kππ triplets
  - Signal sample
    - From data-driven fast-simulation
    - 160M simulated D± decays
- **Number of background events $N_B(p_T)$**
  - From combinatorial background in data
- **Number of signal events $N_S(p_T)$**
  - Estimated using measured D^0 spectrum [1]

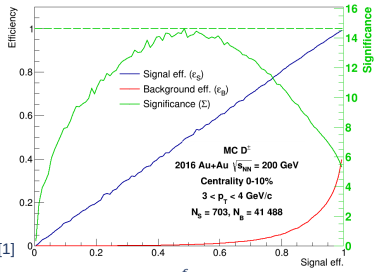

$$N_S(p_T) = \left(\frac{d^2N}{dp_T dy}\right)_{D^0} N_{evt}\, BR_{D^\pm}\, \Delta p_T \Delta y\, \varepsilon(p_T)\, \frac{f_{c\to D^\pm}}{f_{c\to D^0}}$$

  - N_{evt} – number of events, *f* – fragmentation ratios, $\varepsilon(p_T)$ – D± reconstruction efficiency from data-driven fast simulator
- **Optimal cuts selected based on maximum significance**

TMVA Optimization Performance

- Improved D± mesons raw yield extraction with TMVA-optimized topological selection criteria thanks to significantly suppressed combinatorial background

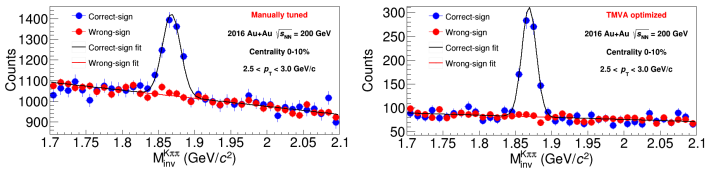

- Improved D± meson raw yield significance extracted with TMVA topological selection criteria with respect to the manually tuned selection criteria for p_T < 4 GeV/c

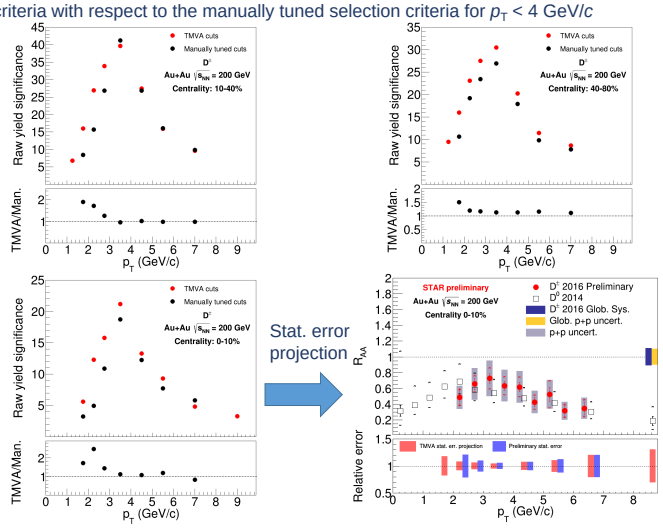

Conclusions

- Optimization of rectangular selection criteria using the TMVA has significantly suppressed the combinatorial background and improved the D± raw yield significance
- Expecting improved statistical precision of D± R_{AA} with the TMVA-optimized topological selection criteria
- Better statistical precision at p_T < 4 GeV/c will allow more precise determination of total D± production cross-section

References

[1] Adam J., *et al.* (STAR), Phys. Rev. C **99**, 034908, (2019).
[2] Adamczyk L., *et al.* (STAR), Phys. Rev. Lett. **118** 212301 (2017)
[3] Tanabashi M., *et al.* (PDG), Phys. Rev. Lett. **98** 030001 (2018)
[4] TMVA official website: http://tmva.sourceforge.net, (October 11, 2019)

This work is supported by project LTT18002 of Ministry of Education, Youth and Sports of the Czech Republic.

EUROPEAN UNION
European Structural and Investment Funds
Operational Programme Research, Development and Education

MINISTRY OF EDUCATION, YOUTH AND SPORTS

Poster supported by:
U.S. DEPARTMENT OF ENERGY
Office of Science

The STAR Collaboration
drupal.star.bnl.gov/STAR/presentations

Production of D± Mesons in Au+Au Collisions at $\sqrt{s_{NN}}$ = 200 GeV at the STAR Experiment

Jan Vaněk *for the STAR Collaboration*

Nuclear Physics Institute of the Czech Academy of Sciences

Faculty of Nuclear Sciences and Physical Engineering, CTU in Prague

Abstract

Charm quarks are a unique probe of the Quark Gluon Plasma (QGP) created in heavy-ion collisions as they are produced at very early stages of these collisions and subsequently experience the whole evolution of the system. Information on charm quark production and dynamics in the QGP medium can be accessed through open charm hadrons. At STAR, measurements of open charm hadrons are enabled by the Heavy Flavor Tracker (HFT), thanks to its excellent track pointing resolution, through direct topological reconstruction. In this poster, we present measurements of D± meson production in Au+Au collisions at $\sqrt{s_{NN}}$ = 200 GeV by the STAR detector using data collected in years 2014 and 2016. In particular, we focus on invariant spectra and nuclear modification factors (R_{AA}) of D± mesons measured in three centrality classes of Au+Au collisions. Both D± and D^0 R_{AA} show significant suppression in central Au+Au collisions for transverse momentum (p_T) above 4 GeV/c. We also report a measurement of D±/D^0 yield ratio which turns out to be in agreement with the PYTHIA 8 calculation, suggesting no modification of the ratio in Au+Au collisions with respect to p+p collisions.

Physics Motivation

- At RHIC energies, charm quarks are produced predominantly through hard partonic scatterings at early stages of Au+Au collisions, making them excellent probe of the QGP
- Suppression of high-p_T D^0 is observed in central Au+Au collisions and is comparable to that of pions and models incorporating both radiative and collisional energy losses, and collective flow [1]

$$R_{AA}(p_T) = \frac{dN^{AA}/dp_T}{\langle N_{coll}\rangle dN^{pp}/dp_T}$$

- The HFT allows direct topological reconstruction of three body decay D±→K∓π±π± at mid-rapidity
  - *BR* = (8.98 ± 0.28)%, *cτ* = (311.8 ± 2.1) μm
- The study of D± production is complementary to that of D^0 and also provides constraints on the total charm cross-section in heavy-ion collisions

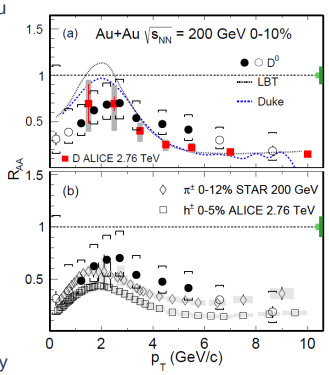

D± Nuclear Modification Factor

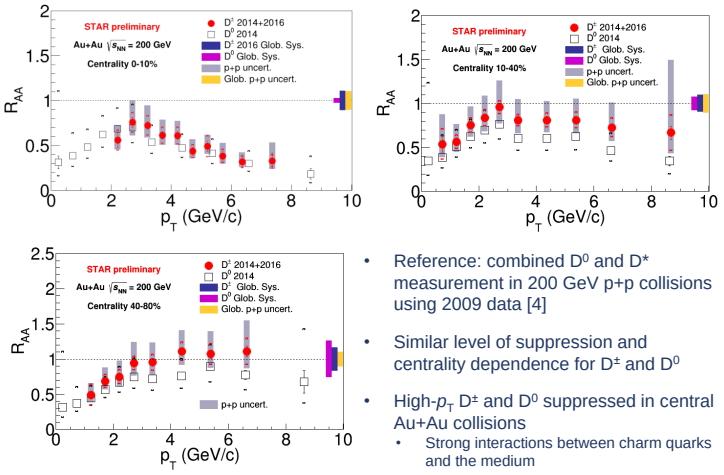

- Reference: combined D^0 and D* measurement in 200 GeV p+p collisions using 2009 data [4]
- Similar level of suppression and centrality dependence for D± and D^0
- High-p_T D± and D^0 suppressed in central Au+Au collisions
  - Strong interactions between charm quarks and the medium

STAR Experiment

- **Heavy Flavor Tracker** (HFT): 4-layer silicon detector used for precise topological reconstruction of heavy-flavor hadrons, such as D±
  - MAPS-based pixel detectors – 2 layers, Strip detectors – 2 layers
- **Time Projection Chamber** (TPC) and **Time Of Flight** (TOF) detector
  - Particle momentum (TPC) and identification (TPC and TOF)

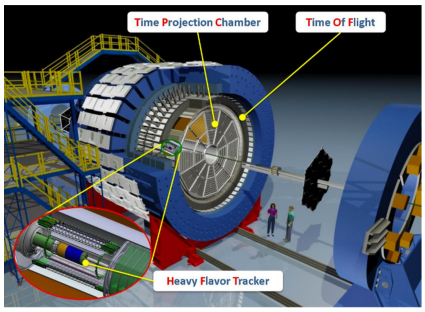

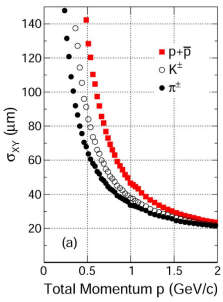

D±/D^0 Yield Ratio

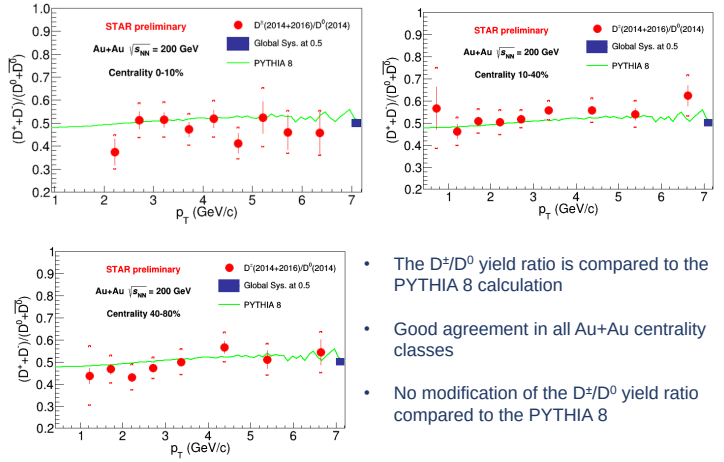

- The D±/D^0 yield ratio is compared to the PYTHIA 8 calculation
- Good agreement in all Au+Au centrality classes
- No modification of the D±/D^0 yield ratio compared to the PYTHIA 8

D± Invariant Spectrum

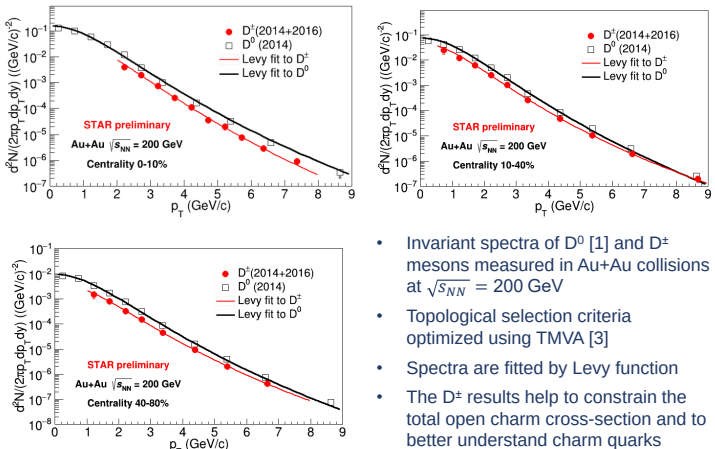

- Invariant spectra of D^0 [1] and D± mesons measured in Au+Au collisions at $\sqrt{s_{NN}}$ = 200 GeV
- Topological selection criteria optimized using TMVA [3]
- Spectra are fitted by Levy function
- The D± results help to constrain the total open charm cross-section and to better understand charm quarks hadrochemistry in Au+Au collisions

Conclusions

- STAR has extensively studied the production of open-charm mesons in Au+Au collisions at $\sqrt{s_{NN}}$ = 200 GeV utilizing the HFT
- The HFT allows direct topological reconstruction of hadronic decays of open-charm mesons
- D± invariant spectrum measured for three centrality classes of Au+Au collisions
  - 0-10%, 10-40%, 40-80%
- D± nuclear modification factor is consistent with that of D^0
  - D^0 and D± mesons are significantly suppressed at high p_T in central Au+Au collisions
  - Charm quarks interact strongly with the QGP
- D±/D^0 yield ratio agrees with the PYTHIA 8 calculation

References

[1] Adam J., *et al.* (STAR), Phys. Rev. C **99**, 034908, (2019).
[2] Adamczyk L., *et al.* (STAR), Phys. Rev. Lett. **118,** 212301, (2017).
[3] TMVA official website: http://tmva.sourceforge.net, (October 11, 2019).
[4] Adamczyk L., *et al.* (STAR), Phys. Rev. D **86,** 072013, (2012).

This work is supported by project LTT18002 of Ministry of Education, Youth and Sports of the Czech Republic and from European Regional Development Fund-Project "Center of Advanced Applied Science" No. CZ.02.1.01/0.0/0.0/16-019/0000778

EUROPEAN UNION
European Structural and Investment Funds
Operational Programme Research, Development and Education

MINISTRY OF EDUCATION, YOUTH AND SPORTS

The STAR Collaboration
drupal.star.bnl.gov/STAR/presentations

CTU CZECH TECHNICAL UNIVERSITY IN PRAGUE

Appendix H

Publications

This document provides an overview of my publications related to my Ph.D. research. First listed are published publications, those submitted or under review are listed at the bottom of the list. During my Ph.D. studies, my research has been conducted at the Nuclear Physics Institute (NPI) of the Czech Academy of Sciences. For that reason, my affiliation within the STAR Collaboration was the NPI and because of STAR internal policies, it was my only affiliation. For that reason, many of my publications have affiliation with NPI only. It was agreed by STAR, that students can have double affiliations on February 22nd 2022. Only recent publications have the Faculty of Nuclear Sciences and Physical Engineering (FNSPE) affiliation. All published publications with my primary authorship are attached below this list.

Publications in this list with FNSPE affiliation are the following:

- Papers: 3. and 4.
- Proceedings: 1., 2., and 7.

Papers

1. J. Vaněk, for the STAR Collaboration, *Open-Charm Hadron Measurements in Au+Au Collisions at* $\sqrt{s_{\mathrm{NN}}} = 200\,\mathrm{GeV}$ *by the STAR Experiment*, Universe 2019, 5(9), 196, `https://www.mdpi.com/2218-1997/5/9/196`.

    - Paper presenting preliminary results (at the time of publication) of my analysis and results from other open-charm analyses at STAR. Paper also includes previously unpublished details about topological selection criteria used in my analysis.

2. J. Adam, *et al.* [STAR Collaboration], *Observation of* $D_s^{\pm}/D^0$ *Enhancement in* Au + Au *Collisions at* $\sqrt{s_{\mathrm{NN}}} = 200\,\mathrm{GeV}$, Phys. Rev. Lett., 127:092301, `https:`

//link.aps.org/doi/10.1103/PhysRevLett.127.092301.

- I was a member of a review committee for this paper on position of Code QA. My contribution was a check of the analysis software and verification of the presented physics results. I was also involved in revision and approval of the text of the paper draft.

3. STAR Collaboration, *Measurement of $D^{\pm}$ meson production and total charm production yield at midrapidity in Au+Au collisions at $\sqrt{s_{\mathrm{NN}}}$ = 200 GeV*, to be submitted to Physics Letters B

   - Paper with my primary authorship, containing results from analysis presented in my thesis. I was responsible for preparation of the results, writing the paper draft and supporting documents (analysis note). I am also the corresponding author for this publication.
   - Publication under review within STAR Collaboration at the time of preparing of this document.

4. STAR Collaboration, *Measurement of D^0 and $D^{\star}$ production in p+p collisions at* $\sqrt{s} = 500\,\mathrm{GeV}$, to be submitted to Physical Review D

   - Paper with my primary authorship, containing results from analysis of D^0 and $\mathrm{D}^{\star}$ mesons in p+p collisions at $\sqrt{s} = 500\,\mathrm{GeV}$. My responsibility is determination of trigger efficiency of high-p_{T} D^0 mesons.
   - Publication under review within STAR Collaboration at the time of preparing of this document.

Proceedings

1. J. Vaněk, for the STAR Collaboration, *Measurements of $D^{\pm}$ meson production and total charm quark production yield at midrapidity in Au+Au collisions at $\sqrt{s_{\mathrm{NN}}}$ = 200 GeV by the STAR experiment*, PoS(PANIC2021)247, https://doi.org/10.22323/1.380.0247.

2. J. Vaněk, for the STAR Collaboration, *Production of $D^{\pm}$ mesons in Au+Au collisions at $\sqrt{s_{\mathrm{NN}}}$ = 200 GeV at the STAR experiment*, PoS(ICHEP2020)584, https://doi.org/10.22323/1.390.0584.

3. J. Vaněk, for the STAR Collaboration, *Measurements of open charm hadrons in Au+Au collisions at $\sqrt{s_{\mathrm{NN}}} = 200\,GeV$ by the STAR experiment*, Slovak Physical Society, Czech Physical Society (ISBN 978-80-89855-13-1), 2020, https://indico.cern.ch/event/851173/attachments/1960505/3658688/sbornikkonference.pdf.

4. J. Vaněk, for the STAR Collaboration, *Measurement of $D^{\pm}$ meson production in Au+Au collisions at $\sqrt{s_{\mathrm{NN}}}$ = 200 GeV with the STAR experiment*, PoS(HardProbes2020)065, https://doi.org/10.22323/1.387.0065.

5. J. Vaněk, for the STAR Collaboration, *Measurements of open-charm hadrons in Au+Au collisions at $\sqrt{s_{\mathrm{NN}}} = 200\,\mathrm{GeV}$ by the STAR experiment*, Springer Proceedings in Physics, vol 250. Springer, https://doi.org/10.1007/978-3-030-53448-6_16.

6. J. Vaněk, for the STAR Collaboration, *Production of Open-Charm Hadrons in Au+Au Collisions at $\sqrt{s_{\mathrm{NN}}} = 200\,\mathrm{GeV}$ Measured by the STAR Experiment*, Proceedings, 10(1), 2019, https://www.mdpi.com/2504-3900/10/1/10.

7. J. Vaněk, for the STAR Collaboration, Measurements of open charm hadrons in Au+Au collisions at $\sqrt{s_{\mathrm{NN}}} = 200\,\mathrm{GeV}$ by the STAR experiment, submitted to International Journal of Modern Physics E.

proceedings

MDPI

Proceedings

Production of Open-Charm Hadrons in Au+Au Collisions at $\sqrt{s_{NN}} = 200$ GeV Mesured by the STAR Experiment †

Jan Vanek

Nuclear Physics Institute, Czech Academy of Sciences, Rez, 250 68, Czech Republic; vanek@ujf.cas.cz; Tel.: +420-266-177-206

† Presented at Hot Quarks 2018—Workshop for young scientists on the physics of ultra-relativistic nucleus-nucleus collisions, Texel, The Netherlands, 7–14 September 2018.

Published: 10 April 2019

Abstract: Charm quarks are primarily produced at the early stages of ultra-relativistic heavy-ion collisions and can therefore probe the quark-gluon plasma throughout its whole evolution. Final-state open-charm hadrons are commonly used to experimentally study the charm quark interaction with the medium. Thanks to the excellent secondary vertex resolution provided by the Heavy Flavor Tracker, STAR is able to directly reconstruct $D^{\pm}$, D^0, D_s, and $\Lambda_c^{\pm}$ via their hadronic decay channels. The topological cuts for signal extraction are optimized using supervised machine learning techniques. In these proceedings, we present an overview of recent open charm results from the STAR experiment. The nuclear modification factors of open-charm mesons and $\Lambda_c^{\pm}/D^0$ ratio are shown as functions of transverse momentum and collision centrality.

Keywords: quark-gluon plasma; STAR experiment; heavy-ion collisions; heavy-flavor mesons; nuclear modification factor; baryon/meson ratio

1. Introduction

At RHIC energies, charm and bottom quarks are produced predominantly through hard partonic scatterings at the early stage of a heavy-ion collision. Therefore, most open-charm hadrons observed at RHIC come from hadronization of primordial charm quarks or decays of b-hadrons. This makes them an ideal probe of the Quark-Gluon Plasma (QGP) because they experience the entire evolution of the medium. A selection of recent open-charm hadron results from Au+Au collisions at $\sqrt{s_{NN}} = 200$ GeV, measured by the STAR experiment using data recorded in 2014 and 2016, is presented and discussed in these proceedings.

The secondary vertices of charm hadrons are reconstructed topologically, utilizing the STAR Heavy Flavor Tracker (HFT) [1,2]. The specific decay channels used in the analysis and basic properties of the open-charm hadron decays are summarized in Table 1. These new measurements will provide insights into phenomena, such as the energy loss of partons inside the QGP and the hadronization process.

Table 1. Summary of open-charm hadrons measured at STAR using the HFT. The left column contains decay channels used for the reconstruction, $c\tau$ is the mean lifetime of a given hadron, and BR is the branching ratio. Numbers are taken from Ref. [3].

Decay Channel	$c\tau$ [μm]	BR [%]
$D^+ \to K^-\pi^+\pi^+$	311.8 ± 2.1	9.46 ± 0.24
$D^0 \to K^-\pi^+$	122.9 ± 0.4	3.93 ± 0.04
$D_s^+ \to \phi\pi^+ \to K^-K^+\pi^+$	149.9 ± 2.1	2.27 ± 0.08
$\Lambda_c^+ \to K^-\pi^+p$	59.9 ± 1.8	6.35 ± 0.33

2. Open-Charm Measurements with the HFT

The main sub-systems for reconstruction of open heavy-flavor hadrons in STAR are the Time Projection Chamber (TPC) which is used for momentum determination and for particle identification, the Time Of Flight (TOF) which improves the particle identification, and the HFT which enables precise reconstruction of the decay topology.

To reconstruct the open-charm hadrons, a series of selection criteria has to be applied to the events and tracks first. The specific selection of the topological variables and values of the criteria depend on the open-charm hadron species and its decay channel. After applying all the selection criteria, the open-charm hadron raw yields (Y_{raw}) are extracted from the invariant mass spectrum. The invariant yield is then calculated from Y_{raw} as:

$$\frac{\mathrm{d}^2N}{2\pi p_{\mathrm{T}}\mathrm{d}p_{\mathrm{T}}\mathrm{d}y} = \frac{Y_{\mathrm{raw}}}{2\pi N_{\mathrm{evt}} BR\, p_{\mathrm{T}}\Delta p_{\mathrm{T}}\Delta y \varepsilon(p_{\mathrm{T}})}, \tag{1}$$

where N_{evt} is number of events, BR is the branching ratio, p_{T} is the transverse momentum, y is the rapidity and $\varepsilon(p_{\mathrm{T}})$ is the reconstruction efficiency. The nuclear modification factor (R_{AA}) is subsequently calculated according to formula:

$$R_{\mathrm{AA}}(p_{\mathrm{T}}) = \frac{\mathrm{d}N^{\mathrm{AA}}/\mathrm{d}p_{\mathrm{T}}}{\langle N_{\mathrm{coll}}\rangle \mathrm{d}N^{\mathrm{PP}}/\mathrm{d}p_{\mathrm{T}}}, \tag{2}$$

where $\mathrm{d}N^{\mathrm{AA}}/\mathrm{d}p_{\mathrm{T}}$ and $\mathrm{d}N^{\mathrm{PP}}/\mathrm{d}p_{\mathrm{T}}$ are the invariant yields measured in heavy-ion collisions and p+p collisions respectively and $\langle N_{\mathrm{coll}}\rangle$ is the mean number of binary nucleon-nucleon collisions computed from the Glauber model. The results presented in this proceedings use a combined measurement of $D^\star$ and D^0 in p+p collisions at $\sqrt{s} = 200$ GeV measured by the STAR experiment in 2009 [4] as a reference.

Figure 1 shows the nuclear modification factor R_{AA} of D^0 and $D^\pm$ mesons as a function of transverse momentum p_{T} for 0–10% central Au+Au collisions at $\sqrt{s_{\mathrm{NN}}} = 200$ GeV. As expected, the level of suppression of D^0 and $D^\pm$ is similar.

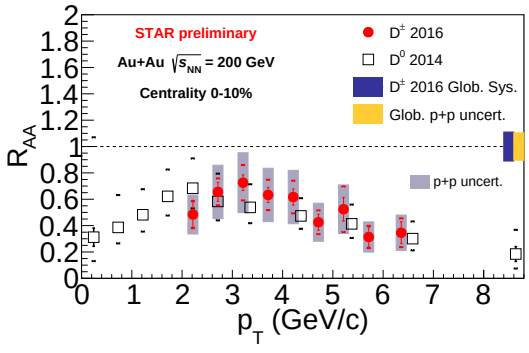

Figure 1. R_{AA} of $D^\pm$ and D^0 mesons as a function p_{T} in 0–10% central Au+Au collisions at $\sqrt{s_{\mathrm{NN}}} =$ 200 GeV.

This result shows that open-charm mesons are significantly suppressed at high p_T, suggesting strong interaction between the charm quarks and the QGP. It is important to note that the Cold Nuclear Matter (CNM) effects may contribute to the suppression as well. Interestingly, the low p_T D^0 mesons also show a suppression. As a result, the integrated R_{AA} of D^0 mesons is below unity which shows that the suppression is likely not only due to the shift in the p_T spectrum, caused by the energy loss in the medium, but also other effects, such as a redistribution of charm quarks among different charm hadrons.

In order to understand the hadronization process in heavy-ion collisions, STAR has measured the D_s/D^0 ratio which is shown in Figure 2. This ratio is larger in Au+Au collisions than predicted by PYTHIA and than that in e+e, p+p and e+p collisions [5]. A better prediction is achieved by the TAMU model [6], but it still underestimates the data. In contrast, the value predicted by the SHM [7] seems to be consistent with the data. This result indicates that the modification of open-charm hadron production in heavy-ion collisions depends on the quark content of the final state hadron.

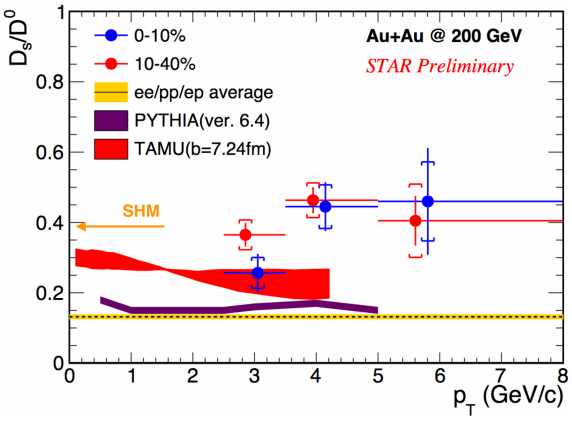

Figure 2. D_s/D^0 ratio as a function of p_T for two centralities. The data is compared to combined e+e, p+p and e+p data [5], PYTHIA, TAMU [6] and SHM [7] models.

For a full understanding of charm production and hadronization in heavy-ion collisions, it is important to study, besides the production of charm mesons, also production of charm baryons. STAR performed the first measurement of Λ_c production in heavy-ion collisions as a functions of collision centrality and p_T. The left panel of Figure 3 shows p_T dependence of the Λ_c/D^0 ratio. PYTHIA and the SHM clearly underestimate the data which indicates significant enhancement of Λ_c production in Au+Au collisions. The coalescence models [8,9] are much closer to the data, but still are not quite able to describe the STAR result, especially at high p_T.

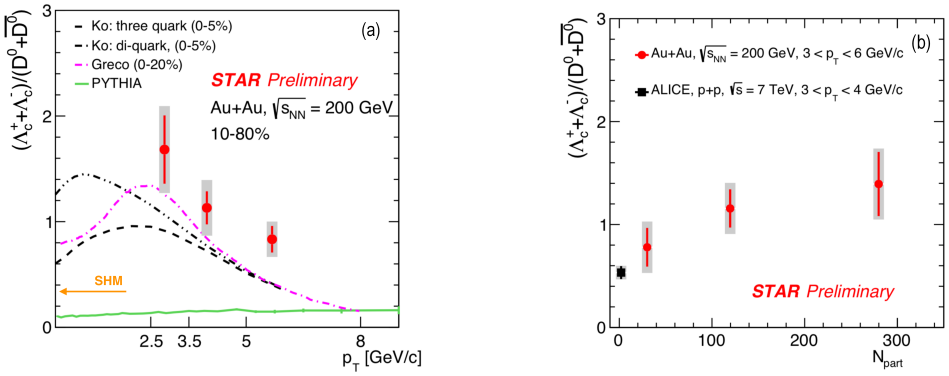

Figure 3. (**a**) The Λ_c/D^0 ratio as a function of p_T for semi-central Au+Au collisions at $\sqrt{s_{NN}} = 200$ GeV. The data is compared to coalescence models [8,9], SHM [7] and PYTHIA. (**b**) The Λ_c/D^0 ratio as a function of centrality. The STAR data is compared to ALICE measurement for p+p collisions at $\sqrt{s} = 7$ TeV [10].

It is very important to note here that, according to this measurement, the production of Λ_c is significantly enhanced in heavy-ion collisions with respect to p+p collisions. This, at least partially, explains the significant suppression of open-charm mesons shown in Figure 1. The right panel of Figure 3 shows that the Λ_c/D^0 ratio increases with the collision centrality which suggests that the larger and the more dense the medium is in a heavy-ion collision, the larger the enhancement of the Λ_c production is observed. Finally, the STAR data are also compared to result from p+p collisions at $\sqrt{s} = 7$ TeV measured by ALICE [10]. The value from the p+p collisions is consistent with that in peripheral Au+Au collisions.

3. Summary

The STAR experiment has measured open-charm hadrons through their hadronic decay channels in Au+Au collisions at $\sqrt{s_{NN}} = 200$ GeV. Topological reconstruction of secondary decay vertices has been used, utilizing the STAR Heavy Flavor Tracker, which has lead to results with exceptional precision. A significant suppression of D^0 and $D^{\pm}$ mesons is observed in central Au+Au collisions, indicating strong interaction of charm quarks with the QGP. The current STAR data also indicate an enhancement of D_s production in Au+Au collisions with respect to e+e, p+p and p+e collisions. This result will help better understand the hadronization process in heavy-ion collisions. The first measurement of Λ_c baryon production as a function of centrality and p_T in Au+Au collisions is also shown. A significant enhancement of the Λ_c production is observed in central Au+Au collisions, suggesting coalescence hadronization of charm quarks in the QGP.

Funding: This paper and the presentation at HQ2018 are funded by project LTT18002 of the Ministry of Education, Youth and Sport of the Czech Republic and by the Grant Agency of the Czech Technical University in Prague, grant No. SGS16/238/OHK4/3T/14.

Acknowledgments: I would like to thank the organizers for giving me the opportunity to present STAR results at the Hot Quarks 2018 conference.

Conflicts of Interest: The author declares no conflict of interest.

References

1. Beavis, D.; Debbe, R.; Lee, J. H.; LeVine, M. J.; Scheetz, R. A.; Videbaek, F.; Xu, Z.; Bielcik, J.; Krus, M.; Dunkelberger, L.E.; et al. The STAR Heavy Flavor Tracker. In *Technical Design Report*; 2011. Available online: https://drupal.star.bnl.gov/STAR/starnotes/public/sn0600 (accessed on 5 April 2019).
2. Contin, G.; Greiner, L.; Schambach, J.; Szelezniak, M.; Anderssen, E.; Bell, J.; Cepeda, M.; Johnson, T.; Qiu, H.; Ritter, H.-G.; et al. The STAR MAPS-based PiXeL detector. *Nucl. Instrum. Meth. A* **2018**, *907*, 60–80, doi:10.1016/j.nima.2018.03.003.
3. Tanabashi, M.; Hagiwara, K.; Hikasa, K.; Nakamura, K.; Sumino, Y.; Takahashi, F.; Tanaka, J.; Agashe, K.; Aielli, G.; Amsler, C.; et al. Review of Particle Physics. *Phys. Rev. Lett.* **2018**, *98*, 030001, doi:10.1103/PhysRevD.98.030001.
4. Adamczyk, L.; Agakishiev, G.; Aggarwal, M. M.; Ahammed, Z; Alakhverdyants, A. V.; Alekseev, I.; Alford, J.; Anderson, B. D.; Anson, C. D.; Arkhipkin, D.; et al. Measuremets of D^0 and D^* production in p+p collisions at $\sqrt{s} = 200$ GeV. *Phys. Rev. D* **2012**, *86*, 072013, doi:10.1103/PhysRevD.86.072013.
5. Lisovyi, M.; Verbytskyi, A.; Zenaiev, O. Combined analysis of charm-quark fragmentation-function measurements. *Eur. Phys. J. C* **2017**, *76*, 397, doi:10.1140/epjc/s10052-016-4246-y.
6. He, M.; Fries, R.J.; Rapp, R. D_s Meson as a Quantitative Probe of Diffusion and Hadronization in Nuclear Collisions. *Phys. Rev. Lett.* **2013**, *110*, 112301, doi:10.1103/PhysRevLett.110.112301.
7. Andronic, A.; Braun-Munzinger, P.; Redlich, K.; Stachel, J. Statistical hadronization of charm in heavy-ion collisions at SPS, RHIC and LHC. *Phys. Lett. B* **2003**, *571*, 36–44, doi:10.1016/j.physletb.2003.07.066.
8. Oh, Y.; Ko, C.M.; Lee, S.H.; Yasui, S. Ratios of heavy baryons to heavy mesons in relativistic nucleus-nucleus collisions. *Phys. Rev. C* **2009**, *79*, 044905, doi:10.1103/PhysRevC.79.044905.

9. Plumari, S.; Minissale, V.; Das, S.K.; Coci, G.; Greco, V. Charmed hadrons from coalescence plus fragmentation in relativistic nucleus-nucleus collisions at RHIC and LHC. *Eur. Phys. J. C* **2018**, *78*, 348, doi:10.1140/epjc/s10052-018-5828-7.
10. Acharya, S.; Acosta, F. T.; Adamová, D.; Adolfsson, J.; Aggarwal, M.M.; Aglieri Rinella, G.; Agnello, M.; Agrawal, N.; Ahammed, Z.; Ahn, S. U.; et al. Λ_c^+ production in pp collisions at $\sqrt{s} = 7$ TeV and in p-Pb collisions at $\sqrt{s_{\rm NN}} = 5.02$ TeV. *J. High Energ. Phys.* **2018**, *9*, 108, doi:10.1007/JHEP04(2018)108.

universe

MDPI

Communication

Open-Charm Hadron Measurements in Au+Au Collisions at $\sqrt{s_{\mathrm{NN}}} = 200$ GeV by the STAR Experiment †

Jan Vanek for the STAR Collaboration

Nuclear Physics Institute, Czech Academy of Sciences, 250 68 Řež, Czech Republic; vanek@ujf.cas.cz; Tel.: +420-266-177-206

† This paper is based on the talk at the 18th Zimányi School, Budapest, Hungary, 3–7 December 2018.

Received: 14 August 2019; Accepted: 5 September 2019; Published: 7 September 2019

Abstract: Study of the open-charm hadron production in heavy-ion collisions is crucial for understanding the properties of the Quark-Gluon Plasma. In these papers, we report on a selection of recent STAR measurements of open-charm hadrons in Au+Au collisions at $\sqrt{s_{\mathrm{NN}}} = 200$ GeV, using the Heavy-Flavor Tracker. In particular, the nuclear modification factors of D^0 and $\mathrm{D}^{\pm}$ mesons, elliptic and directed flow of D^0 mesons, $\mathrm{D_s}/\mathrm{D}^0$ and $\Lambda_\mathrm{c}/\mathrm{D}^0$ yield ratios are discussed. The observed suppression of D^0 and $\mathrm{D}^{\pm}$ mesons suggests strong interactions of the charm quarks with the QGP. The measured elliptic flow of D^0 mesons is large and follows the NCQ scaling, suggesting that charm quarks may be close to thermal equilibrium with the QGP medium. Both $\mathrm{D_s}/\mathrm{D}^0$ and $\Lambda_\mathrm{c}/\mathrm{D}^0$ yield ratios are found to be enhanced in Au+Au collisions. The enhancement can be explained by models incorporating coalescence hadronization of charm quarks. In addition, the directed flow of the D^0 mesons is measured to be negative and larger than that of light-flavor mesons which is in a qualitative agreement with hydrodynamic model predictions with a tilted QGP bulk.

Keywords: Quark-Gluon Plasma; open-charm hadrons; nuclear modification factor; elliptic flow; directed flow

1. Introduction

One of the main goals of the STAR experiment is to study the properties of the Quark-Gluon Plasma (QGP), which can be produced in ultra-relativistic heavy-ion collisions. Charm quarks are an excellent probe of the medium created in these collisions since they are produced predominantly in initial hard partonic scatterings and therefore experience the whole evolution of the medium.

As the charm quark propagates through the QGP, it interacts with the QGP and loses energy. The most common way to access the energy loss is by studying the modification of open-charm hadron yields in heavy-ion collisions with respect to those in p+p collisions using the nuclear modification factor:

$$R_{\mathrm{AA}}(p_{\mathrm{T}}) = \frac{\mathrm{d}N^{\mathrm{AA}}/\mathrm{d}p_{\mathrm{T}}}{\langle N_{\mathrm{coll}}\rangle \mathrm{d}N^{\mathrm{PP}}/\mathrm{d}p_{\mathrm{T}}}, \quad (1)$$

where $\langle N_{\mathrm{coll}}\rangle$ is the mean number of binary collisions, calculated using the Glauber model [1]. $R_{\mathrm{AA}} < 1$ for high-p_{T} open-charm hadrons is considered a signature connected with the presence of the QGP and the level of the suppression gives access to the strength of the interaction between the charm quark and the medium [2,3].

Another way to obtain information about the charm quark interaction with the QGP is to measure the azimuthal anisotropy of the produced charm hadrons (v_2). The magnitude of the v_2 that the charm

quarks develop through the interaction with the surrounding medium carries important information about the transport properties of the medium [2,3].

To have a more complete picture of the open-charm hadron production in heavy-ion collisions, it is also important to understand the charm quark hadronization process. The charm quark hadronization mechanism can be studied through the measurements of the Λ_c/D^0 and D_s/D^0 yield ratios [4,5].

Since the charm quarks are created very early in the heavy-ion collisions, they can be used to probe initial conditions in such collisions. Recent theoretical calculations suggest that measurement of the directed flow v_1 of open-charm mesons can be sensitive to the initial tilt of the QGP bulk and also to the initial electro-magnetic field induced by the passing spectators [6,7].

The following section summarizes recent STAR measurements of open-charm hadrons in the context of the observables and phenomena described above.

2. Open-Charm Measurements with the HFT

All results presented in this summary are from Au+Au collisions at $\sqrt{s_{NN}} = 200$ GeV which were collected by the STAR experiment in years 2014 and 2016. Topological reconstruction of the decays, using an excellent vertex position resolution from the Heavy-Flavor Tracker (HFT) [8], was used to extract the signals of the open-charm hadrons listed in Table 1.

Table 1. List of open-charm hadrons measured using the HFT. The left column contains decay channels used for the reconstruction, $c\tau$ is the proper decay length of a given hadron, and BR is the branching ratio. Charge conjugate particles are measured as well. Values are taken from Ref. [9].

Decay Channel	$c\tau$ [μm]	BR [%]
$D^+ \to K^-\pi^+\pi^+$	311.8 ± 2.1	9.46 ± 0.24
$D^0 \to K^-\pi^+$	122.9 ± 0.4	3.93 ± 0.04
$D_s^+ \to \phi\pi^+ \to K^-K^+\pi^+$	149.9 ± 2.1	2.27 ± 0.08
$\Lambda_c^+ \to K^-\pi^+p$	59.9 ± 1.8	6.35 ± 0.33

The reconstruction of $D^\pm$ mesons in data from 2016 will be used as an example as the steps of reconstruction of all the aforementioned particles are similar. First, a series of selection criteria is applied to the events and tracks. Specific values of the criteria, used in the analysis of $D^\pm$ mesons, are listed in Table 2.

Table 2. Summary of selection criteria used for extraction of $D^\pm$ candidates from the data. For more details, see the text.

Event selection		$\lvert V_z\rvert < 6$ cm
		$\lvert V_z - V_{z(\mathrm{VPD})}\rvert < 3$ cm
Track selection		$p_T > 500$ MeV
		$\lvert\eta\rvert < 1$
		nHitsFit > 20
		nHitsFit/nHitsMax > 0.52
		HFT tracks = PXL1 + PXL2 + (IST or SSD)
Particle identification	TPC	$\lvert n\sigma_\pi\rvert < 3$
		$\lvert n\sigma_K\rvert < 2$
	TOF	$\lvert 1/\beta - 1/\beta_\pi\rvert < 0.03$
		$\lvert 1/\beta - 1/\beta_K\rvert < 0.03$
Decay topology		$DCA_{\mathrm{pair}} < 80$ μm
		30 μm $< L_{D^\pm} < 2\,000$ μm
		$\cos(\theta) > 0.998$
		$\Delta_{\max} < 200$ μm
		$DCA_{\pi-\mathrm{PV}} > 100$ μm
		$DCA_{K-\mathrm{PV}} > 80$ μm

The events are selected so that the position of the primary vertex (PV) along the beam axis (V_z), which is determined using the HFT and Time Projection Chamber (TPC) [10], is no further than 6 cm from the center of the STAR detector. This is necessary due to physical dimensions and acceptance of the HFT. The value of V_z is also compared to that measured by the Vertex Position Detector [11] ($V_{z(\mathrm{VPD})}$) which helps with rejection of pile-up events as the VPD is a fast detector.

From these events, only tracks with sufficiently large transverse momentum ($p_T > 300\,\mathrm{MeV}/c$) are selected to reduce the combinatorial background. The pseudorapidity criterion $|\eta| < 1$ is given by the STAR detector acceptance. All tracks are also required to have sufficient number of hits used for track reconstruction inside the TPC (nHitsFit) and to be properly matched to the HFT to ensure their good quality. In this case, a good HFT track is required to have one hit in each of the inner layers (PXL1 and PXL2) and at least one hit in one of the two outer layers (IST or SSD) [1].

Next, all the selected tracks are identified using the TPC and the Time Of Flight (TOF) [12] detectors. The particle identification (PID) with the TPC is done based on energy loss of charged particles in the TPC gas. The measured energy loss is compared to the expected one, which is calculated with Bichsel formula, using nσ variable [13]. The PID using TOF is done by comparing velocity of given particle measured by TOF (β) and that calculated from its momentum and rest mass (β_π or β_K).

When charged pions and kaons are identified they are combined into K$\pi\pi$ triplets within each event. The topology of the triplet is then constrained using variables shown in Figure 1. More specifically they are: the maximum distance of closest approach of track pairs (DCA_{pair}), $D^\pm$ meson decay length $L_{D^\pm}$, cosine of the pointing angle $\cos(\theta)$, maximum distance between reconstructed secondary vertices of track pairs (Δ_{max}), and the distance of closest approach to the primary vertex of the kaon ($DCA_{K-\mathrm{PV}}$) and each of the pions ($DCA_{\pi-\mathrm{PV}}$). Specific values used for $D^\pm$ signal extraction are listed in Table 2. The topological selection criteria used for $D^\pm$ mesons will be optimized using the TMVA [14] in near future, as was done for other open-charm hadron results presented in the following section, in order to improve statistical significance and also to extend the p_T range.

The $D^\pm$ signal is subsequently extracted from the invariant mass spectrum of the K$\pi\pi$ triplets which are divided into two sets. The first consists of only correct-sign charge combinations, which may come from decay of $D^\pm$ mesons (see Table 1) and contains the signal together with a combinatorial and a correlated background. The combinatorial background shape can be determined using the second set which contains only wrong-sign charge combinations which cannot originate from decay of $D^\pm$ mesons [2]. The correct-sign and the scaled [3] wrong-sign invariant mass spectrum of the K$\pi\pi$ triplets near invariant mass of the $D^\pm$ mesons is shown in top panel of Figure 2. The scaled wrong-sign spectrum can be then subtracted from the correct-sign one which leads to the spectrum shown in the bottom panel of Figure 2. The invariant mass peak is fitted with Gaussian function in order to determine its width σ and mean. The raw yield Y_{raw} is calculated using bin counting method in $\pm 3\sigma$ region around the peak mean.

---

[1] The HFT consists of total of four layers of silicon detectors. The two innermost layers are Monolithic Active Pixel Sensors (MAPS), PXL1 and PXL2. The outer layers are strip detectors, the Intermediate Silicon Tracker (IST) and the Silicon Strip Detector (SSD).

[2] This method is sufficient for $D^\pm$ analysis. In case of e.g., D^0 or Λ_c, the correlated background needs to be addressed separately as it is more significant for those analyses.

[3] For combinatorial reasons, there are approximately three times as many wrong-sign charge combinations as the correct-sign ones in this case. The wrong-sign spectrum is therefore scaled so that it matches the correct-sign one in order to estimate the combinatorial background. The scale factor is determined from ratio of integrals of the correct and wrong-sign spectrum outside the $D^\pm$ mass peak region which is set $1.795\,\mathrm{GeV}/c^2 < M_{\mathrm{inv}} < 1.945\,\mathrm{GeV}/c^2$.

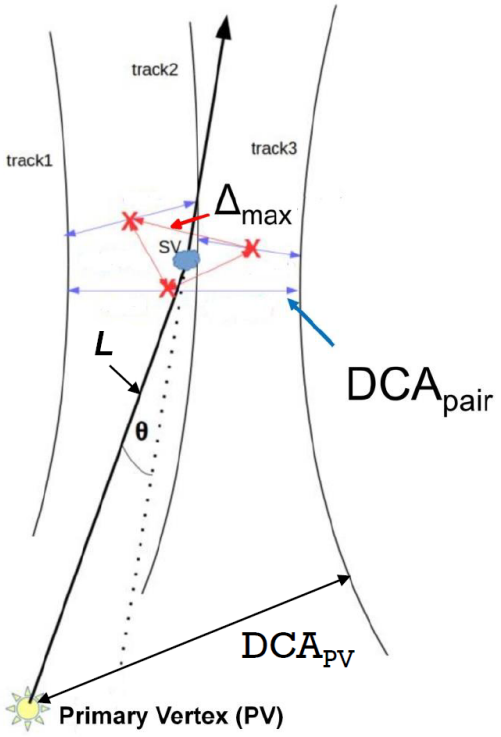

Figure 1. Depiction of a three body decay topology of $D^{\pm}$ mesons. For details about individual variables, see the text.

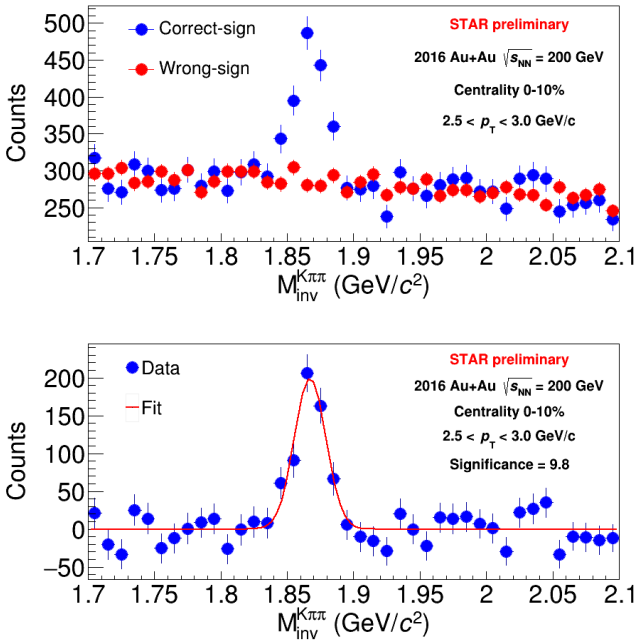

Figure 2. Invariant mass spectrum of $K\pi\pi$ triplets for: (**top**) correct-sign combinations (blue points) and with wrong-sign combinations (red points) and (**bottom**) after background subtraction. The data are fitted with Gaussian function.

The invariant spectrum of the $D^{\pm}$ mesons is then calculated from the raw yield Y_{raw} as:

$$\frac{\mathrm{d}^2N}{2\pi p_{\mathrm{T}}\mathrm{d}p_{\mathrm{T}}\mathrm{d}y} = \frac{1}{2\pi p_{\mathrm{T}}} \frac{Y_{\mathrm{raw}}}{N_{\mathrm{evt}} BR \Delta p_{\mathrm{T}} \Delta y \varepsilon(p_{\mathrm{T}})}, \tag{2}$$

where N_{evt} is number of recorded MB events, BR is the branching ratio (see Table 1) and $\varepsilon(p_{\mathrm{T}})$ is the total reconstruction efficiency calculated using the data-driven fast-simulator. More details about the efficiency calculation can be found in article [15]. An example of reconstruction efficiency of $D^{\pm}$ mesons in 0%–10% central Au+Au collisions extracted with selection criteria from Table 2 is shown in Figure 3.

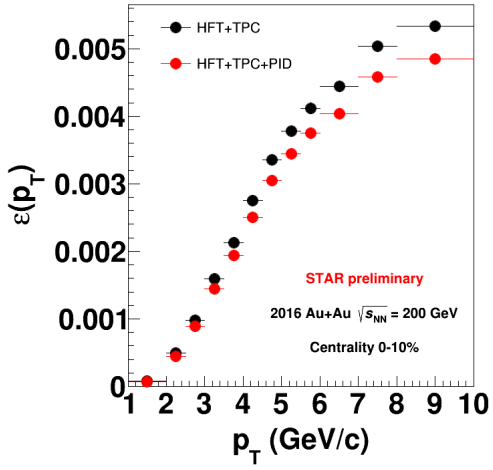

Figure 3. $D^{\pm}$ reconstruction efficiency in 0%–10% central Au+Au collisions calculated using the data-driven fast simulator without (black points) and with the PID efficiency (red points).

3. Results

Figure 4 shows the nuclear modification factor R_{AA} of D^0 [15] and $D^{\pm}$ mesons as a function of p_{T} in 0%–10% central Au+Au collisions. Both D^0 and $D^{\pm}$ are significantly suppressed in high-p_{T} region which suggests a significant energy loss of charm quarks in the QGP. The low to intermediate p_{T} bump structure is consistent with predictions of models incorporating large collective flow of charm quarks [15].

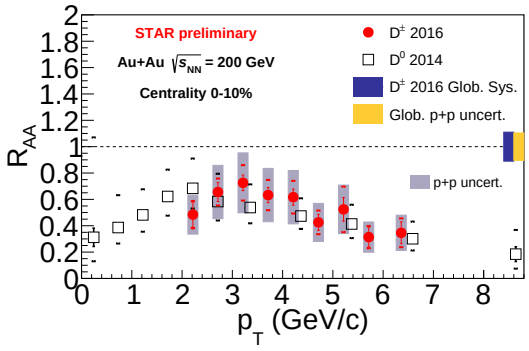

Figure 4. R_{AA} of D^0 [15] and $D^{\pm}$ mesons as a function p_{T} in 0%–10% central Au+Au collisions at $\sqrt{s_{\mathrm{NN}}} = 200$ GeV. The p+p reference is from combined $D^{\star}$ and D^0 measurement by STAR in p+p collisions at $\sqrt{s} = 200$ GeV [16].

STAR has also measured and published the elliptic flow (v_2) of D^0 mesons using 2014 data [17]. Results with improved precision from the combined 2014+2016 data are shown in Figure 5a. The results

Measurements of open-charm hadrons in Au+Au collisions at $\sqrt{s_{\mathrm{NN}}} = 200$ GeV by the STAR experiment

Jan Vanek[1], for the STAR Collaboration

Nuclear Physics Institute, Czech Academy of Sciences, Řež, Czech Republic
vanek@ujf.cas.cz

Abstract. At RHIC energies, charm quarks are primarily produced at early stages of ultra-relativistic heavy-ion collisions. This makes them an excellent probe of the Quark-Gluon Plasma (QGP) produced in these collisions since they experience the whole evolution of the medium. STAR is able to study the production of charm quarks through direct reconstruction of hadronic decays of open-charm hadrons. This is possible thanks to an excellent vertex resolution provided by the Heavy Flavor Tracker. In these proceedings, we present a selection of the most recent results on open-charm hadron production, in particular the nuclear modification factors of $\mathrm{D}^{\pm}$ and D^{0}, elliptic and triangular flow of D^{0}, the $\Lambda_{\mathrm{c}}^{\pm}/\mathrm{D}^{0}$ yield ratio, and the directed flow of D^{0} mesons.

Keywords: Open-charm hadrons, quark-gluon plasma, STAR experiment, Heavy-Flavor Tracker, nuclear modification factor, elliptic flow, directed flow

1 Introduction

One of the main goals of the heavy-ion program at the STAR experiment is to study properties of the Quark-Gluon Plasma (QGP). Charm quarks are an excellent probe of the QGP as they are produced at very early stages of ultra-relativistic heavy-ion collisions and so experience the whole evolution of the hot and dense medium. STAR is able to study production of charm quarks through a precise topological reconstruction of open-charm hadron decays utilizing the Heavy Flavor Tracker (HFT) [1].

Various measurements are used to study interactions of charm quarks with the QGP. In these proceedings, we present a selection of the most recent results on open-charm hadron production from the STAR experiment. In particular, we discuss the nuclear modification factors of $\mathrm{D}^{\pm}$ and D^{0} mesons which give access to the charm quark energy loss in the QGP, and also D^{0} elliptic (v_2) and triangular flow (v_3) coefficients which can probe the charm quark transport in the QGP. We show the $\Lambda_{\mathrm{c}}^{\pm}/\mathrm{D}^{0}$ yield ratio as a function of transverse momentum (p_{T}) and collision centrality that helps us better understand the charm quark hadronization process in heavy-ion collisions. In addition, we present the rapidity-odd directed flow of D^{0} mesons, which can be used to probe the initial tilt of the QGP bulk and the effects of the early-time magnetic field.

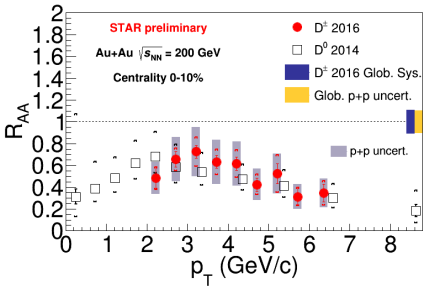

Fig. 1. Nuclear modification factor of D^0 [2] and $D^{\pm}$ mesons as a function of p_T in 0-10% central Au+Au collisions at $\sqrt{s_{NN}} = 200$ GeV.

2 Results

Figure 1 shows the nuclear modification factors (R_{AA}) of D^0 and $D^{\pm}$ mesons as a function of transverse momentum in 0-10% central Au+Au collisions. Both open-charm mesons show a significant suppression at high p_T which suggests strong interactions of the charm quarks with the QGP. The R_{AA} evolution in low to intermediate p_T region suggests a large collective flow of charm quarks [2] which can also be seen in Figure 2.

Figure 2 demonstrates a test of the Number of Constituent Quarks (NCQ, or n_q) scaling [3] for elliptic flow (left panel) and triangular flow (right panel) for both D^0 mesons and light-flavor hadrons. The STAR data show that charm quarks acquire similar level of collectivity as the light quarks in the QGP medium.

The presence of the QGP may also influence the charm quark hadronization. In order to study that, STAR has measured the $\Lambda_c^{\pm}/D^0$ yield ratio as a function of p_T (Figure 3, left panel) and number of participants N_{part} (Figure 3, right panel). The ratio shows an enhancement with respect to p+p collisions and PYTHIA calculation, and is reasonably reproduced by models incorporating coalescence hadronization of the charm quarks [6, 7].

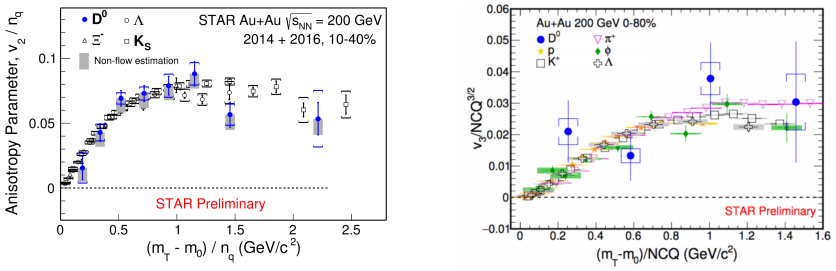

Fig. 2. The NCQ-scaled elliptic **(left)** and triangular **(right)** flow of D^0 mesons and light-flavor hadrons [4] in Au+Au collisions at $\sqrt{s_{NN}} = 200$ GeV.

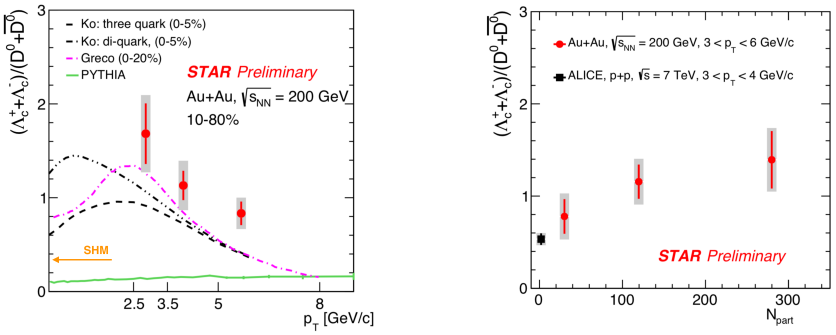

Fig. 3. (left) $\Lambda_c^{\pm}/\mathrm{D}^0$ yield ratio as a function of transverse momentum p_{T} in Au+Au collisions at $\sqrt{s_{\mathrm{NN}}} = 200$ GeV. The data are compared to PYTHIA, Statistical Hadronization Model [5] and coalescence model calculations [6, 7]. **(right)** $\Lambda_c^{\pm}/\mathrm{D}^0$ yield ratio as a function of number of participants N_{part}. The ALICE experiment measurement of the ratio in p+p collisions at $\sqrt{s} = 7$ TeV [8] is shown for comparison.

Theoretical calculations predict that the charm quarks might also be sensitive to the initial tilt of the QGP bulk and the electromagnetic (EM) field induced by the passing spectators [9]. The former leads to a large negative slope of the directed flow versus rapidity ($\mathrm{d}v_1/\mathrm{d}y$) of open-charm mesons, and the latter to a negative slope for D^0 and a positive slope for $\overline{\mathrm{D}^0}$. When combined, the slope is predicted to be negative for both D^0 and $\overline{\mathrm{D}^0}$ but larger for D^0 than for $\overline{\mathrm{D}^0}$ in Au+Au collisions at $\sqrt{s_{\mathrm{NN}}} = 200$ GeV. The STAR result on D^0 and $\overline{\mathrm{D}^0}$ v_1 are shown in Figure 4. The current precision of the measurement is not sufficient to conclude on the EM induced splitting, but the $\mathrm{d}v_1/\mathrm{d}y$ slopes are indeed negative and significantly larger that of light-flavor mesons, as discussed in Ref. [10].

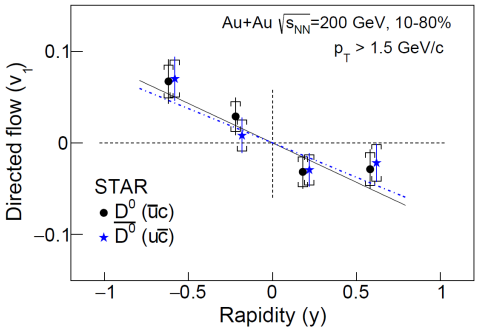

Fig. 4. Directed flow D^0 and $\overline{\mathrm{D}^0}$ mesons as a function of rapidity in 10-80% central Au+Au collisions at $\sqrt{s_{\mathrm{NN}}} = 200$ GeV. The solid black and blue dashed lines are fits to the data. Taken from Ref. [10].

3 Summary

The STAR experiment has extensively studied the production of open-charm hadrons in Au+Au collisions at $\sqrt{s_{NN}} = 200$ GeV through a precise topological reconstruction of their hadronic decays, utilizing the HFT. The latest results show that the D^0 and $D^{\pm}$ mesons are suppressed in central Au+Au collisions, suggesting a substantial energy loss of the charm quarks in the QGP. The charm quarks also exhibit a significant collective motion as suggested by the observed large elliptic and triangular flow of D^0 mesons. The QGP seems to influence the charm quark hadronization. The STAR results on the $\Lambda_c^{\pm}/D^0$ yield ratio are in qualitative agreement with theoretical models incorporating coalescence hadronization of charm quarks. The measured D^0 dv_1/dy slope is qualitatively consistent with hydrodynamical model calculations with tilted QGP bulk [9].

Acknowledgement: These proceedings and presentation are supported by OPVVV grant CZ.02.1.01/0.0/0.0/16_013/0001569 and the project LTT18002 of the Ministry of Education, Youth and Sports of the Czech Republic.

References

1. Beavis, D., et al.: The STAR Heavy-Flavor Tracker, Technical Design Report; 2011. Available online: https://drupal.star.bnl.gov/STAR/starnotes/public/sn0600 (accessed on 6 September 2019).
2. Adam, J., et al. [STAR Collaboration]: Centrality and transverse momentum dependence of D^0-meson production at mid-rapidity in Au+Au collisions at $\sqrt{s_{\rm NN}} =$ 200 GeV. *Phys. Rev. C* **99**, 034908, (2019). doi:10.1103/PhysRevC.99.034908
3. S. Afanasiev, et al [PHENIX Collaboration]: Elliptic flow for phi mesons and (anti)deuterons in Au+Au collisions at $\sqrt{s_{\rm NN}} = 200$ GeV. *Phys. Rev. Lett.* **99**, 052301, (2007). doi:10.1103/PhysRevLett.99.052301
4. Abelev, B.I. et al. [STAR Collaboration]: Centrality dependence of charged hadron and strange hadron elliptic flow from $\sqrt{s_{\rm NN}} = 200$ GeV Au+Au collisions. *Phys. Rev. C* **77**, 054901, (2008). doi:10.1103/PhysRevC.77.054901
5. Andronic, A., et al.: Statistical hadronization of charm in heavy-ion collisions at SPS, RHIC and LHC. *Phys. Lett. B* **571**, 36–44, (2003). doi:10.1016/j.physletb.2003.07.066
6. Oh, Y. et al.: Ratios of heavy baryons to heavy mesons in relativistic nucleus-nucleus collisions. *Phys. Rev. C* **79**, 044905, (2009). doi:10.1103/PhysRevC.79.044905
7. Plumari, S.; Minissale, V.; Das, S.K.; Coci, G.; Greco, V.: Charmed hadrons from coalescence plus fragmentation in relativistic nucleus-nucleus collisions at RHIC and LHC. *Eur. Phys. J. C* **78**, 348, (2018). doi:10.1140/epjc/s10052-018-5828-7
8. Acharya, S.; et al. [The ALICE collaboration]: Λ_c^+ production in pp collisions at $\sqrt{s} = 7$ TeV and in p-Pb collisions at $\sqrt{s_{\rm NN}} = 5.02$ TeV. *J. High Energ. Phys.* **2018**, 108, (2018). doi:10.1007/JHEP04(2018)108
9. Chatterjee, S.; Bozek, P.: Interplay of drag by hot matter and electromagnetic force on the directed flow of heavy quarks. **2018**, arXiv:1804.04893.
10. Adam, J. et al. [STAR Collaboration]: First observation of the directed flow of D^0 and $\overline{D^0}$ in Au+Au collisions at $\sqrt{s_{\rm NN}} = 200$ GeV. *Phys. Rev. Lett.* **123**, 162301, (2019). doi:10.1103/PhysRevLett.123.162301

PROCEEDINGS OF SCIENCE

Measurement of $D^{\pm}$ meson production in Au+Au collisions at $\sqrt{s_{NN}}$ = 200 GeV with the STAR experiment

Jan Vanek ***for the STAR Collaboration***[*]

Nuclear Physics Institute of the Czech Academy of Sciences,
Husinec - Řež 130, Řež, Czech Republic

E-mail: vanek@ujf.cas.cz

Charm quarks are an excellent probe of the Quark-Gluon Plasma created in heavy-ion collisions as they are produced at very early stages of such collisions and subsequently experience the whole evolution of the system. At STAR experiment, charm quark production can be accessed by direct topological reconstruction of open-charm hadrons thanks to an excellent track pointing resolution provided by the Heavy Flavor Tracker. In these proceedings, we present a measurement of $D^{\pm}$ meson production in Au+Au collisions at $\sqrt{s_{NN}}$ = 200 GeV by STAR using data collected in 2014 and 2016. Supervised machine-learning techniques were used to optimize the signal significance of the $D^{\pm}$ three body decay $D^{\pm} \rightarrow K^{\mp}\pi^{\pm}\pi^{\pm}$ reconstruction. The $D^{\pm}$ invariant spectra were then obtained in 0-10%, 10-40%, and 40-80% central Au+Au collisions. The measured nuclear modification factor R_{AA} as a function of transverse momentum (p_T) reveals a significant suppression of high-p_T $D^{\pm}$ mesons in central and mid-central Au+Au collisions with respect to p+p collisions. The $(D^+ + D^-)/(D^0 + \overline{D^0})$ yield ratio has also been extracted and compared to that from PYTHIA 8 calculations.

HardProbes2020
1-6 June 2020
Austin, Texas

[*]Speaker

PoS(HardProbes2020)065

1. Physics motivation

STAR is a versatile experiment which studies a variety of physics phenomena observed in high energy p+p and heavy-ion collisions. One of the main goals of the STAR experiment is to study properties of a hot and dense medium called the Quark-Gluon Plasma (QPG) created in heavy-ion collisions. The charm quarks are an excellent probe of the QGP as they are produced at very early stages of the heavy-ion collisions which means that they experience the whole evolution of the system. One way to access information about the charm quark production in heavy-ion collisions is reconstruction of open-charm hadrons. From year 2014 to 2016, STAR was equipped with the Heavy Flavor Tracker (HFT) [1] which allowed direct topological reconstruction of decays of the open-charm hadrons.

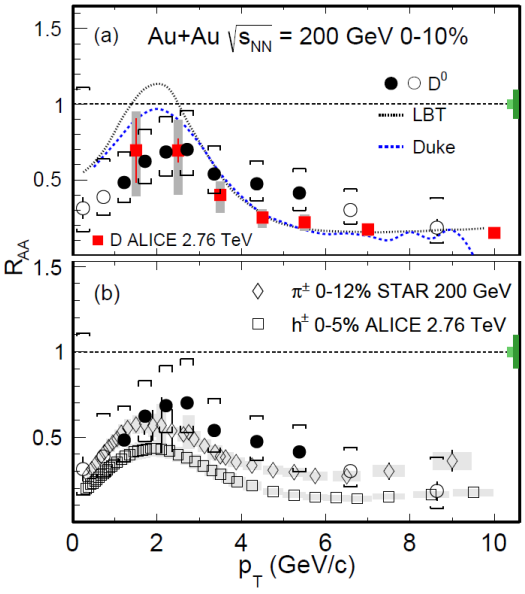

Figure 1: Nuclear modification factor of D^0 mesons measured by STAR in 0-10% central Au+Au collisions at $\sqrt{s_{NN}}$ = 200 GeV [2]. The data are compared to STAR measurement of charged pions in Au+Au collisions at the same energy [3] and also to LBT and Duke model calculations [4, 5] . ALICE measurements of D mesons and charged hadrons are shown for comparison as well [6, 7].

Result from one of the first open-charm hadron measurements with the HFT by STAR is presented in Fig. 1 which shows the nuclear modification factor (R_{AA}) of D^0 mesons as a function of transverse momentum (p_T) for 0-10% central Au+Au collisions at $\sqrt{s_{NN}}$ = 200 GeV. High-p_T D^0 mesons are significantly suppressed in Au+Au collisions with respect to p+p collisions. The suppression is comparable to that of charged pions measured by STAR in Au+Au collisions at $\sqrt{s_{NN}}$ = 200 GeV. The D^0 data are reasonably well reproduced by models incorporating both collisional and radiative energy losses, and collective flow [4, 5].

In these proceedings we present recent results from measurement of $D^{\pm}$ mesons in Au+Au collisions at $\sqrt{s_{NN}}$ = 200 GeV. One key difference between the $D^{\pm}$ and D^0 measurements is that D^0 mesons are reconstructed in two-body hadronic decay channel ($D^0 \rightarrow K^-\pi^+$, and its charge conjugate), but $D^{\pm}$ mesons are accessed through three-body hadronic decay ($D^{\pm} \rightarrow K^{\mp}\pi^{\pm}\pi^{\pm}$).

This is possible only utilizing the precise track reconstruction with the HFT. The measurement of $D^{\pm}$ mesons serves as an independent check for the open-charm suppression and will also play an important role in measuring total open-charm cross section.

2. Results

The invariant spectra of $D^{\pm}$ mesons have been measured for three centrality classes (0-10%, 10-40%, and 40-80%) of Au+Au collisions at $\sqrt{s_{NN}}$ = 200 GeV. The methods for signal reconstruction and reconstruction efficiency correction are analogous to those used for D^0 and described in detail in Ref. [2]. The invariant spectra are used to calculate the nuclear modification factor (R_{AA}) and the $(D^+ + D^-)/(D^0 + \overline{D^0})$ yield ratio.

The R_{AA} of $D^{\pm}$ mesons as a function of p_T is shown in Fig. 2 for 0-10%, 40-80%, and 40-80% central Au+Au collisions at $\sqrt{s_{NN}}$ = 200 GeV. The R_{AA} of D^0 mesons is plotted for comparison [2]. As expected, the level of suppression of $D^{\pm}$ and D^0 mesons is comparable and the larger suppression for more central Au+Au collisions suggests stronger interactions of the charm quarks with the QGP compared to peripheral collisions.

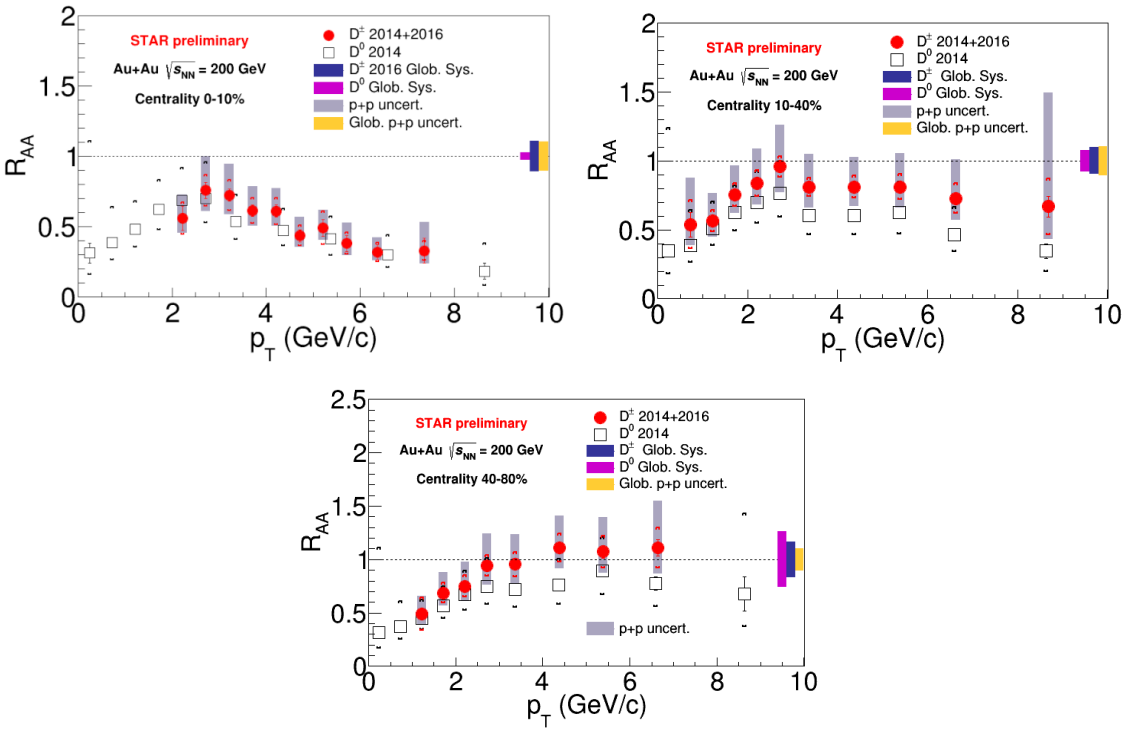

Figure 2: R_{AA} of D^0 [2] and $D^{\pm}$ mesons as a function of p_T measured by STAR in 0-10%, 10-40%, and 40-80% central Au+Au collisions at $\sqrt{s_{NN}}$ = 200 GeV.

The $(D^+ + D^-)/(D^0 + \overline{D^0})$ yield ratio is shown in Fig. 3 for 0-10%, 10-40%, and 40-80% central Au+Au collisions at $\sqrt{s_{NN}}$ = 200 GeV. The data are in agreement with PYTHIA 8 calculation which suggests that no modification of the ratio is observed in Au+Au collisions with respect to p+p collisions. The agreement is observed in all studied centrality classes which means that the ratio has no or very week centrality dependence.

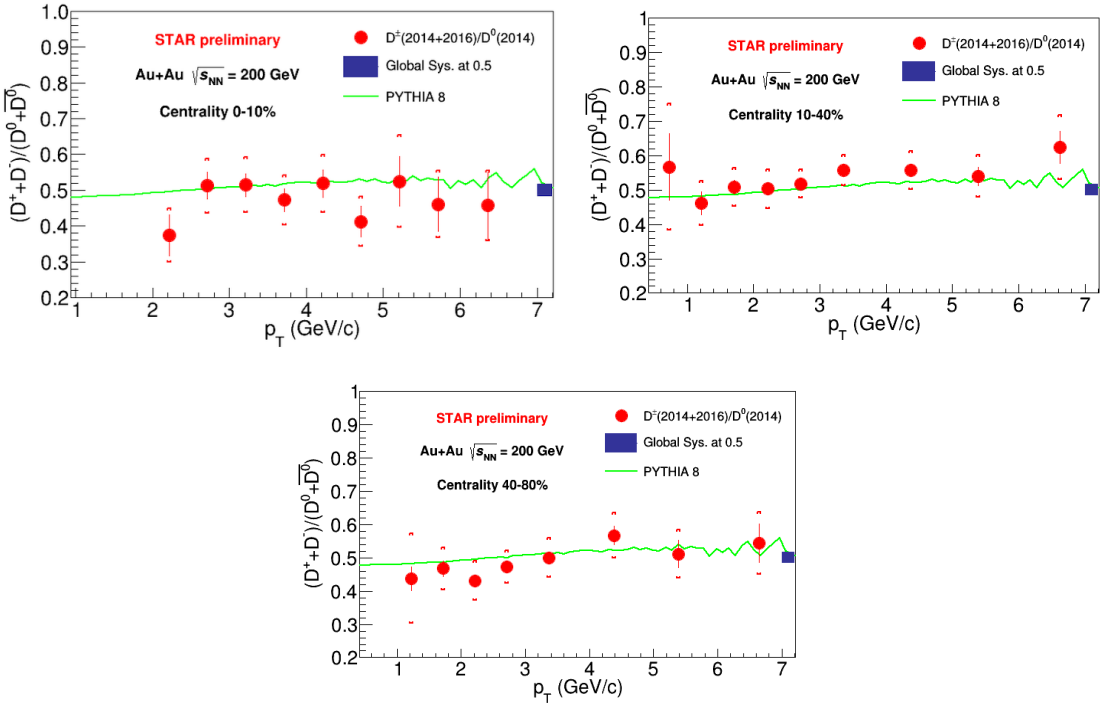

Figure 3: $(D^+ + D^-)/(D^0 + \overline{D^0})$ yield ratio measured as a function of p_{T} by STAR in 0-10%, 10-40%, and 40-80% central Au+Au collisions at $\sqrt{s_{\mathrm{NN}}}$ = 200 GeV. The data are compared to PYTHIA 8 theoretical calculation.

3. Summary

The STAR experiment has extensively studied production of open-charm hadrons in heavy-ion collisions utilizing the HFT which allows direct topological reconstruction of hadronic decays of these hadrons. The invariant spectra of $\mathrm{D}^{\pm}$ mesons have been measured for three centrality classes (0-10%, 10-40%, and 40-80%) of Au+Au collisions at $\sqrt{s_{\mathrm{NN}}}$ = 200 GeV and were subsequently used to calculate the R_{AA} and $(D^+ + D^-)/(D^0 + \overline{D^0})$ yield ratio. The R_{AA} of $\mathrm{D}^{\pm}$ mesons reveals a similar level of suppression as observed for D^0 mesons which suggests that charm quarks strongly interact with the QGP. The $(D^+ + D^-)/(D^0 + \overline{D^0})$ yield ratio is consistent with PYTHIA 8 calculation which means that no modification of the ratio is observed in Au+Au collisions with respect to the p+p collisions. In the near future, the $\mathrm{D}^{\pm}$ measurement will help to constrain the total open-charm cross section in Au+Au collisions at $\sqrt{s_{\mathrm{NN}}}$ = 200 GeV.

Acknowledgments

This research is funded by the project LTT18002 of the Ministry of Education, Youth, and Sport of the Czech Republic.

References

[1] Beavis, D., *et al.*, *The STAR Heavy-Flavor Tracker*, Technical Design Report, (2011). Available online: https://drupal.star.bnl.gov/STAR/starnotes/public/sn0600 (Accessed on 16 July 2020).

[2] Adam, J., *et al.* [STAR Collaboration], *Centrality and transverse momentum dependence of D^0-meson production at mid-rapidity in Au+Au collisions at* $\sqrt{s_{\rm NN}}$ = 200 *GeV*, *Phys. Rev. C* **99**, 034908, (2019).

[3] Abelev, B.I., *et al.* [STAR Collaboration], *Energy dependence of* $\pi^{\pm}$, p *and* $\overline{p}$ *transverse momentum spectra for Au+Au collisions at* $\sqrt{s_{\rm NN}}$ = 62.4*and*200 *GeV*, *Phys. Lett. B* **655**, 104-113, (2007).

[4] Cao, S., *et al.*, *Linearized Boltzmann transport model for jet propagation in the quark-gluon plasma: Heavy quark evolution*, *Phys. Rev. C* **94**, 014909, (2016).

[5] Xu, Y., *et al.*, *Data-driven analysis for the temperature and momentum dependence of the heavy-quark diffusion coefficient in relativistic heavy-ion collisions*, *Phys. Rev. C* **97**, 014907, (2018).

[6] Abelev, B.I., *et al.* [ALICE Collaboration], *Transverse momentum dependence of D-meson production in Pb-Pb collisions at* $\sqrt{s_{\rm NN}}$ = 2.76 *TeV*, *J. High Energ. Phys.* **2016**, 81, (2016).

[7] Adam, J., *et al.* [ALICE Collaboration], *Centrality dependence of charged particle production at large transverse momentum in Pb–Pb collisions at* $\sqrt{s_{\rm NN}}$ = 2.76 *TeV*, *Phys. Lett. B* **720**, 52-62, (2013).

PROCEEDINGS OF SCIENCE

Production of $D^{\pm}$ mesons in Au+Au collisions at $\sqrt{s_{NN}} = 200$ GeV with the STAR experiment

Jan Vanek ***for the STAR Collaboration***[a,b,*]

[a] *Nuclear Physics Institute of the Czech Academy of Sciences, Husinec - Řež 130, Řež, Czech Republic*

[b] *Faculty of Nuclear Sciences and Physical Engineering, Czech Technical University in Prague, Břehová 78/7, 115 19 Staré Město, Prague, Czech Republic*

E-mail: vanek@ujf.cas.cz

Charm quarks are an excellent probe of the quark-gluon plasma created in heavy-ion collisions as they are produced at a very early stage of such collisions and subsequently experience the whole evolution of the system. With the STAR experiment, charm quark production can be measured by direct topological reconstruction of open-charm hadrons thanks to the exceptional spatial resolution of the Heavy Flavor Tracker detector. In these proceedings, we present a measurement of $D^{\pm}$ meson production in Au+Au collisions at $\sqrt{s_{NN}}$ = 200 GeV by the STAR experiment using data collected in 2014 and 2016. Supervised machine-learning techniques were used to maximize signal significance in raw yield extraction from the three-body hadronic decay channel $D^{\pm} \rightarrow K^{\mp}\pi^{\pm}\pi^{\pm}$. The $D^{\pm}$ invariant spectra were measured in 0-10%, 10-40%, and 40-80% Au+Au collisions. The measured transverse-momentum (p_T) differential nuclear modification factor $R_{AA}(p_T)$ reveals a significant suppression of high-p_T $D^{\pm}$ mesons in central (0-10%) Au+Au collisions with respect to p+p collisions. The $(D^+ + D^-)/(D^0 + \overline{D^0})$ yield ratio has also been extracted and compared to that from PYTHIA calculations.

40th International Conference on High Energy physics - ICHEP2020
July 28 - August 6, 2020
Prague, Czech Republic (virtual meeting)

*Speaker

PoS(ICHEP2020)584

STAR is a versatile experiment which studies a variety of physics phenomena observed in high energy p+p and heavy-ion collisions. One of the main goals of the STAR experiment is to study the properties of a hot and dense medium called the Quark-Gluon Plasma (QPG) created in heavy-ion collisions. The charm and bottom quarks are an excellent probe of the QGP as they are produced in the very early stage of heavy-ion collisions which means that they experience the whole evolution of the system. One way to access information about the charm quark production in heavy-ion collisions is through the reconstruction of open-charm hadrons. From year 2014 to 2016, STAR was equipped with the Heavy Flavor Tracker (HFT) [1] which allowed direct topological reconstruction of decays of open-charm hadrons.

In these proceedings, we present recent results from measurement of $D^{\pm}$ mesons in Au+Au collisions at $\sqrt{s_{NN}}$ = 200 GeV. One key difference between the $D^{\pm}$ and D^0 measurements is that D^0 mesons are reconstructed in two-body hadronic decay channel ($D^0 \rightarrow K^-\pi^+$, and its charge conjugate), but $D^{\pm}$ mesons are accessed through three-body hadronic decay ($D^{\pm} \rightarrow K^{\mp}\pi^{\pm}\pi^{\pm}$). This is possible thanks to excellent track pointing resolution provided by the HFT. The measurement of $D^{\pm}$ mesons serves as an independent check for the open-charm suppression and will also play an important role in measuring the total charm cross section in heavy-ion collisions.

The invariant yields of $D^{\pm}$ mesons as a function of transverse momentum (p_T) have been measured in three centrality classes (0-10%, 10-40%, and 40-80%) of Au+Au collisions at $\sqrt{s_{NN}}$ = 200 GeV. The methods for signal reconstruction and reconstruction efficiency correction are analogous to those used for D^0 and described in detail in Ref. [2]. The p_T spectra are used to calculate the nuclear modification factor (R_{AA}) and the $(D^+ + D^-)/(D^0 + \overline{D^0})$ yield ratio.

The R_{AA} of $D^{\pm}$ mesons as a function of p_T is shown in Fig. 1 for 0-10% and 10-40% central Au+Au collisions at $\sqrt{s_{NN}}$ = 200 GeV. The R_{AA} of D^0 mesons is plotted for comparison [2]. As expected, the level of suppression for $D^{\pm}$ and D^0 mesons is comparable. The suppression is observed to be larger for 0-10% central than for 10-40% central Au+Au collisions which is likely caused by different size of the QGP bulk in the two collision centrality classes.

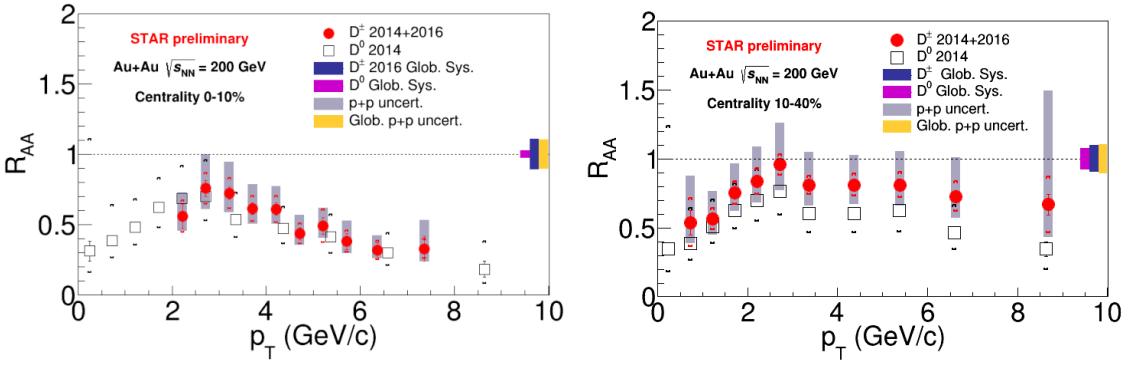

Figure 1: R_{AA} of D^0 [2] and $D^{\pm}$ mesons as a function of p_T measured in 0-10% (left) and 10-40% (right) central Au+Au collisions at $\sqrt{s_{NN}}$ = 200 GeV.

The $(D^+ + D^-)/(D^0 + \overline{D^0})$ yield ratios are shown in Fig. 2 for 0-10% and 10-40% central Au+Au collisions at $\sqrt{s_{NN}}$ = 200 GeV. The data are in agreement with PYTHIA 8 calculations which suggests that no modification of the ratio is observed in Au+Au collisions with respect to

p+p collisions. The agreement is observed in all studied centrality classes indicating that the ratio has no or very week centrality dependence.

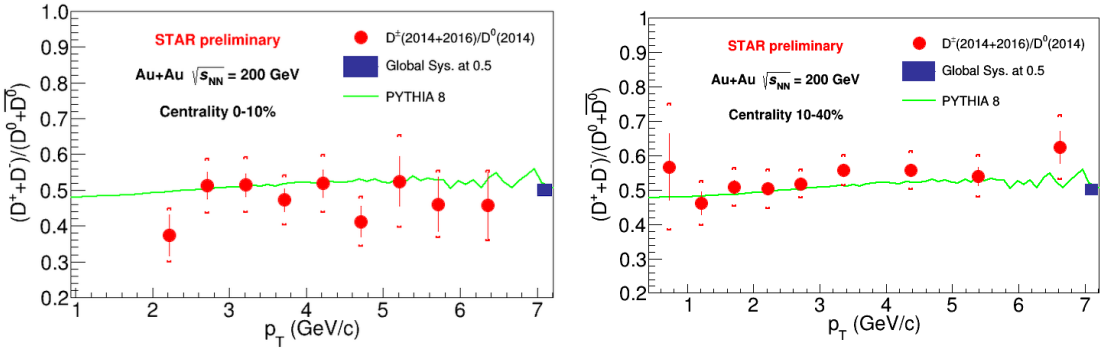

Figure 2: $(D^+ + D^-)/(D^0 + \overline{D^0})$ yield ratio measured as a function of p_T by STAR in 0-10% and 10-40% central Au+Au collisions at $\sqrt{s_{NN}}$ = 200 GeV. Data are compared to PYTHIA 8 calculation.

Summary

The STAR experiment has extensively studied the production of open-charm hadrons in heavy-ion collisions utilizing the HFT which allows direct topological reconstruction of hadronic decays of these hadrons. The invariant yields of $D^{\pm}$ mesons have been measured for three centrality classes (0-10%, 10-40%, and 40-80%) of Au+Au collisions at $\sqrt{s_{NN}}$ = 200 GeV and were subsequently used to calculate the R_{AA} and $(D^+ + D^-)/(D^0 + \overline{D^0})$ yield ratio. The R_{AA} of $D^{\pm}$ mesons reveals a significant suppression at high p_T, similar to that observed for D^0 mesons, which suggests that charm quarks strongly interact with the QGP. The $(D^+ + D^-)/(D^0 + \overline{D^0})$ yield ratio is consistent with a PYTHIA 8 model calculation indicating that no modification of the ratio is observed in Au+Au collisions with respect to the p+p collisions. The $D^{\pm}$ measurement will help to constrain the total charm quark cross section in Au+Au collisions at $\sqrt{s_{NN}}$ = 200 GeV.

Acknowledgments

This research is funded by the project LTT18002 of the Ministry of Education, Youth, and Sport of the Czech Republic and by European Regional Development Fund-Project "Center of Advanced Applied Science" No. CZ.02.1.01/0.0/0.0/16_019/0000778.

References

[1] Giacomo, C., *et al.*, *The STAR MAPS-based PiXeL detector*, *Nucl. Instrum. Methods. Phys. Res. A* **907**, 60-80, (2018).

[2] Adam, J., *et al.* [STAR Collaboration], *Centrality and transverse momentum dependence of D^0-meson production at mid-rapidity in Au+Au collisions at $\sqrt{s_{NN}}$ = 200 GeV*, *Phys. Rev. C* **99**, 034908, (2019).

MEASUREMENT OF OPEN-CHARM HADRONS IN Au+Au COLLISIONS AT $\sqrt{s_{\rm NN}} = 200$ GeV BY THE STAR EXPERIMENT

J. Vanek for the STAR Collaboration, vanek@ujf.cas.cz, Nuclear Physics Institute of the Czech Academy of Sciences, Prague, Czech republic

PHYSICS MOTIVATION

One of the main goals of the heavy-ion program at the STAR experiment is to study properties of the Quark-Gluon Plasma (QGP). Charm quarks are an excellent probe of the QGP as they are produced at very early stages of ultra-relativistic heavy-ion collisions and therefore experience the whole evolution of the hot and dense medium. STAR is able to study production of charm quarks through a precise topological reconstruction of open-charm hadron decays utilizing the Heavy Flavor Tracker (HFT) [1].

Various measurements are used to study interactions of charm quarks with the QGP. In these proceedings, we present a selection of recent results on open-charm hadron production from the STAR experiment. In particular, we discuss the nuclear modification factors ($R_{\rm AA}$) of $\rm D^{\pm}$ and $\rm D^0$ mesons which give access to the charm quark energy loss in the QGP. We show the $\Lambda_c^{\pm}/\rm D^0$ and $\rm D_s/D^0$ yield ratios which help us better understand the charm quark hadronization process in heavy-ion collisions. In addition, we present the rapidity-odd directed flow of $\rm D^0$ mesons, which can be used to probe the initial tilt of the QGP bulk and the effects of the early-time magnetic field.

RESULTS

Figure 1 shows the $R_{\rm AA}$ of $\rm D^0$ [2] and $\rm D^{\pm}$ mesons as a function of transverse momentum ($p_{\rm T}$) in 0-10% central Au+Au collisions. Both open-charm mesons show a significant suppression at high $p_{\rm T}$ which suggests strong interactions of the charm quarks with the QGP. The $R_{\rm AA}$ evolution in low to intermediate $p_{\rm T}$ region suggests a large collective flow of charm quarks [2].

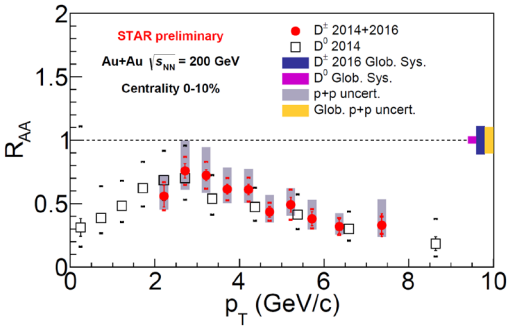

Fig. 1. $R_{\rm AA}$ of $\rm D^0$ [2] and $\rm D^{\pm}$ mesons as a function of $p_{\rm T}$ in 0-10% central Au+Au collisions at $\sqrt{s_{\rm NN}} = 200$ GeV.

The presence of the QGP may also influence the charm quark hadronization. In order to study that, STAR has measured the $\Lambda_c^{\pm}/\rm D^0$ yield ratio as a function of number of participants ($N_{\rm part}$) [3] as shown in Fig. 2. In central collisions, the ratio shows an enhancement with respect to PYTHIA 8.2 p+p calculations (Monash tune [4]) with and without color reconnection (CR) [5]. The centrality dependence follows a similar trend as baryon to meson ratio of light flavor hadrons [6, 7]. The data are reasonably reproduced by the Catania model incorporating coalescence and fragmentation hadronization of the charm quarks [8].

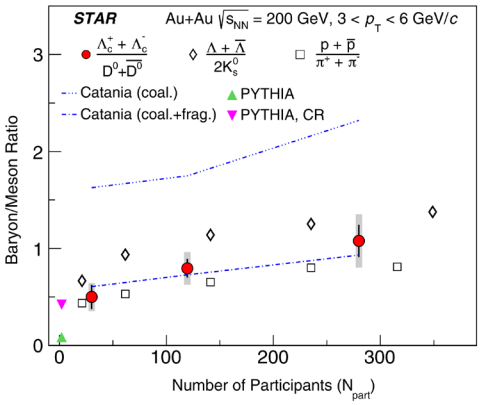

Fig. 2. $\Lambda_c^{\pm}/\rm D^0$ yield ratio as a function of number of participants $N_{\rm part}$. The open-charm hadron data are compared to measurements of light flavor hadrons [6, 7], PYTHIA calculation and the Catania model incorporating coalescence and fragmentation hadronization of the charm quarks [8]. Taken from Ref. [3].

To get more detailed information about hadronization of charm quarks, STAR has also measured the $\rm D_s/D^0$ yield ratio, as shown in Fig. 3. The ratio is enhanced with respect to a PYTHIA 8.2 calculation, suggesting enhanced $\rm D_s$ production in Au+Au collisions with respect to p+p collisions. The data are qualitatively described by various models incorporating coalescence and fragmentation hadronization [8, 9, 10].

Theoretical calculations predict that the charm quarks could also be used to probe the initial tilt of the QGP bulk and the electromagnetic (EM) field induced by the passing spectators [11]. The former leads to a large negative slope of the directed flow versus rapidity ($\rm d$$v_1$/$\rm d$$y$) of open-charm mesons, and the latter to a negative slope for $\rm D^0$ and a positive slope for $\overline{\rm D^0}$. When combined, the slope is predicted to be negative for both $\rm D^0$ and $\overline{\rm D^0}$ but larger for $\rm D^0$ than for $\overline{\rm D^0}$ in Au+Au collisions at $\sqrt{s_{\rm NN}} = 200$ GeV. The STAR results on $\rm D^0$ and $\overline{\rm D^0}$ v_1 are shown in Fig. 4. The current precision of the measurement is not sufficient to conclude on the EM induced splitting, but the $\rm d$$v_1$/$\rm d$$y$ slope is indeed negative and significantly larger than that of light-flavor mesons, as discussed in Ref. [12].

CONCLUSIONS

The STAR experiment has extensively studied the production of open-charm hadrons in Au+Au collisions at $\sqrt{s_{\rm NN}} = 200$ GeV through a precise topological reconstruction of their hadronic decays, uti-

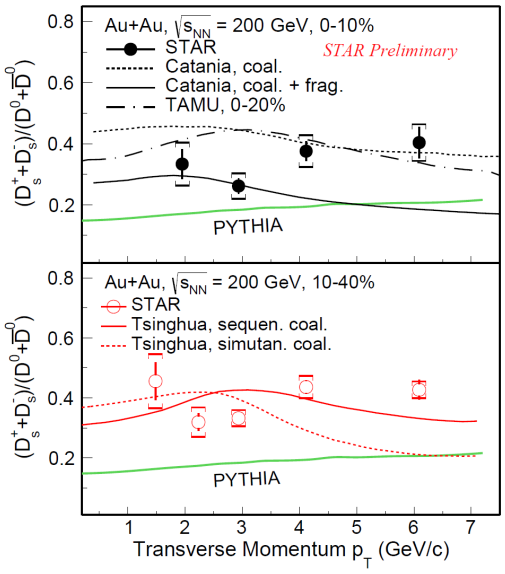

Fig. 3. D_s/D^0 yield ratio as a function of p_T. The data are compared to various models incorporating coalescence and fragmentation hadronization of charm quarks [8, 9, 10] and PYTHIA p+p calculations.

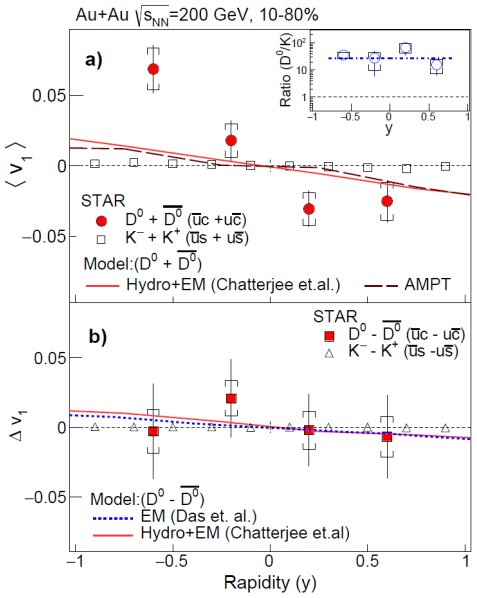

Fig. 4. **(a)** Directed flow of D^0 and $\overline{D^0}$ mesons at $p_T > 1.5$ GeV/c as a function of rapidity in 10-80% central Au+Au collisions at $\sqrt{s_{NN}} = 200$ GeV, compared to calculations of a hydrodynamic model with an initial EM field [13] and the AMPT model [14]. (b) Difference in v_1 between D^0 and $\overline{D^0}$ compared to a model prediction with only the initial EM field [13] and one that combines EM effects with hydrodynamics [11]. The D^0 data are compared to measurement of charged kaons [15]. Taken from Ref. [12].

lizing the HFT. The latest results show that the D^0 and $D^{\pm}$ mesons are suppressed in central Au+Au collisions, suggesting a substantial energy loss of the charm quarks in the QGP. The QGP seems to influence the charm quark hadronization. The STAR results on the $\Lambda_c^{\pm}/D^0$ and D_s/D^0 yield ratios are in qualitative agreement with theoretical models incorporating coalescence and fragmentation hadronization of charm quarks. The measured D^0 dv_1/dy slope is qualitatively consistent with hydrodynamical model calculations with tilted QGP bulk [11].

ACKNOWLEDGMENT:

This work was also supported from European Regional Development FundProject "Center of Advanced Applied Science" No. CZ.02.1.01/0.0/0.0/16-019/0000778 and by the grant LTT18002 of Ministry of Education, Youth and Sports of the Czech Republic.

REFERENCES

1. D. Beavis et al., Technical Design Report, 2011. Available online: https://drupal.star.bnl.gov/STAR/starnotes/public/sn0600(accessed on 6 September 2019).
2. J. Adam et al., [STAR Collaboration], Phys. Rev. C **99**, 034908 (2019).
3. J. Adam et al., [STAR Collaboration], Phys. Rev. Lett. **124**, 172301 (2020).
4. P. Skands, S. Carrazza, J. Rojo, Eur. Phys. J. C **74**, 3024 (2014).
5. C. Bierlich, J. R. Christiansen, Phys. Rev. **D 92**, 094010 (2015).
6. B.I. Abelev et al., [STAR Collaboration], Phys. Rev. Lett. **97**, 152301 (2006).
7. G. Agakishiev et al., [STAR Collaboration], Phys. Rev. Lett. **108**, 072301 (2012).
8. S. Plumari et al., Eur. Phys. J. C **78**, 348 (2018).
9. M. He et al., Phys. Rev. Lett. **110**, 112301 (2013).
10. J. Zhao et al., arXiv1805.10858, (2018).
11. S. Chatterjee, P. Bozek, Phys. Lett. B **798**, 134955 (2019).
12. J. Adam et al., [STAR Collaboration], Phys. Rev. Lett. **123**, 162301 (2019).
13. S.K. Das et al., Phys Lett B **768**, 260 (2017).
14. M. Nasim, S. Singha, Phys. Rev. C 97, 064917 (2018).
15. L. Adamczyk et al., [STAR Collaboration], Phys. Rev. Lett. 120, 062301 (2018).

PROCEEDINGS OF SCIENCE

Measurements of $D^{\pm}$ meson production and total charm quark production yield at midrapidity in Au+Au collisions at $\sqrt{s_{NN}}$ = 200 GeV by the STAR experiment

Jan Vanek[a,b,1,*]

[a] *Nuclear Physics Institute of the Czech Academy of Sciences, Husinec - Řež 130, Řež, Czech Republic*

[b] *Faculty of Nuclear Sciences and Physical Engineering, Czech Technical University in Prague, Břehová 78/7, 115 19 Staré Město, Prague, Czech Republic*

E-mail: vanek@ujf.cas.cz

Charm quarks are produced at very early stage of ultra-relativistic Au+Au collisions at RHIC top energy. This makes them an ideal probe of the Quark-Gluon Plasma, as they experience the whole evolution of the hot and dense medium. At STAR, production of charm quarks can be accessed via a direct topological reconstruction of hadronic decays of open charm hadrons, utilizing the excellent resolution of the Heavy Flavor Tracker. In these proceedings, we present measurements of $D^{\pm}$ meson production in Au+Au collisions at $\sqrt{s_{NN}}$ = 200 GeV. The invariant yields are extracted in 0-10%, 10-40%, and 40-80% central Au+Au collisions. The result is then used to calculate the nuclear modification factor, which reveals a strong suppression of high-p_T $D^{\pm}$ mesons in Au+Au collisions with respect to p+p collisions. In addition, the $D^{\pm}/D^0$ yield ratio as a function of transverse momentum is calculated and compared to PYTHA 8 prediction. No significant modification of the ratio in Au+Au collisions is observed. The measurement of $D^{\pm}$ completed the measurements of the major ground states of open charm hadrons (D^0, $D^{\pm}$, D_s, Λ_c), that are used to calculate the total charm quark production cross section per binary nucleon-nucleon collision in 10-40% central Au+Au collisions. The measured value in Au+Au collisions is consistent with that measured in p+p collisions.

**** Particles and Nuclei International Conference - PANIC2021 ****
**** 5 - 10 September, 2021 ****
**** Online ****

[1] For the STAR Collaboration.
[*] Speaker

PoS(PANIC2021)247

1. Physics motivation

One of the main goals of the STAR experiment is to study properties of the Quark-Gluon Plasma (QGP) created in Au+Au collisions. One very important probe to the QGP is by measurement of charm quark production, as the charm quarks are produced in hard partonic scatterings before the formation of the hot and dense medium. This means that they experience the whole evolution of the QGP medium. When traversing the medium, charm quarks lose energy via radiative and collisional processes. The information about the charm quark production at the STAR experiment can be accessed via direct topological reconstruction of hadronic decays of open charm hadrons, which is made possible thanks to the excellent pointing resolution of the Heavy Flavor Tracker [1].

STAR has measured the nuclear modification factor $R_{\rm AA}$ of directly reconstructed $\rm D^0$ mesons, as shown in Fig. 1. The $\rm D^0$ mesons show a strong suppression for $p_{\rm T} > 3\,{\rm GeV}/c$ in central Au+Au collisions at $\sqrt{s_{\rm NN}}$ = 200 GeV compared to p+p collisions at the same energy. The level of suppression is similar that of charged pions at $\sqrt{s_{\rm NN}}$ = 200 GeV, which suggests that the charm quarks interact stronlgy with the QGP and loose significant portion of their momentum and energies.

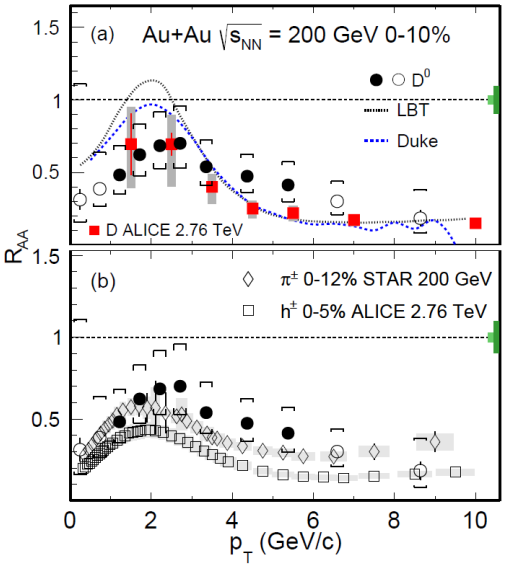

Figure 1: Nuclear modification factor of $\rm D^0$ mesons as a function of $p_{\rm T}$ measured in 0-10% central Au+Au collisions at $\sqrt{s_{\rm NN}}$ = 200 GeV. The open circles indicate data points for which the p+p reference [2] had to be extrapolated. The data are compared to measurements of $\pi^{\pm}$ mesons in Au+Au collisions at $\sqrt{s_{\rm NN}}$ = 200 GeV by STAR [3] and to D mesons [4] and charged hadrons [5] in Pb-Pb collisions at $\sqrt{s_{\rm NN}}$ = 2.76 TeV by ALICE. Taken from Ref. [6].

The measurement of $\rm D^{\pm}$ mesons in Au+Au collisions provides additional insight into the charm quark production in heavy-ion collisions and can help to better understand charm quark energy loss in the QGP. The $\rm D^{\pm}$ measurement, together with measurements of other major ground state open charm hadrons ($\rm D^0$, $\rm D_s$, Λ_c) [6–8], are used for calculation of the total charm quark production cross section in Au+Au collisions.

2. Results

The $D^{\pm}$ mesons are reconstructed through the topological reconstruction of their hadronic decays $D^{\pm} \rightarrow K^{\mp}\pi^{\pm}\pi^{\pm}$. The topological selection criteria are optimized using rectangular cut optimization (CutsSA method) from the TMVA ROOT package [9] in order to maximize the signal significance. The invariant yields are extracted in 0-10%, 10-40%, and 40-80% central Au+Au collisions at $\sqrt{s_{\rm NN}}$ = 200 GeV.

The invariant yields are then used to calculate the $R_{\rm AA}$ of $D^{\pm}$ mesons as a function of transverse momentum ($p_{\rm T}$), as shown in Fig. 2. The $D^{\pm}$ measurement is compared to that of the D^0 mesons [6]. Both $D^{\pm}$ and D^0 mesons show comparable level of suppression in all three centrality classes, within the uncertainties. The high-$p_{\rm T}$ $D^{\pm}$ mesons show a significant suppression in central Au+Au collisions, which indicates strong interactions of the charm quarks with the QGP. The suppression gets weaker towards more peripheral collisions, further supporting that the attenuation is caused by a medium created in the central Au+Au collisions at $\sqrt{s_{\rm NN}}$ = 200 GeV. At the same time, both the $D^{\pm}$ and D^0 mesons show a suppression for $p_{\rm T} < 2\,{\rm GeV}/c$. The p+p reference used for calculation of the $R_{\rm AA}$ is taken from Ref. [2].

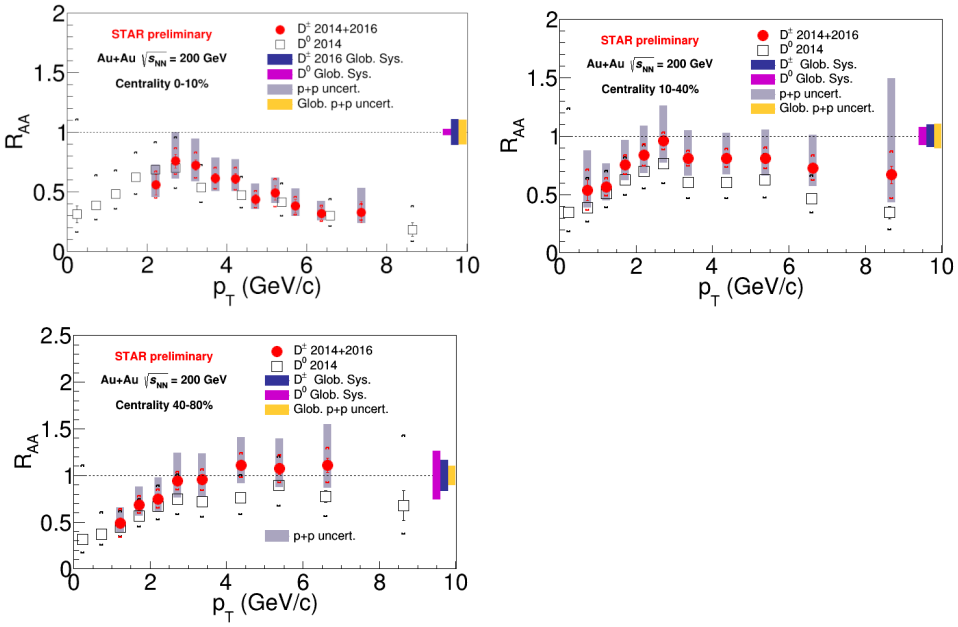

Figure 2: Nuclear modification factor of D^0 [6] and $D^{\pm}$ mesons measured in Au+Au collisions at $\sqrt{s_{\rm NN}}$ = 200 GeV. High-$p_{\rm T}$ D^0 and $D^{\pm}$ mesons show a significant suppression in 0-10% central Au+Au collisions, suggesting strong interactions of the charm quarks with the QGP.

To better understand the charm quark hadronization process one can examine the $D^{\pm}/D^0$ yield ratio, which is shown in Fig. 3. The measured ratio is consistent with PYTHIA 8 calculation [10] indicating that the ratio is not modified in Au+Au collisions with respect to p+p collisions. This observation suggests that both mesons are suppressed by the same mechanism and their hadronization mechanisms are likely very similar in Au+Au collisions.

In order to have a better understanding of the hadronization process of the charm quarks in Au+Au collisions, STAR has calculated the total charm production cross section per binary

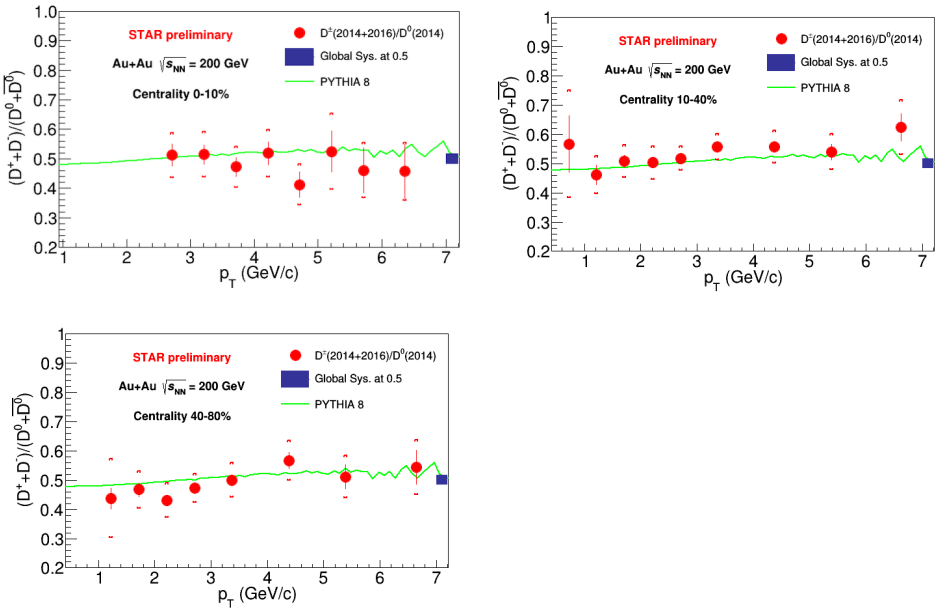

Figure 3: The $D^{\pm}/D^0$ yield ratio as a function of p_T measured in Au+Au collisions at $\sqrt{s_{NN}}$ = 200 GeV. The data are in a good agreement with PYTHIA 8 prediction [10].

nucleon-nucleon collision in 10-40% central Au+Au collisions at $\sqrt{s_{NN}}$ = 200 GeV, using four major ground states of open charm hadrons: D^0, $D^{\pm}$, D_s, Λ_c. The resulting cross section $d\sigma_{Au+Au}/dy$ = 152 ± 13 (stat.) ± 29 (sys.) µb is consistent with that measured in p+p collisions at the same energy [2], i.e. $d\sigma_{p+p}/dy$ = 130 ± 30 (stat.) ± 26 (sys.) µb, as listed in Tab. 1. The cross section appears to follow the number-of-binary-collision scaling. However, the individual contributions to the total cross section are different. The cross sections of D^0 and $D^{\pm}$ mesons are smaller than those in p+p collisions in central and mid-central collisions, as shown in Fig. 1, but the cross sections of D_s [7] and Λ_c [8] are enhanced, most likely due to coalescence hadronization of charm quarks. This calculation indicates that the production of charm quarks is likely unaffected by nuclear effects in Au+Au collisions, but the hadronization process is modified by the medium which leads to a re-distribution of the charm quarks among the open charm hadron species.

Collision system	**Hadron**	$d\sigma/dy$ [µb]
Au+Au at 200 GeV Centrality: 10-40%	D^0	41 ± 1 (stat.) ± 5 (sys.)
	$D^{\pm}$	18 ± 1 (stat.) ± 3 (sys.)
	D_s	15 ± 1 (stat.) ± 5 (sys.)
	Λ_c	78 ± 13 (stat.) ± 28 (sys.)
	Total:	152 ± 13 (stat.) ± 29 (sys.)
p+p at 200 GeV	Total:	130 ± 30 (stat.) ± 26 (sys.)

Table 1: Total open charm hadron cross section as measured in 10-40% central Au+Au collisions and in p+p collisions at 200 GeV.

Summary

Measurements of open charm hadrons is an essential part of the physics program of the STAR experiment. An important contribution to this effort is the measurement of $D^{\pm}$ mesons in Au+Au collisions at $\sqrt{s_{NN}}$ = 200 GeV. Similar to the D^0 mesons, the high-p_T $D^{\pm}$ mesons show a significant suppression in central Au+Au collisions, which is likely caused by strong interactions of the charm quarks with the QGP. The mechanism of the suppression is probably the same for $D^{\pm}$ and D^0 mesons, as the $D^{\pm}/D^0$ yield ratio measured in Au+Au is compatible with the ratio calculated using PYTHIA 8. The D^0, $D^{\pm}$, D_s, and Λ_c invariant yields are used to calculate the total charm quark production cross section per binary nucleon-nucleon collision in Au+Au collisions. The calculated value is comparable with that measured in p+p collisions within the uncertainties, indicating that the total charm yield in heavy-ion collisions follows the number-of-binary-collision scaling. The individual contributions to the cross section are different, on the other hand, with D^0 and $D^{\pm}$ being suppressed, and D_s and Λ_c enhanced in the Au+Au collisions. This observation is consistent with a significant contribution of the coalescence hadronization in the QGP in Au+Au collisions, leading to a re-distribution of charm quarks among the open-charm hadron species.

Acknowledgments

The work is supported by European Regional Development Fund-Project "Center of Advanced Applied Science" No. CZ.02.1.01/0.0/0.0/16-019/0000778 and by the grant LTT18002 of Ministry of Education, Youth and Sports of the Czech Republic.

References

[1] Giacomo, C., *et al.*, *Nucl. Instrum. Methods. Phys. Res. A* **907**, 60-80, (2018).

[2] Adamczyk, L., *et al.* [STAR Collaboration], *Phys. Rev. D* **86**, 072013, (2012).

[3] Abelev, B.I., *et al.* [STAR Collaboration], *Phys. Lett. B* **655**, 104, (2007).

[4] Adam, J., *et al.* [ALICE Collaboration], *J. High Energ. Phys.* **2016**, 81, (2016).

[5] Abelev, B.I., *et al.* [ALICE Collaboration], *Phys. Lett. B* **720**, 52, (2013). 720, 52 (2013).

[6] Adam, J., *et al.* [STAR Collaboration], *Phys. Rev. C* **99**, 034908, (2019).

[7] Adam, J., *et al.* [STAR Collaboration], *Phys. Rev. Lett.* **127**, 092301, (2021).

[8] Adam, J., *et al.* [STAR Collaboration], *Phys. Rev. Lett.* **124**, 172301 , (2020).

[9] TMVA official website: `http://tmva.sourceforge.net`, (Accessed on: 10/19/2021).

[10] Trotbjörn, S., *et al.*, *Comput. Phys. Commun.* **191**, 159-177, (2015).

Bibliography

[1] H. Voss, A. Höcker, J. Stelzer, and F. Tegenfeldt. TMVA, the Toolkit for Multivariate Data Analysis with ROOT. *PoS*, ACAT:040, 2009. doi:10.22323/1.050.0040.

[2] J. Adam and *et al.* [STAR Collaboration]. Centrality and transverse momentum dependence of D^0-meson production at mid-rapidity in Au+Au collisions at $\sqrt{s_{NN}} = 200$ GeV. *Phys. Rev. C*, 99:034908, Mar 2019. URL: https://link.aps.org/doi/10.1103/PhysRevC.99.034908, doi:10.1103/PhysRevC.99.034908.

[3] J. Adam and *et al.* [STAR Collaboration]. Observation of $D_s^{\pm}/D^0$ enhancement in Au + Au collisions at $\sqrt{s_{\mathrm{NN}}} = 200$ GeV. *Phys. Rev. Lett.*, 127:092301, Aug 2021. URL: https://link.aps.org/doi/10.1103/PhysRevLett.127.092301, doi:10.1103/PhysRevLett.127.092301.

[4] J. Adam and *et al.* [STAR Collaboration]. First measurement of Λ_{c} baryon production in Au + Au collisions at $\sqrt{s_{NN}} = 200$ GeV. *Phys. Rev. Lett.*, 124:172301, May 2020. URL: https://link.aps.org/doi/10.1103/PhysRevLett.124.172301, doi:10.1103/PhysRevLett.124.172301.

[5] C. Giacomo and *et al.* The star maps-based pixel detector. *Nuclear Instruments and Methods in Physics Research Section A: Accelerators, Spectrometers, Detectors and Associated Equipment*, 907:60–80, 2018. Advances in Instrumentation and Experimental Methods (Special Issue in Honour of Kai Siegbahn). URL: https://www.sciencedirect.com/science/article/pii/S0168900218303206, doi:https://doi.org/10.1016/j.nima.2018.03.003.

[6] M. Gell-Mann. A schematic model of baryons and mesons. *Physics Letters*, 8(3):214–215, 1964. URL: https://www.sciencedirect.com/science/article/pii/S0031916364920013, doi:https://doi.org/10.1016/S0031-9163(64)92001-3.

[7] G. Zweig. An SU_3 model for strong interaction symmetry and its breaking; Version 2. page 80 p, Feb 1964. Version 1 is CERN preprint 8182/TH.401, Jan. 17, 1964. URL: https://cds.cern.ch/record/570209.

[8] J.I. Friedman and H.W. Kendall. Deep inelastic electron scattering. *Annual Review of Nuclear Science*, 22(1):203–254, 1972. arXiv:https://doi.org/10.1146/annurev.ns.22.120172.001223, doi:10.1146/annurev.ns.22.120172.001223.

[9] J.C. Collins and M.J. Perry. Superdense matter: Neutrons or asymptotically free quarks? *Phys. Rev. Lett.*, 34:1353–1356, May 1975. URL: https://link.aps.org/doi/10.1103/PhysRevLett.34.1353, doi:10.1103/PhysRevLett.34.1353.

[10] L. McLerran. The physics of the quark-gluon plasma. *Rev. Mod. Phys.*, 58:1021–1064, Oct 1986. URL: https://link.aps.org/doi/10.1103/RevModPhys.58.1021, doi:10.1103/RevModPhys.58.1021.

[11] E.V. Shuryak. Quantum chromodynamics and the theory of superdense matter. *Physics Reports*, 61(2):71–158, 1980. URL: https://www.sciencedirect.com/science/article/pii/0370157380901052, doi:https://doi.org/10.1016/0370-1573(80)90105-2.

[12] J. Engels, F. Karsch, H. Satz, and I. Montvay. High temperature SU(2) gluon matter of the lattice. *Physics Letters B*, 101(1):89–94, 1981. URL: https://www.sciencedirect.com/science/article/pii/0370269381904974, doi:https://doi.org/10.1016/0370-2693(81)90497-4.

[13] R. Stock. The parton-hadron phase transition in central nuclear collisions at the CERN SPS. *Progress in Particle and Nuclear Physics*, 42:295–309, 1999. Heavy Ion Collisions from Nuclear to Quark Matter. URL: https://www.sciencedirect.com/science/article/pii/S0146641099000848, doi:https://doi.org/10.1016/S0146-6410(99)00084-8.

[14] F.R. Brown and *et al.* On the existence of a phase transition for QCD with three light quarks. *Phys. Rev. Lett.*, 65:2491–2494, Nov 1990. URL: https://link.aps.org/doi/10.1103/PhysRevLett.65.2491, doi:10.1103/PhysRevLett.65.2491.

[15] Z. Fodor and S.D. Katz. Lattice determination of the critical point of QCD at finiteTand μ. *Journal of High Energy Physics*, 2002(03):014–014, mar 2002. doi:10.1088/1126-6708/2002/03/014.

[16] F. Becattini, M. Gazdzicki, A. Keränen, J. Manninen, and R. Stock. Chemical equilibrium study in nucleus-nucleus collisions at relativistic energies. *Phys. Rev. C*, 69:024905, Feb 2004. URL: https://link.aps.org/doi/10.1103/PhysRevC.69.024905, doi:10.1103/PhysRevC.69.024905.

[17] M. Alford, K. Rajagopal, and F. Wilczek. Color-flavor locking and chiral symmetry breaking in high density QCD. *Nuclear Physics B*, 537(1):443–

458, 1999. URL: https://www.sciencedirect.com/science/article/pii/S0550321398006683, doi:https://doi.org/10.1016/S0550-3213(98)00668-3.

[18] D.H. Rischke. The quark–gluon plasma in equilibrium. *Progress in Particle and Nuclear Physics*, 52(1):197–296, 2004. URL: https://www.sciencedirect.com/science/article/pii/S0146641003001133, doi:https://doi.org/10.1016/j.ppnp.2003.09.002.

[19] M. Kliemant, R. Sahoo, T. Schuster, and R. Stock. *Global Properties of Nucleus–Nucleus Collisions*, pages 23–103. Springer Berlin Heidelberg, Berlin, Heidelberg, 2010. doi:10.1007/978-3-642-02286-9_2.

[20] C. R. Allton, S. Ejiri, S. J. Hands, O. Kaczmarek, F. Karsch, E. Laermann, and C. Schmidt. Equation of state for two flavor QCD at nonzero chemical potential. *Phys. Rev. D*, 68:014507, Jul 2003. URL: https://link.aps.org/doi/10.1103/PhysRevD.68.014507, doi:10.1103/PhysRevD.68.014507.

[21] T. Hirano, N. van der Kolk, and A. Bilandzic. Hydrodynamics and flow. In S. Sarkar, H. Satz, and B. Sinha, editors, *The Physics of the Quark-Gluon Plasma*, chapter 4, pages 139–178. Springer, Berlin, 2009. doi:10.1007/978-3-642-02286-9_4.

[22] R.J. Glauber. High-energy collision theory. In W.E. Brittin and L.C. Dunham, editors, *Lectures on Theoretical Physics, Vol. 1*, chapter 7, page 315. Interscience Publishers: Inc., New York, 1959. doi:10.1007/978-3-642-02286-9_2.

[23] M.L. Miller, K. Reygers, S.J. Sanders, and P. Steinberg. Glauber modeling in high-energy nuclear collisions. *Annual Review of Nuclear and Particle Science*, 57(1):205–243, 2007. arXiv:https://doi.org/10.1146/annurev.nucl.57.090506.123020, doi:10.1146/annurev.nucl.57.090506.123020.

[24] F. Gelis, E. Iancu, J. Jalilian-Marian, and R. Venugopalan. The color glass condensate. *Annual Review of Nuclear and Particle Science*, 60(1):463–489, 2010. arXiv:https://doi.org/10.1146/annurev.nucl.010909.083629, doi:10.1146/annurev.nucl.010909.083629.

[25] B. Müller. Investigation of hot QCD matter: theoretical aspects. T158:014004, dec 2013. doi:10.1088/0031-8949/2013/t158/014004.

[26] M. Kliemant, R. Sahoo, T. Schuster, and R. Stock. Global properties of nucleus–nucleus collisions. In Sinha B. Sarkar S., Satz H., editor, *The Physics of the Quark-Gluon Plasma*, chapter 2, pages 23–103. Springer, Berlin, 2009. doi:10.1007/978-3-642-02286-9_2.

[27] A. Abbot. Cern claims first experimental creation of quark–gluon plasma. *Nature*, 403:581, Feb 2000. doi:10.1038/35001196.

[28] M.M. Aggarwal and *et al.* Transverse mass distributions of neutral pions from ^{208}Pb-induced reactions at 158·a GeV. *The European Physical Journal C*, 23(2):225–236, Mar 2002. URL: http://dx.doi.org/10.1007/s100520100886, doi:10.1007/s100520100886.

[29] D. d'Enterria. Indications of suppressed high p_{T} hadron production in nucleus–nucleus collisions at CERN-SPS. *Physics Letters B*, 596(1):32–43, 2004. URL: https://www.sciencedirect.com/science/article/pii/S0370269304009372, doi:https://doi.org/10.1016/j.physletb.2004.06.071.

[30] A. Adare and *et al.* [PHENIX Collaboration]. Suppression pattern of neutral pions at high transverse momentum in Au + Au collisions at $\sqrt{s_{NN}} = 200$ GeV and constraints on medium transport coefficients. *Phys. Rev. Lett.*, 101:232301, Dec 2008. URL: https://link.aps.org/doi/10.1103/PhysRevLett.101.232301, doi:10.1103/PhysRevLett.101.232301.

[31] J. Adams and *et al.* [STAR Collaboration]. Transverse-momentum and collision-energy dependence of high-p_T hadron suppression in Au + Au collisions at ultrarelativistic energies. *Phys. Rev. Lett.*, 91:172302, Oct 2003. URL: https://link.aps.org/doi/10.1103/PhysRevLett.91.172302, doi:10.1103/PhysRevLett.91.172302.

[32] K. Aamodt and *et al.* Suppression of charged particle production at large transverse momentum in central Pb–Pb collisions at $\sqrt{s_{\mathrm{NN}}} = 2.76$ TeV. *Physics Letters B*, 696(1):30–39, 2011. URL: https://www.sciencedirect.com/science/article/pii/S0370269310013973, doi:https://doi.org/10.1016/j.physletb.2010.12.020.

[33] S. Chatrchyan and *et al.* [CMS Collaboration]. Study of high-p_{T} charged particle suppression in PbPb compared to pp collisions at $\sqrt{s_{\mathrm{NN}}} = 2.76$ TeV. *The European Physical Journal C*, 72(3), Mar 2012. URL: http://dx.doi.org/10.1140/epjc/s10052-012-1945-x, doi:10.1140/epjc/s10052-012-1945-x.

[34] A. Dainese, C. Loizides, and G. Paic. Leading-particle suppression in high energy nucleus-nucleus collisions. *The European Physical Journal C*, 38(4):461–474, Jan 2005. URL: http://dx.doi.org/10.1140/epjc/s2004-02077-x, doi:10.1140/epjc/s2004-02077-x.

[35] I. Vitev and M. Gyulassy. High-p_T tomography of d + Au and Au + Au at SPS, RHIC, and LHC. *Phys. Rev. Lett.*, 89:252301, Dec 2002. URL: https://link.aps.org/doi/10.1103/PhysRevLett.89.252301, doi:10.1103/PhysRevLett.89.252301.

[36] I. Vitev. Jet tomography. *Journal of Physics G: Nuclear and Particle Physics*, 30(8):S791–S800, jul 2004. doi:10.1088/0954-3899/30/8/019.

[37] C.A. Salgado and U.A. Wiedemann. Calculating quenching weights. *Phys. Rev. D*, 68:014008, Jul 2003. URL: https://link.aps.org/doi/10.1103/PhysRevD.68.014008, doi:10.1103/PhysRevD.68.014008.

[38] N. Armesto, A. Dainese, C.A. Salgado, and U.A. Wiedemann. Testing the color charge and mass dependence of parton energy loss with heavy-to-light ratios at BNL RHIC and CERN LHC. *Phys. Rev. D*, 71:054027, Mar 2005. URL: https://link.aps.org/doi/10.1103/PhysRevD.71.054027, doi:10.1103/PhysRevD.71.054027.

[39] T. Renk, Hannu Holopainen, Risto P., and K.J. Eskola. Systematics of the charged-hadron P_T spectrum and the nuclear suppression factor in heavy-ion collisions from $\sqrt{s_{NN}}$ = 200 gev to $\sqrt{s_{NN}}$ = 2.76 TeV. *Phys. Rev. C*, 84:014906, Jul 2011. URL: https://link.aps.org/doi/10.1103/PhysRevC.84.014906, doi:10.1103/PhysRevC.84.014906.

[40] A. Mócsy. Potential models for quarkonia. *The European Physical Journal C*, 61(4):705–710, jan 2009. URL: https://doi.org/10.1140%2Fepjc%2Fs10052-008-0847-4, doi:10.1140/epjc/s10052-008-0847-4.

[41] S. Chatrchyan and *et al.* [CMS Collaboration]. Observation of sequential Υ suppression in PbPb collisions. *Phys. Rev. Lett.*, 109:222301, Nov 2012. URL: https://link.aps.org/doi/10.1103/PhysRevLett.109.222301, doi:10.1103/PhysRevLett.109.222301.

[42] Matsui T. and H. Satz. J/ψ suppression by quark-gluon plasma formation. *Physics Letters B*, 178(4):416–422, 1986. URL: https://www.sciencedirect.com/science/article/pii/0370269386914048, doi:https://doi.org/10.1016/0370-2693(86)91404-8.

[43] C. Young and E. Shuryak. Recombinant charmonium in strongly coupled quark-gluon plasma. *Phys. Rev. C*, 81:034905, Mar 2010. URL: https://link.aps.org/doi/10.1103/PhysRevC.81.034905, doi:10.1103/PhysRevC.81.034905.

[44] J. Adams and *et al.* [STAR Collaboration]. Pion, kaon, proton and anti-proton transverse momentum distributions from p+p and d+Au collisions at

$\sqrt{s_{NN}} = 200\,\mathrm{GeV}$. *Physics Letters B*, 616(1):8–16, 2005. URL: https://www.sciencedirect.com/science/article/pii/S0370269305005381, doi:https://doi.org/10.1016/j.physletb.2005.04.041.

[45] J. Adams and *et al.* [STAR Collaboration]. Identified hadron spectra at large transverse momentum in p+p and d+Au collisions at $\sqrt{s_{NN}} = 200\,\mathrm{GeV}$. *Physics Letters B*, 637(3):161–169, 2006. URL: https://www.sciencedirect.com/science/article/pii/S0370269306004928, doi:https://doi.org/10.1016/j.physletb.2006.04.032.

[46] P. Abreu and *et al.* [DELPHI Collaboration]. $\pi^{\pm}$, $\mathrm{k}^{\pm}$, p and $\bar{\mathrm{p}}$ production in $\mathrm{z}^0 \to q\bar{q}$, $\mathrm{z}^0 \to b\bar{b}$, $\mathrm{Z}^0 \to u\bar{u}$, $d\bar{d}$, $s\bar{s}$. *Eur. Phys. J. C*, 5:585–620, 1998. doi:https://doi.org/10.1007/s100529800989.

[47] R.C. Hwa and C.B. Yang. Recombination of shower partons at high p_T in heavy-ion collisions. *Phys. Rev. C*, 70:024905, Aug 2004. URL: https://link.aps.org/doi/10.1103/PhysRevC.70.024905, doi:10.1103/PhysRevC.70.024905.

[48] R. J. Fries, B. Müller, C. Nonaka, and S. A. Bass. Hadron production in heavy ion collisions: Fragmentation and recombination from a dense parton phase. *Phys. Rev. C*, 68:044902, Oct 2003. URL: https://link.aps.org/doi/10.1103/PhysRevC.68.044902, doi:10.1103/PhysRevC.68.044902.

[49] B.I. Abelev and *et al.* [STAR Collaboration]. Identified baryon and meson distributions at large transverse momenta from Au + Au collisions at $\sqrt{s_{NN}} = 200$ GeV. *Phys. Rev. Lett.*, 97:152301, Oct 2006. URL: https://link.aps.org/doi/10.1103/PhysRevLett.97.152301, doi:10.1103/PhysRevLett.97.152301.

[50] R. Fries, V. Greco, and P. Sorensen. Coalescence models for hadron formation from quark-gluon plasma. *Annual Review of Nuclear and Particle Science*, 58(1):177–205, 2008. arXiv:https://doi.org/10.1146/annurev.nucl.58.110707.171134, doi:10.1146/annurev.nucl.58.110707.171134.

[51] U. Heinz. The strongly coupled quark–gluon plasma created at RHIC. *Journal of Physics A: Mathematical and Theoretical*, 42(21):214003, may 2009. doi:10.1088/1751-8113/42/21/214003.

[52] B. Alver and G. Roland. Collision-geometry fluctuations and triangular flow in heavy-ion collisions. *Phys. Rev. C*, 81:054905, May 2010. URL: https://link.aps.org/doi/10.1103/PhysRevC.81.054905, doi:10.1103/PhysRevC.81.054905.

[53] P. Huovinen and P.V. Ruuskanen. Hydrodynamic models for heavy ion collisions. *Annual Review of Nuclear and Particle Science*, 56(1):163–206, 2006.

arXiv:https://doi.org/10.1146/annurev.nucl.54.070103.181236, doi:10.1146/annurev.nucl.54.070103.181236.

[54] B.I. Abelev and *et al.* [STAR Collaboration]. Centrality dependence of charged hadron and strange hadron elliptic flow from $\sqrt{s_{NN}} = 200$ GeV Au+Au collisions. *Phys. Rev. C*, 77:054901, May 2008. URL: https://link.aps.org/doi/10.1103/PhysRevC.77.054901, doi:10.1103/PhysRevC.77.054901.

[55] G. Aad and *et al.* [ATLAS Collaboration]. Measurement of the azimuthal anisotropy for charged particle production in $\sqrt{s_{NN}} = 2.76$ TeV lead-lead collisions with the atlas detector. *Phys. Rev. C*, 86:014907, Jul 2012. URL: https://link.aps.org/doi/10.1103/PhysRevC.86.014907, doi:10.1103/PhysRevC.86.014907.

[56] B. Abelev and *et al.* [ALICE Collaboration]. Directed flow of charged particles at midrapidity relative to the spectator plane in Pb-Pb collisions at $\sqrt{s_{\rm NN}} = 2.76$ TeV. *Phys. Rev. Lett.*, 111:232302, Dec 2013. URL: https://link.aps.org/doi/10.1103/PhysRevLett.111.232302, doi:10.1103/PhysRevLett.111.232302.

[57] L. Adamczyk and *et al.* [STAR Collaboration]. Beam-energy dependence of directed flow of Λ, $\overline{\Lambda}$, $K^{\pm}$, K^0_s, and ϕ in Au + Au collisions. *Phys. Rev. Lett.*, 120:062301, Feb 2018. URL: https://link.aps.org/doi/10.1103/PhysRevLett.120.062301, doi:10.1103/PhysRevLett.120.062301.

[58] V. Khachatryan and *et al.* [CMS Collaboration]. Evidence for collectivity in pp collisions at the lhc. *Physics Letters B*, 765:193–220, 2017. URL: https://www.sciencedirect.com/science/article/pii/S037026931630747X, doi:https://doi.org/10.1016/j.physletb.2016.12.009.

[59] R.D. Weller and P. Romatschke. One fluid to rule them all: Viscous hydrodynamic description of event-by-event central p+p, p+Pb and Pb+Pb collisions at $\sqrt{s} = 5.02\,\text{TeV}$. *Physics Letters B*, 774:351–356, 2017. URL: https://www.sciencedirect.com/science/article/pii/S037026931730789X, doi:https://doi.org/10.1016/j.physletb.2017.09.077.

[60] S. Cremonini, U. Gürsoy, and P. Szepietowski. On the temperature dependence of the shear viscosity and holography. *Journal of High Energy Physics*, 2012(8), aug 2012. URL: https://doi.org/10.1007%2Fjhep08%282012%29167, doi:10.1007/jhep08(2012)167.

[61] M. d‘ Enterria and B. Betz. High-$p_{\rm T}$ hadron suppression and jet quenching. In Sinha B. Sarkar S., Satz H., editor, *The Physics of the Quark-Gluon Plasma*, chap-

ter 9, pages 285–339. Springer, Berlin, 2009. doi:10.1007/978-3-642-02286-9_9.

[62] J. Adams and *et al.* [STAR Collaboration]. Evidence from $d + \mathrm{Au}$ measurements for final-state suppression of high-p_T hadrons in $\mathrm{Au} + \mathrm{Au}$ collisions at rhic. *Phys. Rev. Lett.*, 91:072304, Aug 2003. URL: https://link.aps.org/doi/10.1103/PhysRevLett.91.072304, doi:10.1103/PhysRevLett.91.072304.

[63] A.M Sirunyan and *et al.* [CMS Collaboration]. Study of jet quenching with isolated-photon+jet correlations in PbPb and pp collisions at $\sqrt{s_{NN}} = 5.02$ TeV. *Physics Letters B*, 785:14–39, 2018. URL: https://www.sciencedirect.com/science/article/pii/S0370269318306245, doi:https://doi.org/10.1016/j.physletb.2018.07.061.

[64] Y. He, T. Luo, X.-N. Wang, and Y. Zhu. Linear boltzmann transport for jet propagation in the quark-gluon plasma: Elastic processes and medium recoil. *Phys. Rev. C*, 91:054908, May 2015. URL: https://link.aps.org/doi/10.1103/PhysRevC.91.054908, doi:10.1103/PhysRevC.91.054908.

[65] Y. He, T. Luo, X.-N. Wang, and Y. Zhu. Erratum: Linear boltzmann transport for jet propagation in the quark-gluon plasma: Elastic processes and medium recoil [Phys. Rev. C 91, 054908 (2015)]. *Phys. Rev. C*, 97:019902, Jan 2018. URL: https://link.aps.org/doi/10.1103/PhysRevC.97.019902, doi:10.1103/PhysRevC.97.019902.

[66] Y. He, S. Cao, W. Chen, T. Luo, L.-G. Pang, and X.-N. Wang. Interplaying mechanisms behind single inclusive jet suppression in heavy-ion collisions. *Phys. Rev. C*, 99:054911, May 2019. URL: https://link.aps.org/doi/10.1103/PhysRevC.99.054911, doi:10.1103/PhysRevC.99.054911.

[67] J. Casalderrey-Solana, D.C. Gulhan, J.G. Milhano, and *et al.* Angular structure of jet quenching within a hybrid strong/weak coupling model. *Journal of High Energy Physics*, 2017(3), mar 2017. URL: https://doi.org/10.1007%2Fjhep03%282017%29135, doi:10.1007/jhep03(2017)135.

[68] Y.-T. Chien and I. Vitev. Towards the understanding of jet shapes and cross sections in heavy ion collisions using soft-collinear effective theory. *Journal of High Energy Physics*, 2016(5), may 2016. URL: https://doi.org/10.1007%2Fjhep05%282016%29023, doi:10.1007/jhep05(2016)023.

[69] Y.-T. Chien, A. Emerman, Z.-B. Kang, G. Ovanesyan, and I. Vitev. Jet quenching from QCD evolution. *Phys. Rev. D*, 93:074030, Apr 2016. URL: https:

//link.aps.org/doi/10.1103/PhysRevD.93.074030, doi:10.1103/PhysRevD.93.074030.

[70] I. Vitev and B.-W. Zhang. Jet tomography of high-energy nucleus-nucleus collisions at next-to-leading order. *Phys. Rev. Lett.*, 104:132001, Mar 2010. URL: https://link.aps.org/doi/10.1103/PhysRevLett.104.132001, doi:10.1103/PhysRevLett.104.132001.

[71] W. Ke, Y. Xu, and S.A. Bass. Modified boltzmann approach for modeling the splitting vertices induced by the hot QCD medium in the deep landau-pomeranchuk-migdal region. *Phys. Rev. C*, 100:064911, Dec 2019. URL: https://link.aps.org/doi/10.1103/PhysRevC.100.064911, doi:10.1103/PhysRevC.100.064911.

[72] W. Ke, X.-N. Wang, W. Fan, and S. Bass. Study of heavy-flavor jets in a transport approach, 2020. URL: https://arxiv.org/abs/2008.07622, doi:10.48550/ARXIV.2008.07622.

[73] J. Adam and *et al.* [STAR Collaboration]. Measurement of inclusive charged-particle jet production in Au + Au collisions at $\sqrt{s_{NN}} = 200$ GeV. *Phys. Rev. C*, 102:054913, Nov 2020. URL: https://link.aps.org/doi/10.1103/PhysRevC.102.054913, doi:10.1103/PhysRevC.102.054913.

[74] D. Pablos. Jet suppression from small to large radius, 2020. URL: https://arxiv.org/abs/2009.02202, doi:10.48550/ARXIV.2009.02202.

[75] L. Adamczyk and *et al.* [STAR Collaboration]. Dijet imbalance measurements in Au + Au and *pp* collisions at $\sqrt{s_{NN}} = 200$ GeV at star. *Phys. Rev. Lett.*, 119:062301, Aug 2017. URL: https://link.aps.org/doi/10.1103/PhysRevLett.119.062301, doi:10.1103/PhysRevLett.119.062301.

[76] P. A. Zyla and *et al.* [Particle Data Group]. Review of Particle Physics. *Prog. Theor. Exp. Phys.*, 2020(8), 08 2020. 083C01. arXiv:https://academic.oup.com/ptep/article-pdf/2020/8/083C01/34673722/ptaa104.pdf, doi:10.1093/ptep/ptaa104.

[77] S.L. Glashow, J. Iliopoulos, and L. Maiani. Weak interactions with lepton-hadron symmetry. *Phys. Rev. D*, 2:1285–1292, Oct 1970. URL: https://link.aps.org/doi/10.1103/PhysRevD.2.1285, doi:10.1103/PhysRevD.2.1285.

[78] J. J. Aubert and *et al.* Experimental observation of a heavy particle *J*. *Phys. Rev. Lett.*, 33:1404–1406, Dec 1974. URL: https://link.aps.org/doi/10.1103/PhysRevLett.33.1404, doi:10.1103/PhysRevLett.33.1404.

[79] J.-E. Augustin and *et al.* Discovery of a narrow resonance in e^+e^- annihilation. *Phys. Rev. Lett.*, 33:1406–1408, Dec 1974. URL: https://link.aps.org/doi/10.1103/PhysRevLett.33.1406, doi:10.1103/PhysRevLett.33.1406.

[80] G. Goldhaber and *et al.* Observation in e^+e^- annihilation of a narrow state at 1865 MeV/c^2 decaying to $K\pi$ and $K\pi\pi\pi$. *Phys. Rev. Lett.*, 37:255–259, Aug 1976. URL: https://link.aps.org/doi/10.1103/PhysRevLett.37.255, doi:10.1103/PhysRevLett.37.255.

[81] I. Peruzzi and *et al.* Observation of a narrow charged state at 1876 MeV/c^2 decaying to an exotic combination of $K\pi\pi$. *Phys. Rev. Lett.*, 37:569–571, Sep 1976. URL: https://link.aps.org/doi/10.1103/PhysRevLett.37.569, doi:10.1103/PhysRevLett.37.569.

[82] A. Chen and *et al.* Evidence for the F meson at 1970 MeV. *Phys. Rev. Lett.*, 51:634–637, Aug 1983. URL: https://link.aps.org/doi/10.1103/PhysRevLett.51.634, doi:10.1103/PhysRevLett.51.634.

[83] E. G. Cazzoli and *et al.* Evidence for $\Delta S = -\Delta Q$ currents or charmed-baryon production by neutrinos. *Phys. Rev. Lett.*, 34:1125–1128, Apr 1975. URL: https://link.aps.org/doi/10.1103/PhysRevLett.34.1125, doi:10.1103/PhysRevLett.34.1125.

[84] B. Knapp and *et al.* Observation of a narrow antibaryon state at 2.26 GeV/c^2. *Phys. Rev. Lett.*, 37:882–885, Oct 1976. URL: https://link.aps.org/doi/10.1103/PhysRevLett.37.882, doi:10.1103/PhysRevLett.37.882.

[85] R. Aaij and *et al.* [LHCb Collaboration]. Observation of the doubly charmed baryon Ξ_{cc}^{++}. *Phys. Rev. Lett.*, 119:112001, Sep 2017. URL: https://link.aps.org/doi/10.1103/PhysRevLett.119.112001, doi:10.1103/PhysRevLett.119.112001.

[86] B. Abelev and *et al.* [ALICE Collaboration]. Measurement of charm production at central rapidity in proton-proton collisions at \sqrt {s} = 7{ }TeV. *Journal of High Energy Physics*, 2012(1), jan 2012. doi:10.1007/jhep01(2012)128.

[87] M. Cacciari, M. Greco, and P. Nason. The p_{T} spectrum in heavy-flavour hadroproduction. *Journal of High Energy Physics*, 1998(05):007–007, may 1998. doi:10.1088/1126-6708/1998/05/007.

[88] M. Cacciari, S. Frixione, and P. Nason. The p_{T} spectrum in heavy-flavour photoproduction. *Journal of High Energy Physics*, 2001(03):006–006, mar 2001. doi:10.1088/1126-6708/2001/03/006.

[89] M. Cacciari and *et al.* Theoretical predictions for charm and bottom production at the LHC. *JHEP*, 10:137, 2012. arXiv:1205.6344, doi:10.1007/JHEP10(2012)137.

[90] B.A. Kniehl, G. Kramer, I. Schienbein, and H. Spiesberger. Reconciling open-charm production at the Fermilab Tevatron with QCD. *Phys. Rev. Lett.*, 96:012001, Jan 2006. URL: https://link.aps.org/doi/10.1103/PhysRevLett.96.012001, doi:10.1103/PhysRevLett.96.012001.

[91] Kniehl, B.A., Kramer, G., Schienbein, I., and Spiesberger, H. Inclusive charmed-meson production at the CERN LHC. *Eur. Phys. J. C*, 72(7):2082, 2012. doi:10.1140/epjc/s10052-012-2082-2.

[92] S. Chatterjee and B. Bozek. Interplay of drag by hot matter and electromagnetic force on the directed flow of heavy quarks. *Physics Letters B*, 798:134955, 2019. URL: https://www.sciencedirect.com/science/article/pii/S037026931930677X, doi:https://doi.org/10.1016/j.physletb.2019.134955.

[93] S. Chatterjee and P. Bozek. Large directed flow of open charm mesons probes the three-dimensional distribution of matter in heavy-ion collisions. *Phys. Rev. Lett.*, 120:192301, May 2018. URL: https://link.aps.org/doi/10.1103/PhysRevLett.120.192301, doi:10.1103/PhysRevLett.120.192301.

[94] S.K. Das, S. Plumari, S. Chatterjee, J. Alam, F. Scardina, and V. Greco. Directed flow of charm quarks as a witness of the initial strong magnetic field in ultra-relativistic heavy ion collisions. *Physics Letters B*, 768:260–264, 2017. URL: https://www.sciencedirect.com/science/article/pii/S0370269317301594, doi:https://doi.org/10.1016/j.physletb.2017.02.046.

[95] Y. Xu, J.E. Bernhard, S.A. Bass, M. Nahrgang, and S. Cao. Data-driven analysis for the temperature and momentum dependence of the heavy-quark diffusion coefficient in relativistic heavy-ion collisions. *Phys. Rev. C*, 97:014907, Jan 2018. URL: https://link.aps.org/doi/10.1103/PhysRevC.97.014907, doi:10.1103/PhysRevC.97.014907.

[96] S. Cao, T. Luo, G.-Y. Qin, and X.-N. Wang. Linearized boltzmann transport model for jet propagation in the quark-gluon plasma: Heavy quark evolution. *Phys. Rev. C*, 94:014909, Jul 2016. URL: https://link.aps.org/doi/10.1103/PhysRevC.94.014909, doi:10.1103/PhysRevC.94.014909.

[97] J. Adam and *et al.* [ALICE Collaboration]. Transverse momentum dependence of D-meson production in Pb-Pb collisions at $\sqrt{s_{NN}} = 2.76$ TeV. *Journal of*

High Energy Physics, 2016(3), Mar 2016. URL: http://dx.doi.org/10.1007/JHEP03(2016)081, doi:10.1007/jhep03(2016)081.

[98] B. Abelev and *et al.* [ALICE Collaboration]. Centrality dependence of charged particle production at large transverse momentum in Pb–Pb collisions at $\sqrt{s_{\rm NN}}$ = 2.76 TeV. *Physics Letters B*, 720(1):52–62, 2013. URL: https://www.sciencedirect.com/science/article/pii/S0370269313000920, doi:https://doi.org/10.1016/j.physletb.2013.01.051.

[99] B.I. Abelev and *et al.* [STAR Collaboration]. Energy dependence of $\pi^{\pm}$, p and $\overline{\rm p}$ transverse momentum spectra for Au+Au collisions at $\sqrt{s_{\rm NN}}$ = 62.4 and 200 GeV. *Physics Letters B*, 655(3):104–113, 2007. URL: https://www.sciencedirect.com/science/article/pii/S037026930700679X, doi:https://doi.org/10.1016/j.physletb.2007.06.035.

[100] L. Adamczyk and *et al.* [STAR Collaboration]. Observation of D^0 meson nuclear modifications in Au + Au collisions at $\sqrt{s_{\rm NN}}$ = 200 GeV. *Phys. Rev. Lett.*, 113:142301, Sep 2014. URL: https://link.aps.org/doi/10.1103/PhysRevLett.113.142301, doi:10.1103/PhysRevLett.113.142301.

[101] L. Adamczyk and *et al.* [STAR Collaboration]. Erratum: Observation of D^0 meson nuclear modifications in Au + Au collisions at $\sqrt{s_{\rm NN}}$ = 200 GeV [phys. rev. lett. 113, 142301 (2014)]. *Phys. Rev. Lett.*, 121:229901, Nov 2018. URL: https://link.aps.org/doi/10.1103/PhysRevLett.121.229901, doi:10.1103/PhysRevLett.121.229901.

[102] L. Adamczyk and *et al.* [STAR Collaboration]. Measurement of D^0 azimuthal anisotropy at midrapidity in Au + Au collisions at $\sqrt{s_{NN}}$ = 200 GeV. *Phys. Rev. Lett.*, 118:212301, May 2017. URL: https://link.aps.org/doi/10.1103/PhysRevLett.118.212301, doi:10.1103/PhysRevLett.118.212301.

[103] S. Cho, K.-J. Sun, Ch.M. Ko, S.H. Lee, and Y. Oh. Charmed hadron production in an improved quark coalescence model. *Phys. Rev. C*, 101:024909, Feb 2020. URL: https://link.aps.org/doi/10.1103/PhysRevC.101.024909, doi:10.1103/PhysRevC.101.024909.

[104] S. Plumari and *et al.* Charmed hadrons from coalescence plus fragmentation in relativistic nucleus-nucleus collisions at rhic and lhc. *Eur. Phys. J. C*, 78:348, 2018. doi:10.1140/epjc/s10052-018-5828-7.

[105] J. Zhao, S. Shi, N. Xu, and P. Zhuang. Sequential coalescence with charm conservation in high energy nuclear collisions, 2018. arXiv:1805.10858.

[106] M. He and R. Rapp. Hadronization and charm-hadron ratios in heavy-ion collisions. *Phys. Rev. Lett.*, 124:042301, Jan 2020. URL: https://link.aps.org/doi/10.1103/PhysRevLett.124.042301, doi:10.1103/PhysRevLett.124.042301.

[107] S. Cao and *et al.* Charmed hadron chemistry in relativistic heavy-ion collisions. *Physics Letters B*, 807:135561, 2020. URL: https://www.sciencedirect.com/science/article/pii/S0370269320303658, doi:https://doi.org/10.1016/j.physletb.2020.135561.

[108] B. I. Abelev and *et al.* [STAR Collaboration]. Identified baryon and meson distributions at large transverse momenta from Au + Au collisions at $\sqrt{s_{NN}} = 200$ GeV. *Phys. Rev. Lett.*, 97:152301, Oct 2006. URL: https://link.aps.org/doi/10.1103/PhysRevLett.97.152301, doi:10.1103/PhysRevLett.97.152301.

[109] G. Agakishiev and *et al.* [STAR Collaboration]. Strangeness enhancement in cu-cu and au-au collisions at $\sqrt{s_{NN}} = 200$ GeV. *Phys. Rev. Lett.*, 108:072301, Feb 2012. URL: https://link.aps.org/doi/10.1103/PhysRevLett.108.072301, doi:10.1103/PhysRevLett.108.072301.

[110] M. Nasim and S. Singha. Directed flow of open charm in Au+Au collisions at $\sqrt{s_{NN}} = 200$ GeV using a quark coalescence model. *Phys. Rev. C*, 97:064917, Jun 2018. URL: https://link.aps.org/doi/10.1103/PhysRevC.97.064917, doi:10.1103/PhysRevC.97.064917.

[111] L. Adamczyk and *et al.* [STAR Collaboration]. Beam-energy dependence of directed flow of Λ, $\overline{\Lambda}$, $K^{\pm}$, K^0_s, and ϕ in Au + Au collisions. *Phys. Rev. Lett.*, 120:062301, Feb 2018. URL: https://link.aps.org/doi/10.1103/PhysRevLett.120.062301, doi:10.1103/PhysRevLett.120.062301.

[112] J. Adam and *et al.* [STAR Collaboration]. First observation of the directed flow of D^0 and $\overline{D^0}$ in Au + Au collisions at $\sqrt{s_{NN}} = 200$ GeV. *Phys. Rev. Lett.*, 123:162301, Oct 2019. URL: https://link.aps.org/doi/10.1103/PhysRevLett.123.162301, doi:10.1103/PhysRevLett.123.162301.

[113] S. Cao, G.-Y. Qin, and S.A. Bass. Energy loss, hadronization, and hadronic interactions of heavy flavors in relativistic heavy-ion collisions. *Phys. Rev. C*, 92:024907, Aug 2015. URL: https://link.aps.org/doi/10.1103/PhysRevC.92.024907, doi:10.1103/PhysRevC.92.024907.

[114] W. Cassing and E.L. Bratkovskaya. Parton transport and hadronization from the dynamical quasiparticle point of view. *Phys. Rev. C*, 78:034919, Sep 2008. URL: https://link.aps.org/doi/10.1103/PhysRevC.78.034919, doi:10.1103/PhysRevC.78.034919.

[115] W. Cassing and E.L. Bratkovskaya. Parton–hadron–string dynamics: An off-shell transport approach for relativistic energies. *Nuclear Physics A*, 831(3):215–242, 2009. URL: https://www.sciencedirect.com/science/article/pii/S0375947409005995, doi:https://doi.org/10.1016/j.nuclphysa.2009.09.007.

[116] M. S. Abdallah and *et al.* [STAR Collaboration]. Evidence of mass ordering of charm and bottom quark energy loss in Au+Au collisions at RHIC, 2021. URL: https://arxiv.org/abs/2111.14615, doi:10.48550/ARXIV.2111.14615.

[117] S. Acharya and *et al.* [ALICE Collaboration]. Measurement of D^0, D^+, D^{*+} and D_s^+ production in Pb-Pb collisions at $\sqrt{s_{NN}} = 5.02$ TeV. *JHEP*, 10:174, 2018. arXiv:1804.09083, doi:10.1007/JHEP10(2018)174.

[118] A.M. Sirunyan and *et al.* [CMS Collaboration]. Nuclear modification factor of D^0 mesons in PbPb collisions at $\sqrt{s_{NN}} = 5.02$ TeV. *Physics Letters B*, 782:474–496, 2018. URL: https://www.sciencedirect.com/science/article/pii/S0370269318304386, doi:https://doi.org/10.1016/j.physletb.2018.05.074.

[119] M. Djordjevic and M. Djordjevic. Predictions of heavy-flavor suppression at 5.1 TeV Pb + Pb collisions at the CERN Large Hadron Collider. *Phys. Rev. C*, 92:024918, Aug 2015. URL: https://link.aps.org/doi/10.1103/PhysRevC.92.024918, doi:10.1103/PhysRevC.92.024918.

[120] M. He, R.J. Fries, and R. Rapp. Heavy flavor at the large hadron collider in a strong coupling approach. *Physics Letters B*, 735:445–450, 2014. URL: https://www.sciencedirect.com/science/article/pii/S0370269314003591, doi:https://doi.org/10.1016/j.physletb.2014.05.050.

[121] T. Song, H. Berrehrah, D. Cabrera, W. Cassing, and E. Bratkovskaya. Charm production in Pb + Pb collisions at energies available at the CERN Large Hadron Collider. *Phys. Rev. C*, 93:034906, Mar 2016. URL: https://link.aps.org/doi/10.1103/PhysRevC.93.034906, doi:10.1103/PhysRevC.93.034906.

[122] A. Beraudo, A. De Pace, M. Monteno, Nardi M., and F. Prino. Heavy flavors in heavy-ion collisions: quenching, flow and correlations. *Eur. Phys. J. C*, 75:121, Mar 2015. doi:10.1140/epjc/s10052-015-3336-6.

[123] M. Nahrgang, J. Aichelin, P.B. Gossiaux, and K. Werner. Influence of hadronic bound states above T_c on heavy-quark observables in Pb + Pb collisions at the CERN Large Hadron Collider. *Phys. Rev. C*, 89:014905, Jan 2014. URL: https:

//link.aps.org/doi/10.1103/PhysRevC.89.014905, doi:10.1103/PhysRevC.89.014905.

[124] S. Cao, T. Luo, G.-Y. Qin, and X.-N. Wang. Heavy and light flavor jet quenching at RHIC and LHC energies. *Physics Letters B*, 777:255–259, 2018. URL: https://www.sciencedirect.com/science/article/pii/S0370269317310006, doi:https://doi.org/10.1016/j.physletb.2017.12.023.

[125] J. Uphoff, O. Fochler, Z. Xu, and C. Greiner. Elastic and radiative heavy quark interactions in ultra-relativistic heavy-ion collisions. *Journal of Physics G: Nuclear and Particle Physics*, 42(11):115106, oct 2015. doi:10.1088/0954-3899/42/11/115106.

[126] S. Acharya and *et al.* [ALICE Collaboration]. Λ_c production in Pb–Pb collisions at $\sqrt{s_{NN}} = 2.76$ TeV. *Physics Letters B*, 793:212–223, 2019. URL: https://www.sciencedirect.com/science/article/pii/S0370269319302795, doi:https://doi.org/10.1016/j.physletb.2019.04.046.

[127] H.-H. Li, F.-L. Shao, J. Song, and R-Q. Wang. Production of single-charm hadrons by the quark-combination mechanism in p-pb collisions at $\sqrt{s_{NN}} = 5.02$ TeV. *Phys. Rev. C*, 97:064915, Jun 2018. URL: https://link.aps.org/doi/10.1103/PhysRevC.97.064915, doi:10.1103/PhysRevC.97.064915.

[128] J. Song, H.-H. Li, and F.-L. Shao. New feature of low p_T charm quark hadronization in pp collisions at $\sqrt{s_{NN}} = 7$ TeV. *The European Physical Journal C*, 78(4), Apr 2018. URL: http://dx.doi.org/10.1140/epjc/s10052-018-5817-x, doi:10.1140/epjc/s10052-018-5817-x.

[129] S. Acharya and *et al.* [ALICE Collaboration]. Transverse momentum spectra and nuclear modification factors of charged particles in pp, p-Pb and Pb-Pb collisions at the LHC. *Journal of High Energy Physics*, 2018(11), Nov 2018. URL: http://dx.doi.org/10.1007/JHEP11(2018)013, doi:10.1007/jhep11(2018)013.

[130] S. Acharya and *et al.* [ALICE Collaboration]. Measurement of D^0, D^+, and D^{*+} production in Pb-Pb collisions at $\sqrt{s_{NN}} = 5.02$ TeV. *JHEP*, 01:174, 2022. arXiv:2110.09420, doi:10.1007/JHEP01(2022)174.

[131] S. Li and J. Liao. Data-driven extraction of heavy quark diffusion in quark-gluon plasma. *Eur. Phys. J. C*, 80(671), 2020. doi:10.1140/epjc/s10052-020-8243-9.

[132] S. Shi, J. Liao, and M. Gyulassy. Global constraints from RHIC and LHC on transport properties of QCD fluids in CUJET/CIBJET framework. *Chinese Physics C*, 43(4):044101, apr 2019. doi:10.1088/1674-1137/43/4/044101.

[133] S. Li, W. Xiong, and R. Wan. Relativistic langevin dynamics: charm versus beauty. *Eur. Phys. J. C*, 80(1113), 2020. doi:10.1140/epjc/s10052-020-08708-y.

[134] S. Acharya and *et al.* [ALICE Collaboration]. Measurement of beauty production via non-prompt D^0 mesons in Pb-Pb collisions at $\sqrt{s_{NN}} = 5.02$ TeV, 2022. URL: https://arxiv.org/abs/2202.00815, doi:10.48550/ARXIV.2202.00815.

[135] S. Acharya and *et al.* [ALICE Collaboration]. Measurement of electrons from semileptonic heavy-flavour hadron decays at midrapidity in pp and Pb–Pb collisions at $\sqrt{s_{NN}} = 5.02$ TeV. *Physics Letters B*, 804:135377, 2020. URL: https://www.sciencedirect.com/science/article/pii/S0370269320301817, doi:https://doi.org/10.1016/j.physletb.2020.135377.

[136] BNL north campus map, 2022. URL: https://www.bnl.gov/maps/linkable_files/pdf/north_campus.pdf.

[137] Kanesue T. and K. Okamura. Laser ion source activities at brookhaven national laboratory. *Radiation Effects and Defects in Solids*, 170(4):347–354, 2015. arXiv:https://doi.org/10.1080/10420150.2015.1036427, doi:10.1080/10420150.2015.1036427.

[138] T. Kanesue and *et al.* The Commissioning of the Laser Ion Source for RHIC-EBIS. In *Proc. 5th International Particle Accelerator Conference (IPAC'14), Dresden, Germany, June 15-20, 2014*, number 5 in International Particle Accelerator Conference, pages 1890–1892, Geneva, Switzerland, July 2014. JACoW. https://doi.org/10.18429/JACoW-IPAC2014-WEOAB01. URL: http://jacow.org/ipac2014/papers/weoab01.pdf, doi:https://doi.org/10.18429/JACoW-IPAC2014-WEOAB01.

[139] A. Pikin and *et al.* RHIC EBIS: basics of design and status of commissioning. *Journal of Instrumentation*, 5(09):C09003–C09003, sep 2010. doi:10.1088/1748-0221/5/09/c09003.

[140] A. Schempp and *et al.* RFQ and IH accelerators for the new EBIS injector at BNL. In *2007 IEEE Particle Accelerator Conference (PAC)*, pages 1439–1441, 2007. doi:10.1109/PAC.2007.4440782.

[141] W. Fisher. Run overview of the relativisti heavy ion collider, 2022. URL: https://www.agsrhichome.bnl.gov/RHIC/Runs/.

[142] D. Beavis and *et al.* *The STAR Heavy Flavor Tracker, Technical Design Report.* 2011.

[143] M. Anderson and *et al.* The STAR time projection chamber: a unique tool for studying high multiplicity events at RHIC. *Nuclear Instruments and Methods in Physics Research Section A: Accelerators, Spectrometers, Detectors and Associated Equipment*, 499(2):659–678, 2003. The Relativistic Heavy Ion Collider Project: RHIC and its Detectors. URL: https://www.sciencedirect.com/science/article/pii/S0168900202019642, doi:https://doi.org/10.1016/S0168-9002(02)01964-2.

[144] P. Fachini and *et al.* [STAR TOF Collaboration]. *Proposal of a Larg Area Time of Flight System for STAR.* 2004.

[145] J. Abelev and *et al.* The laser system for the STAR time projection chamber. *Nuclear Instruments and Methods in Physics Research Section A: Accelerators, Spectrometers, Detectors and Associated Equipment*, 499(2):692–702, 2003. The Relativistic Heavy Ion Collider Project: RHIC and its Detectors. URL: https://www.sciencedirect.com/science/article/pii/S0168900202019666, doi:https://doi.org/10.1016/S0168-9002(02)01966-6.

[146] E.G. Judd and *et al.* The evolution of the STAR Trigger System. *Nuclear Instruments and Methods in Physics Research Section A: Accelerators, Spectrometers, Detectors and Associated Equipment*, 902:228–237, 2018. URL: https://www.sciencedirect.com/science/article/pii/S0168900218304224, doi:https://doi.org/10.1016/j.nima.2018.03.070.

[147] W.J. Llope. The large-area time-of-flight upgrade for STAR. *Nuclear Instruments and Methods in Physics Research Section B: Beam Interactions with Materials and Atoms*, 241(1):306–310, 2005. The Application of Accelerators in Research and Industry. URL: https://www.sciencedirect.com/science/article/pii/S0168583X05012267, doi:https://doi.org/10.1016/j.nimb.2005.07.089.

[148] W.J. Llope and *et al.* The star vertex position detector. *Nuclear Instruments and Methods in Physics Research Section A: Accelerators, Spectrometers, Detectors and Associated Equipment*, 759:23–28, 2014. URL: https://www.sciencedirect.com/science/article/pii/S0168900214004938, doi:https://doi.org/10.1016/j.nima.2014.04.080.

[149] C. Adler and *et al.* The RHIC zero degree calorimeters. *Nuclear Instruments and Methods in Physics Research Section A: Accelerators, Spectrometers, Detectors and Associated Equipment*, 470(3):488–499, 2001. URL: https://www.sciencedirect.com/science/article/pii/S0168900201006271, doi:https://doi.org/10.1016/S0168-9002(01)00627-1.

[150] YF. Xu, JH. Chen, YG. Ma, and *et al.* Physics performance of the STAR zero degree calorimeter at relativistic heavy ion collider. *Nuclear Science and Techniques*, 27(126), 2016. doi:https://doi.org/10.1007/s41365-016-0129-z.

[151] C. A. Whitten. The Beam-Beam counter: A local polarimeter at STAR. *AIP Conference Proceedings*, 980(1):390–396, 2008. URL: https://aip.scitation.org/doi/abs/10.1063/1.2888113, arXiv:https://aip.scitation.org/doi/pdf/10.1063/1.2888113, doi:10.1063/1.2888113.

[152] M. Beddo and *et al.* The STAR barrel electromagnetic calorimeter. *Nuclear Instruments and Methods in Physics Research Section A: Accelerators, Spectrometers, Detectors and Associated Equipment*, 499(2):725–739, 2003. The Relativistic Heavy Ion Collider Project: RHIC and its Detectors. URL: https://www.sciencedirect.com/science/article/pii/S0168900202019708, doi:https://doi.org/10.1016/S0168-9002(02)01970-8.

[153] T.C. Huang and *et al.* Muon identification with Muon Telescope Detector at the STAR experiment. *Nuclear Instruments and Methods in Physics Research Section A: Accelerators, Spectrometers, Detectors and Associated Equipment*, 833:88–93, 2016. URL: https://www.sciencedirect.com/science/article/pii/S0168900216307392, doi:https://doi.org/10.1016/j.nima.2016.07.024.

[154] C.E. Allgower and *et al.* The STAR endcap electromagnetic calorimeter. *Nuclear Instruments and Methods in Physics Research Section A: Accelerators, Spectrometers, Detectors and Associated Equipment*, 499(2):740–750, 2003. The Relativistic Heavy Ion Collider Project: RHIC and its Detectors. URL: https://www.sciencedirect.com/science/article/pii/S016890020201971X, doi:https://doi.org/10.1016/S0168-9002(02)01971-X.

[155] J. Adams and *et al.* The STAR event plane detector. *Nuclear Instruments and Methods in Physics Research Section A: Accelerators, Spectrometers, Detectors and Associated Equipment*, 968:163970, 2020. URL: https://www.sciencedirect.com/science/article/pii/S0168900220304344, doi:https://doi.org/10.1016/j.nima.2020.163970.

[156] S. Zhou and *et al.* Design of the readout electronics system for the STAR sTGC detector. *Nuclear Instruments and Methods in Physics Research Section A: Accelerators, Spectrometers, Detectors and Associated Equipment*, 1021:165797, 2022. URL: https://www.sciencedirect.com/science/article/pii/S0168900221007828, doi:https://doi.org/10.1016/j.nima.2021.165797.

[157] Y Shi, C. Yang, and Q. Yang. The sTGC prototyping and performance test for the STAR forward upgrade. *Journal of Instrumentation*, 15(09):C09021–C09021, sep 2020. doi:10.1088/1748-0221/15/09/c09021.

[158] O.D. Tsai and *et al.* Development of a forward calorimeter system for the STAR experiment. *Journal of Physics: Conference Series*, 587:012053, feb 2015. doi:10.1088/1742-6596/587/1/012053.

[159] F. Niecknig and B. Kubis. Dispersion-theoretical analysis of the $d^+ \to k^-\pi^+\pi^+$ Dalitz plot. *JHEP*, 10:142, 2015. arXiv:1509.03188, doi:10.1007/JHEP10(2015)142.

[160] A. Ryd and *et al.* EvtGen: A Monte Carlo Generator for B-Physics. 5 2005.

[161] M. Lisovyi, A. Verbytskyi, and O. Zenaiev. Combined analysis of charm-quark fragmentation-fraction measurements. *Eur. Phys. J. C*, 76(397), 2016. doi:10.1140/epjc/s10052-016-4246-y.

[162] M. Tanabashi and *et al.* [Particle Data Group]. Review of particle physics. *Phys. Rev. D*, 98:030001, Aug 2018. URL: https://link.aps.org/doi/10.1103/PhysRevD.98.030001, doi:10.1103/PhysRevD.98.030001.

[163] L. Adamczyk and *et al.* [STAR Collaboration]. Measurements of D^0 and D^* production in $p+p$ collisions at $\sqrt{s} = 200\,\text{GeV}$. *Phys. Rev. D*, 86:072013, Oct 2012. URL: https://link.aps.org/doi/10.1103/PhysRevD.86.072013, doi:10.1103/PhysRevD.86.072013.

[164] H. Abramowitz and *et al.* [ZEUS Collaboration]. Measurement of charm fragmentation fractions in photoproduction at HERA. *JHEP*, 09:058, 2013. arXiv:1306.4862, doi:10.1007/JHEP09(2013)058.

[165] S. Acharya and *et al.* [ALICE Collaboration]. Measurement of D^0 , D^+ , D^{*+} and D_s^+ production in pp collisions at $\sqrt{s} = 5.02$ TeV with ALICE. *Eur. Phys. J. C*, 79(5):388, 2019. arXiv:1901.07979, doi:10.1140/epjc/s10052-019-6873-6.

[166] R. Reed. A new detector at RHIC, sPHENIX goals and status. *Journal of Physics: Conference Series*, 779:012019, Jan 2017. doi:10.1088/1742-6596/779/1/012019.

[167] D. Adamova and *et al.* [ALCIE Collaboration]. A next-generation lhc heavy-ion experiment, 2019. URL: https://arxiv.org/abs/1902.01211, doi:10.48550/ARXIV.1902.01211.